Interplay between anisotropy and disorder in ferroelastics: structures and thermodynamics

Pol Lloveras Muntané

Interplay between anisotropy and disorder in ferroelastics: Structures and thermodynamics

Tesi presentada per

Pol Lloveras Muntané

per optar al títol de Doctor en Física

UNIVERSITAT DE BARCELONA

Departament d'Estructura i Constituents de la Matèria
Universitat de Barcelona

Interplay between anisotropy and disorder in ferroelastics: Structures and thermodynamics

Tesi presentada per

Pol Lloveras Muntané

per optar al títol de Doctor en Física

Barcelona, maig de 2010

Teresa Castán Vidal

Agraïments

La realització d'aquesta tesi ha sigut possible gràcies a la meva directora, la Teresa Castán, que en el seu moment em va donar la oportunitat d'incorporar-me al seu grup. En tot moment 'ha demostrat un interès i una disponibilitat inestimables i, d'entre les seves innombrables ensenyances, en voldria destacar la santíssima paciència que ha tingut en les inacabables correccions i millores, tant literàries com formals, dels articles que hem publicat, i de les quals n'he après molt. Vull agraïr enormement també l'ajuda i els consells d'en Toni Planes. Ha tingut temps i respostes per les meves preguntes més variades sense excepció i m'ha mostrat una intuïció per la física i un bagatge envejables. M'agradaria remarcar que, junt amb l'Eduard Vives i en Lluís Mañosa, formen un grup de treball inmillorable tant a nivell personal com professional.

Evidentment en Marcel Porta també ha d'ocupar un lloc principal en aquestes línies. Per a mi és el màxim exponent del rigor i la perseverància en el treball. M'ha ajudat incondicionalment en tot moment i m'ha fet veure que sempre es pot donar una altra volta a problemes aparentment esgotats. També li vull agraïr molts moments compartits fora dels despatxos, sobretot durant la meva estada a Los Alamos, com unes llenties exquisides i unes excursions literalment eternes, de les quals en guardo, a part d'uns records inoblidables, l'espinada d'un cèrvol.

From my stage in Los Alamos, I would like to thank Avadh Saxena and Turab Lookman for very kind hospitality, including several wonderful and spicy dinners. I owe them abundant fruitful discussions and english corrections.

Per tradició, també faré menció de la gent més propera que m'ha compartit durant tots aquests anys.

En l'ambient departamental vull destacar sobretot a la María, l'Oriol i tots els companys de despatx: Carlos Triguero, Xavi Illa, Erell Bonnot i especialment el Xavi Moya, el David, el Pau, l'efímer Francesc, i la sort de tenir la Laura a la taula d'enfront en un món tan masculí. També a tants d'altres, que ja saben qui són, amb qui he compartit moltes estones al passadís.

El suport dels meus pares, l'un en cos i l'altra en esperit, és, ja se sap, incondicional i perenne. A la Glòria, com sempre, li dec tot, i la tesi no n'és excepció.

Finalment, a l'Ammiel i la Clara, de fet, no els puc agraïr del que han fet per la tesi ja que més aviat l'han entorpit deliciosament.

Barcelona, maig de 2010

Preface

For decades, materials exhibiting the unusual ability of recovering large deformations by means of the shape-memory effect and superelasticity have attracted a great interest due to the broad variety of technological applications. They range from medical devices (stents, heart valve tools, bone anchors, dental arch wires, glass frames, etc.), to sensors and actuators (thermostats, control valves) as well as muscular wires in robotics, mechanical aeronautic and underwater couplings and many others. The martensitic, stoichiometric Ti-Ni alloy, commonly known as Nitinol, is currently the most used shape-memory alloy due to its lasting durability (wear and corrosion resistance), repeatability and biocompatibility. However, nitinol exhibits large hysteresis in stress and temperature and a narrow operating temperature range, which challenges a further technological development. Looking for more appropriate working conditions, many other alloy families exhibiting these smart properties have been investigated.

Alternatively, doping has also been observed to substantially (and often critically) modify the stability regimes of a given alloy from the stoichiometric composition –as well as many other aspects of the transition–and arises as a good way to explore and identify new regions of the phase space that are likely to be useful to design materials of technological interest. In fact, over the last years many research efforts have been focused on off-stoichiometric and doped alloys. Actually, for decades it has been known that there exists a critical amount of doping–that depends on the specific alloy–which leads to the suppression of the martensitic transition. Recent studies in some materials like Ti and Ti-Ni based alloysand others have revealed that the non-martensitic structures arising in the non-transforming composition regime show glassy features with the lattice strain as the frozen degree of freedom. Fortunately, shape memory effect and superelasticity are also observed to occur in this regime. This expands significantly the horizons for new, promising nonmartensitic shape memory alloys.

At a mesoscopic level, the final responsible for the management of the resulting thermomechanical behavior is the ferroelastic transition undergone by the material. This is mainly mediated by long-range elastic interactions between the cells of the crystallographic lattice. These interactions depend on the specific cell sym-

metries as well as on the elastic constants, which determine the soft directions of the crystal. Consequently, the elastic interactions may be highly anistropic and may crucially affect the morphology of the internal microstructures. However, this clean description partially breaks down due to the presence of intrinsic inhomogeneities, which put up energy and entropy barriers that cut short the long-range correlations, resulting in a rich behavior landscape. As mentioned, doping arises as the main experimental tool to introduce deliberately a certain amount of disorder in alloys. This general scheme points to the anisotropy and disorder as important ingredients in such systems, which is the main subject of this thesis: How these competing factors affect the morphology of structural patterns and thermodynamic behavior in ferroelastic systems.

This topic may be placed within a more general framework concerning the research on systems exhibiting spatially inhomogeneous states at the mesoscale. In a broad class of functional materials (including high-temperature superconductors, ionic conductors, colossal magentoresistance manganites, ferromagnets and ferroelectrics), intrinsic heterogeneities have been observed to play a key role in determining their properties. Sometimes the presence of disorder even gives rise to fruitful, entirely new properties, absent in pure materials.

The thesis is organized as follows: A brief introduction to ferroelastic materials, and in particular to thermoelastic martensites is given in chapter 1. Chapter 2 is devoted to describe the model used in this work. Chapters 3-5 shows the results derived from computer simulations of the model. In particular, chapter 3 focuses on the morphology of the strain structures; chapter 4 approaches some aspects of the thermodynamic behavior and in chapter 5 thermomechanical behavior is studied. Chapter 6 is devoted to a model describing a magnetoelastic system and shows preliminary results. Chapter 7 summarizes the main results and conclusions of the thesis. Some theoretical mathematical and other details that can be useful for the reader can be found attached in the appendices.

Notation

Letters in bold-face type denote vectors

$\mathcal{A} = C_{44}/C'$: Elastic anisotropy factor

$\mathcal{C}$: Heat capacity

$C' = 1/2(C_{11} - C_{12}) \sim A_2$: Elastic response associated to deviatoric strain

$C_{11} + C_{12} \sim A_1$: Bulk modulus

$C_{44} \sim A_3$: Shear modulus

σ: Stress field

e_1: Bulk strain

e_2: Deviatoric strain: Landau order parameter

e_3: Shear strain

F_{L}: Landau free energy

F_{G}: Ginzburg free energy

F_{GL}: Ginzburg-Landau free energy

$F_{\mathrm{non\text{-}OP}}$: Non-order parameter free energy

F_{η}: Disorder free energy

F_{anis}: Magnetic anisotropy free energy

F_{exch}: Heisenberg free energy

F_{ms} Magnetostatic energy

F_{me} Magnetoelastic energy

F_{ext}: Zeeman free energy

f: Energy density

H_d: Magnetostatic field, demagnetizing field

$\mathbf{m}$: Unit magnetization vector

MT: Martensitic transformation

OP: Order parameter

PBC: Periodic boundary conditions

SMA: Shape memory alloy

SME: Shape memory effect

T: Temperature

T_c: Low stability limit of the high temperature phase in the clean limit

$T_c(\mathbf{r})$: Local distribution of characteristic temperatures due to disorder coupling

T_i: High stability limit of the low temperature phase in the clean limit

T_0: Equilibrium transition temperature in the clean limit

β: Fourth-order Landau coefficient

γ: sixth-order LAndau coefficient

η: Disorder variable

κ: Ginzburg coefficient

ς: Transformed fraction

ξ: Correlation length of the disorder

ζ: Disorder amplitude

Contents

Chapter 1

Introduction to ferroelasticity

The ferroelastic transition allowing for superelasticity and the shape-memory effect (SME) [1] consists of a solid-to-solid nondisruptive phase transformation mediated by an external control parameter such as temperature or stress[1]. Upon cooling the crystallographic structure of the parent phase becomes unstable giving rise to a spontaneous deformation that entails a loss of symmetry so that the point groups of the crystallographic unit cells of the parent and product phases fulfill a group-subgroup relationship [2,3]. Due to this, the parent phase is often called the high-symmetry or disordered phase whereas the product phase is called the low-symmetry or ordered (i.e. close-packed) phase. They are also termed as paraelastic and ferroelastic respectively for analogy with ferromagnetism. By non-disruptive [4]–or displacive–transformation we mean that it takes place by a cooperative rearrangement of the atoms of the lattice in such a way that, despite that there is a lattice distortion and the crystalline structure changes, there is no atomic interchange, so that the neighborhood of each atom remains unalterable from the point of view of local atomic order, atomic bonds and so on. Atomic motion is at the most of the order of the interatomic distances, so that there is no diffusion[2].

---

[1]Later on it will be seen that multiferroics exhibit transitions induced by other parameters like a magnetic field, etc.

[2]Sometimes it is referred as military transformation, opposite to civilian changes, that are dominated by diffusive processes.

1.1 Self-accommodation: Interfaces and microstructure

As a consequence of the symmetry breaking, the unit cell of the product phase may take multiple equivalent states, called variants, that have the same crystal structure but differ in their mutual orientation. The number of such different *symmetry-related* variants depends on the specific symmetry of the cell. In particular, such number is given by the ratio between the number of symmetry elements in the high-symmetry phase and the number of symmetry elements of the low-symmetry phase [5].

Usually, nucleation and growth of the product phase takes place embedded within a host matrix of the parent phase. At the phase boundaries, the lattice misfit is accommodated by elastic strain [6] that, up to a certain extent, is able to hold the continuity of the lattice across the interfaces. However, when the transformation continues, the lattice mismatch may increase in such a way that it cannot be absorbed any more by keeping deforming the same way. Then, in order to preserve coherency, the lattice is forced to deform according a variant of opposite strain, thus reducing the average deformation –and hence the total energy– along the wall. The recurrence of this process gives rise to a microstructure of alternating variants that is energetically favorable since succeeds in making easier the continuity of the displacement field. The macroscopically undistorted planes joining the different phases are called habit planes, and the mechanism by which the strain is induced to modulate in order to enable such invariant planes is called *self-accommodation*. Actually, this process occurs not only at the phase boundaries (para-ferroelastic interfaces) but also at the domain boundaries between different ferroelastic variants. A schematic view of the geometric grounds of self-accomodation is shown in Fig. 1.1 for a square to rectangular transition. The modulations of–averaged–vanishing strain manage to spread out well in the bulk of the product phase due to a knock-on effect [7], which is the essence of the long-range nature of the elastic interactions. Due to the anisotropic nature of the crystallographic cells and to the *will* of the system of mantaining also a coherent fit of the variants along the domain boundaries, *large*, anisotropic structural domains arise. Such long-range multidomain pattern is called *twinning*, and each one of the variants that make it up is called *twin*, due to consisting of at least two equivalent strain states. Therefore, twinning is not an *inherent fact* to the phase transition but the response of the degenerate multi-well structure of the energy to certain –usual– boundary conditions, i.e. a way for the material to reduce its energy.

Figure 1.2 shows two images of different microstructures, belonging to a poly-
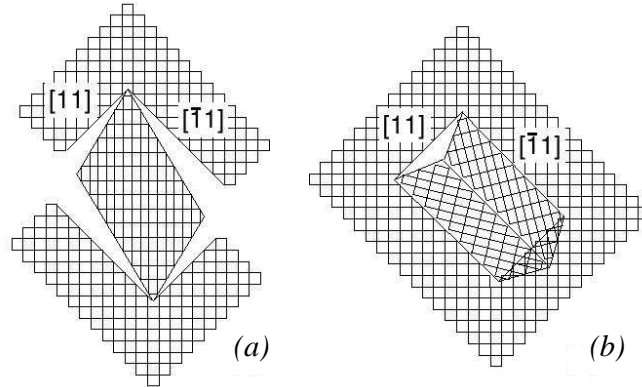
Figure 1.1: The nucleation of the ferroelastic phase usually takes place in a surrounding paraelastic matrix. (*a*) A single domain is completely unfavorable, since the elastic strain required for the accomodation would be too large. (*b*) Actually, to minimize the energy the system takes advantage of the degeneracy of the differently oriented variants and accomodates by alternating twins. This mechanism allows for a macroscopically invariant plane and zero volume net change. In particular, in the square to rectangular transition depicted here, the domain boundaries are properly oriented parallel to [11] direction due to the specific crystallographic symmetries. Notice that additional microscopic strain is needed to coherently match the different phases in the phase boundaries parallel to [$\bar{1}$1] directions. This also contributes to determine the resulting structure.

crystalline sample of tetragonal $Ni_{54}Mn_{25}Ga_{21}$ (*a*) and a sample of monoclinic $Pb_3(VO_4)_2$ (*b*). In both cases, the mesoscopic geometry of the domains is determined by the coherence between twins, which in turn is strongly influenced by the crystallographic symmetries. In case (*a*), tetragonal symmetry leads to parallel twin bands whereas in (*b*) monoclinic symmetry also gives rise to star patterns.

Furthermore, it is worth mentioning that twinning allows for a microscopically deformed material that does not exhibit macroscopic, net change of shape, which is at the origin of the SME. This is schematically shown in (i) and (ii) of Fig. 1.3. Experimentally, it has been observed that twins exhibit a characteristic width l which scales well as $l \propto \sqrt{L}$, where L is the longitudinal size of the transformed region [10–12]. This relationship has been also obtained theoretically as the result of the energetic competition between the interfacial cost of the twin boundaries and the self-accomodation process that favors a periodic twinning with a large wave number. The lowest-energy configuration resulting from the balance between these two contributions consists precisely of twins of equal width fulfilling the relation above.

However, often this is not the case. The actual microstructure of a given ferroelastic material depends on the specific composition, specimen size, grain
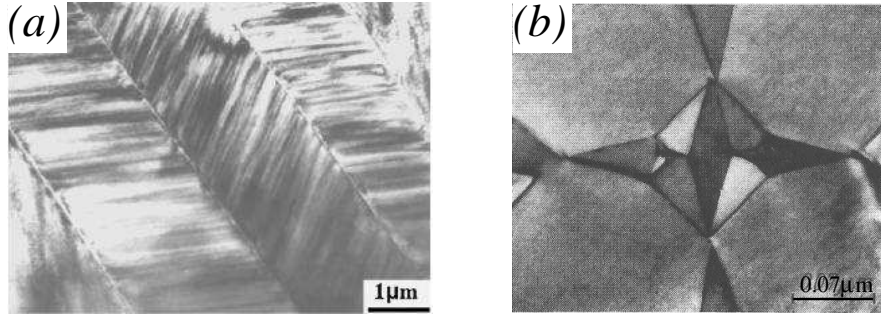
Figure 1.2: (*a*) TEM bright field image at room temperature of twinned microstructure with parallel domain boundaries yielded from a cubic-to-tetragonal transition in $Ni_{54}Mn_{25}Ga_{21}$. Extracted from Ref. [8]. (*b*) TEM image of a twinned microstructures with parallel bands and star patterns originated from a rhombohedral-to-monoclinic transition in $Pb_3(VO_4)_2$. Extracted from Ref. [9].

size, history, external conditions, coupling with other magnitudes like magnetic fields, etc., and may be of high degree of complexity. The length scale of twins may go from few nanometers to tenths of milimeters [13]. Selfsimilar patterns –twins within twins, etc.– have also been observed. Polycrystals show also a coexistence of variants with multiple length scales, etc.

1.2   The shape memory effect

Perhaps, the most relevant aspect related to ferroelasticity is the so-called SME that refers to the ability of a material to recover its original macroscopic shape upon heating after being notably deformed by applying an external stress field. It is based on the fact that the ferroelastic variants can be *easily* switched from one to another by means of a stress field. Again, the crystal takes advantage of the degenerate multi-well nature of the energy since domain switching is an energetically free way for the material to change its shape, whereas a lattice deformation is costly. In particular, upon loading below the transition, the material presents a first elastic stage where the crystallographic cells undergo a low recoverable deformation so that they become slightly stretched according to the specifities of the field. However, when the stress field reaches a certain value, the system undergoes a large deformation, with strains up to 10%, for instance, in Ti-Ni. If the stress field is increased further, the system retakes (retoma,repren) the elastic regime until reaching the plastic regime, and fracture.

Actually, what it happens during the high-response stage is that the specific direction of the stress field favors the coherent growth of one of the variants to the detriment of the others, by moving the domain boundaries (i.e. energy barriers)

existing among them. The growth of the selected variant entails a corresponding change in the macrosopic shape of the specimen, that becomes maximum when it reaches the single variant state. Since any of the ferroelastic variants is stable at the product phase, this structural configuration survives when the field is removed, thus not recovering the multidomain original state. From this point of view such deformation can be labeled as a plastic one. However, it is said to be *apparent* because it is not plastic in the usual sense: ideally, there is no creation and/or motion of dislocations, etc, and the original macroscopic shape can be recovered upon heating. Therefore, it has been called a *pseudoplastic* deformation. Due to the group-subgroup relationship between the phases, upon heating any ferroelastic variant transforms back to the same unique variant of the parent phase. Thus, to a *large* number of possible multidomain configurations and shapes of the product phase corresponds only a single parent phase configuration. This makes the ferroelastic transition to be crystallographically reversible and allows for recovering the original macroscopic shape, i.e. the SME. An schematic representation can be found in Fig. 1.3. Starting from a ferroelastic twinned structure (ii), the macroscopic shape can be pseudoplastically deformed upon loading due to domain switching (iii). Upon unloading, the system remains unaltered and, finally, upon heating the paraelastic phase is reached with the initial shape (i).

It must be pointed out that in practice, although the final state is ideally unique, the retransformation paths that the system can undertake may lead to the creation of defects that moves the final state away from the shape-recovered one. Then, what is desirable is the forward and backward transformations to follow the same path forth and back. With respect to this, long range order helps to keep a single path for both directions of the transition, that results in a small hysteresis in temperature [14].

Let us mention the two-way SME (opposite to the one-way SME explained above), according which upon heating and cooling the system can recover the same low temperature, twinned microstructure. This is due to the fact that in the ferroelastic phase defects cluster at the twin boundaries. Upon heating, twinning disappears but defects may remain *at rest* much more time in such a way that upon cooling the clusters of defects act as pinning centers for new twin boundaries, thus resulting in the same previous microstructure. In fact, samples can be trained by thermomechanical treatment in order to *quench* defects at certain sites where nucleation and/or growth of specific ferroelastic variants occur. All this makes easier the crystallographic reversibility and hence the two-way shape memory effect. This reversible cooling-heating path corresponds to (i)↔(iii) in Fig. 1.3.

(i) Austenite   (ii) Twinned martensite   (iii) Deformed martensite

Macroscopic view
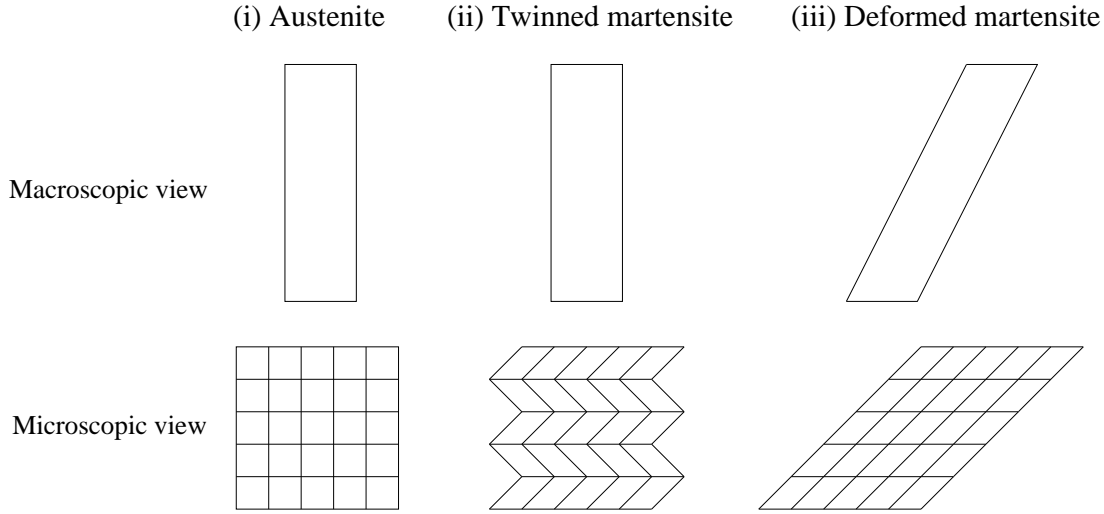
Microscopic view

Figure 1.3: Schematic representation of the microstructures that ferroelastic materials exhibit under different conditions, accompanied by the corresponding macroscopic shapes. This allows for the shape-memory effect and superelasticity.

1.3   Superelasticity

The ferroelastic transformation can be also induced by applying a stress field. The loading process starting from the paraelastic phase is apparently similar to that occurring from the ferroelastic phase: After the usual elastic regime, the system undergoes a large deformation until finally reaching a single variant microstructure. Nevertheless, the underlying mechanisms governing the high-response stage are essentially different. As mentioned in the previous section, in the ferroelastic phase the mechanism is the domain switching whereas in the superelastic regime the material transforms stress-induced to the ferroelastic phase. Note that, in contrast with the temperature-induced transition, no twinning is obtained as a result of the stress-induced transition, since all the crystallographic cells are strained according to the applied stress field and no self-accommodation process takes place.

Focusing on the superelastic behavior, when removing the stress field the system transforms back to the parent phase so that the unit cell (i.e. the whole system) recovers its initial shape. Such ability is called pseudoelasticity and, more recently, also superelasticity. In Fig. 1.3, superelasticity corresponds to the same path as in the case of the two-way SME [(i)↔(iii)] although now this path is reached upon loading-unloading. The critical stresses upon and below which the material undergoes the forward and backward stress-induced transitions respectively are different due to the existence of metastability regimes, so that the system exhibits hysteresis that becomes larger as the temperature of the zero-stress transition is approached.

It is worth highlighting the cross-scale response between different levels of organization that play a relevant role in the properties mentioned above. Thus, macroscopic properties like SME and superelasticity lie on the mesoscale twinned microstructure, that in turn is crucially affected by the crystallographic symmetry properties on the molecular scale.

1.4 Inhomogeneities

In a broad sense, by inhomogeneities we understand any physical magnitude in the material that is not uniform through it. Up to now, the only example of spatial heterogeneities in crystals that we have seen is twinning, that comes from finite-size and shape effects and that turns out to be behind the SME that has many important applications [15]. In fact, spatial inhomogenities in materials are of great interest since often they are known to play a crucial role in confering them relevant and/or useful properties, from both physical and technological points of view. Nevertheless, twinning can be interpreted approximately as a uniform periodic modulation of the strain. In that sense, an intuitive, maybe *more appropriate* definition of *inhomogeneity* should include the presence of some kind of randomness, i.e. more related to the meaning of *disorder*. Precisely, as it is well known, materials (specially alloys) are characterized by the presence of intrinsic, random disorder that cannot be removed, since it is a consequence of imperfect preparation and treatment of the samples.

More specifically, structural inhomogeneities refer to any lattice imperfection that move the crystal away from the pure, regular Bravais lattice [16]. Some lattice points cannot be obtained by a translational operation of the Wigner-Seitz cell but they are singularities such as point defects like impurities coming from compositional fluctuations, vacants, interstitial atoms, substitutional atoms, etc., line defects like dislocations, etc. Alloys should be mentioned as one of the prominent examples containing inherent disorder, in form of compositional fluctuations. Moreover, disorder may be easily increased by means of changing the percentage of each element through off-stoichiometric composition or doping with an extra element. Some experimental studies have approached the distribution of doping through the material. It has been found that doping prefers to substitute those atoms with which shares more similarities from the point of view of electronic affinity, size, etc., although it is clear that it does not entail any order in the material.

1.4.1   Effects on structures and thermodynamic responses

Besides the mentioned effect of acting as pinning sites for twin boundaries, the presence of impurities may of course affect any physical variable, that indeed essentially depends directly on the specific composition of the material. In general, disorder has been found to have many different effects on materials [17]. In particular, it is worth mentioning two effects which are of our interest: First, the presence of impurities may result in a rounding of phase transitions [18], moving away from the sharp case in the ideal clean limit (i.e. in absence of disorder), and giving rise to multiphase coexistence well above and below the transition point. Second, and intimately related to the first, disorder may erect local free-energy barriers in such a way that the total free-energy of the system can adopt a *bumpy* profile with many degenerated and nearly degenerated low-energy states that, however, in general do not correspond to the global minimum of energy, if it still exists [17]. Eventually (and also often), disorder may lead the system to freeze in metastable states and even exhibit glassy features, as will be seen later.

Despite that impurities have a local character, the stress field that is created around them may affect global physical magnitudes mediated by long-range interactions. Actually, a great amount of papers has been devoted to study the influence of doping, i.e. off-stoichiometry composition in thermodynamic properties. In general, it is observed that impurities blur the transition, resulting in anomalies in the specific heat like softening and shift of the peak towards lower temperatures, changes in the baseline, power-law singularities, etc. Indeed, a more accurate sample preparation and annealing results in a decrease and even removing of the anomalies. With respect to this, anomalies in C_p have been proposed to be an indicator of the level of dopant in a material. Also, impurities have been observed to modify the elastic constants of the material. As said, materials can be very sensitive to the presence of impurities, so that the phase diagrams strongly depend on the level of doping. Slightly changing the relative weight of each element in an alloy can result in a large shift of the transition temperature or even inhibition of the transformation. Consequently, the onset temperature above which superelasticity may be obtained by applying a stress as well as the conditions under the SME may take place are crucially affected by the specific composition of the material [19–24].

1.4.2   Pretransitional effects

Pretransitional effect refers to any phenomena occurring in a system that warns of the proximity of a phase transition. Although the abrupt nature of first-order transitions is in principle contradictory with these effects, they are often observed
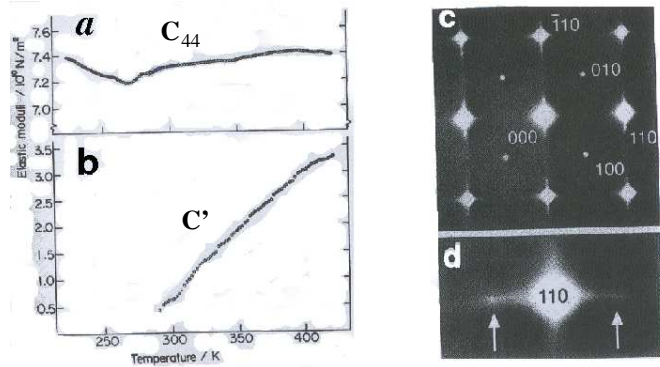
Figure 1.4: (a) and (b): Dependence of C_{44} and C' on temperature in $Fe_{70}Pd_{30}$. Typically, C' softens significantly whereas C_{44} not. This leads to an increase of the elastic anisotropy $\mathcal{A} = C_{44}/C'$. From Ref. [27]. (c) Diffuse streakings in selected area from electron diffraction pattern $Ni_{43.8}Mn_{42.4}Ti_{13.8}$. ($d$) Detail of ($c$). From Ref. [28].

in SMAs already well above the transformation. Prominent examples are the softening of both the TA_2 phonon branch[3] and C' elastic constant upon cooling [2], related to an incipient instability of the parent phase. In fact, this will provide the system with easy channels to develop the oncoming transition. [4] In the diffraction pattern, the phonon and C' softening leads to diffuse scattering [26]. Softening of C' in Fe-Pd and diffuse scattering for Ni-Mn-Ti are shown in Fig. 1.4.

A pretransitional effect involving some strain is termed precursor. The phonons, i.e. random fluctuations of the atoms of the lattice, have a typical relaxation time of the order of 10^{-12}s. This prevents such fluctuations to be observable by any experimental technique. However, sometimes these fluctuations might couple with defects of the lattice, whose lifetime is theoretically unlimited. This coupling leads to fluctuations whose relaxation times are much longer than the free ones, giving rise to long-lived microstructures that are termed *embryos*. Additionally, the mentioned softening of certain elastic constants make such strain fluctuations

---

[3]Occasionally, at a certain nonvanishing wave vector the TA_2 phonon branch also shows an anomalous dip, associated with satellites in the diffraction pattern [25]. Moreover, this dip becomes more pronounced as the transition is approached. In the some ferroelastics, the softening of the anomalous phonon is only partial and is not sufficient to cause the transition, that in this case is dominated by an homogeneous stress-free distortion. By contrast, in others the transition takes place precisely when the energy of the anomalous phonon vanishes [5]. However, the origin of this anomaly still remains unclear.

[4]Some pretransitional effects are, however, observed *independently* of an occurrence of a phase transition. Whether the such effects *announce* the transition or simply they occur independently of it, is actually a current discussion. It seems not to obey a general law but to depend on the specific case. In general, martensitic transitions do not require pretransitional effects but if they occur, the transformation may be affected, for instance, in the specific pathway.

prefer to correlate according to the corresponding soft directions of the crystal. Although the magnitude of the strain is so low that it cannot be considered as a phase coexistence, the occurring symmetry breaking anticipates the new lattice symmetries of the product phase [29].

Murakami *et al.* [30] have suggested that the morphology and in particular the directionality exhibited by the resulting pretransitional structural pattern depends on the elastic anisotropy factor $\mathcal{A}$ of the material. For a cubic system in particular, it is defined as $\mathcal{A} = C_{44}/C'$ where C_{44} and C' denote elastic constants associated to shear and deviatoric stresses respectively. According to this, it has been observed that materials with low $\mathcal{A}$, like Ti-Ni, exhibit embryos of almost spherical shape (mottled structure) whereas materials with high $\mathcal{A}$ are observed to exhibit a typical structural pattern called *tweed*[5] [31], wich is a modulation in the strain consisting of striations parallel to the traces of $\{110\}$ planes appearing at intervals of few nanometers.[6] Cu-Zn-Al, for instance, exhibits tweed only in the vicinity of the surface (not in the bulk as in Ni-Al) and it has been attributed to a higher $\mathcal{A}$ for this region than for the bulk. This is believed to occurr because the observed high concentration of atoms of Zn and Al in the surface might raise the transition temperature, which is related to a lower C' constant [32]. A comparison between the values of the elastic anisotropy between different alloys is given in table 1.1. It can be seen that Ti-Ni and Ti-based alloys show a particularly low value of $\mathcal{A}$ compared to other alloys. Altough all of them exhibit softening of C' when decreasing the temperature, tweed is only reported in those alloys with a high value of $\mathcal{A}$.

It is accepted that, at *very* high temperatures, due to thermal fluctuations tweed appears to be dynamic [7, 33] in the sense that cannot be observed by any imaging techniques but the diffuse streakings in the Bragg peaks reveal the existence of such fluctuations. As the temperature is lowered, thermal fluctuations decrease and tweed can be considered to be static from the point of view of the laboratory time scale so that it can be captured [33], for instance, by transmission electron microscope (TEM) technique. Generally, on further cooling below the transition point, any pretransitional strain pattern usually evolves toward the more coarsened transformed twinned structure of larger strain. Nevertheless, if, as menioned above, high defect concentration leads to inhibit the ferroelastic transition, the coarsening of the domains is prevented and the pretransitional patterns may survive even down to 0 K [34].

---

[5] *Tweed* refers to the typical scottish textile pattern.

[6] Although the precise periodicity in the tweed structure depends critically on the imaging conditions, there exists a general agreement in that it is on the scale of ten to hundreds of lattice constants.

Alloy	Softening of C'	$\mathcal{A}$	Tweed	Ref.
$Fe_{70}Pd_{30}$	yes	~ 15	yes	[27]
$Ni_{62.5}Al_{37.5}$	yes	~ 9	yes	[30]
Cu-Zn	yes	~ 11	yes	[35]
$Cu_{68}Zn_{16}Al_{16}$	yes	~ 14	yes	[32,36]
Cu-Al-Ni	yes	~ 13	-	[37]
Au-Zn-Cu	yes	$\sim 12-20$	-	[37]
Au-Cd	yes	$\sim 11-14$	-	[37]
Ni_2MnGa	yes	~ 23	yes	[38,39]
$Ti_{49.7}Pd_{43.8}Cr_{6.5}$	-	~ 3.6	weak	[40–42]
$Ti_{50}Ni_{50}$	yes	~ 2	no	[37]
$Ti_{50}Ni_{48}Fe_2$	yes	~ 2	no	[30]
$Ti_{50}Ni_{40}Cu_{10}$	yes	~ 2.4	-	[37]
$Ti_{50}Ni_{30}Cu_{20}$	yes	~ 2.8	-	[37]

Table 1.1: Comparison of elastic anisotropy values for several SMAs (Values near the transformation temperature). The existence of softening in C' and tweed is also mentioned, together with the corresponding references. Dash symbol means that the corresponding feature is unknown for the specific alloy (at least to us).

1.5 Martensites

Martensites refer to those materials undergoing a diffusionless first-order[7] structural phase transition that are dominated by a shear or combination of shears [44]. Hence, it is clear that they are good candidates to be ferroelastic. In martensites it is common to refer to the high-symmetry phase as austenite and to the low-symmetry one as martensite itself. From the point of view of the magnitude of the spontaneous strain, three classes of martensites can be identified: M1, M2 and M3 involving small, moderate and very large strains respectively. Moderate and large strains can involve atomic displacements of the order of the unitcell dimensions in such a way that they can entail important changes of symmetry. For instance, new symmetry elements can appear that break the group-subgroup relationship between the phases and the transformation loses reversibility. Moreover, in M3 martensites the transformation occurs explosively (called the *burst* effect [4, 43]) in such a way that the transformation is morphologically irreversible. The elastic strains are not able to remove the large internal stresses during the transition but the material undergoes a notable plastic (i.e. non-recoverable) plastic deformation, with many lattice imperfections. All this prevents such class of martensites from exhibiting the SME. Instead, in M1 class the nucleation and growth of martensitic

---

[7]In fact, a martensitic transition can also be second order, when, for instance, couples to other second order transitions, like ferromagnetic transition [43].

domains are observed to occur thermoelastically, that means that at each step of the transformation, the system is in thermoelastic equilibrium. It is given by a local balance between the driving force originated from the difference between free energies of the two phases and the elastic energy [45]. This makes the transition be reversible. Such class of martensites is precisely that displaying the SME.

The martensitic transition (MT) process occurs in sudden jumps, giving rise to an avalanche-type dynamics. At each jump the partial transformation occurs instantaneously, in comparison with laboratory time scales. Thermal fluctuations are not the triggering factor leading up to the transition. In order the material to keep transforming it needs to be continuously driven by an external field, either the temperature or a mechanical stress. In that sense the temperature acts as an external control parameter. Actually, the long-range character of the elastic interactions supresses the otherwise decisive role of the critical fluctuations, thus making the transition athermal [46].The complete temperature-induced forward transition (austenite to martensite) takes place between two temperatures called *martensite start* (M_s) and *martensite finish* (M_f) whereas the backward transition (martensite to austenite) occurs between the *austenite start* (A_s) and *austenite finish* (A_f) temperatures.

MTs have been observed in a wide range of materials like metals, alloys, ceramics and even biological systems [13]. Here we will focus in martensites exhibiting SME like several iron-based alloys, Ti-Ni-based alloys, Heusler alloys, Ni-Al and many others. For simplicity, from now on, MT will refer exclusively to this class of martensites exhibiting SME.

1.6   Ferroics and multiferroics

Ferroelasticity shares many features with other phenomena like ferromagnetism [47,48] and ferroelectricity [49], where magnetization and polarization play the role of the strain respectively. All of them have in common the existence of a physical magnitude (those just mentioned) which takes spontaneously nonvanishing values below a certain temperature due to the existence of a phase transition from a high-symmetry, disordered phase to a low-symmetry, ordered phase, which shows long-range patterns such as magnetic/polarized domains, etc. These patterns originate from a combination between a degenerated multiwell energy profile, long-range interactions of dipole-dipole type decaying with distance as $1/r^3$ and geometric considerations of the system such as the symmetries of the underlying lattice, size and shape effects, interfaces, etc. It is worth mentioning that the square root scaling relationship between the domain stripe width and the product phase

size observed in ferroelastics also holds for both ferromagnets and ferroelectrics. Moreover, other dynamical-geometrical relations have been found [50].

Also, at low temperatures the response of such systems to the conjugated external field forms a characteristic field-variable hysteresis loop, resulting from an easy domain switching. Despite the evident differences among these systems[8], the interesting parallelisms in their underlying physics make them to be brought together under the more general name of *ferroics* [4].

It is clear that the microscopic origin of the different macroscopic pysical variables lies in the same underlying bricks consisting of the fundamental electromagnetic interactions It is therefore expectable the various physical magnitudes to be coupled to a certain extent. Many times this coupling is weak and therefore it is logic to treat such variables independently as above. However, a strong coupling among them is often observed macroscopically in such a way that some materials exhibit a relevant cross-variable response: for instance, the electric field can affect the magnetization as well as the magnetic field affects the polarization, which is called magnetoelectric coupling.[9] An immediate consequence of this coupling are the mixed-variable patterns, and the possibility of controlling the corresponding macroscopic physical properties by different external fields has led to an important technological interest.. Magnetic twins depend on structural twins, and vice versa, and, consequently, a structural variant can be switched by a magnetic field. Magnetostriction [51] and the magnetic SME [52] are changes in volume and shape by means of an external magnetic field. Also, magnetocaloric effect is observed to be enhanced when it is accompanied by a structural transition. Colossal magnetoresistance (CMR) effect [53] refers to dramatic changes in conductivity due to the presence of a magnetic field. Materials exhibiting coupling between different variables are called *multiferroics* [2]. A visual scheme accounting for this cross-variable response is shown in Fig. 1.5.

Many properties in materials have been observed to be very sensitive to the presence of inhomogeneities, and the cross-variable coupling exhibited by multiferroics enhances considerably the range of phenomenology. Nowadays such inhomogeneities are even well nourished with the aim of improving known properties or discovering novel ones[10]. It is well known that the gap in semiconductors appears when the system is conveniently doped. CMR only occurs when two phases (metal and insulator) are in competition [55–57]. Polar nanoregions significantly affect the structural properties in relaxor ferroelectrics and it has been suggested

---

[8]Note that, for instance, strain is a second-rank tensor whereas and magnetization is of first rank.

[9]Actually, the magnetoelectric coupling is mediated by strain.

[10]Of course, many times this is not the case, being the disorder an incovenient for the desired properties.

Figure 1.5: Coupling between different magnitudes gives rise to a cross-variable response in multiferroics. Extracted from Ref. [54].
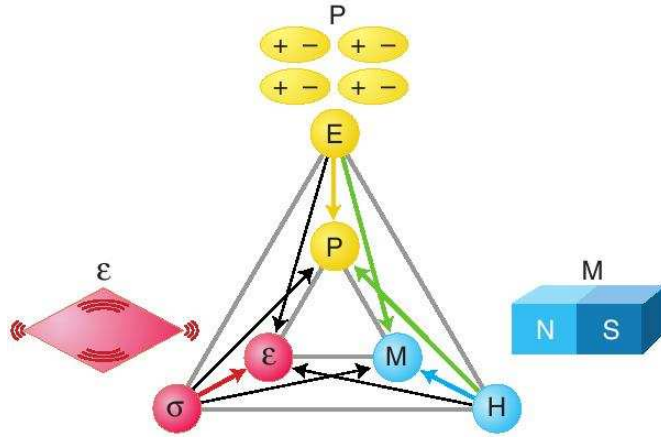
to contribute to the ultrahigh piezoelectric effect observed in these materials [58]. Semiconductors, ionic conductors, high-T_c superconductors, colossal magnetoresistive (CMR) materials [59, 60], ferromagnets [61, 62] and ferroelectrics [63] are only few examples whose behavior lies in the presence of inhomogeneities.

Also, nanoscale precursor modulations are not exclusive to ferroelastic systems, but instead they occur in a broad class of ferroic materials including ferromagnetic [61] and ferroelectric materials [63]. Thus, ferromagnetic nanoclusters in the paramagnetic phase, called Griffiths phase, are known to occur in systems with quenched disorder. [64, 65]. The specific symmetry properties of the anisotropy determine the selected pattern. High anisotropy pretransitional stripe-like pure magnetic patterns, observed for instance in Co-Ni-Al [61], have been labelled as magnetic tweed by analogy with structural tweed [62, 66]. Cross-hatched magnetoelastic tweed resulting from the coupling between elastic tweed and magnetic degrees of freedom has been also observed [66]. Moreover, all these pretransitional textures are accompanied with anomalies in susceptibilities and other response functions.

1.7 Brief introduction to glasses

Although the glass phenomenon was in principle far from ferroelasticity, in a series of recent experiments [20, 34, 67–73] glassy behavior has been detected in the strain of some ferroelastic martensites and has popularized the term *strain glass*. Because of this, here we give a very short overview about glasses.

The material historically known as *glass* has some particular characteristics that prevent a conventional, equilibrium thermodynamic understanding. Structural glasses [74], as they are known among physicists, are materials in the solid state which differs from crystals in the lack of any long-range order. Instead of

the typical crystallographic translational symmetry, the atomic arrangement is disordered; only a short-range order survives due to the chemical bonds with the surrounding neighbors, but at some atomic distances the configuration may be completely different. Neither a Wigner-Seitz cell nor any Bravais lattice can be defined and this results, for instance, in a X-ray diffraction pattern consisting only in a few broad peaks [75] instead of the typical multiple-narrow-peak pattern. Such glasses are formed by rapid melt quenching from the liquid phase that prevents the crystallization and leads to a freezing of an amorphous structure, like supercooled liquids. Nevertheless, they mantain all the mechanical properties of solids, since the only degrees of freedom that survive are precisely phonons, whereas rotational and translational motion is arrested.

Nowadays, in physical science, the meaning of glass has been extended to include a wide range of systems that share some general features similar to those explained above. They mainly differ in the particular degree of freedom that freezes and blocks in a disordered state. For instance, spin glasses [76] are systems in which the magnetic degrees of freedom are anchored in random orientations. In orientational glasses [77], translational order exists but the molecules exhibit frozen, disordered orientations, whereas ferroelectric relaxors [78] show static, random electrical dipoles. Other examples are vortex glasses in superconducors [79].

All of them are characterized by a high-temperature phase where the degrees of freedom of interest fluctuate freely. Moreover, in most cases such systems undergo a phase transition when decreasing the temperature towards a more ordered state, like liquid-crystal, para-ferromagnetic, para-ferroelectric, etc. However, under certain conditions, the transition can be supressed and instead of that fluctuations freeze, leaving the system in a disordered, glass state. Usually, such a state is metastable with respect to the true equilibrium, ordered state. The material, that is said to undergo a glass transition, is not able to reach this equilibrium state since it is characterized by a slowing-down dynamics and ergodicity breaking [80], which are associated to the dilation of the relaxing time scales. In many cases, relaxing times become infinite to all intents and purposes and make the system remain forever in the metastable state. This can be explained by a total energy with a bumpy profile with multiple (nearly) degenerated low-lying states which makes it difficult for the system to find an optimal way to reach the global minimum. Eventually, this way may not exist or may be thermodynamically unaccessible.

Curiously, although the phenomenology among these kind of different systems is very similar, from a thermodynamic point of view glasses may have different origins. Thus, structural glasses arise as a consequence of an ultra fast cooling, whereas other glasses occur due to geometrical frustration [81–83], like the paradigmatic antiferromagnetic triangular lattice. In this case, all the antiferromagnetic bonds cannot be satisfied simultaneously, i.e. the exchange energy

cannot be minimized due to the geometry of the lattice and, hence, the thermo-
dynamic equilibrium state does not exist. Instead, many spin configurations of
very similar low energy are unlikely to evolve towards little lower states since it
may imply to flip spins wich would lead to nonfavorable parallel bonds in other
neighboring regions. On the other hand, and more interestingly, it has been
observed that phase coexistence may give rise to glassy features due to kinetic
freezing [84]. It is believed that point defects are at the origin of the such glassy
behavior in ferroics when doping, which links with some comments on inhomo-
geneities in Sec. 1.4.1. In contrast with geometrical frustration, here a true
thermodynamical phase is likely to exist although it is unaccessible due to energy
and/or entropy barriers [85]. Actually, this is our case here, where glassy behavior
has been observed in the non-transforming composition of the martensitic system
Ti_{50-x}-Ni_{50+x} for $x > 1.5$. There the frozen disordered degree of freedom is only
the lattice deformation[11] and hence this glassy system has been called *strain glass*.

1.8   Shape memory alloys. Fe-Pd and Ti-Ni

The type of alloys exhibitng SME is enormous, although all of them can be grouped
within the huge family of intermetallic alloys; that is, compounds containing two or
more metallic elements, containing optionally one or more non-metallic elements,
typically some rare earths (La, Pr, Nd, Sm, etc.) or even alkalyne elements (Sr,
Ca, Ba, etc.) forming manganites.[12] Here metallic elements also include poor
metals and metaloids. Thus, we find SME in binary alloys like Au-Cd [86], Fe-
Pt [87], Ni-Al [88], Cu-Al [89], Ti-Pd [90], In-Tl [91], Cu-Zn [92], Ta-Ru and Nb-
Ru [93], ternary alloys like Cu-Zn-Al [94], Au-Cu-Zn [95], Cu-Al-(Ni,Be) [96,97],
Pd-In-Fe [98], Ni-Co-Al [99], Ni-Mn-(Sn,In,Ga) [23, 100, 101], Ni-Ti-Cu [22], Ni-
Ga-Fe [102], quaternary like Ni-Mn-Ga-(Fe,Co,In) [103–105], Ni-Co-Mn-In [24],
Ni-Al-Mn-Fe, Ni-Fe-Al-B [106], Cu-Al-Zn-Mn [107], Ti-Hf-Ni-Re [108], etc.

More than 20 years ago a series of papers led by R. Oshima [27, 109–113] were
devoted to characterize Fe-Pd SMA. With respect to the famous Ti-Ni alloy, a
complete review from K. Otsuka and X. Ren can be found in Ref. [114]. In the
following we give a comparative brief overview between these two SMA, Fe-Pd
and Ti-Ni, that will serve as a summary of the different aspects approached in
this introductory chapter. We focus on them because they show very different
peculiarities that are of our interest:

---

[11]Note that other glasses mentioned above may show freezing of the lattice deformation but
it is usually accompanied by freezing of other degrees of freedom

[12]Manganites are compounds of the type $R_{1-x}M_xMnO_3$, where R is a rare earth and M an
alkalyne element

- $Fe_{70}Pd_{30}$ undergoes a very weak first-order phase transition from a cubic to tetragonal crystal structure whereas equiatomic TiNi shows a more complex behavior, with various possible martensitic transformation paths: $B2 \rightarrow B19$ ($\rightarrow B19'$), $B2 \rightarrow B19'$ and $B2 \rightarrow R$ ($\rightarrow B19'$) where $B2$, $B19$, R, $B19'$ stand for cubic, orthorhombic, trigonal and monoclinic crystallographic lattices respectively.

- Ti-Ni exhibit a low value of the elastic anisotropy factor, $\mathcal{A} \sim 2$ whereas Fe-Pd has a high value, $\mathcal{A} \sim 15$. This is consistent with the fact that Fe-Pd shows the strongly anisotropic pretransitional tweed pattern [112, 113, 115, 116] whereas Ti-Ni exhibits very rich precursor effects but no tweed contrast has been observed. Instead, Ti-Ni shows small domains of the incoming phase down to 5nm of almost spherical shape [34]. The low value of $\mathcal{A}$ for Ti-Ni comes from the fact that, although C' softens as it is usual, C_{44} also decreases with decreasing temperature, which is unusual among most of such alloys [37].

- Both Fe-Pd and Ti-Ni show a very high sensitivity on composition. $Fe_{70}Pd_{30}$ transforms to martensite at $T \simeq 257$ K whereas in $Fe_{68}Pd_{32}$ the transition temperature drops to 0 K [33]. Stoichiometric Ti-Ni transforms at $T \simeq$ K whereas in $Ti_{48.5}Ni_{50.5}$ the martensitic transition is suppressed as well [34]. Doping in both Fe-Pd [117] and Ti-Ni [37] modifies significantly many aspects as characteristic temperatures, transformation paths, etc. The elastic constants are observed to depend on composition.

- Ti-Ni is able to recover strains up to $\sim 7-8\%$ by means of SME and SE [19] and shows high mechanical performances [118] as mentioned in the preface. In contrast, Fe-Pd exhibits very poor superelasticity, with strain recovery as small as 1% or less [119].

- Fe-Pd (as well as the ferrous SMAs) shows strong magnetoelastic coupling [52, 120] which leads to giant magnetostriction [51, 121] up to 3% and ferromagnetic shape memory effect [122]. Instead, in Ti-Ni (which is paramagnetic) no magnetic-field induced martensitic transitions have been observed [123] due to a small diference in magnetic moment between austenite and martensite. It is worth mentioning that, recently, some efforts [124, 125] have been adressed to design composites containing both Ti-Ni and a ferrous component as an attempt of combining the excellent mechanical properties of the former and the fast actuation of the latter.

Chapter 2

Elastic model

Modeling of ferroelastic martensites has been adressed from decades. Although a displacement-based picture has been eventually used [126], most of efforts have point at the strain field as the *natural* variable, suitable to describe deformations on solids. Eshelby [127] was the first in approaching the problem of the equilibrium strain of an inclusion within an undeformed matrix by means of microelasticity. The stresses that appear relax thus creating the stress-free strain field in the inclusion and in the surrounding matrix, given by the condition of mechanical equilibrium in the stress field.[1] He pointed out that that problem could be solved by a sequence of simple operations. However, an analytical solution could be found only in a few simple cases. As keystone, Khachaturyan [128] proposed a method based on the decomposition of the elastic strain field in a macroscopic strain and an internal strain which took advantage of the Fourier transform properties. Toghether with some elastic energy considerations, this theory gave rise to some important results, as the fact that, in general, the inclusion is strained as necessary to provide a crystallographically coherent match to the matrix in its habit plane. This confines the elastic energy and elastic strain to the inclusion and makes the habit plane a strain-free junction. Khachaturyan easily connected this with the martensitic transformation (MT), which simultaneously was also approached by Roitburd [129] in a very similar way. Khachaturyan also succeeded in explaining the periodicity of the twin patterns to depend on the width of the transformed region, finding the experimentally observed square root scaling law [130]. Later on, this phase-field microelasticity-based theory [131] has been widely used to model other phenomena related to martensites as, for instance, stress-strain behavior in polycrystalline materials [132] and the ferromagnetic SME [133].

---

[1]The mechanical equilibrium is given by the Cauchy's first law or, more generally, generalized Hooke's law which is simply the Newton's second law applied to elasticity in a continuous, solid media. We recall that an introduction to the linear theory of elasticity can be found in App. A.1, in which the Hooke's law is described in eq. (A.8).

Earlier, Wechsler [134] developed the crystallographic theory of martensite, according to which the alternation of thin strips of different crystallographic variants of the transformed product(twins) allows for invariant planes, as it has been mentioned in chapter 1. This non-linear crystallographic theory has the advantage of automatically accounting for finite strains and rotations but, instead, it does not involve energy considerations as the linear elastic model of Khachaturyan and Roitburd does, and which, in some cases, become necessary. Ball & James [135] developed a model which approximately put together the advantages of both crystallographic and linear elastic theories. It was based on a nonlinear elastic free energy that was invariant with respect to rotations and crystallographic symmetries.

The first detailed analytical description of the SME by means of the Landau theory is due to Falk [136], who also realized that the Landau free energy could be rescaled in such a way that no free parameters remained in the model. Later, he also introduced a gradient (Ginzburg) term to make an analytical study of the interfaces [137]. The large flexibility of the Ginzburg-Landau (GL) theory due to its partial phenomenological nature has been used to approach a wide variety of problems in a simple manner. Elastic solitons were studied by Jacobs [138] and later by Barsch and Krumhansl [139] using a GL model including long-range interactions. GL models including long-range interactions coming from St. Vénant compatibility constraints [140–142] have been successful in modeling a wide variety of problems, including three-dimensional structures [143], different group-subgroup transitions (like square to rectangular, triangular to rectangular [144], tetragonal to orthorhombic, monoclinic and triclinic transformations [145]), star patterns like in Fig. 1.2, inertial, Langrange-Rayleigh type dynamics [144], etc. A three-dimensional Landau model including more realistic, inertial dynamics as well as the strain as the control variable by means of a multiple order parameter free energy has focused on the dynamical evolution of strain-induced stress-strain behavior [146]. Another quite refined phase-field Landau model allows for a quantitative characterization pf stress-strain relations by means of all temperature-dependent thermomechanical properties of both phases such as second and third order elastic constants, transformation strain independent of stress and temperature, and little temperature dependence of hysteresis [147,148]. Recently, spin-based approaches to the Landau model have also been proposed [46,85,149]. Other models have also focused on diverse aspects of the SME [150–152].

The model used in this thesis is based on a GL free energy extended to include both long-range anisotropic interactions coming from compatibility, and disorder coupling to the strain through the harmonic coefficient. Such a model contains the four required ingredients to perform simulations of a system undergoing a MT and exhibiting pretransitional phenomena and effects coming from

inhomogeneities in general. These are the following: (i) Temperature-depending free energy to account for the transition, which are provided by the Landau free energy.(ii) Interfacial energy and (iii) long-range anisotropic interactions giving rise to domain boundaries. And (iv) quenched-in random disorder allowing for inhomogeneities. In the following sections these four terms constituting the model are described in detail. Last one is devoted to numerical details and some other comments.

2.1 Landau free energy

The Landau theory [153] is a phenomenological theory that attempts to describe phase transitions. It is lacking in microscopic basis, so that it does not take into account the level of atomic interactions, thus moving away from atomistic models. Instead, it is based on a coarse-graining of the system in order to place the length scale in a mesoscopic level[2]. According to this theory, during the phase transition the given system usually suffers a symmetry breaking, going from a high-symmetry –disordered– phase towards a low-simmetry –ordered– phase. Associated with the symmetry breaking an order parameter (OP) can be defined[3] in such a way that vanishes above the transition and takes non-zero values below it. Examples of OP are difference of densities in liquid-vapor transitions[4], magnetization and polarization in ferromagnetic and ferroelectric materials respectively, some strain tensor components in structural transitions, etc. Landau theory was first proposed to describe the transformation near the transition temperature, i.e. for small values of the OP, but later it has been widely used to describe the transition in an extended temperature interval so that the OP can take relatively large values. All this ensures that a full thermodynamic treatment is indeed appropiate, giving rise to mean field results. This theory is based on the assumption that near equilibrium the Landau free energy of the system –denoted by F_L– is analytical, continuous and differentiable[5], and can be written in a functional form as an expansion in power series of the OP ϕ about $\phi = 0$. Accordingly, F_L can be expressed as follows:

$$F_L(\phi; T, \psi) = F_{L_0} + \sum_{i=1}^{N} \frac{A_i}{i} \phi^i \tag{2.1}$$

---

[2]This will be discussed with more detail at the end of this chapter.

[3]More than a single OP may be used if required.

[4]Nevertheless, there is no symmetry breaking in this case

[5]Note that, since F_L is analytic, continuous and differentiable also in the transition point, it cannot take into account the singularities of diverging thermodynamical potentials and therefore it is not able no reproduce the actual critical exponents, etc.

where T denotes the temperature and ψ the conjugated field of the OP ϕ whereas the coefficients A_i are suposed to be analytic functions of T and ψ. The role of T and ψ is fundamentally different from that of ϕ. Indeed, T and ψ are state variables that can take any pair of independent values, thus characterizing other state variables like thermodynamical potentials, etc. Actually, they are external control parameters that can induce the transition. Instead, ϕ takes only meaningful values when $F_{\rm L}$ is minimum. There, $F_{\rm L}$ becomes a function only of T and ψ and coincides with a particular termodynamical potential, depending on the specific case. The expression for $F_{\rm L}$ in eq. 2.1 is versatile enough to characterize a considerable wide range of phase transitions.

If we deal with a spatially extended, continuous system, the OP ϕ is a spatial field $\phi(\mathbf{r})$. Then, $F_{\rm L}$ denotes the total energy of the system and can be calculated as an integral of the Landau free-energy density f over the whole system: $F = \int_\Omega f[\phi(\mathbf{r})]d\mathbf{r}$, where f takes the same expression as in eq. 2.1 with the additional spatial dependence given through the field $\phi(\mathbf{r})$, and, in general, through the coefficients $A_i(\mathbf{r})$.

Symmetry adapted strains

Our aim consists of modeling a first-order, cubic-to-tetragonal MT. However, given that many times the important acoustic waves and, consequently, the related inhomogeneous strain fluctuations of interest are observed not to occur in 3D but in subspaces of lower dimensionality [5], the modeling can be confined to the same subspaces. This is indeed the case of some cubic-to-tetragonal MTs, where the transformation may be performed in the rectangular cross section of the tetragonal phase, giving rise to an effective 2D square-to-rectangular transition. Obviously, this makes easier the code and improves the computation time, without loss of generality. On the other hand, it should be pointed out that a pure 2D model seems not to be appropriate to perform simulations for thin films since the presence of free surfaces are relevant for the possible modulations of the strain. Actually, surface relaxations may cause important bendings in the third dimension like, for instance, tunnel and tent-like structures, etc. [13].

Within this framework, it is more convenient to work with the so-called *symmetry adapted strains* as the natural, irreducible deformations that a square can undergo. In a system with square symmetry, the elastic modulus tensor has only three different nonvanishing elastic constants: C_{11}, C_{12} and C_{44}. By diagonalizing this matrix we find the eigenvalues to be $A_1 = C_{11} + C_{12}$, $A_2 = C_{11} - C_{12} \equiv 2C'$ and $A_3 = 4C_{44}$, that are elastic constants associated, respectively, with the bulk modulus and deviatoric and shear modes. The corresponding eigenvectors are the
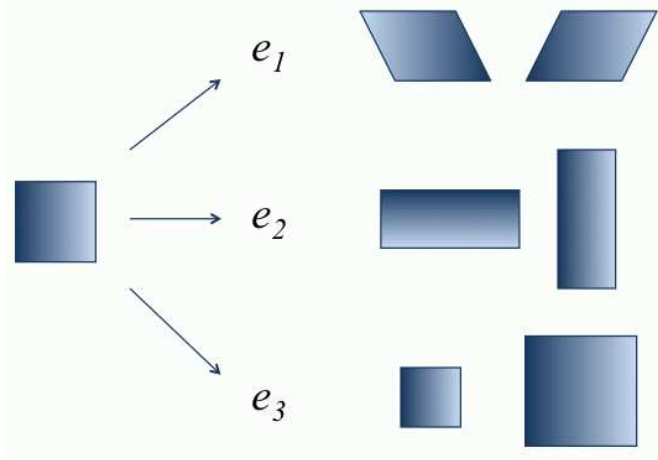
Figure 2.1: Symmetry adapted strains: e_1, e_2 and e_3 stand for the shear, deviatoric and bulk strains.

symmetry adapted strains, that, in terms of the strain tensor components ϵ_{ij} are:

$$e_1 = \frac{1}{\sqrt{2}}(\epsilon_{xx} + \epsilon_{yy}), \qquad e_2 = \frac{1}{\sqrt{2}}(\epsilon_{xx} - \epsilon_{yy}), \qquad e_3 = \epsilon_{xy} \qquad (2.2)$$

where e_1 is the *compressional strain*, that accounts for deformations of volume not shape, e_2 is the *deviatoric strain* (also called diagonal shear), accounting for deformations with no change of angles and e_3 is the *shear strain*, acting parallel to the sides of the square. The opposite relations are:

$$\epsilon_{xx} = \frac{\sqrt{2}}{2}(e_1 + e_2), \qquad \epsilon_{yy} = \frac{\sqrt{2}}{2}(e_1 - e_2) \qquad (2.3)$$

A schematic represention of e_1, e_2 and e_3 is shown in Fig. 2.1. Thus, any deformation can be expressed in terms of these three symmetry adapted strains. As can be seen, the appropriate OP for the square-to-rectangular transition is the deviatoric strain e_2.

The existence of two energetically equivalent variants in the ordered phase (in 2D the two possible rectangle orientations, as can be seen in Fig. 2.1) imposes the symmetry $F_{\mathrm{L}}(e_2) = F_{\mathrm{L}}(-e_2)$. This toghether with the requirement of nonlinearities accounting for the transition lead to the following *Landau free energy density* f_{L}:

$$f_L(e_2(\mathbf{r})) = \frac{A_2}{2}e_2^2(\mathbf{r}) + \frac{\beta}{4}e_2^4(\mathbf{r}) + \frac{\gamma}{6}e_2^6(\mathbf{r}) \qquad (2.4)$$

where it can be easily proved that it must be fulfilled $\beta < 0$ and $\gamma > 0$, whereas A_2 is a sign-variable function of T, that can be written as $A_2 = \alpha_T(T - T_c)$. Here T_c is a metastability limit as will be seen below. In fact, A_2 is called the harmonic coefficient, since it corresponds to the generalized Hooke's law of elasticity, which describes the harmonic motion [154]. Hence, as seen previously, A_2 can be expressed in terms of second order elastic constants[6]: $A_2 = C_{11} - C_{12} = 2C'$. Note

---

[6]Note that the expression may vary (and indeed it does) depending on the dimensionality of the system.

that the dependence of A_2 on temperature makes C' partially soften upon cooling
as it is commonly observed in SMAs in the pretransitional regime.

Temperature-induced transition

Carrying out a simple mathematical analysis[7] of f_L in eq. (2.4) one obtains
the stability values for the strain $e_2 = 0$ and $e_2 = \pm\{\beta/(2\gamma) + [(\beta/(2\gamma))^2 - A_2/\gamma]^{1/2}\}^{1/2} \equiv \pm e_M$ and the following stability limits:

$$T_0 = T_c + \frac{3\beta^2}{16\gamma} \qquad\qquad T_i = T_c + \frac{3\beta^2}{4\gamma} \qquad\qquad (2.5)$$

where T_c is the low stability limit of the high-T phase, T_i is the high stability limit
of the low T phase and T_0 is the equilibrium transition temperature.

Obviously, $e_2 = 0$ corresponds to the unstrained -non-transformed-, square
phase whereas $e_2 = \pm e_M$ corresponds to the rectangular, strained -transformed-
phase, each sign corresponding to one of the two possible orientational variants.
Figure 2.2 shows the evolution of the triple well structure of $f_\mathrm{L}(e_2)$ as function
of T. At $T > T_i$, f_L presents a single minimum at $e_2 = 0$, i.e. the system is in
the high symmetry, square phase. When T is decreased below T_i ($T_0 < T < T_i$),
the global miminum remains at $e_2 = 0$ but two local minima appear at $e_2 = \pm e_M$, meaning that the low-symmetry phase is metastable. At $T = T_0$ the three
minima are of equal energy, thus setting the equilibrium transition temperature.
At $T_c < T < T_0$ the global minima are observed at $e_2 = \pm e_M$ and the minimum
at $e_2 = 0$ is now local, corresponding to the metastability regime of the high-T
phase. Finally, at $T < T_c$, this minimum disappears and only the two minima
$e_2 = \pm e_M$ remain. Figure 2.3 shows the equilibrium (continuous line) and maximal
metastable (dashed line) values of e_2 as function of T. It reveals the discontinuity
of the OP during the transformation and phase coexistence, due to the first order
character of the transition. It also allows for hysteresis, latent heat, etc.

Stress-induced transition

The Landau model is also appropriate to describe isothermal transitions induced
by applying the conjugated, external stress field σ. The total free energy in the
presence of a stress field σ comes from the corresponding Legendre transformation
of f_L:

$$f_{\mathrm{L},\sigma}(e_2) = f_\mathrm{L}(e_2) + \sigma e_2 \qquad\qquad (2.6)$$

---

[7]A phase will be stable if and only if it corresponds to a minimum of the free energy density
f_L. This results from imposing the requirements $\frac{\partial f_\mathrm{L}}{\partial e_2}|_{e_{2_0}} = 0$ and $\frac{\partial^2 f_\mathrm{L}}{\partial e_2^2}\Big|_{e_{2_0}} > 0$
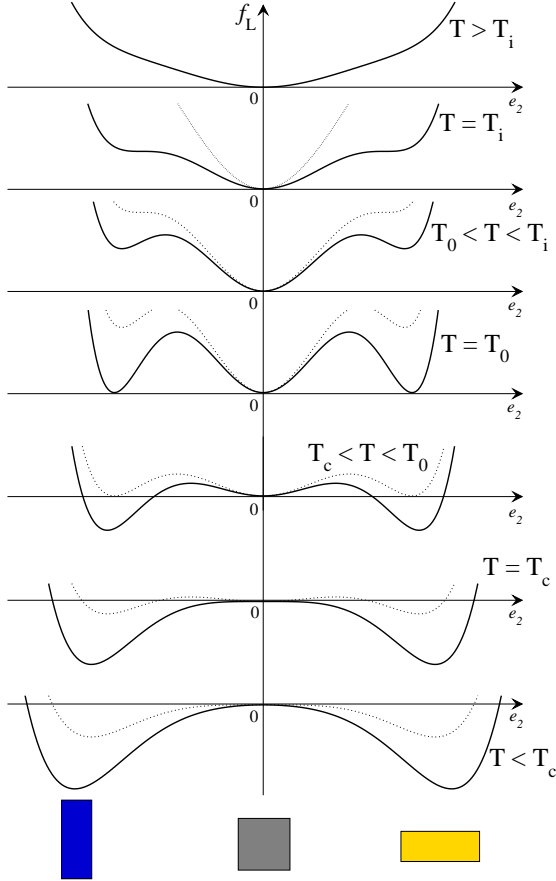
Figure 2.2: $f_L(e_2)$ for different values of temperature T. Since the vertical scale is not conserved in the figure when varying T, in order to make clear the relative size of $f_L(e_2)$, dotted lines that refer to the f_L of the higher contiguous T are drawn. Instead, horizontal scale is kept constant among the different axis.
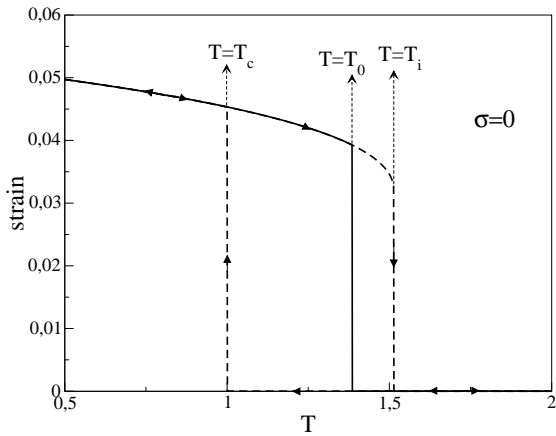
Figure 2.3: Dependence on temperature T of equilibrium (continuous line) and maximal metastable (dashed line) values of e_2. Arrows specify the directions of the trajectories in T, either heating or cooling.

The presence of the stress field deforms the free-energy structure in such a way that, beyond the usual elastic regime, also accounts for the interesting thermo-mechanical phenomena described in Chap. 1, such as superelasticity and pseudo-plasticity, the latter giving rise to the Shape Memory Effect. Profiles of $f_{L,\sigma}$ for different values of σ at different temperatures are shown in Fig. 2.4. Case (a) lead to superelastic behavior whereas (c) and (d) show pseudoplasticity. Case (b) is susceptible to show either superelasticity or pseudoplasticity since in the asbence of the stress field the ferroelastic phase remains metastable.
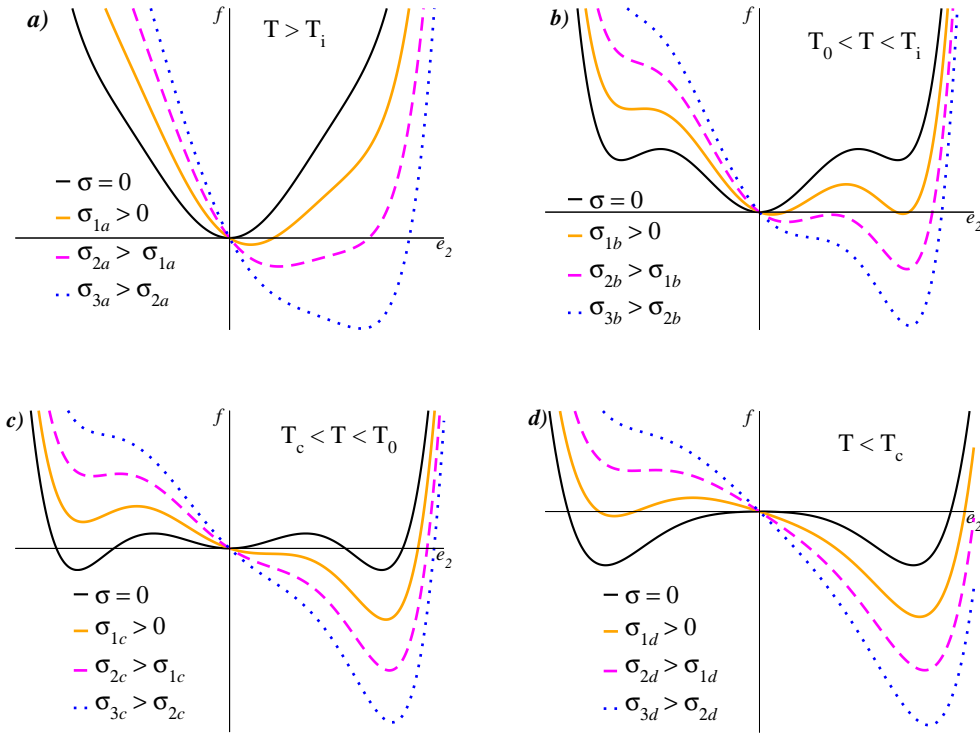
**Figure 2.4:** $f_{L,\sigma}$ for different values of σ and T.

We now proceed analogously to the T-induced transitions and carry out a stability analysis of $f_{L,\sigma}(e_2)$. It has to be computed numerically since it has no analytical solution. Figure 2.5 shows the dependence of e_2 at the minima of $f_{L,\sigma}(e_2)$ as function of T. We can also analyze the dependence of the minima of e_2 on σ, which is shown at three different temperatures in Figure 2.6. Here, σ is displayed in the y-axis for better comparison with the usual strain-induced stress-strain experiments. Continuous line indicates the equilibrium trajectory and dashed lines are the maximal metastability regime. Case (a): Below the transition, the system shows pseudoplastic behavior, since the strain cannot be
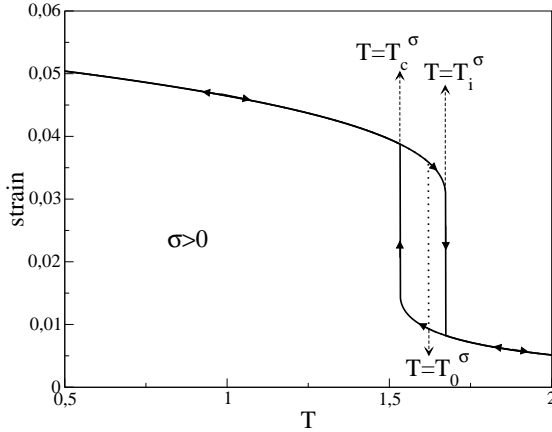
Figure 2.5: Evolution of e_2 at the minima of $f_{L,\sigma}(e_2)$ as function of T at constant $\sigma > 0$. The maximal hysteresis area is reduced and shifted to higher T as σ is increased. Here, T_c^σ and T_i^σ retain the corresponding meanings of stability limits but take different (non-analytic) values that those in eq. 2.5. The same is also valid for the transition temperature T_0^σ.
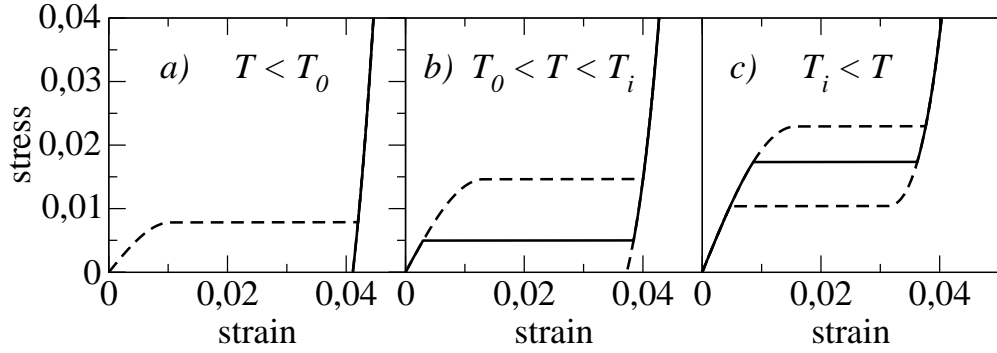
Figure 2.6: Different mechanical behavior at three different increasing temperatures.

recovered[8] when removing the stress. However, the system is susceptible to exhibit SME upon heating. Case (b) corresponds to an intermediate regime whithin which both pseudoelastic and superelastic behavior could be observed, depending on the specific return path followed by the system. Case (c) shows superelastic behavior.

2.2 Ginzburg energy

A system undergoing a MT typically achieves a multivariant phase, with the presence of domain boundaries, i.e. interfaces separating the different variants. Experimentally domain boundaries are often observed to be rather sharp, in the range of at the most few interatomic distances [13]. Instead, although interfaces are energetically unfavorable in an spatially extended homogeneous Landau system,[9] the continuous and differentiable nature of the free-energy leads to smooth

---

[8]Recall that in this case the initial strain is zero due to the self-accomodation process leading to a domain microstructure with no macroscopic net change.

[9]In the interfaces, the strain field must take values that are locally unstable: A continuous and differentiable domain boundary (as it is in the Landau model) separating variants of equilibrium

interfaces, with a certain width in the mesoscopic scale. Ginzburg proposed an extra energetic penalty for variations of the OP $f_{\mathrm{G}} = \frac{\kappa}{2}|\nabla e_2|^2$. Thus, any interface results in an extra energetic cost that results in sharper interfaces than in the absence of f_{G} which is closer to experiments. In fact, it can be proved that the energetic cost of the interphases due to the Ginzburg energy is equal to that of the homogeneous contribution [155]. For a more compact notation, we define $f_{\mathrm{GL}} = f_{\mathrm{L}} + f_{\mathrm{G}}$.

2.3   Long-range anisotropic interactions

In addition to the OP deviatoric strain, the other symmetry-adapted strains e_1 and e_3 may appear as a consequence of the transition in order to make easier the coherent match between different crystallographic cells, corresponding to either different variants or different phases. Moreover, since the stable, low-temperature crystallographic cells come from a pure OP (i.e. deviatoric) deformation (in our cubic-to-tetragonal transition), the non-OP contributions must be energetically costly and therefore the domain boundaries must adopt the morphology that minimizes this contribution. Then, since they are non-OP of the transformation and thus their contribution is assumed to be small, they are taken into account only up to the harmonic term. Thus we can write:

$$f_{\mathrm{non\text{-}OP}} = \frac{A_1}{2}e_1^2 + \frac{A_3}{2}e_3^2 \tag{2.7}$$

Similar to the harmonic coefficient A_2, A_1 and A_3 may also be expressed as function of elastic constants: $A_1 = C_{11} + C_{12}$ and $A_3 = 4C_{44}$, being both A_1 and A_3 positive which confirms that this contribution is indeed unfavorable. The total free energy density can be then written as $f_{\mathrm{T}}(e_1, e_2, e_3) = f_{\mathrm{GL}}(e_2) + f_{\mathrm{non\text{-}OP}}(e_1, e_2, e_3)$. As it is shown in App. A, the three symmetry adapted strains e_1, e_2 and e_3 are obtained as derivatives of the same underlying 2-dimensional displacement field $\mathbf{u} = (u_x, u_y)$, which are the two true degrees of freedom of the system. Consequently, the strain components are not independent but are linked through the Saint-Vénant compatibility condition[10] [140], that ensures that the transformation is defect-free, thus mantaining the lattice integrity. This leads to express $f_{\mathrm{non\text{-}OP}}$ in terms of e_1 and e_2 and, hence, $f_{\mathrm{T}}(e_1, e_2)$, where we have eliminated the dependence of the total free energy on e_3. Moreover, we consider that e_1 takes at any time the values that minimize the total free energy, so that we impose the

---

strain $e_2 = +e_M$ and $e_2 = -e_M$ must include points with all the possible values in between, that therefore do not correspond to the equilibrium values $e_2 = \pm e_M$.

[10]The mathematical details of the Saint-Vénant compatibility condition can be found in App. A.

condition $\frac{\partial f_T}{\partial e_1} = 0$. This allows us to get a final expression for $f_{\text{non-OP}}$ in terms only of e_2:

$$f_{\text{non-OP}}(e_2) = \int e_2(\mathbf{r})U(\mathbf{r} - \mathbf{r}')e_2(\mathbf{r}')d\mathbf{r}' \qquad (2.8)$$

where the kernel $U(\mathbf{r} - \mathbf{r}')$ goes as $\sim \cos(4[\theta - \theta']/r^2)$ in 2D[11]. The integral in the free-energy density contribution $f_{\text{non-OP}}$ reveals that this term is non-local since relates any two cells in the system by means of the kernel U. The $1/r^2$ falloff indicates that it is long-ranged whereas the cos makes $f_{\text{non-OP}}$ vanish for values $\theta = \pm 45 \deg$. This can be easily seen in Fourier space, where the free-energy density takes the following form[12]:

$$f_{\text{non-OP}}(k_x, k_y) = \frac{A_3}{2} \frac{\left(k_x^2 - k_y^2\right)^2}{(A_3/A_1)\, k^4 + 8\left(k_x k_y\right)^2} |e_2(\mathbf{k})|^2 = V(\mathbf{k})|e_2(\mathbf{k})|^2 \qquad (2.9)$$

This expression makes clear why cross-hatched correlations along the diagonals $k_x = \pm k_y$ are favored. Such correlations are more likely and stronger for larger values of A_3 whereas, formally, they vanish when $A_3 \to 0$.[13] We point out that such correlations are at the origin of the diagonal interfaces of both tweed textures and martensitic twins. Kernels $U(\mathbf{r} - \mathbf{r}')$ and the corresponding Fourier transform $V(\mathbf{k})$ are shown in Fig. 2.7(a) and (b) respectively, where A_3/A_1 and A_3 are taken to be $A_3/A_1 = 2$ and $A_3 = 2$. It is of interest to state specifically the relation between the parameter A_3 and the elastic anisotropy factor $\mathcal{A}$, which we recall that for a cubic system it is defined as $\mathcal{A} = C_{44}/C'$. Taking into account the expressions relating C' and C_{44} with the parameters of the model (which have been given previously), we find that $\mathcal{A}$ can be written as $\mathcal{A} = A_3/2A_2$. Given that A_2 is a function of temperature, at constant temperature A_3 and $\mathcal{A}$ are proportional. Thus, variations on the elastic anisotropy factor (which is one of the main targets of this work) can be carried out through variations on A_3. As seen above, this entails modifying the strength of the long-range interactions. In the following, we analyze in depth the effects of variations in the parameters appearing on the kernel $V(\mathbf{k})$.

From the expression above we can see that, regardless of the value of A_1 (provided that $A_1 \neq 0$), an increase in the value of A_3 results in an increase of the non-OP free energy contribution, which in turn favors the diagonal correlations.[14] Moreover, in Fig. 2.8 we plot the kernel $V(\mathbf{k})$ for two different values of the factor A_3/A_1: (a) $A_3/A_1 = 20$ and (b) $A_3/A_1 = 0.2$. We have set $A_3 = 4.54$.

---

[11]The power of r does depend on the dimensionalilty of the system.

[12]The mathematical details of the calculi can be found in App. A.

[13]Note that $f_{\text{non-OP}}$ also vanishes for $A_1 = 0$, although this formal limit is uninteresting as it will be seen below.

[14]This is easier to see if we divide both the denominator and the numerator by A_3.
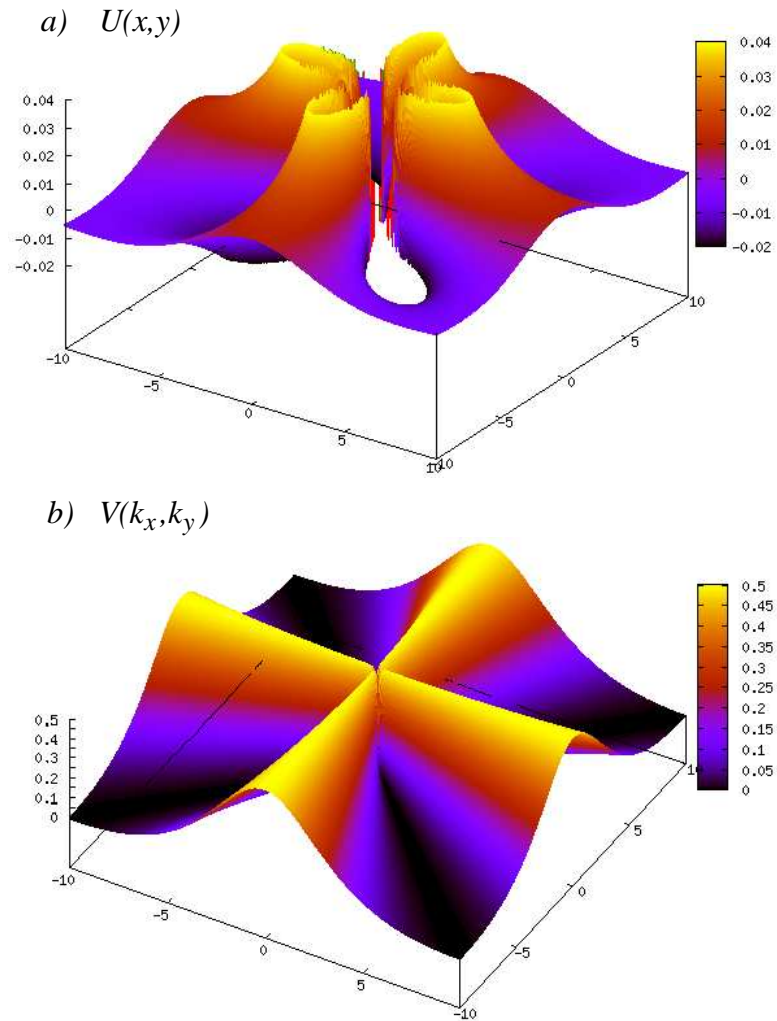
a)   U(x,y)

b)   V(k_x,k_y)

Figure 2.7: Kernel of the non-OP free-energy density in real (a) and reciprocal (b) spaces. The preferred diagonal directions can be clearly appreciated.
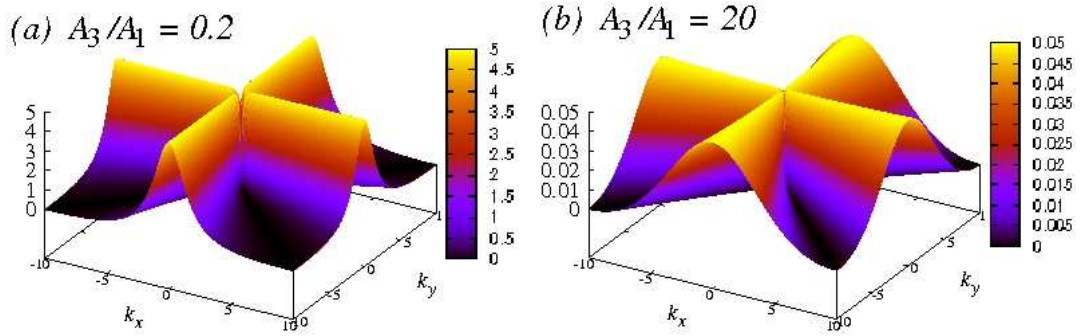
Figure 2.8: Kernel of the non-OP free-energy density in reciprocal space $V(\mathbf{k})$ for two values of A_3/A_1: (a) $A_3/A_1 = 0.2$ and (b) $A_3/A_1 = 20$. Here, $A_3 = 4.54$ in both cases.

It can be seen that the structure of the potential remains robust with respect to changes in this factor. However, as A_3/A_1 decreases, the decay in the off-diagonal directions becomes more abrupt since the value of the kernel in these directions increases. Notice the significant difference on the vertical scale. It means that, for a given value of the weight A_3 of the kernel $V(\mathbf{k})$, (diagonal) tweed textures and twin boundaries are favored more and more as the value of the factor A_3/A_1 is decreased. This also occurs when, for a given value of A_3/A_1, the value of A_3 is increased. This has been further checked through simulations with different values of this ratio, which will be shown when convenient, in Sec. 3. Consequently, we can control the weigth of the long-range interactions (and consequently the magnitude of the elastic anisotropy factor $\mathcal{A}$ at a given temperature) through variations only in the parameter A_3 but simultaneously keeping constant the ratio $A_3/A_1 = 2$.

2.4   Quenched-in disorder

Effects of inhomogeneities in SMA have been approached from diverse points of view. In Refs. [156, 157], the spatial variation of either the stress field of defects or chemical driving force accounts for athermal friction in the evolution of stress-induced martensitic variants. The introduction of thermal fluctuations has succeeded in obtaining the dynamic tweed, either as a pretransitional effect itself [7] or a low-temperature transient state before evolving towards the more ordered structure [158]. Assuming the disorder to have a much larger lifetime than any process involving elastic mechanisms, like phonon relaxation (which is of the order of $\sim 10^{-12} s$) and other slower time scales like boundary movements, and considering that no difussion is expected in such systems, the role of inhomogeneities in causing precursors was studied also by Becquart *et al.* [159] through the presence

of static perturbing fields. They observed that an ordered field did not produced tweed, but it was obtained through a random field. It supports the idea that the random nature of inhomogeneities intrinsic to materials is a necessary condition for such pretransitional textures to develop. Also Khachaturyan modeled tweed with static disorder [160].

It is well known that the composition is a statistically fluctuating random variable in alloys, which varies locally from on site to another. Altough these variations are in general slightly, the high sensitivity of the transition temperature on the specific concentration of each element observed in many SMAs led Kartha *et al.* to think about a variable local transition temperature. For instance, in the case of $Fe_{70}Pd_{30}$, regions with slightly higher (lower) concentration of Pd than the average value (30%at.) would lead to a lower (higher) local transition temperature[15]. Thus, in the context of Landau, they proposed a static, spatially random, fluctuating field coupling to the strain through the harmonic coefficient, which led to a distribution of local transition temperatures. This, together with long-range anisotropic interactions, enabled them to obtain static tweed.

Here we essentially adopt this scheme, and introduce the following distorting field:

$$f[\eta(\mathbf{r})] = \frac{\alpha_T}{2}\eta(\mathbf{r})e_2^2(\mathbf{r}) \tag{2.10}$$

where $\eta(\mathbf{r})$ is a random variable, gaussian distributed with zero mean and spatially correlated by means of an exponential pair correlation function.

$$\langle\eta(\mathbf{r})\eta(\mathbf{r}')\rangle = G(|\mathbf{r} - \mathbf{r}'|) = \frac{A}{2\pi}e^{-|\mathbf{r}-\mathbf{r}'|/\xi}$$

and $g(\eta) = \frac{1}{\sqrt{2\pi}\zeta}e^{-\frac{\eta^2}{2\zeta^2}}$. Here, ξ is the correlation length. The amplitude A of the correlation function is related to the standard deviation of the Gaussian distribution so that $\zeta = \sqrt{\frac{A}{2\pi}}$. The proof of this relation is given in App. A.3.3.

Note that this kind of coupling has the effect of producing a distribution of local characteristic temperatures, so that we can define local stability limits $\tilde{T}_c(\mathbf{r}) = T_c + \eta(\mathbf{r})$ and $\tilde{T}_i(\mathbf{r}) = T_i + \eta(\mathbf{r})$ and equilibrium temperatures $\tilde{T}_0(\mathbf{r}) = T_0 + \eta(\mathbf{r})$. For simplicity, we rename $\tilde{T}_c(\mathbf{r})$ as $T_c(\mathbf{r})$, and correspondingly the other characteristic temperatures. To avoid confusion $T_c(\mathbf{r})$ with the Landau T_c, the spatial dependence will be always stated specifically. This enables local regions of the high temperature phase to be locally stable below T_c and vice versa, which are separated by free energy barriers. Since $T_c(\mathbf{r})$ is exponentially correlated, it gives rise to islands of similar local stability limits, that will act either as pinning sites for nucleation and growth of martensite (and which are at the origin

---

[15]We recall that an increase in the average concentration of Pd leads to a decrease in the transition temperature of the sample

of premartensitic strain modulations) or as retainning sites for austenite upon cooling[16] (and for martensite upon heating). For a given value of ξ much lower than the simulation cell size, these islands are short-ranged at high temperatures and grow progressively as the temperature is decreased. Obviously, the higher the value of ξ the larger the size of the island. On the other hand, at a given T and ξ, the higher disorder intensity ζ the larger the system fraction that will be unstable. Hence, this will increase the onset temperature of the precursor regime. Moreover, a higher ζ also enhances the mean local unstability of the system, which will favor the stability of the precursor structures. Since statistically the mean value $\langle \eta \rangle$ vanishes, disorder favors equally both phases with respect the equilibrium transition temperature in the clean limit (T_0). Consequently, higher values of ζ gives rise to higher energy barriers. This is analyzed in depth in the following. Before going into this issue, it should be pointed out that the fact that $\langle \eta \rangle = 0$ is not in agreement with experimental results, which indicate that doping entails a destabilization of the martensite so that the transition takes place at lower temperatures, as commented in Sec. 1.4.1. However, a nonvanishing value of $\langle \eta \rangle$ does not give rise to new qualitative findings, but only would shift all the phenomenology to be observed around the specific new value $T_c + \langle \eta \rangle$.

Discretization of disorder: Effects of ξ and ζ

The disorder variable $\eta(\mathbf{r})$ has been defined above as a variable in the continuum, as the Landau theory essentially is. As seen, $\eta(\mathbf{r})$ contains two free parameters: the amplitude of the gaussian distribution[17] ζ and the correlation length ξ. Theoretically they would completely determine the specific profile of $\eta(\mathbf{r})$ in any region of the space. However, for computational purposes, $\eta(\mathbf{r})$ needs to be discretized in the coarse-grained mesh. The discretization procedure introduces a new parameter Λ which corresponds to the length of the unit cell of the system, that is defined as $\Lambda = L/N$, where L is the linear size of the square simulation cell, and N^2 is the total number of unit cells contained in the simulation cell. In principle, as the discretization premises state, the discretization of the space should be as fine as not to affect the simulation results. It means that Λ must be chosen in a range within which variations of its specific value does not entail any change in the results in order to be consistent with the theory. If it happens, the value of the Λ is too large and must be diminished. In the case of our model, tests have been carried out to check it and it has been observed that the value of Λ below

---

[16]This simple analysis does not take into account the long-range interactions, that also affect the stability of each system site.

[17]The mean value of the distribution $\langle \eta \rangle$ has been set to zero and it is not taken into account here.
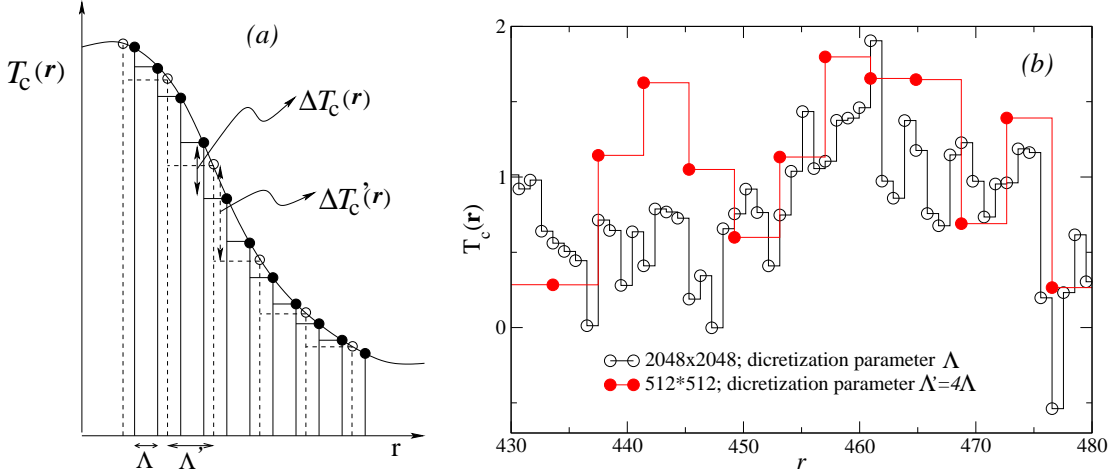
Figure 2.9: (*a*) Schematic profile of the local distribution of the characteristic temperature T_c in the continuous and discretized spaces. (*b*) Real profile of $T_c\mathbf{r}$ for two values of the discretization parameter.

which results do not change depends on the specific value of ζ. In particular, the higher ζ the lower the required Λ. Since this thesis refers to the behavior of the system for different values of ζ it is important to go depth into this aspect. By looking with detail at the nature of the dependence of the results on Λ for a given ζ, this dependence may be valid here and, in fact, leads to relevant results.

First, we analyze the dependence of the specific profile of the disorder on the discretization parameter Λ. The definition of $\eta(\mathbf{r})$ in the continuum leads to a smooth profile of $T_c(\mathbf{r})$, such that the difference $T_c(\mathbf{r}) - T_c(\mathbf{r}')$ between any two points $\mathbf{r}$ and $\mathbf{r}'$ tends to zero as the distance between the points $\mathbf{r} - \mathbf{r}'$ tends to zero. However, the discretization of the space introduces a minimum distance between nearest neighbor sites, which is precisely Λ. Consequently, $T_c(\mathbf{r}) - T_c(\mathbf{r}')$ does not vanish between the nearest neighbor cells but take finite values. They can be arbitrarily defined, for instance, as $\Delta T_c(\mathbf{r}) = T_c(i,j) - T_c(i-1,j)$. Figure 2.9(*a*) shows a schematic, theoretical profile of $T_c(\mathbf{r})$ in a given segment of the space. It is clearly seen that in the continuous case (continuous curve) $T_c(\mathbf{r})$ take an infinite set of values that give rise to vanishing local differences of $T_c(\mathbf{r})$ between infinitely close points. Instead, if the space is discretized in a mesh with discretization parameter Λ, $T_c(\mathbf{r})$ takes the values only at the black dots, giving rise to finite $\Delta T_c(\mathbf{r})$. If now we use a new discretization parameter $\Lambda' = 2\Lambda$ (white dots), the resulting $\Delta T_c'(\mathbf{r})$ will be larger on average, as it is schematically indicated by the vertical arrows. This can also be seen in Fig. 2.9(*b*).

Since $T_c(\mathbf{r})$ contributes to the total energy profile of the system, say $E(\mathbf{r})$, the high of $\Delta T_c(\mathbf{r})$ plays a key role in determining the height of finite local energy

barriers $\Delta E(\mathbf{r})$. The precise relationship between both $\Delta T_c(\mathbf{r})$ and $\Delta E(\mathbf{r})$ cannot be derived easily due to the presence of long-range elastic interactions. However, from a given value of $\Delta T_c(\mathbf{r})$, the pure relaxational dynamics used in the model is observed to be unable to overcome the resulting $\Delta E(\mathbf{r})$. In short, the kinetics of the system, that is crucial for the final stabilized structures, is directly (critically) affected by the finite nature of the discretized disorder variable, that in turn depends on the discretization parameter.

In fact, some of the relevant results, as mentioned, come out precisely from the fact that disorder leads to finite energy barriers. In other words, the important property that disorder must have is that it precisely does give rise to such finite $\Delta T_c(\mathbf{r})$'s in order to show the desired behavior. Thus, the disorder may be redefined as a discrete variable with all the properties mentioned above, but that is, indeed, independent of the discretization parameter. The dependence may be absorbed by reformulating the correlation length ξ in units of the discretization parameter, and letting ξ without any physical meaning. Then, the dependence of $\Delta T_c(\mathbf{r})$ on ξ must be analyzed.

The dependence of the mean value of $\Delta T_c(\mathbf{r})$, denoted by $\langle \Delta T_c(\mathbf{r}) \rangle$ on both ζ and ξ is shown in Fig. 2.10(a) and (b) and respectively. It can be deduced that variations on ξ shift the behavior in the parameters' space, in such a way that the lower ξ the larger ζ required to obtain similar behavior. Looking at the slope of the curves, the dependence of $\langle \Delta T_c(\mathbf{r}) \rangle$ on ξ is strong only for relatively low values of ξ and high values of ζ. With respect to this, simulations for the more critical value $\xi = 10$, which is lower than that used in most of the simulations ($\xi = 20$), have been carried out in order to check the effect of variations in this parameter. These results will be shown later when convenient but in any case they do not affect qualitetively the findings and conclusions of the work. Consequently, from now on, ξ is kept constant and the study of the effect of the disorder will be carried out as function of the amplitude ζ.

2.5 Total free energy

Summarizing the previous sections, the total free energy of the system can be written as the sum of the following contributions: $F_{\mathrm{T}} = F_{\mathrm{L}} + F_{\mathrm{G}} + F_{\eta} + F_{\mathrm{non\text{-}OP}}$. More explicitly:

$$
\begin{aligned}
F_{\mathrm{T}} = \int & \left[\frac{\alpha_{\mathrm{T}}}{2} \left(T - T_c + \eta(\mathbf{r}) \right) e_2(\mathbf{r})^2 - \frac{\beta}{4} e_2(\mathbf{r})^4 + \frac{\gamma}{6} e_2(\mathbf{r})^6 + \frac{\kappa}{2} |\nabla e_2(\mathbf{r})|^2 \right] d\mathbf{r} \\
& + \frac{A_3}{2(2\pi)^2} \int \left[\frac{\left(k_x^2 - k_y^2 \right)^2}{\frac{A_3}{A_1}(k_x^2 + k_y^2)^2 + 8 k_x^2 k_y^2} \right] |e_2(\mathbf{k})|^2 d\mathbf{k}
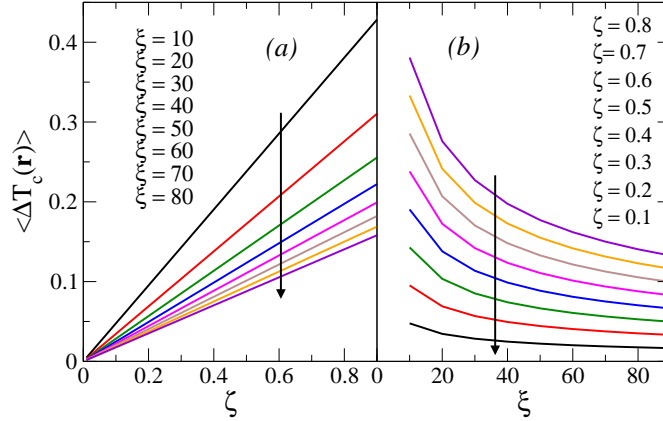\end{aligned}
\tag{2.11}
$$

Figure 2.10: Mean finite local differences of $T_c(\mathbf{r})$, denoted by $\langle T_c(\mathbf{r}) \rangle$, as a function of ζ for different valuees of ξ (a) and vice versa (b).

The system consists of a 2-dimensional continuous lattice with square symmetry. The numerical implementation requires the discretization of the expression above on a mesh. Numerical details can be found in App. A.

2.6   Numerical details and other comments

Parameters

The material parameters that we use in the simulations are taken from experimental data for $Fe_{70}Pd_{30}$ [33] and can be found in App. C in S.I. and reduced units. The aim of this thesis is to explore the thermodynamic behavior of the model in the parameters' space, in particular the effect of the anisotropy factor (through variations in the coefficient A_3) and the amplitude (standard deviation ζ) of the disorder distribution.

In fact, Falk [136] showed that the Landau free-energy has no free parameters but temperature. Moreover, we have seen that variations on the ratio A_3/A_1 as well as on the correlation length of the disorder do no lead to new phenomenology. Therefore, beyond the primordial experimental justifications given in the previous chapter pointing to these parameters as important factors in ferroelastic systems, the region of the parameters' space of this model that gives rise to qualitative thermodynamic behavior with physical relevance can be approximately reduced to the two-dimensional subspace determined by the two parameters A_3 and ζ. Variations of disorder should be understood as airising from compositional changes, doping or quenching effects. Concerning the elastic anisotropy $\mathcal{A}$, significant variations necessarily entail changing the material.

Although a quantitative analysis of the ferroelastic properties is beyond the scope of this thesis, it is worth noting that the parameter values used here give rise to quantitative results that in general are in reasonable (and often notably) agreement with experimental observations. Despite that the simulations are shown in reduced units for simplicity, in some cases the values of the magnitudes have been specified in physical units in order to highlight such quantitative agreement, which gives additional support to our simulation results.

Relaxational dynamics

Stabilized configurations are obtained by minimizing the total free energy F_{T} given in eq. (2.11). This is carried out by means of pure relaxational (overdamped) dynamics which consists of applying the following dynamical equation over all the unit cells of the system[18]

$$\frac{\partial e_2(\mathbf{r})}{\partial t} = -\frac{\delta F_{\mathrm{T}}}{\delta e_2(\mathbf{r})} \tag{2.12}$$

As seen, no fluctuations have to be taken into account, since almost all martensitic transitions are athermal. In discretized form, $e_2(t + \Delta t) = e_2(t) - \frac{\delta F_{\mathrm{T}}}{\delta e_2}\Delta t$. Here, time is meaningless since we are not interested in intermediate but final stabilized –static in our time scale– configurations, Δt is chosen as large as possible in order to optimize the computation time. To avoid numerical problems, it may be modified depending on the particular characteristics of each simulation. Usually, its order of magnitude is of $\Delta t \sim 10^{-2}$. We consider that a configuration has been stabilized when $\sqrt{\sum(e_2(t + \Delta t) - e_2(t)/\Delta T)^2} = \sqrt{\frac{1}{N}\sum(\frac{\delta F_{\mathrm{T}}}{\delta e_2}\Delta t)^2} < 10^{-14}$, where the sum is over all the unit cells of the system. According to eq. (2.12) derivatives of F_{T} must be calculated. This is shown in detail in App. A.3.2.

Metastability and equilibrium

The true equilibrium state can be derived through a simple analysis from the minimization of the total free energy of the system. At temperatures low enough, all the cells in the sytem transform to the ferroelastic phase. Landau potential is doubly degenerated, which allows for multivariant coexistence. Long-range anisotropic interactions lead this coexistence to adopt modulated structures along the diagonal directions, but do not select any specific wave vector for such modulations due to the existence of periodic boundary conditions. Then, Ginzburg energy favors a low number of interfaces, making the global minimum be a single

---

[18]It is easy to see that recursive application of eq. 2.12 brings the system to decrease progressively its energy: $\frac{\partial F}{\partial t} = \frac{\delta F}{\delta e_2}\frac{\partial e_2}{\partial t}$ and then, substituting eq. 2.12 one obtains $\frac{\partial F}{\partial t} = -\left(\frac{\delta F}{\delta e_2}\right)^2 < 0$.

domain. By definition, such a configuration lacks of internal microstructure and hence it is inappropriate to study structural patterns and associated thermodynamic behavior.

However, the overdamped dynamics is not able to overcome finite free-energy barriers.[19]. In our case, this allows for stabilized metastable states. This is of our interest because typically the system ends up stabilizing in twinned structures or glassy states, and the single domain is only rarely reached.

Nevertheless, it should be pointed out that the obtained twins exhibit random widths instead of the characteristic width according to the square root scaling law observed in experiments. We recall that the real internal microstructure emerges from the existence of an habit plane, i.e. from size and shape effects. The absence of such a characteristic width in our simulation results comes from the fact that the system is infinite, since we have imposed periodic boundary conditions in our simulation cell. Actually, this does not prevent us from studying many aspects of ferroelasticity, although the analysis of domain sizes does require such a characteristic width. Since the latter is also of our interest, modifications will be carried out in the present model, by means of specific disorder fields or additional energetic terms, which will be discussed in detail in Sec. 3.4.

Computational details

The algorithm used to perform the Fourier transforms is the so-called $FFTW$ (Fast Fourier Transform in the West) [161] and, in our case, it has been shown to be of the order of ten times faster than that in Ref. [162], that is the book of reference for Fortran codes. Typically, simulations have been carried out in a square lattice of linear size $L = 10^3 u.l.$, discretized onto a $512{\times}512$ mesh. Occasionally, this may have been modified and it will be indicated. Periodic boundary conditions have been used in order to compute the non-OP contribution in Fourier space. It has considerably cut down the cost of computation time, since for a system of N cells, the computation of the F_{nonOP} in real space requires a computation time of the order of $\sim N^2$ whereas in reciprocal space the order is only $\sim N \log N$. Averages have been carried out over independent realizations of the disorder. The initial state depends on the characteristics of the specific simulations. For instance, the initial configuration in quench-type simulations as well as in simulations starting from a high temperature state consist of a random strain, Gaussian distributed with zero mean and standard deviation equal to 10^{-6}.

---

[19]Strictly speaking, this only holds in the continuum. In discretized form, there exists a low but finite treshold for the barriers that can be overcome by this type of dynamics.

Representation of the configurations

The fully relaxed configurations obtained by solving numerically the model are shown in snapshots of the strain field $e_2(\mathbf{r})$. It is worth noting that the starting point of the model is the strain tensor. In that sense, the Ginzburg-Landau free-energy density f_{GL} is independent from the definition of the strain tensor components in terms of the displacement field $\mathbf{u}(\mathbf{r})$. That is to say, f_{GL} does not depend on whether linear or nonlinear elasticity is used, and only the representation of the configurations in terms of $\mathbf{u}(\mathbf{r})$ forces one to choose the specific dependence of e_2 on $\mathbf{u}(\mathbf{r})$. Instead, this is not the case of the nonOP contribution, i.e. the long-range interactions, since they partially come from the Saint Vénant compatibility condition, which is indeed derived by using the linear definition of elasticity. Then, in order to represent the configuration in terms of the displacement field, it should be used the linear definition of elasticity.

Chapter 3

Structures

In this chapter we study the structural patterns resulting from solving numerically the model presented in the previous chapter. In particular, we address the influence of the anisotropy and disorder on the structures, and their evolution in temperature. To characterize the morphology the configurations, the local strain distribution, domain wall profiles and diffraction patterns have been analyzed. Surface effects are also discussed and implemented in several ways, and used to calculate the domain size distribution.

3.1   Anisotropy vs. disorder. A simple analysis

Long-range anisotropic interactions and local disorder interact in a complex way. They often have conflicting interests although sometimes they cooperate successfully as it is the case of pretransitional tweed textures. To go depth into the understanding of this interplay it may help to do the following simple exercise. We design an ideal system containing only an isolated square region of homogeneous disorder and analyze systematically the patterns that appear for different values of A_3. The homogeneous disordered region is characterized by the width of the window D and the intensity of the disorder $T_c(\mathbf{r} \in D) \equiv I$. The distribution and a snapshot of the resulting $T_c(\mathbf{r})$ are shown in Fig. 3.1 in the upper pannels of each case $(a) - (d)$. Concerning these cases, note that the width of the disordered window increases from top $(I = 1.7)$ to bottom $(I = 1.9)$ whereas the disorder intensity D increases from left $D = 10$ to right $D = 30$. The lower pannels in each case show the relaxed strain profiles along the diagonal direction for different values of the anisotropy. At the right side of each case, a series of snapshots of the corresponding configurations (in color) is shown.

First of all, we recall that in absence of long-range interactions the austenite is unstable inside the disordered regions. Then, since the free energy density is

local, the strain takes the values $e_2 = 0$ and $e_2 = \pm e_M$ outside and inside the disordered region respectively, regardless of the values of D and I. As long-range interactions are introduced, this scheme changes. Let us first focus on case (a). As long as the value A_3 is low enough, the disorder dominates the kinetics of the system and inside the disordered region the strain e_2 adopts approximately a Gaussian profile, only slightly deviating from the value e_M and exhibiting tails of very small amplitude that decay outside the disordered region. However, above a certain critical value of A_3, the anisotropy is the dominant factor and the long-range interactions do not allow the disordered region to deform. Instead, they make the strain to approximately vanish over all the spacethus giving rise to a homogeneous structure. Consequently, one can deduce that a strong anisotropy contributes to the stability of the thermodynamic phase of the system.

Different behavior is observed in $(b) - (d)$ cases. Here, two different crossovers can be identified. As in case (a), low values of A_3 give rise to the Gaussian-like strain profile whereas high values lead to a homogeneous structure everywhere in the system, as mentioned above. Nevertheless, for intermediate values of A_3 a new phenomenon arises as a consequence of the balance between anisotropy and disorder, which consists of diagonal, wavy modulations of the strain inside the disordered region. Such modulations are at the origin of the pretransitional cross-hatched tweed. As can be seen in the figure, the critical values of A_3 depend on both the width D and the intensity I of the disordered region. The larger the width D, the higher A_3 needed to inhibit the deformation. Moreover, the larger the width D, the lower A_3 needed to modulate the strain. Therefore, as the width D increases, the intermediate regime exhibiting modulations of the strain also increases. The same holds for the intensity I of the disordered region.

In other words, for a given value of the anisotropy factor, the unstable regions are allowed to deform provided they have a minimum size (D), that in turn depend on the degree of instability (I). Below such minimum size, anisotropic long-range interactions are able to stabilize the disordered region by correlating it with the surrounding austenite-stable system. Moreover, tweed modulations require a minimum value of A_3 to occur, below which only homogeneously distorted regions arise.

Although this is a simplification of the configuration that will be used in the relevant simulations, it captures the essence of how the system reacts to the presence of both long-range anisotropic interactions and local disorder. The disorder defined in the model produces a distribution of local transition temperatures that are exponentially correlated. Therefore, although it is a purely local term, at a given temperature T such correlations lead to a set of Landau-unstable islands with a particular mean size. Inside a given island, the degree of instability (i.e. the difference $T_c\mathbf{r} - T$) is spatially variable, and the maximum instability is placed

typically close to the center of the island. When T is decreased, the degree of instability as well as the mean size of the islands increase. In this sense, at a given temperature when the standard deviation ζ of the disorder is increased both the mean size and the degree of instability of the islands increase. Instead, the correlation length only affects the mean size of the regions and not the degree of instability.

3.2 Effect of anisotropy on the structures. Temperature dependence

In this section we perform simulations of the full model, and the obtained strain textures and their dependence on temperature T are shown and described as a function of temperature A_3 and ζ. First we limit ourselves to variations on A_3. Figure 3.2 shows snapshots of representative configurations obtained as a function of T for three different values of A_3. At the right side of each configuration we have plotted the local strain distribution averaged over 10 different realizations of the disorder. In the high-temperature phase and for the three values of A_3 the distribution is single peaked around zero strain. In spite of some differences, when decreasing T this peak evolves towards a two-peak distribution corresponding to the two possible equilibrium values of the OP, corresponding to the two degenerated low-T variants. Nevertheless, only for the largest value of A_3 [column (I)] the configuration shows the characteristic twinned martensitic structure. This is consistent with the fact that for a given value of T the anisotropy $\mathcal{A}$ decreases from left to right and the system loses directionality when decreasing the value of A_3. Interestingly, for the smallest value of A_3 [column (III)] we obtain a nanocluster phase separated state. Tweed textures can be observed in case (I) at intermediate temperatures above the phase transition $T_t \simeq 1$ whereas case (III) exhibits almost circular domains.

A three-peaks regime is observed around the transition in the three cases, indicating phase coexistence according to the first order character of the transition. As the anisotropy is lowered, this regime gradually widens in temperature. It is consequence of the presence of disorder, that makes some regions of the high-T phase to be stable well below the transition point. Of course, the contrary also holds: Some regions of the low-T phase may be stable well above the transition point.
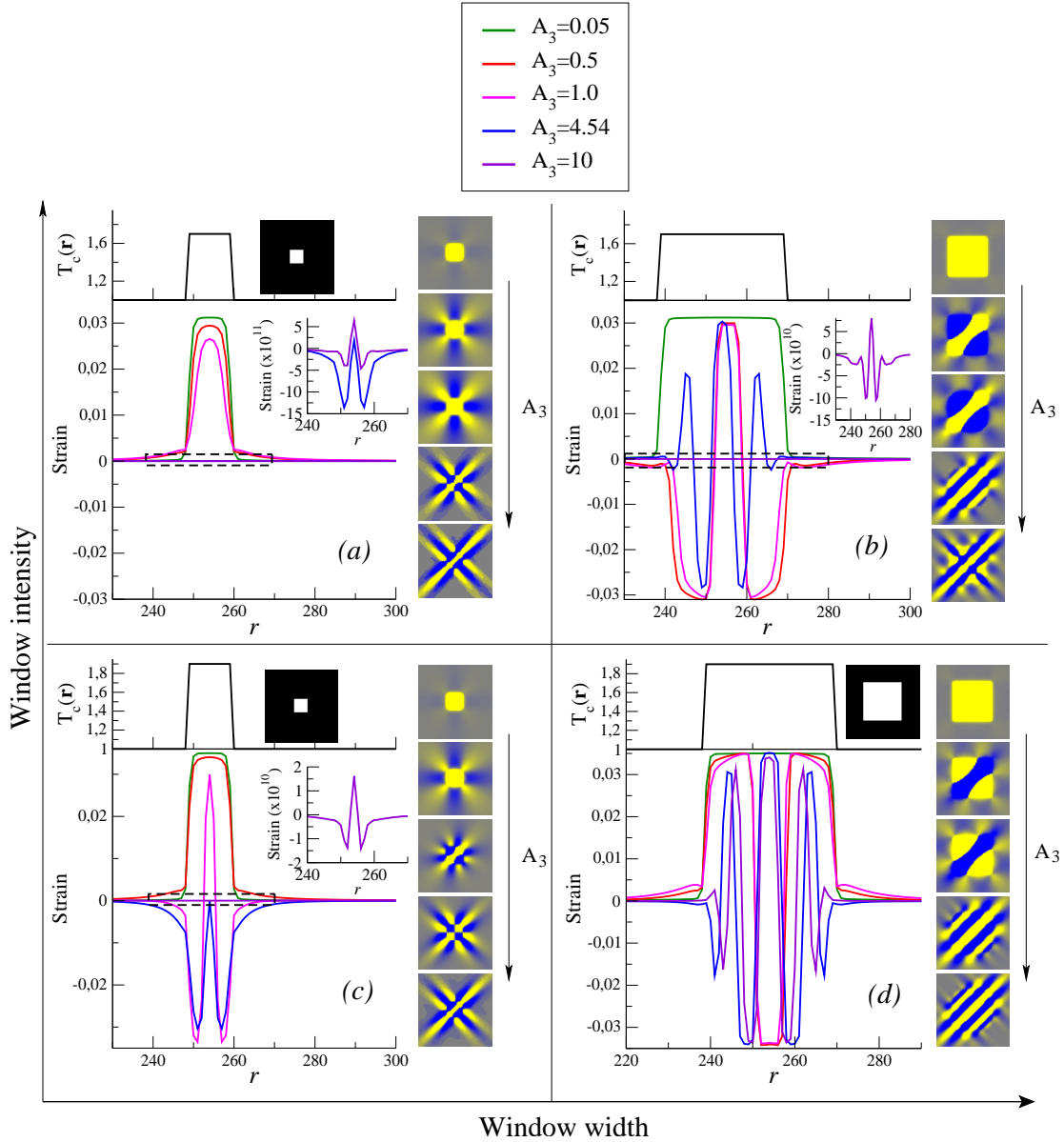
Figure 3.1: In each of the cases (a)-(d), strain profiles along the diagonal are shown for different values of the anisotropy (A_3), for a system without disorder but a centered square window of variable width D and intensity I: (a) $D = 10$, $I = 1.7$; (b) $D = 30$, $I = 1.7$; (c) $D = 10$, $I = 1.9$; (d) $D = 30$, $I = 1.9$. Above the strain profiles in each case, the corresponding disorder profiles are depicted, i.e. $T_c(\mathbf{r})$ with a snapshot of the zone of the system containing the disorder window. At the right side of each case, a series of snapshots of the corresponding profile's configurations are shown. The profiles in the small insets [cases (a)-(c)] are an enlargement of the area enclosed in the dashed box. The strain is so small that, actually, has no physical meaning.

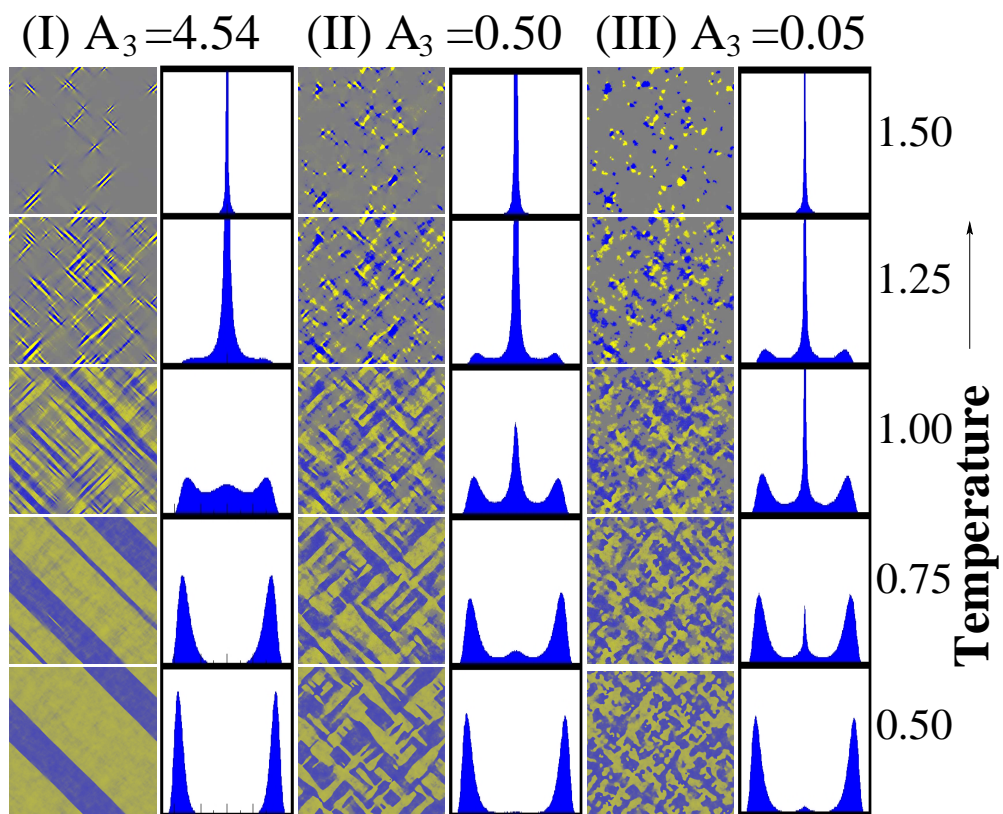**Figure 3.2:** Snapshots of selected configurations and local strain distribution, for three different values of A_3, as a function of T. The elastic anisotropy $\mathcal{A}$ decreases from left to right and the temperature from top to bottom.
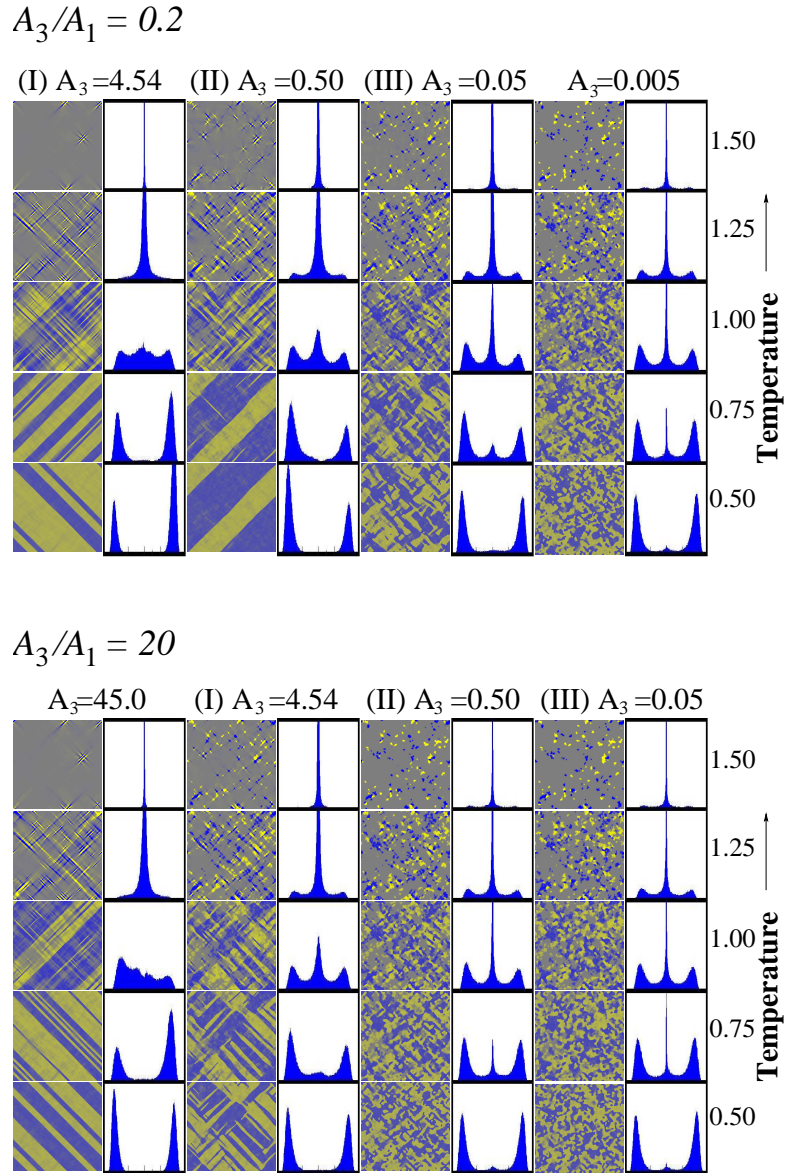
$A_3/A_1 = 0.2$

(I) A_3=4.54   (II) A_3 =0.50   (III) A_3 =0.05 A_3=0.005

Figure 3.3: Illustrative phase diagram for $A_3/A_1 = 0.2$ and $A_3/A_1 = 20$, for different values of A_3 and temperature T.

$A_3/A_1 = 20$

A_3=45.0   (I) A_3 =4.54   (II) A_3 =0.50   (III) A_3 =0.05

Effect of variations in the ratio A_3/A_1

In order to further check that variations in the ratio A_3/A_1 do no entail any qualitative change of our findings, in Fig. 3.3 we show similar figures to Fig. 3.2, where $A_3/A_1 = 0.2$ and $A_3/A_1 = 20$ have been used respectively. By comparing them, it can be seen that larger ratios need higher values of A_3 in order to reproduce the same structural patterns. Specifically, a decrease (increase) of an order of magnitude in the ratio A_3/A_1 needs a decrease (increase) of an order of magnitude in the value of A_3. For instance, the lowest set of values $\{A_3/A_1, A_3\}$ for which a twinned structure is observed at $T = 0.5$ are $\{0.2, 0.5\}$, $\{2, 4.54\}$ and $\{20, 45\}$.

Precursor textures

To compare the simulation results obtained in Fig. 3.2 with real premartensitic nanostructures we show in Fig. 3.4a tweed contrast in Ni-Al, whose anisotropy is high ($\mathcal{A} \sim 9$). Simulation results (b) of a system with high $\mathcal{A}$ shows a very similar pattern above the transition. The length scale approximates very well to experiments and, if not indicated, all the snapshots in the thesis keep the same proportion as in this case.

Figures 3.4(c)-(e) show a series of images of $Ti_{50}Ni_{48}Fe_2$ in the premartensitic regime upon cooling. We recall that the mottled structure has been suggested to appear due to the low anisotropy value ($\mathcal{A} \sim 2$) [30], which is in agreement with simulation results at high temperatures for low anisotropy in Fig. 3.2. Since, upon further cooling, $Ti_{50}Ni_{48}Fe_2$ transforms to twinned martensite, it is in correspondence to the intermediate value $A_3 = 0.5$. Moreover, this high-temperature series show that the premartensitic mottled-like domains progressively become visible as the temperature is lowered from (c) to (e). This phenomenon is obtained also in our simulations in Fig. 3.2 shown previously. All this is observed to occur in the precursor regime in other alloys like stoichiometric Ti-Ni and Ni-rich Ti-Ni.

Strain profiles

The analysis of the strain profiles of the configurations can give additional information which cannot be extracted from simply looking at snapshots. For this purpose, we refer again to the configurations shown previously in Fig. 3.2. In particular the strain profiles of an arbitrary section of the structures for the cases of high (I) and low value (III) of A_3 are depicted in Fig. 3.5. Their evolution in temperature helps in the understanding of the dynamics resulting from the interplay between anisotropy and disorder. For the high value $A_3 = 4.54$, some short-ranged, tiny modulations arise at high temperature T. As T is decreased, they gradually increase in number, intensity, and range, corresponding to tweed patterns just above the transition temperature $T \simeq 1$. This is consequence of fair play between anisotropy and disorder, since both contribute essentially to the resulting structure. Instead, at low T, no signature of the modulations observed at high T survive but the profile becomes high-strained and long-ranged since the system is purely dominated by the long-range anisotropic interactions. They are able to induce large motion of twin boundaries, eventually eliminating some domains and coarsening others.

For $A_3 = 0.05$ the evolution is completely different, since it is mainly dictated by the presence of disorder. At high T, islands of strain are observed, with either positive or negative sign, but do not exhibit modulated (sign-variable)
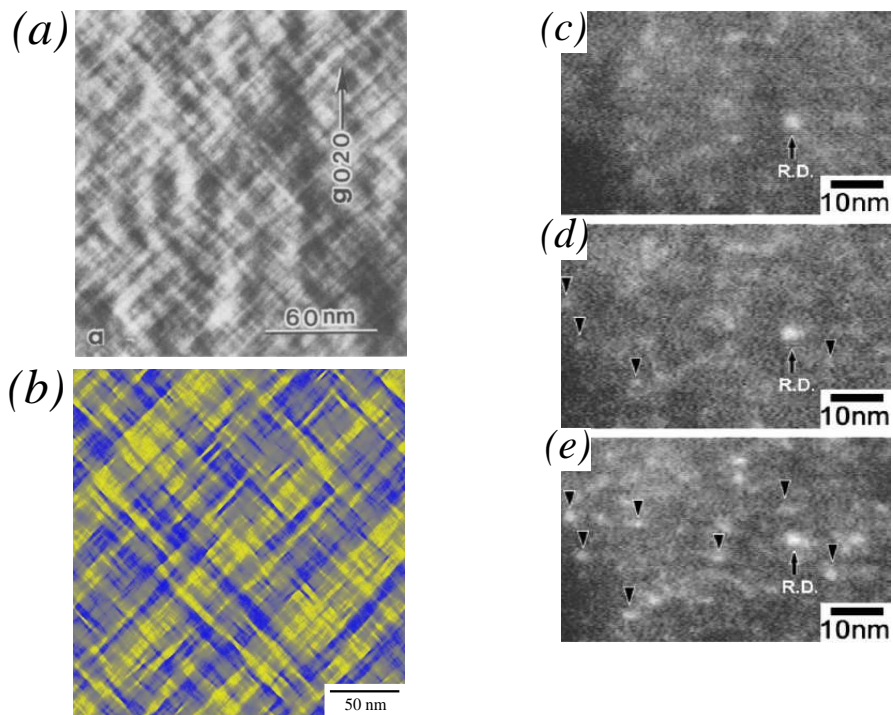
Figure 3.4: (a) Pretransitional tweed pattern in $Ni_{63}Al_{37}$, whose anisotropy is $\mathcal{A} \sim 9$. TEM bright field image extracted from Ref. [26]. (b) Simulated tweed, with high $\mathcal{A}$, which agrees with (a) also in the length scale. (c)-(e) A cooling series showing pre-martensitic mottled structures in $Ti_{50}Ni_{48}Fe_2$, with $\mathcal{A} \sim 2$. Dark-field images extracted from Ref. [30].
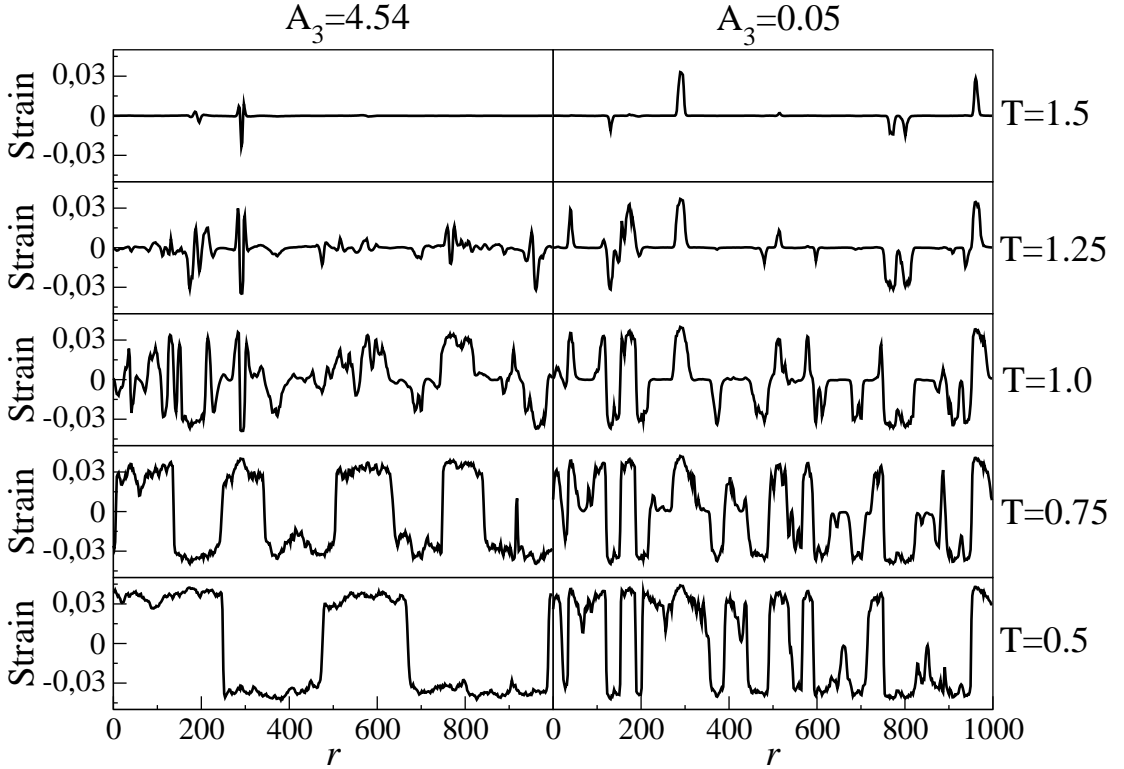
Figure 3.5: Evolution of the strain profile of an arbitrary section when the temperature is decreased, for high and low values of the anisotropy.

strains within any island. Once the specific variant is chosen in a particular transformable region during the initial nucleation process, it is not able to switch to the another variant by decreasing T, but it will remain in the given variant *forever*. The domain only can grow incorporating new non-transformed zones to the given domain. Otherwise, if a domain wall separates two transformed regions corresponding to the two different variants, the wall cannot move at all, but remain static. Hence, the structure at low T strongly depends on the high-T configuration and on the specific evolution of the local stability given by the specific configuration of disorder. Consequently, it can be deduced that the system *freezes* due to the *quenched-in* disorder in metastable states, since, as it will be seen later, the energy is higher than that of a twinned structure.

Non-OP strains

It is interesting to look at the non-OP e_1 and e_3, that can be calculated from e_2 by means of eq. A.31 and eq. A.20. An example of snapshots of their configurations and profiles of an arbitrary section of them are shown in eq. 3.6, in the tweed regime (a) as well as in the twinned phase (b). As indicated, the magnitude

of the profiles of both e_1 and e_3 have been enhanced four times to improve the comparison with the OP e_2. The color of the snapshots has been also adapted to better observe the structures. As can be easily seen in (a), they mainly concentrate in the smooth interfaces of the cross-hatched modulations. This is more difficult to see in the profiles in (b) because the presence of disorder makes the strain fluctuate sharply inside the twin variants themselves, and it leads to a fluctuating profile along the whole section of the system. However, by looking with detail at the corresponding snapshots of e_1 and e_3, fine straight lines can be observed along the twin boundaries, superposed to the random, isotropic fluctuating spots due to the disorder. The fact that the non-OP strains concentrate in the interfaces confirms (i) that these deformations appear to make easier the coherent fit between the cells of different variants along the domain boundaries, and (ii) that it is precisely the minimization of these strains which determine the morphology of the boundaries.[1]

3.3   Effect of anisotropy and disorder at low temperatures

Disorder effects

In the previous Fig. 3.2 the inhibition of martensitic twins at low temperatures has been carried out by decreasing the value of A_3. Here, in Fig. 3.7(a)-(b) we show that for a given value of A_3 which shows no tweed in the precursor regime, but twinned martensite below the transition [case (a)], twins can be suppressed by increasing the amount of disorder ζ, and, instead, the mottled structure survives down to low temperatures [case(b)]. This is in agreement with the experimental results in Ti_{1-x}-Ni_{1+x} as shown in the images (c)-(d). Upon cooling stoichiometric Ti-Ni exhibits a pretransitional mottled structure before undergoing a martensitic transition. When the content of Ni is increased at the expense of Ti atoms, the transition temperature decreases and finally it is suppressed for $Ti_{48.5}$-$Ni_{51.5}$ [34]. Then, mottled patterns survive down to 0 K. This also occurs in iron-doped Ti-Ni [30, 163].

---

[1]In other models that only allow for deformations corresponding to order-parameter strains, the proper orientations of the domain boundaries are obtained automatically [131]. This occurs because these orientations are the only crystallographic way to match geometrically the cells corresponding to different, pure variants. In our model, the minimization of such strains is needed to obtain the proper orientations. Moreover, the minimization of the energy associated to disorder can lead to stabilize other morphologies, resulting in a rich landscape which is of our interest.
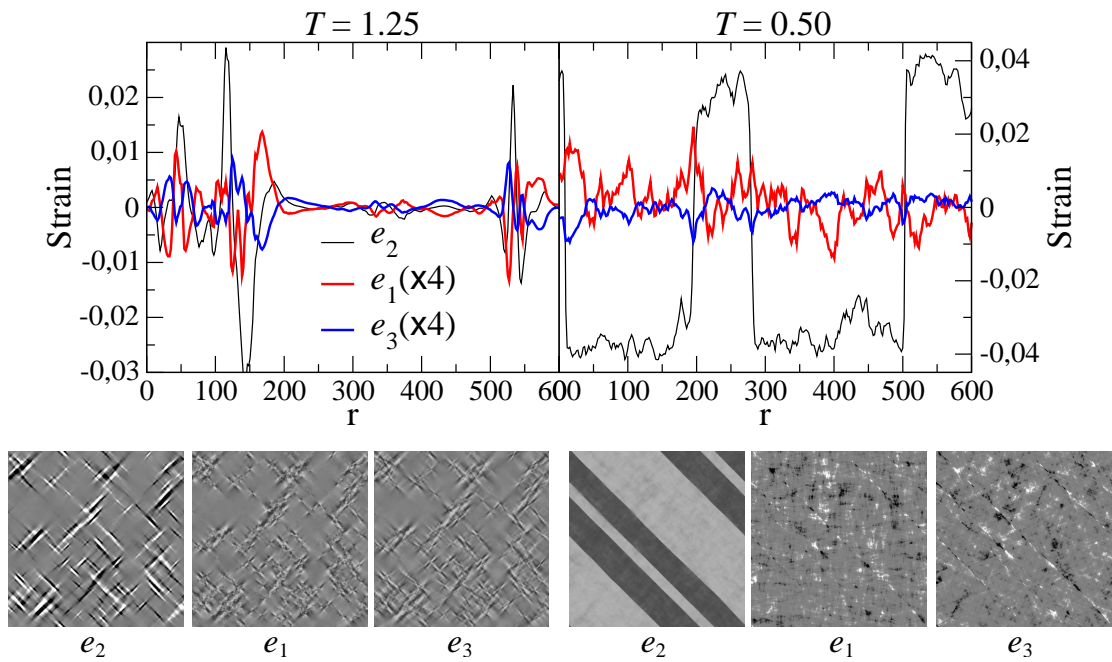
Figure 3.6: Symmetry adapted strains: Section profiles (above) and snapshots (below) of (a) tweed and (b) twins. Non-OP strains e_1 and e_3 have been enhanced four times to distinguish their profiles opposite to the OP e_2. Gradients of the OP entail an increase in the non-OP contribution.
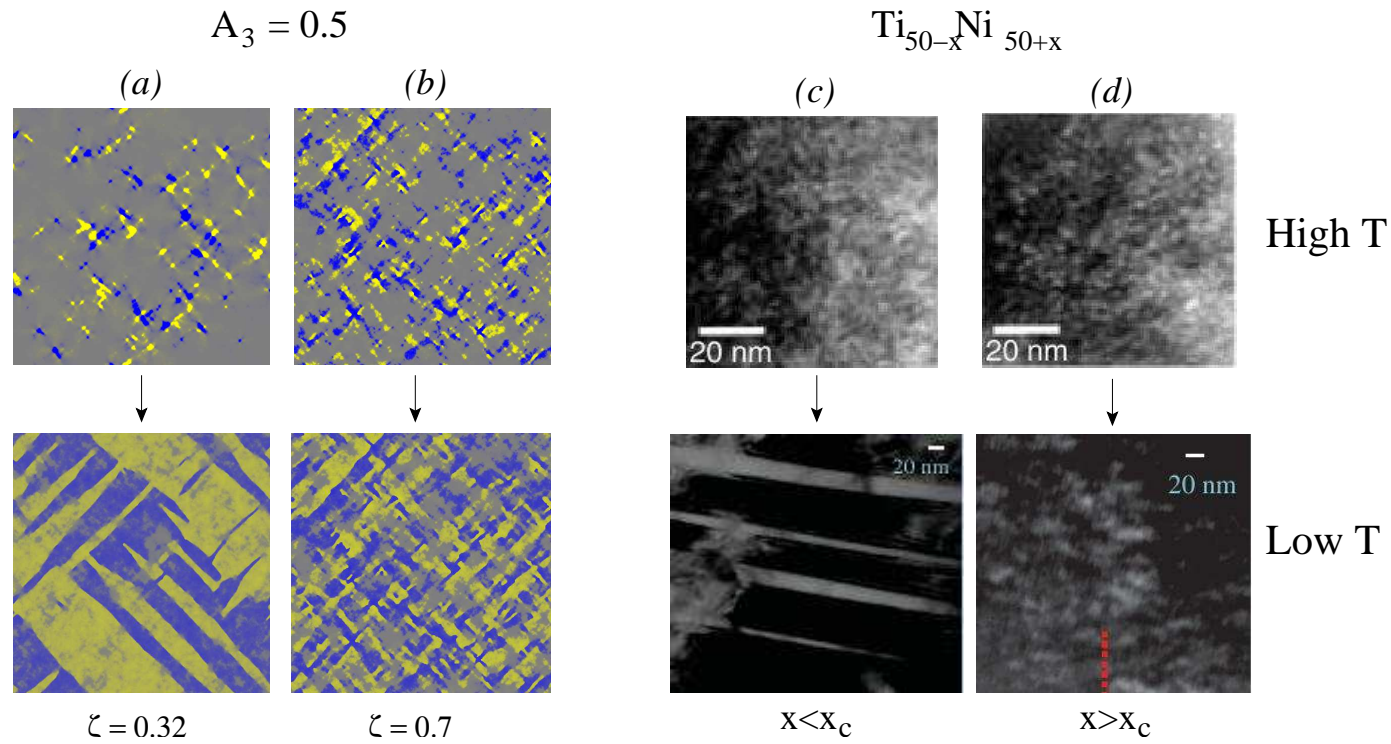
Figure 3.7: (a)-(b) For a set of values $\{\zeta, A_3\}$ the system shows premartensitic mottled structure which transforms to twinned martensite upon cooling. If the amount of disorder ζ is increased, twins are inhibited. (c)-(d) Experimental TEM images in Ni-rich Ti-Ni extracted from Ref. [34]. (c) Transforming composition. (d) *High* Nontransforming composition.

Anisotropy and disorder effects

In the following we focus on the effect of anisotropy and disorder in the structures at low temperatures. In figure 3.8 we show snapshots of selected structural patterns at $T = 0.5$ ($< T_c$, i.e. well inside the low-temperature regime) and for different values of A_3 and ζ. In order to highlight the differences among the configurations, at their right side we have plotted the diffraction patterns, corresponding to the intensity of the Fourier transform[2] $|\mathsf{F}(e_2)|^2$, averaged over 20 independent realizations of disorder. Several overall trends can be identified in Fig. 3.8:

(i) From left to right the texture loses directionality as reflected in the diffraction pattern, that changes from a cross-hatched to a circular shape. This is consistent with decreasing anisotropy.

(ii) From bottom to top the domain size decreases, consistent with the increase of ζ and the associated energy barriers. This is confirmed by the widening of the diffraction pattern towards higher values of the wave vector.

(iii) Twin boundaries exist only for relatively low values of ζ. Actually, as we shall demonstrate later, they appear for the values of disorder below a critical ζ^*, which in turn depends on A_3 in such a way that the higher A_3 the higher ζ^*.

(iv) Cross-hatched patterns are obtained for high values of both A_3 and ζ, for high values of A_3, whereas a mottled structure appears for low values of A_3.

(v) Finally, for the lowest value $A_3 = 0.05$, mottled structures are observed. In fact, only for very low values of ζ the pattern shows some directionality.

We notice that, although tweed and mottled structures are characteristic of the precursor regime, as seen in Fig. 3.2, in the present case they correspond to low-temperature structures. Actually this is not surprising since the amount of disorder suppresses the martensitic transition and the otherwise pretransitional structures survive down to very low temperatures. It is worth mentioning that these results are in complete agreement with experiments in a wide range of alloys. For instance, superconducting $YBa_2Cu_3O_{7-\delta}$ undergoes a tetragonal-to-orthorhombic ferroelastic transition, showing tweed patterns above the transition and twinning in the ferroelastic phase. When it is doped with either with Al, Fe [164, 165] or Co [166] at the expense of Cu the twin spacing is reduced progressively. Finally, there exists a critical amount above which the transition is suppressed and tweed is observed at low temperatures instead of twinning. In the case of low-anisotropy systems, which show a mottled structure, it has been analyzed in detail in Fig. 3.7(c)-(d).

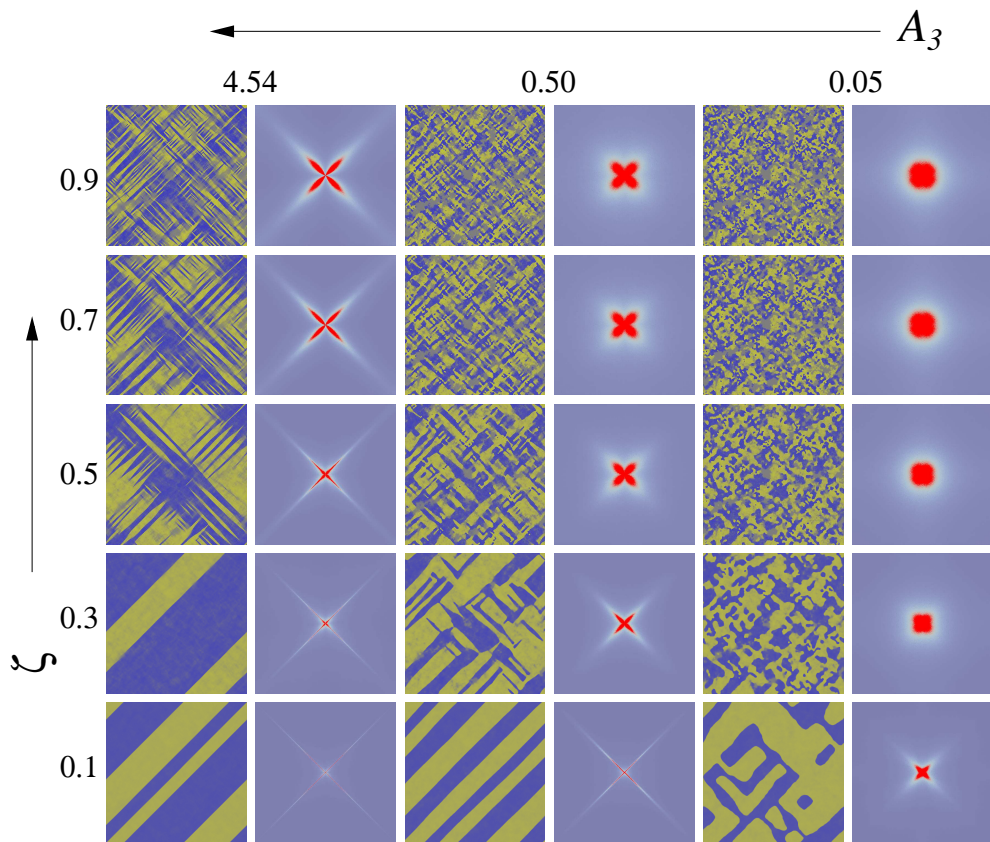[2]An expression for the Fourier transform can be found in App. B.1.

Figure 3.8: Illustrative phase diagram at low temperature ($T = 0.5$) for different values of A_3 ($\sim$ elastic anisotropy A) and disorder intensity ζ. Each configuration is shown with its corresponding Fourier-transformed intensity $\mathsf{F}(e_2)^2$.

3.4   Finite size effects

As discussed in Sec. 1, one of the most intriguing features of martensites concerns the strain configuration at the habit planes, which match austenitic and martensitic phases. It is commonly known that the notion of such well localized, invariant interfaces is often at the origin of the self-accommodation process consisting of minimizing the energy by taking advantage of the multiple degenerated minima. It gives rise to strain modulations in these planes that spread out in the martensitic bulk due the long-range nature of the elastic interactions, and consequently, a multidomain microstructure is created. Moreover, it is well known that such modulations are characterized by a characteristic wave length, i.e. a twin width λ that is related to the size of the embedded martensitic grain D according to $\lambda \sim \sqrt{D}$. This problem has been addressed successfully, by means of microelasticity [130], displacement field picture [167], etc. However, a full understanding of this problem in the context of Landau was lacking.

In the model presented in Chap. 2 the existence of a habit plane was not taken into account, since periodic boundary conditions were imposed. Actually, the observed twinned microstructure was consequence of metastable states stabilized by the dynamics and the long-range anisotropic interactions, rather than a true thermodynamic equilibrium configuration. Indeed, no characteristic twin length was identifiable, but a large range of widths of similar probability of occurring.

3.4.1   Habit plane

Within a Ginzburg-Landau framework we study the boundary problem of a semi-infinite martensite domain in an austenite host matrix, finding the strain and stress fields matching the austenite-martensite interface (habit plane). The calculation is huge and was carried out mainly by Marcel Porta. It is inspired in the previous works carried out by Horovitz *et al.* [167] and Shenoy *et al.* [168]. Here it is presented an outline of the approach and results, that attempts to avoid mathematical details[3]. Starting from the previous model presented here in the absence of disorder, new boundary conditions are imposed. Instead of being periodic in both axis, in the x axis we define a transformable strip of finite width L which borders in both sides on a region forced to remain in the austenite phase by means of a harmonic free energy in the symmetry adapted strains: $f_{\mathrm{aus}} = \frac{A_1}{2}e_1^2 + \frac{A(T-T_c)}{2}e_2^2 + \frac{A_3}{2}e_3^2$. Periodic boundary conditions are used in the y axis.

---

[3]Full work can be found in M. Porta *et al.*, Phys. Rev. B **79**, 214117 (2009).

The general procedure is as follows: First, the strain field in the austenite region is determined by imposing mechanical equilibrium $\nabla \cdot \sigma = 0$ (that is equivalent to minimize the energy), elastic compatibility and the requirement that the strain field must vanish far from the habit plane. The latter condition together with the periodic boundary conditions in the y axis lead to transform the above mentioned equations by Laplace in the x direction and Fourier in the y direction, which ensures decaying and periodic strain fields in the respective directions. The resulting free energy in the austenite is a nonlocal function of the order-parameter (OP) strain field e_2 in the habit planes only, and contains a Fourier kernel $1/|k_y|$. This kernel guarantees the habit plane to be invariant, i.e. the strain vanishes on average along this plane. The expressions for the non-OP strains e_1 and e_3 as well as $\partial_x e_1$ are obtained in terms of the OP e_2 in the habit plane as well as its x-derivatives. It allows to obtain an expression for the non-OP free-energy of the martensitic bulk in terms of the OP e_2 containing the factor $(k_x^2 - k_y^2)^2$, which favors modulations of the OP with $k_y = \pm k_x$. Also, it is found that it scales as $\sim 1/|k_y|$, inducing the formation of narrow twins. Since this scaling means that the non-OP free energy is an increasing function of the wavelength, the specific twin width will be given by a balance between this term and the Ginzburg term, that attempts to remove any interface. Simulation results show that the equilibrium twin width λ fulfills the experimentally observed relationship $\lambda \sim \sqrt{L}$. The full strain fields e_1, e_2 and e_2 are characterized both in the martensite and in the austenite. Also, the size of the transformable region appears to be crucial in determining the resulting equilibrium structure. Actually, there exists a minimum length for the nucleation of twinned martensite, which increases with temperature and diverges as T approaches the transition temperature of Landau. In this size regime, a checker-board pattern that alternates parent and product phases is stabilized instead of diagonal twins. The effect of the shape of a finite martensite inclusion (finite in x and y directions instead of finite only in x) on the resulting pattern has been also studied.

3.4.2 Simulating austenite

This method consists in simulating explicitly a surrounding austenite matrix. It is carried out by means of defining in a half the system an austenite stability limit T_c well below any temperature T in order to strongly stabilize the austenite phase from the point of view of Landau. This is equivalent to define a free energy purely harmonic in the OP in the austenite region, which was done in the analytical previous method. Periodic boundary conditions are maintained in both axis. This method succeeds in reaching the main target that is to obtain an habit plane along which the total strain vanishes by modulating it with a narrow
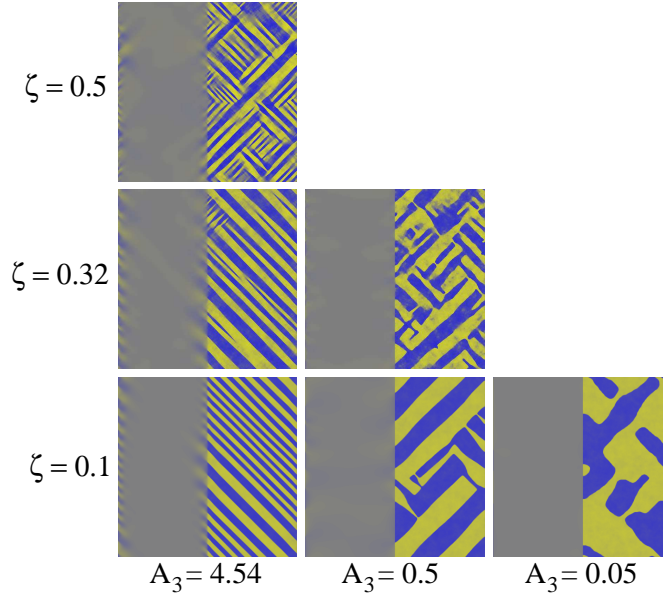
Figure 3.9: Low temperature configurations showing half austenite (left side) and half twinned martensite (right side) for different values of anisotropy and disorder. Twin width increases as anisotropy is decreased. Disorder does not affect twin width directly, but may break domains which in turn does affect the domain size.

distribution of *low* wavelengths, which contrasts with what obtained previously. Figure 3.9 shows snapshots of the simulation cell at low temperatures for different values of anisotropy and disorder. It can be seen that in all cases one half of the system is retained in the austenite phase. This naturally imposes the requirement of a globally invariant habit plane, which leads the system to exhibit the same proportion of the different martensitic variants along this plane. Mediated by the long-range anisotropic interactions, long thin twins with a similar width are formed. Moreover, it can be observed that the strain field decays in the austenite, consistently with the previous analytical method.

The specific value of the anisotropy affects the resulting twin width, in agreement with the fact that the constant of proportionality of the scaling relation $\lambda \sim \sqrt{L}$ contains elastic constants related to the anisotropy factor [167]. In particular, a lower value of A_3 results in a broader twin width. Domain size distributions will be analyzed in detail later.

It is worth noting that high values of disorder make break down long twins into *small* regions with differently oriented twins. It is observed that the smaller the region the narrower the twin width, which is in agreement with the scaling relation above $\lambda \sim \sqrt{L}$. Note that in the regions surrounded by other twinned regions, the appropriate modulation length of twins comes from domain boundaries and the austenite region (the left half side of the snapshots) has no effect in it. This is

important since it highlights the fact that the notion of invariant plane, either in phase boundaries or domain boundaries, is inherent in the original model. Thus, to attain the correct modulation the unique additional condition that is required to include in the model is the existence of a plane separating two phases or differently oriented twins, but, once such a plane exists, the energetic ingredients needed to form thin twins are already included in the initial model. In fact, this phenomenon was already observed in a different context in the case of tweed. Indeed, tweed grains emerged initially in regions where T_c was higher than the surrounding austenite matrix, leading to a natural (crosshatched) modulation that minimized the total strain along the austenite-tweed interface.

Domain size distribution

Now we attempt to characterize the structures through the domain size distributions. This analysis requires surfaces effects giving rise to the right twin widths. Since the method of simulating austenite do not entail additional coding, the computation cost is equivalent to the usual model from the point of view of storage and time. Therefore, we have chosen this method to systematically compute the evolution of the domain size distribution from the high- to the low-temperature regime for different values of anisotropy and disorder, which is of crucial interest for the purposes of this thesis. Figure 3.10 shows the domain size distribution for the same values of ζ and A_3 as in Fig. 3.8 and for three different temperatures: $T = 1.5$ ($> T_0 > T_c$), $T = 1.0$ ($= T_c$) and $T = 0.5$ ($< T_c$). For relatively high anisotropy and small ζ values–martensitic systems, in the small figures at the bottom left corner–tweed precursor is found at high T with a characteristic length that changes towards the characteristic length of twins when undergoing the martensitic transition.[4] Instead, when ζ is high enough to block twin formation, the characteristic domain size at high-T survives when T is lowered well below the transition. Domains are not allowed to grow due to the presence of relatively high levels of disorder but freeze thus rendering the system to anchor in metastable states. Actually, these states show glassy features, that will be shown in ZFC/FC experiments in chapter 4. Anticipating these results, glassy states have been indicated in the figure to make clear the general landscape. Note that the minimum value of ζ required to inhibit twins increases when the value of A_3 increases.

---

[4]The distributions showing a large characteristic length are much less peaked (and hence broader) mainly due to two reasons: In one hand, when the twin width increases, the number of twins decreases and this entails a distribution which is statistically more poor. Second, when the twin width is considerable large, compared to the simulation cell size, periodic boundary conditions may play an undesirable key role in determining the twin width.
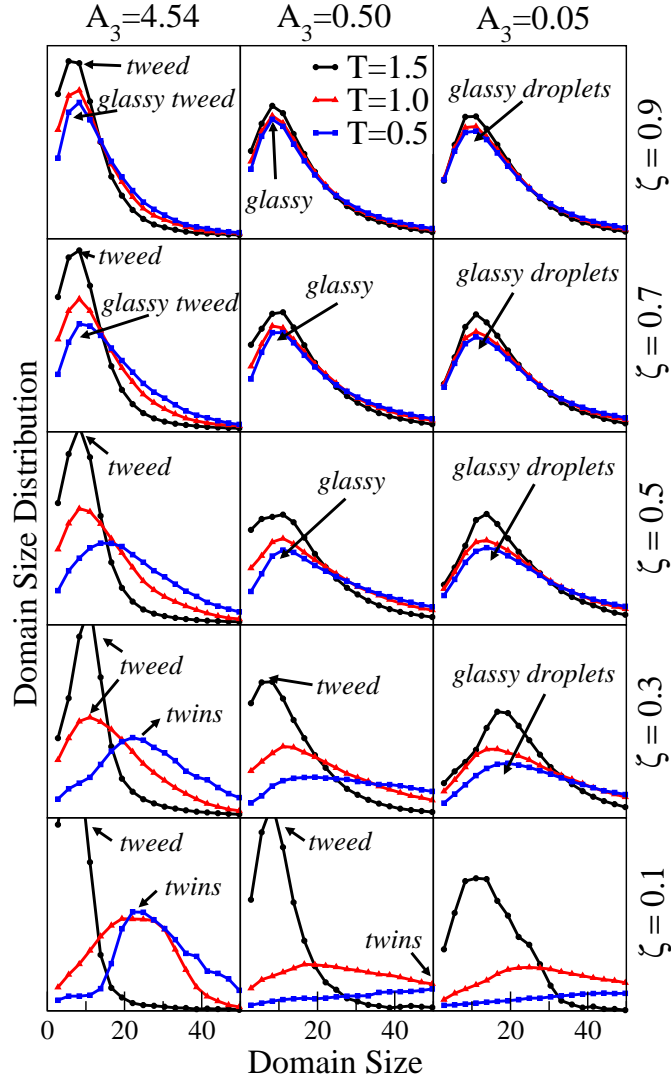
Figure 3.10: Domain size distribution for different values of σ and A_3 and for three different temperatures: at the parent phase ($T = 1.5$), near the transition temperature ($T = 1.0$) and in the martensitic phase ($T = 0.5$). The corresponding patterns are specified in the unambiguous cases. Frozen states are obtained in those cases where the characteristic domain sizes do not change by decreasing T but retain the high-T structures down to low T. Same vertical scale (in units that normalize the distribution) applies to all cases and therefore it does not need to be specified.

Checkerboard pattern

Taking advantage from this easy method to simulate austenitic boundary conditions, we analyze qualitatively the effect of small sizes in the structures. This is shown in Fig. 3.11. The initial configuration (a) consists of a half the system lying in the austenite phase and the another half in the martensite. Then, we proceed to decrease the martensitic region by changing the configuration of $T_c(\mathbf{r})$ in such a way that we set $T_c(\mathbf{r}) = 0$ in a narrow strip at the austenite-martensite interface, and we let the system relax again. We repeat this procedure progressively as it is shown in selected snapshots (b)-(f). We have done that for two different temperatures, $T = 0.5$ and $T = 0.9$. It can be observed that when the size of the martensitic region is decreased below a certain value, twinning is no longer observed but a checker-board pattern. This is in qualitative agreement with simulation results in Sec. 3.4.1 where such patterns are referred to as *lattice martensite*. There, we recall that a free-energy contribution was derived analytically from imposing finite size effects. Hence, that was a physically more meaningful method. Instead, the current method arises as powerful due to its simplicity and reveals that checkerboard structures are already contained in the original model.

It must be noted that, due to the presence of disorder $T_c(\mathbf{r})$, the checkerboard pattern is observed to be inhomogeneous and/or discontinuous along the martensitic strip. This is also in agreement with results in Sec. 3.4.1, where a dependence of the pattern on temperature is observed. Focusing at $T = 0.9$ in Fig. 3.11, in (d) the checkerboard pattern starts to appear and coexist simultaneously with twin boundaries. As the strip is progressively reduced, the checkerboard grows to the detriment of twinning [(e)]. This trend is also observed at $T = 0.5$ although, as expected, the martensite appears to be more stable. Note that the morphology of the decaying strain fields in the austenite (which are larger in strain and range at lower temperatures), also shows the twin-checkerboard crossover.

Checkerboard strain structures have been observed experimentally in decomposing metal alloys (Co-Pt [169], AuCu(-Pt,-Ag) [170], etc.) and in oxide ceramics (ZMnGa0$_4$ [171], (Nd$_{2/3-x}$Li$_{3x}$)TiO$_3$ [172], etc.), although, in general, they are not associated to the confinement of the strain field.

3.4.3   Phenomenological long-range potential

Previous to the analytical work explained in Sec. 3.4.1, Shenoy *et al.* [168] proposed a free-energy contribution coming from the existence of a habit plane. Anticipating the full kernel found subsequently, that term already contained the $\sim 1/|k_y|$ factor, essential for capturing the scaling resulting from the free-energy
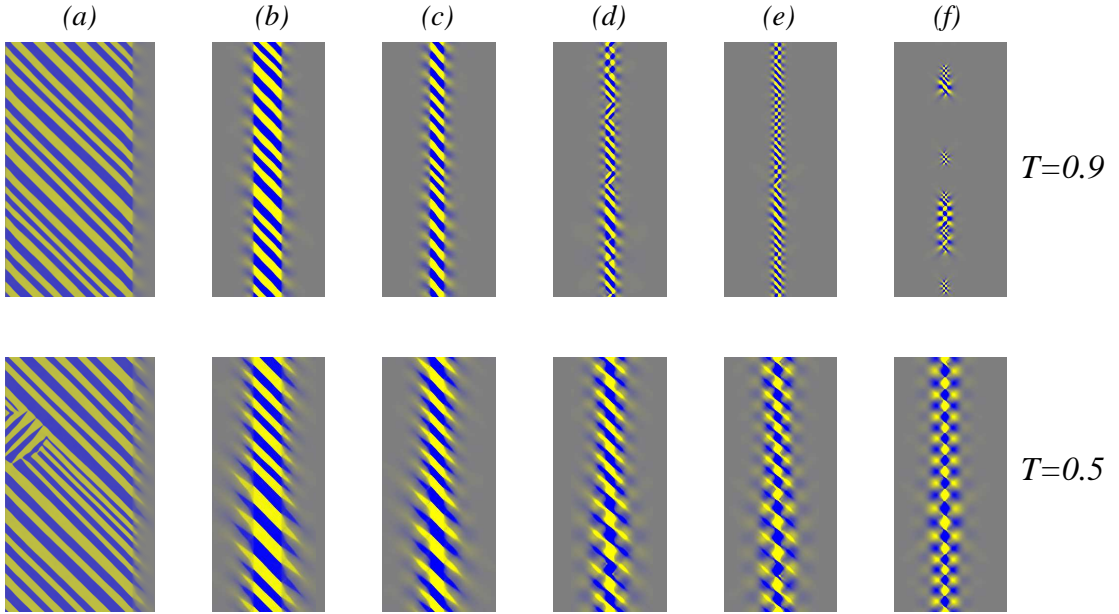
Figure 3.11:

minimization including both martensitic and austenitic regions. Motivated by this idea, we introduced a phenomenological term in the free energy with a unique kernel that goes as $\sim 1/|k_y|$. Mathematically:

$$F_{\mathrm{S}} = C_s \int dx \int \frac{1}{|k_y|} |\tilde{e}_2(x, k_y)|^2 dk_y, \qquad (3.1)$$

where $\tilde{e}_2(x, k_y)$ is a Fourier transform of the OP strain $e_2(x, y)$ only in the y direction[5]. Here C_s is the constant of proportionality of this contribution. As pointed out before, such a kernel makes the different martensitic variants exist in the same proportion (self-accomodation), leading to a zero net strain, i.e. a macroscopically invariant habit plane. Otherwise, a non-vanishing contribution of $e_2(k_y = 0)$ would remain, which would make the energy term $\sim 1/|k_y|$ diverge.

This free-energy contribution increases with the wavelength of the strain modulations. Thus, it favors a structure of narrow twins. Given that the Ginzburg energy penalizes the interfaces (i.e. prefers $\mathbf{k} = 0$), the equilibrium configuration will be given by a balance between these two terms, and approaches the equal-width twinning. Since this term emerges from habit plane effects, it will be referred to as the surface potential, in contrast to the potential coming from bulk compatibility. Actually, our simulation cell has periodic boundary conditions, which leads to an infinite system. Nevertheless, the surface potential introduces

---

[5]Discretization and derivatives of this term, which are necessary for the dynamics, can be found in App. A

an effective, finite size $\mathcal{L}$, which is given through the weight C_s. Since this term is purely phenomenologic, the value of C_s is arbitrarily chosen. In fact, its choice will determine this effective size $\mathcal{L}$ in such a way that, larger values of C_s entail narrower twins which means lower sizes $\mathcal{L}$. The other way round, for $C_s \to 0$ we obtain $\mathcal{L} \to \infty$ that means a single domain, and we recover the original model.

Before going into the simulation results, it should be noted that the computational cost of this term is large. Therefore the linear system size has to be diminished to $500l_0$, discretized on a 256×256 mesh. Moreover, disorder is Gaussian correlated (instead of exponentially correlated)[6] since in this case it has been observed to be faster in stabilizing the configurations.

We explore the space of configurations for some values of the coefficient C_s. We have also studied the effect of varying the correlation length of the disorder ξ, since it affects directly the local stability islands, in order to look for possible effects of it on the typical twin width. Figure 3.12 shows two sets of snapshots of configurations corresponding to high (a) and low (b) temperatures. In each set of snapshots, the correlation length ξ increases from left to right and the surface weigth C_s increases from top to bottom. The case $C_s = 0$ is included to compare the results with those obtained previously, in the absence of the surface potential. In order to highlight the effect of C_s the disorder configuration is the same for all cases with the same ξ.

As can be seen, in case (a) C_s appears not to have relevant effects on the obtained configurations. This occurs due to the fact explained in the previous section: The presence of disorder in the austenite gives rise to regions within which the martensite phase is stable. Since such regions are of finite size, they behave as finite martensite domains, thus trying to vanish the global strain at the boundaries that, in fact, act as habit planes. This forces the strain to be modulated inside these regions, leading to tweed textures. The length of such modulations coming from the real surface effects in disordered regions dominate over the phenomenological surface potential. Hence, no effects of it are appreciable in this temperature range. In that sense, cross-hatched tweed modulations also make the surface free energy be small. Due to the same reason, these precursor structures strongly depend on the value of ξ, since it partially[7] determines the size of the regions with high $T_c(\mathbf{r})$. More specifically, as it is increased, the modulation length of the precursor domains increases, in agreement with the scaling law $\lambda \sim \sqrt{L}$.

---

[6] A study in a very similar magnetic model concerning the effect of the particular functional form of the correlation function on the disorder has been shown that such specifities do not affect the obtained structure.

[7] Let us recall that the disorder is completely determined by ξ and the disorder amplitude ζ.
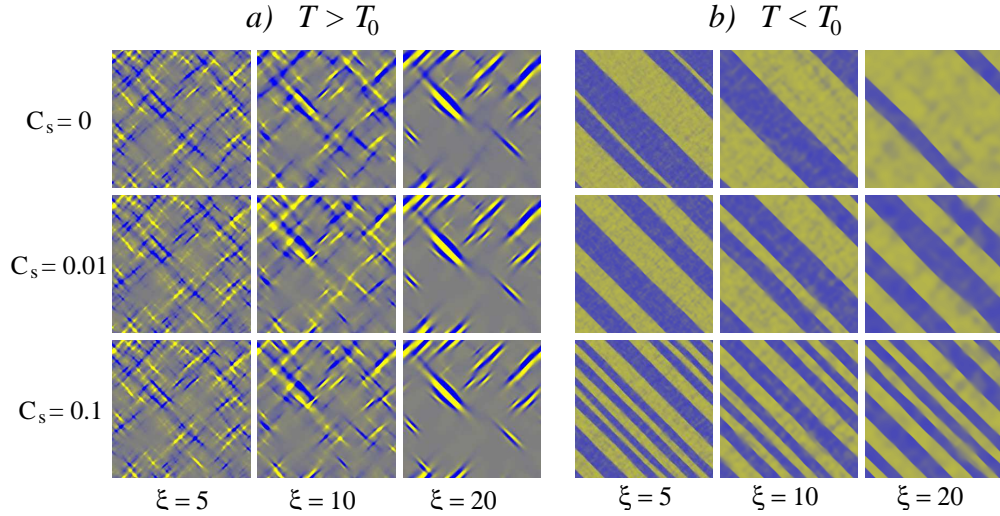
Figure 3.12: Snapshots of selected configurations including $1/|k_y|$ potential as a function of the weigth C_s and the correlation length of the disorder ξ, at two temperatures: (a) well above and (b) well below the transition. In (a), tweed textures are not affected by the phenomenological potential but by the specific value of ξ: The high the ξ the larger the strain modulation. In contrast with that, twinned structures in (b) are not affected by ξ but by C_s: The higher the C_s the smaller the twin width.

Instead, the opposite behavior is observed in the martensitic phase [case (b)]. The obtained twinned structure does not depend on the correlation length and, in general, on the disorder configuration. It was already observed in the absence of the surface potential in Sec. 3.4.2, since twinning was originated from strong diagonal correlations between cells, overcoming the barriers erected by disorder.[8] On the other hand, as it is expected, the typical twin width decreases with the surface coefficient C_s.

Domain size distribution

We also address the analysis of the domain size distribution through the method of the surface potential $\sim 1/|k_y|$. Here the value for the correlation length is set to $\xi = 20l_0$ and will be kept constant. We recall that, if not indicated explicitly, the values for A_3 and ζ are set to $A_3 = 4.54$ and $\zeta \simeq 0.3$. We then proceed to study the evolution in temperature of the characteristic lengths of the patterns for two values of the coefficient C_s, $C_s = 0.1$ and $C_s = 0.01$. Results are shown in Fig. 3.13.

---

[8]Actually, as obtained in Sec. 3.3 there exists a treshold for the disorder amplitude ζ above which it is able to inhibit the martensitic transformation but below which disorder has indeed little effect on twinning features.

Let us focus first on the value $C_s = 0.1$. At high temperatures a peak is observed at small lengths which corresponds to tweed modulations (indicated by the dahsed line), and is mainly determined by the characteristics of the disorder, as has been discussed previously. When T is decreased, the domain size distribution broadens, due to the widening of the modulation length which is consistent with an enlargement of the disordered regions. At the same time, new regions arise that keep on nourishing small wavelengths. Although in the coexistence region the future twins can already be discerned, the shorter wavelength of tweed still breaks them and no twinning signature can be appreciated in the domain size distribution. It is just below the transition, when the twins are clearly formed, that a rather different, much broader distribution can be observed. It can be regarded as the sum of two contributions: one corresponding to some small wavelengths that still survive (as the one observed at high T), and the other coming from the twin width (indicated by the dotted line). This is in agreement with the first-order character of the transition which allows for phase coexistence around the transition point. When the system is cooled further, only the twin contribution remains, which gives rise to a single, narrow peak confirming the existence of a characteristic twin width. It is important to recall that this peak would not appear when the surface potential is removed, but the resulting twins exhibit widths in a very wide region that spreads out from small sizes up to the simulation cell size (which corresponds to the single domain).

Similar trends may be observed in the evolution in temperature for $C_s = 0.01$. The characteristic length of tweed (that naturally coincides with that for $C_s = 0.1$) evolves towards the much larger characteristic length of twins, that in this case is larger than that for $C_s = 0.1$. Due to the absence of a clear peak in the distribution (due to the same reasons as in broad distributions in Fig. 3.10) dotted line has been omitted in this case. In a very similar magnetic model, consisting of a two-well Landau potential extended to include quenched disorder coupling to the harmonic term and long-range dipolar interactions, a similar study was carried out where a single peak of small size was observed at high temperatures corresponding to magnetic tweed, and a single peak of larger size was observed at low T corresponding to magnetic twins. However, opposite to the elastic case, coexistence of the peaks was not observed at any temperature, which corroborates the second-order character of the transition, that makes the OP to transform continuously from one phase to the another, thus preventing a coexistence region.
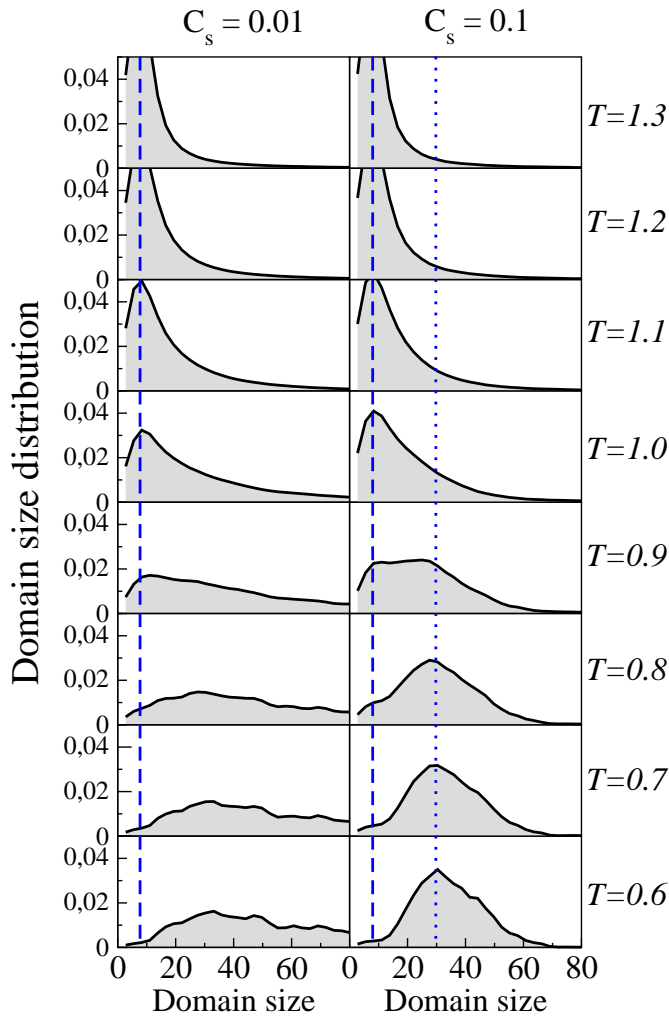
Figure 3.13: Evolution in temperature of the domain size distribution in a martensitic system for two different values of the coefficient C_s. Typical tweed length observed at high temperatures, is indicated by the dashed lines whereas the dotted line points at the typical twin width (dotted line is ommited for $C_s = 0.01$ due to the ambiguous broad distribution). It is worth noting that coexistence of peaks is clearly observed close to the transition for $C_s = 0.1$.

3.5   Needles

It is worth looking at the morphology that appears when different twin laminates
(polytwinning) meet perpendicular to each other. A domain reaching a domain
boundary perpendicularly typically accomodates by taking a needle-like shape
close to the boundary if the two perpendicular domains are of the same orien-
tational variant [173]. Our original model also accounts for this phenomenon,
although perpendicular domains do not occur often because twinning typically
correlates the whole system according to a single direction. However, finite size
effects mentioned in the previous section allow for a more rich internal twinned
structure, with twins in both diagonal directions. This may give rise to per-
pendicular junctions and hence, needles can be observed. We have selected two
low-temperature snapshots which clearly exhibits this morphology. Both experi-
mental [(a)-(d)] and simulated [(e)-(f)] twins with needles are shown in Fig. 3.14.
Case (e) incorporates surface effects through the phenomenological potential and
case (f) through the method of simulating austenite.[9] Moreover, when moving
away from the perpendicular junctions, needles often widen and even join other
needles thus forming a broader and broader twin domain. This may give rise to
self-similar patterns [174]. Some other times needles die before becoming *true*,
long-range twins. Both phenomena can be observed experimentally in case (a)
and (c) of Fig. 3.14. Case (f) shows a simulated configuration exhibiting both
joined and dead needles.

---

[9]We remark that finite size effects are not needed for this phenomenon to occur, but they
are introduced to make easier the formation of domain walls joining perpendicularly.
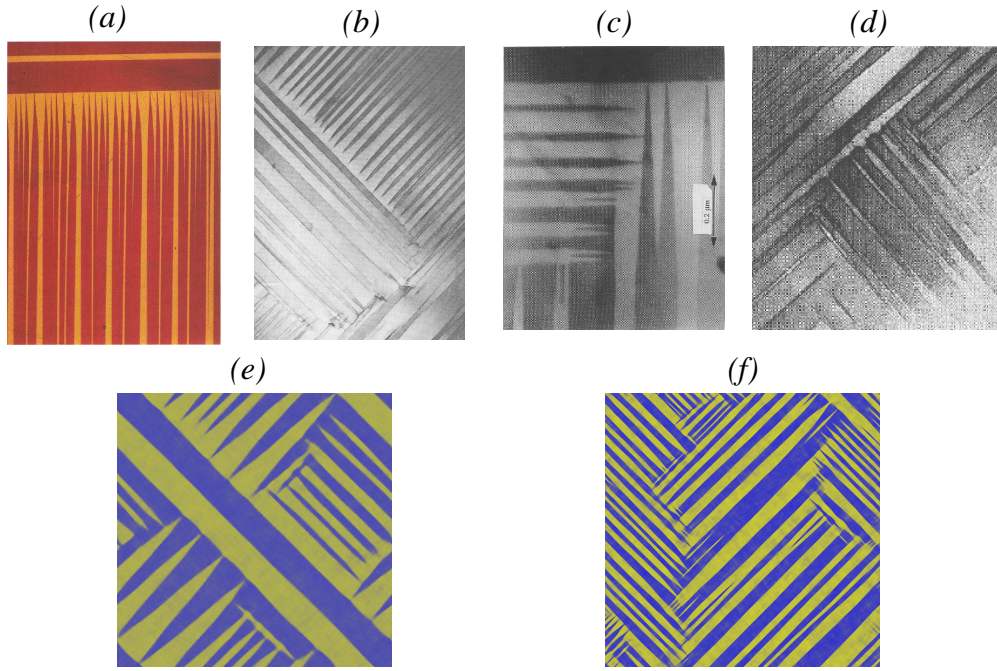
Figure 3.14: Experimental images [(a)-(d)] and simulation snapshots [(e)-(f)] exhibiting needle-like domain walls in perpendicular junctions. (a) Optical micrograph of Cu-Al-Ni has been extracted from Ref. [13]. (b), (c) and (d) show TEM images of Y-Ba-Cu-O, extracted from Ref. [5]. (e) This configuration has been obtained by including the surface potential $\sim 1/|k_y|$. Linear system size of (e) is $500l_0$ discretized on a 256×256 mesh. Snapshot in (f) is a $1000l_0 \times 1000l_0$ section of a larger system of linear size of $4000l_0$ discretized on a 2048×2048 grid which includes the simulated austenite region. This is the reason why (f) does not exhibit periodic boundary conditions.

Chapter 4

Thermodynamic properties

4.1 Heat capacity and transformed fraction

This chapter is devoted the study of the thermodynamic behavior that underly the structures shown in the previous chapter. First, the behavior of the heat capacity $\mathcal{C}$ has been studied as function of the parameter A_3, which we recall that, at constant T, it is proportional to the elastic anisotropy factor $\mathcal{A}$. The heat capacity $\mathcal{C}$ can be obtained according to the well known relation with the Helmoltz free energy F: $\mathcal{C} = -T \partial^2 F / \partial T^2$. In our case, the Helmoltz free energy corresponds to the total free energy of the model F_{T}.

In order to reproduce the standard experimental procedure, the simulations have been carried out upon cooling from the high-temperature phase ($T = 1.62$) down to well below the low-T phase ($T = 0.3$), with a step of $\Delta T = -0.02$. For the specific value of the disorder used in these simulations ($\zeta = 0.32$) the range of T is wide enough to comprise almost all the local stability limits $T_c(\mathbf{r})$s and thus capture all the relevant features in the heat capacity. From 10 to 40 independent seeds (depending on the fluctuations of $\mathcal{C}$, that in turn depend on the value of A_3) have been used in the average of the curve. However, this has been insufficient to completely remove the irregularities without thermodynamic meaning and further smoothing has been necessary by fitting each point of the curve by a parabola with the closest eight temperatures (four of higher T and four lower). This procedure has left approximately only the relevant behavior, which was detected previously by analyzing different independent groups of seeds.

The similarities observed between the first derivative of the free energy $F' = \partial F / \partial T$ and the transformed area fraction ς inspired us to compute the first derivative of the latter $\varsigma' = \partial \varsigma / \partial T$, to compare it with the heat capacity $\mathcal{C}$. The transformed fraction ς has been specifically computed as the fraction of the system

with a strain e_2 such that: $|e_2| > \frac{1}{2}\sqrt{\frac{1}{N}\sum_{i,j} e_2^2(i,j)}$. In order to follow the same procedure as in the computation of $\mathcal{C}$, ς' has been smoothed by fitting each point of the curve with the closest four points, since it is a first derivative (instead of a second derivative as in the case of $\mathcal{C}$) of the original data.

First we have performed simulations both upon cooling from the high-T phase and upon heating from the low-T phase. The resulting curves for $\mathcal{C}$ are shown in the top right panel in Fig. 4.1 for the value $A_3 = 1.0$. It can be observed that the cooling curve exhibits a peak shifted to temperatures lower than the transition temperature $T_0 \simeq 1.03$ in the clean limit. Instead, the peak in the heating curve is shifted to higher temperatures. Hence, one can deduce that these peaks corresponds to metastability limits of the phases. Moreover, in both cases the position of the peak coincides with the position of the peak observed in the first derivative of the transformed fraction $d\varsigma/dT$, which is shown in the bottom right panel. This gives confidence about the robustness of the results. The free-energy density f and the transformed fraction ς are displayed for completeness in the upper left and lower left panels respectively. The curves of ς upon cooling and heating are very close to each other indicating little hysteresis, which is in agreement with the weak character of the first-order martensitic transition (MT) undergone by Fe-Pd, from which we have taken the material parameters used in this model. The wide temperature range whithin which the transition occurs is due to the presence of disorder.

Given that we know from the previous Fig. 4.1 that the peak is related to a metastability limit, to save computation time, from now on we restrict ourselves to the computation of the cooling curves. In Fig. 4.2 we extend the comparison between the heat capacity $\mathcal{C}$ and the transformed fraction ς to three different values of A_3: (I) $A_3 = 4.54$, (II) $A_3 = 0.50$ and (III) $A_3 = 0.05$. The temperature dependence of both the free energy density f and the heat capacity $\mathcal{C}$ are shown in the upper panels whereas the lower panels show ς and ς'. One can see that in all cases both $\mathcal{C}$ and ς display anomalies at the same values of T, thus supporting such anomalies as robust behavior.

For the highest value of A_3 [case (I)], $\mathcal{C}$ shows a broad bump and a sharp peak around $T \leq 1$. The bump is associated with the development of tweed precursors whereas the peak is the signature of the structural transition. In case (II), $\mathcal{C}$ shows a smoother and lower peak than can be observed over the bump at $T \simeq 0.75$. As pointed above, such a peak is related to the low temperature stability limit of the high temperature phase. This is in agreement with the small peak centered at zero observed in the local strain distribution below $T \sim 0.75$ shown in Fig. 3.2. In case (III) only the smooth bump associated with nanoclusters of the phase separated pattern is observed. In any case, notice that some amount of the high
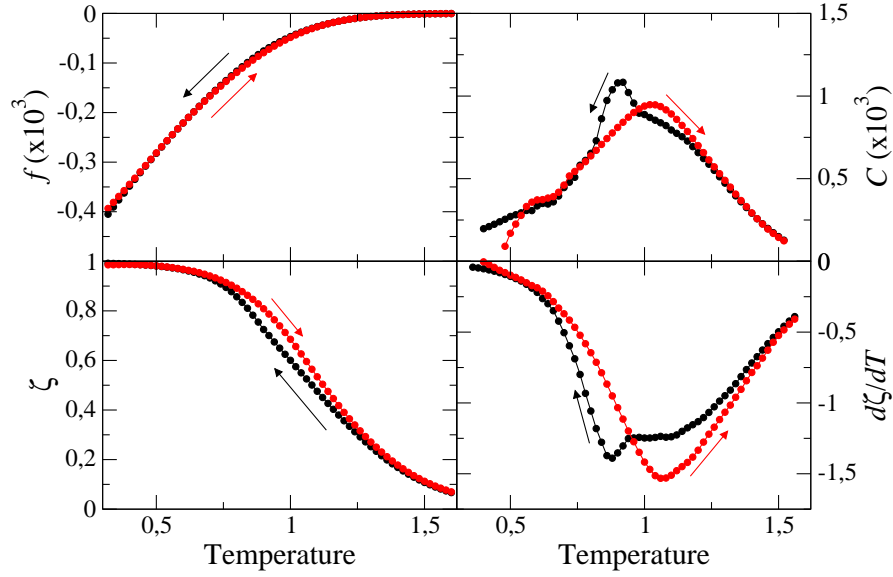
Figure 4.1: The free-energy density f and the transformed fraction ς for $A_3 = 1.0$ are displayed in the upper left and lower left panels respectively whereas the heat capacity $\mathcal{C}$ and $d\varsigma/dT$ are shown in the upper right and lower right panels respectively, both upon cooling and heating.

temperature phase remains down to very low temperature ("retained austenite", see Fig. 3.2).

We now proceed to compute systematically the heat capacity $\mathcal{C}$ as a function of A_3 in order to visualize the dependence of the anomalies on it. Figure 4.3 shows the behavior of $\mathcal{C}$ for several values of A_3 ranging from $A_3 = 0$ to $A_3 = 10$. The observed general trends are those described above and the peak shifts to lower temperatures as A_3 decreases. Notice that only for values of $A_3 \geq 1$ the peak can be associated to the structural transition, accompanied with the development of long range order (twinned structure). For values of $A_3 \leq 1$ the peak is associated to the the stability limit of the high temperature phase and rapidly goes to zero as $A_3 \to 0$. We emphasize that comparable anomalies have been found experimentally [163] in Ni-Ti(Fe) alloys, where an increase in Fe content diminishes and shifts the peak in $\mathcal{C}$ to lower temperatures. In particular, it is found that for 6 at.%Fe, no signature of peak in $\mathcal{C}$ is observed and the transition is suppressed. It is shown in Fig. 4.4(a). The same occurs in Ti-Pd(Cr) [70]: when Pd is substituted by Cr the peak softens and shifts to lower temperatures. For 10 at.%Cr no MT is observed. This is shown in Fig. 4.4(b).

The peak temperature of $\mathcal{C}$ in Fig. 4.3 as a function of A_3 has been plotted in Fig. 4.5a and it can be regarded as a phase diagram. The region under the curve indicates the values of temperature and A_3 by which twinned martensite
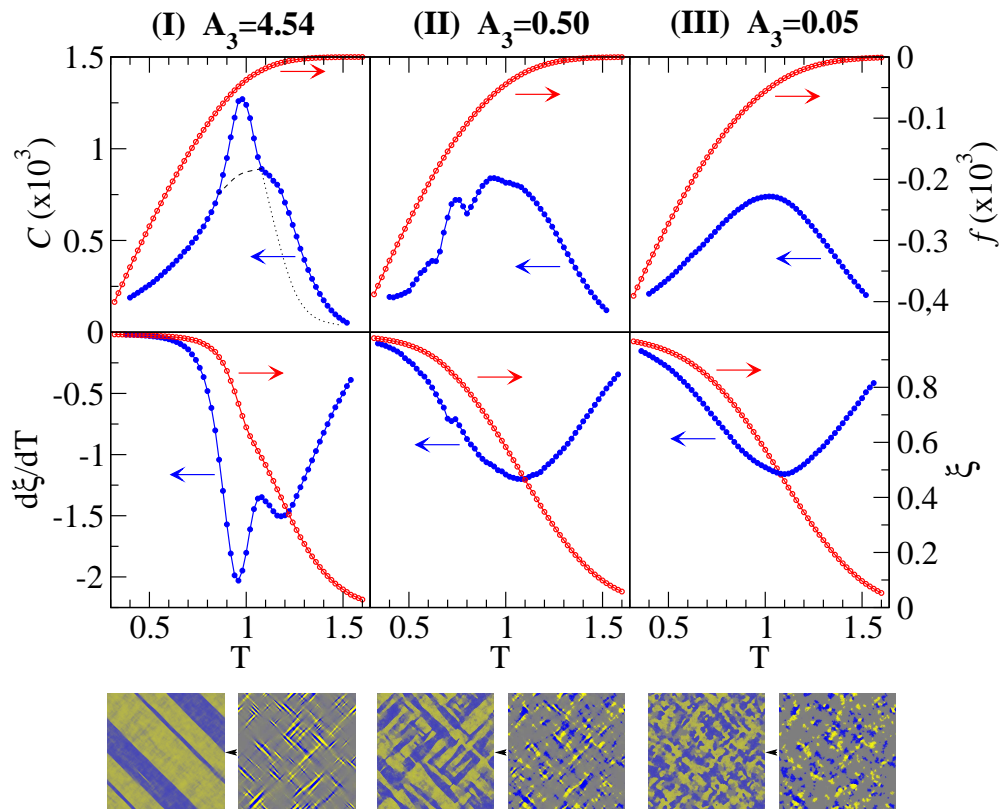
Figure 4.2: Upper panels: Temperature behavior of the free energy density f (right axis) and the heat capacity C (left axis) for three different values of A_3. Lower panels: Temperature behavior of the transformed fraction ξ (right axis) and $\xi' = d\xi/dT$ (left axis). Dotted lines in (I) are guides to the eyes intended to differentiate between the two underlying contributions: Inhomogeneous textures and structural transition.
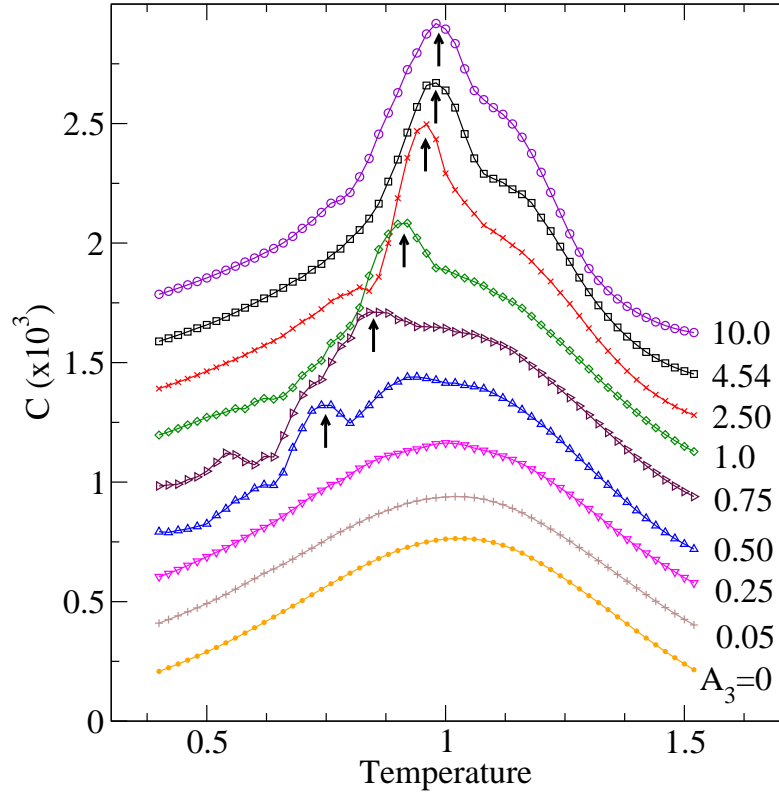
Figure 4.3: Heat capacity $\mathcal{C}$ as a function of T for different values of A_3. The characteristic peak shifts, diminishes, and finally disappears as A_3 is decreased. For the sake of clarity the curves are successively shifted. Arrows indicate the position of the peak for each value of A_3
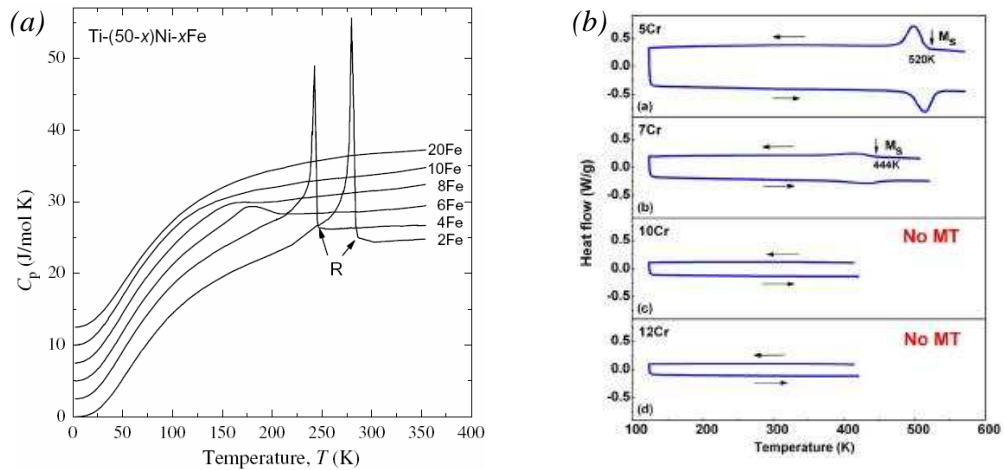

Figure 4.4: (a) Heat capacity for Ti-Ni(Fe) measured by using a relaxation method in a physical properties measurement system (quantum design), extracted from Ref. [163]. (b) DSC measurements of the heat capacity of Ti-Pd(Cr), extracted from [70] respectively.
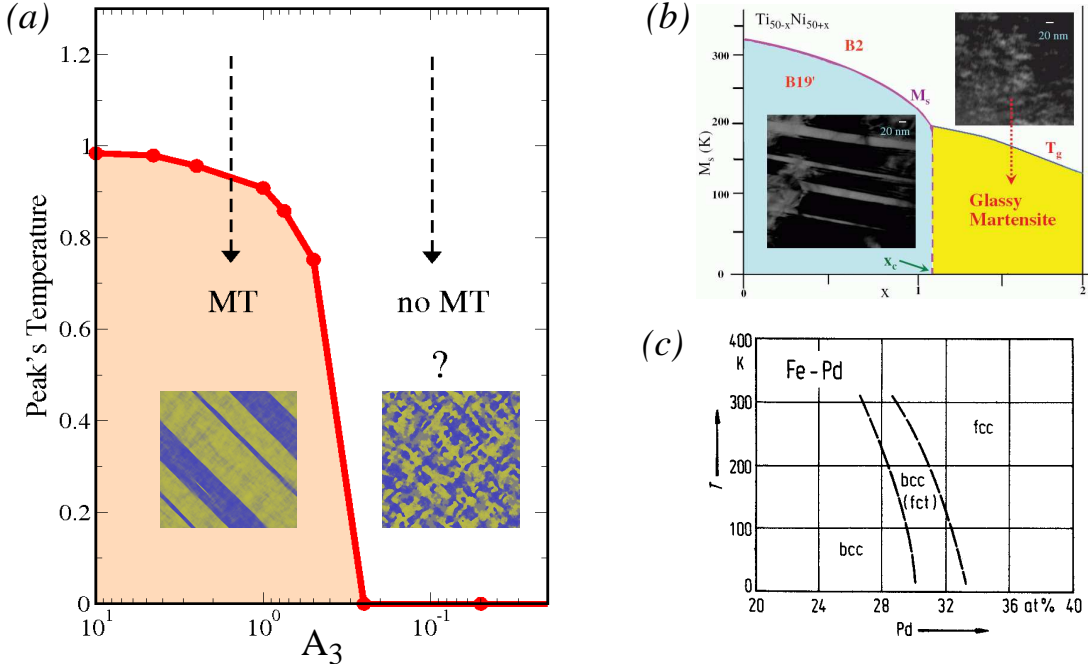
Figure 4.5: (a) Temperature of the peak of $\mathcal{C}$ as a function of A_3, extracted from Fig. 4.3. (b) and (c) Phase diagrams of Ti_{50-x}-Ni_{50+x} (extracted from Ref. [34]) and $Fe_x Pd_{1-x}$ (extracted from Ref. [112]) respectively.

is obtained whereas the region in which the curve vanishes indicates that no MT takes place. Actually, this is qualitatively very similar to those obtained in real materials when varying composition. As examples, in Fig. 4.5b we show the phase diagrams of Ti_{50-x}-Ni_{50+x} and $Fe_{1-x}Pd_x$. These results confirm the general scheme given by the structures observed in Chap. 3.

We recall that the mean value of the local low stability limit $\langle T_c(\mathbf{r}) \rangle \simeq 1$ is kept constant and the shift of the peak (to low T upon cooling and to high T upon heating) corresponds to an increase of the hysteresis, i.e. to a decrease in the M_s temperature and an increase in A_s. Instead, experimentally the decrease occurs in both M_s and A_s temperatures, which reflects an unstabilization of the martensitic phase. This is corroborated by signatures in other quantities like resistivity. Concerning this issue, few comments should be pointed out: As mentioned above, simulations upon heating that show the shift of the peak to high temperatures have been carried out only for one value of A_3 ($A_3 = 1$), which gives rise to long-range twins. Although the mathematical reasons concerning the local stability limits are apparently clear, the shift of the peak to high T appears to be smaller than the shift to lower T. Similarly, it is also not sure that intermediate values of the anisotropy–which give rise to broken twins and still show a peak in $\mathcal{C}$– would show a shift of the peak to high temperatures upon heating analogous to that

observed upon cooling. Additional simulation results should be needed to take out convincent conclusions with respect to that.

We want remark that the suppression of the transition observed in experiments when varying the alloy composition is qualitatively reproduced by our simulations. Moreover, it is expected that the suppression may also occur by increasing the disorder for a given constant A_3, which will be closer to experiments, instead of decreasing the anisotropy for a given value of the disorder as it has been done here.

Maybe the most relevant point concerning these simulation results is that the suppression of the transition occurs due to the fact that the system is retained in a metastable state. Again, it is known from the fact that $\langle T_c(\mathbf{r}) \rangle \simeq 1$ is kept constant and therefore, at low temperatures the thermodynamic equilibrium state is the martensite, which will be confirmed in the next sections through the calculation of other thermodynamic quantities and simulation experiments. In real alloys, the general landscape is unclear. First, the phase diagrams of alloys (like those shown here in Fig. 4.5(b)) are not *thermodynamic* phase diagrams, although it is not specifically stated. In fact, it is widely believed that the unstabilization of the martensite drops down to 0 K. However, recent discoveries in some Ti-based alloys (like off-stoichiometric Ti-Ni [67] and Ti-Pd-Cr [70]) have pointed out to the martensitic phase fact as the true thermodynamic phase at low temperatures and therefore the stabilized nontwinned structures upon cooling are indeed metastable. They are based on the fact that the structures observed in the nontransforming regime exhibit shape memory effect. We recall that such alloys exhibit a very low anisotropy value and the metastable structures are correspondingly almost isotropic, as mentioned in Chap. 3. As far as we now, similar experiments in other alloys with high anisotropy (and exhibiting tweed contrast at low temperatures) have not been published yet and it remains as an open question. This will be discussed in Chap. 5 and 7. Next sections are devoted to confirm the suppression of the transition, the metastability of such low-temperature states and to characterize the kinetic behavior.

4.2   Elastic response C'

The elastic response C' of the system to an external, constant stress field has been studied. The computation has been carried out in two ways: Upon cooling and upon quenching. The former method consists of the following steps:
(i) Starting from a high temperature $(T = 2)$ stabilized configuration, a constant stress field $\sigma \approx 2.5 \cdot 10^{-9}$ is applied in one direction until the system reaches a new stabilized configuration of total strain $e_2^+(T)$.

(ii) Then, the stress field is reversed to the opposite direction, $-\sigma$ and we let the system relax again to another stable state of total strain $e_2^-(T)$.

(iii) The elastic response at the given temperatures is then calculated as $C' = \sigma/(e_2^+(T) - e_2^-(T))$.

(iv) The stress field is removed and the temperature is decreased $\Delta T = -0.01$.

Then, at this new temperature, the system evolves towards a stable state and the cycle starts again: the stress field σ is applied, etc. Instead, in order to compute C' upon quenching the procedure is the same from (i) to (iii), but the starting configuration at each temperature is independent from each other, and has been obtained by relaxing to the desired temperature from a disordered state. The temperatures have been chosen at intervals of $\Delta T = 0.02$ and $\Delta T = 0.03$ ($T = 2, 1.97, 1.95.1.92$,etc.)

The behavior of C' for $A_3 = 4.54$ and $A_3 = 0.05$ is shown in Fig. 4.6(a). For each one of these values, curves obtained upon cooling and quenching appear to be very similar to each other, thus indicating the robustness of the behavior. Again, a large number of seeds have been needed to get smooth enough curves. Unfortunately, the computational cost of C' has been very high in time. Therefore, additional simulations for other values of A_3 and/or disorder, that would be of interest, have not been carried out. For $A_3 = 4.54$, the pronounced dip of the curve clearly confirms the existence of a phase transition. In addition, similar to the behavior observed in $\mathcal{C}$ curves, a flat region lies in the temperature range $1.0 \lesssim T \lesssim 1.25$ that coincides with the precursor (tweed) region. Instead, for $A_3 = 0.05$, the dip amplitude becomes much lower so that the curve and thus the transition broadens. Similar qualitative results have experimentally been obtained in the elastic response when varying the composition in Ni-rich $Ni_{50+x}Ti_{50-x}$ alloys [34], which are shown in Fig. 4.6(b). As the content of Ni increases above $x \geq 1.5$, the curve flatens significantly, which is consistent with the suppression of the martensitic transition for this composition regime.

4.3   Energy analysis: Metastability

In order to compare the relative stability of the relaxed structures, in Fig. 4.7 we show the behavior of the free-energy density f averaged over 40 realizations of disorder as a function of both ζ and A_3. The upper panels show the dependence of f on ζ for the same three values of A_3 as in Fig. 2. Filled symbols have been obtained by gradually decreasing ζ with $\Delta \zeta = -0.02$ from the highest value $\zeta = 0.98$, for which metastable states exist. Actually, we have checked that they are very close to those obtained independently and shown in Fig. 3.8, i.e., those that can be observed experimentally. On the contrary, empty symbols have been
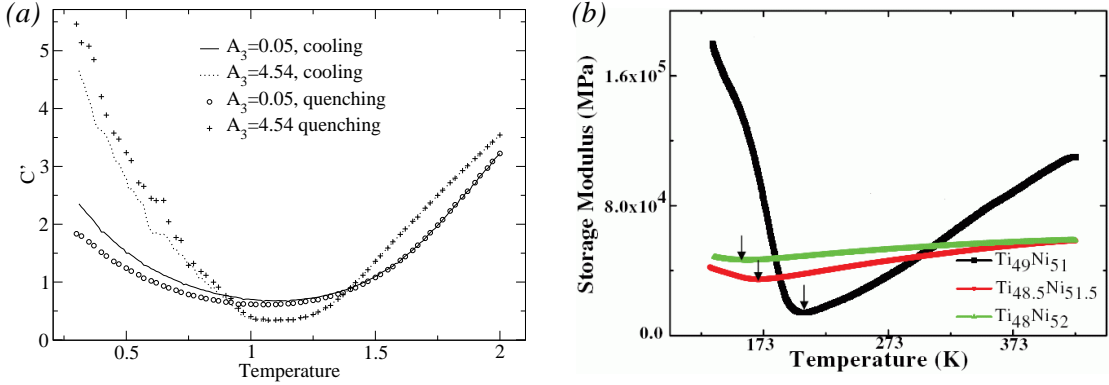
Figure 4.6: (*a*) Elastic response for two different values of A_3, which are in qualitative agreement with (*b*) experimental measurements of the ac storage modulus in $Ti_{50-x}NiTi_{50+x}$, $x = 1, 1.5, 2$, extracted from Ref. [34]

obtained by increasing gradually, starting from the lowest value $\zeta = 0.08$. At this low value, twins are easily formed and, once created, they survive despite the increase in ζ. Consistently, one can observe that f is always lower in the ζ-increasing curve than in the ζ-decreasing one. Actually, the former may be considered as the free energy of the global minimum and any deviation between the two curves provides a measure of the degree of metastability of the latter. In fact, the existence of such global minimum proves that the origin of the metastability is kinetic, as opposed to geometrically frustrated systems like the paradigmatic antiferromagnetic triangle. Additional arguments confirming this kinetic origin will be given in the next section. As a general trend, in both curves the total free energy decreases with increasing ζ. This is because the Landau free-energy contribution (here represented by the dashed lines) prevails over the other terms (Ginzburg and long-range anisotropic terms) and decreases as ζ increases. This can be deduced easily as follows: the regions with $T - T_c(\mathbf{r}) > 0$ are stable in the austenite phase, and their free energy vanishes regardless of the magnitude of $|T - T_c(\mathbf{r})|$. Instead, the regions with $T - T_c(\mathbf{r}) < 0$ are stable in the martensite phase, and their free energy decreases as the value $|T - T_c(\mathbf{r})|$ increases. Then, an increase in the value of ζ increases the amplitud of the distribution $T_c(\mathbf{r})$ and there will exist more regions with a high value of $|T - T_c(\mathbf{r})|$. Consequently, the free energy will decrease.

Interestingly, focusing on the ζ-decreasing curve, f exhibits an anomaly around a particular value of ζ (denoted by an arrow) which depends on A_3. This is precisely the critical disorder $\zeta^*(A_3)$ above which the formation of long-range twins is inhibited. Indeed, the deviation of f from the free energy of the global minimum increases remarkably for $\zeta > \zeta^*$. This is a signature of the degree of metastability of the nontwinned states. For completeness, in Fig. 4.7(*d*) we have

calculated the dependence of f on A_3 for two different values of ζ at intervals $\Delta A_3 = 0.05$ from $A_3 = 0.0$ up to $A_3 = 5.0$. Smooth of the curves has been necessary to extract the thermodynamically relevant behavior. Again, f reveals the existence of an anomaly around a critical value of A_3 (denoted by an arrow) which depends on ζ and A_3. Twins are only observed for $A_3 > A_3^*$. Similar to cases (a)-(c), for $A_3 < A_3^*$ the system is no longer able to reach the twinned state, resulting in an increase in f and therefore of metastability. All these features are consistent with the configurations observed in Fig. 3.8.

4.4   Zero-field-cooling/field-cooling simulation experiments

Up to this point, we have focused on several response functions such as the heat capacity or the elastic response that show that, indeed, for sufficient levels of disorder, the MT is suppressed, in agreement with many experimental results. Also, we have studied the large metastability associated with untwinned low-temperature configurations. Related with the suppression of the MT and the corresponding metastable states, it seems natural to ask oneself whether the stabilized configurations have any relation with glassy systems. In the case of Ti-Ni, one of the experiments performed in Ref. [68] that is indicative of glassy behavior is the so-called zero-field-cooling/field-cooling (ZFC/FC) experiment. Such experiments were first carried out in magnetic systems to detect possible spin glasses [175, 176] and later they have been also applied, for instance, to ferroelectric relaxors [78]. They have in common that ZFC/FC experiments show glassy features in states exhibiting phase coexistence. For instance, in $Pr_{1-x}Tb_xMn_2Ge_2$, they reveal the pinning of ferromagnetic regions (with crystal structure L2_1) due to antiferromagnetic surrounding areas (structure B2) and vice versa [84]. Thus, in order to detect possible glassy behavior in our system, we have performed ZFC/FC simulation experiments, whose procedure is explained in the following section.

Procedure for ZFC/FC experiments

ZFC/FC experiments consist of four steps:
(i) Starting from a high temperature state the system is freely cooled down to a low temperature state.
(ii) Then, a low stress field is applied and the system is heated again up to the high temperature state. The resulting strain curve as a function of temperature is the so-called Zero-Field-Cooling curve.
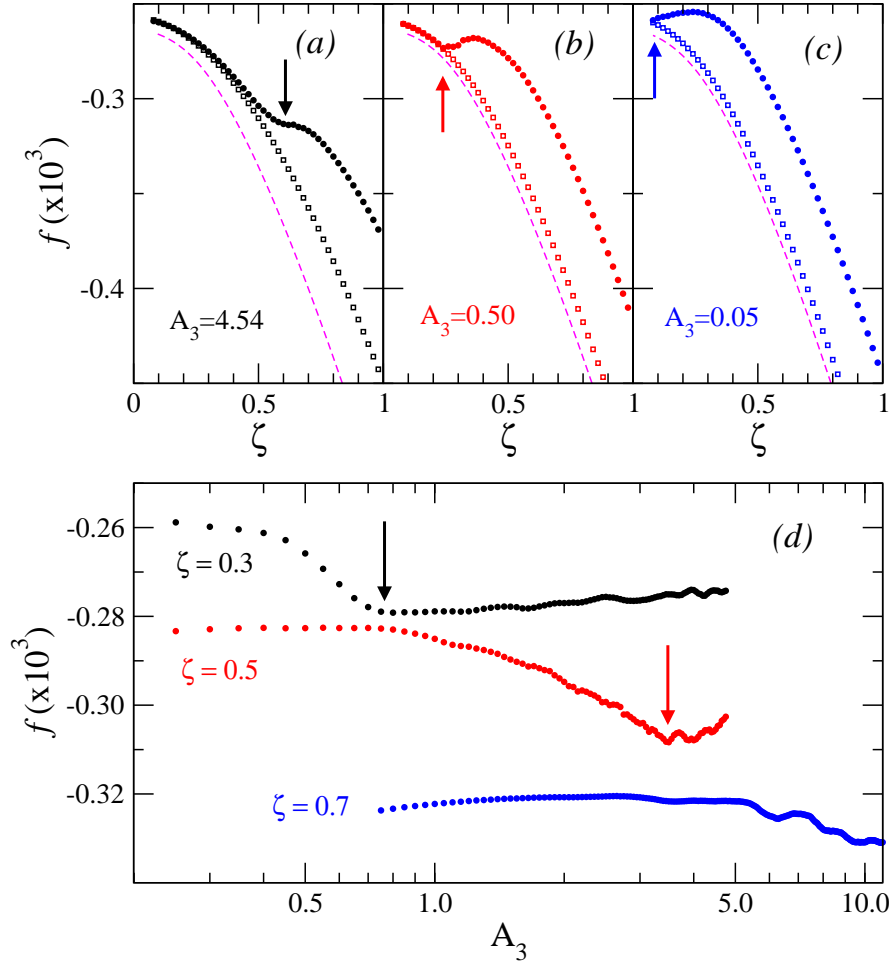
Figure 4.7: [(*a*)-(*c*)] Averaged free-energy density f as a function of ζ for three different values of A_3. Filled symbols are obtained starting from the highest value $\zeta = 0.98$ and gradually decreasing ζ whereas empty symbols have been obtained by increasing ζ starting from the lowest value $\zeta = 0.08$. Arrows indicate the values of ζ below which twin formation is allowed. Dashed lines indicate just the Landau free-energy contribution. (*d*) f as a function of A_3 for two different values of ζ. Arrows point to the critical value of A_3 above which twins exist.

(iii) the system is cooled again with the presence of the stress field.

(iv) Finally, the system is heated again, giving rise to the Field-Cooling curve.

The four steps are displayed in Fig. 4.8. The upper figures show a schematic evolution of temperature and stress field in the corresponding steps. In particular, we have used $T_{\min} = 0.02$, $T_{\min} = 1.62$, $\sigma_0 = 2.5 \cdot 10^{-3}$ and the temperature step is $\Delta T = 0.02$. In the lower figures, two examples of the strain response as function of temperature are explicitly shown in the four stages. One is a high anisoptroy ($A_3 = 4.54$) system and the another has low anisotropy ($A_3 = 0.05$). In the first stage, both systems show a slightly increase in the strain as they are cooled. This occurs because the fraction of one of the martensitic variants is higher than the fraction of the another variant, thus leading to a non-vanishing net strain due to the absence of finite size effects. However, it has no relevance in what concerns the ZFC/FC results. The second stage, which corresponds to the ZFC curve, is of crucial importance. The stress field induces the growth of a selected variant at the expense of the another, thus increasing considerably the total strain. The specific growing path is a signature of the dynamics followed by the system, and, as it can be observed, is different for the two different values of A_3. For the high value ($A_3 = 4.54$), the strain increases rapidly, easily reaching the single domain configuration just when the stress is applied, that corresponds to the equilibrium state. On the contrary, for the low value ($A_3 = 0.05$), the strain increases rather slowly and the system needs to be heated to higher temperatures –and hence takes a longer time– to reach the single domain configuration, as it is indicated by the region enclosed by a dotted border. At that point it is important to note that the applied stress field must be low enough [177], otherwise, high stresses would be able to induce an easy, rapid domain growth of the selected variant and a switching of the other domains regardless of the anisotropy and the disorder values and an undistinguishable behavior would be obtained for all cases. Once the equilibrium, single domain configuration is reached, the total strain evolves mainly according to Landau, drawing a monotonically decreasing curve with increasing T, with a larger slope in the region where the ferroelastic transition takes place. In the third and fourth stages, a similar behavior is observed in both cases, in which the system follows similar cooling and heating paths, with the maximum total strain at the lowest temperature.

Relevant information can be extracted from the comparison between the ZFC and FC curves. Deviations among them indicate that the behavior is history-dependent, and has been related to a loss of ergodicity [68] and glassy behavior. What can be clear observed from ZFC/FC curves in the lower panels of Fig. (4.8) is that for the high anisotropy value ($A_3 = 4.54$) ZFC and FC curves coincide whereas for the low value ($A_3 = 0.05$) they deviate in the region enclosed by the dotted line. This is indicative of kinetic freezing.
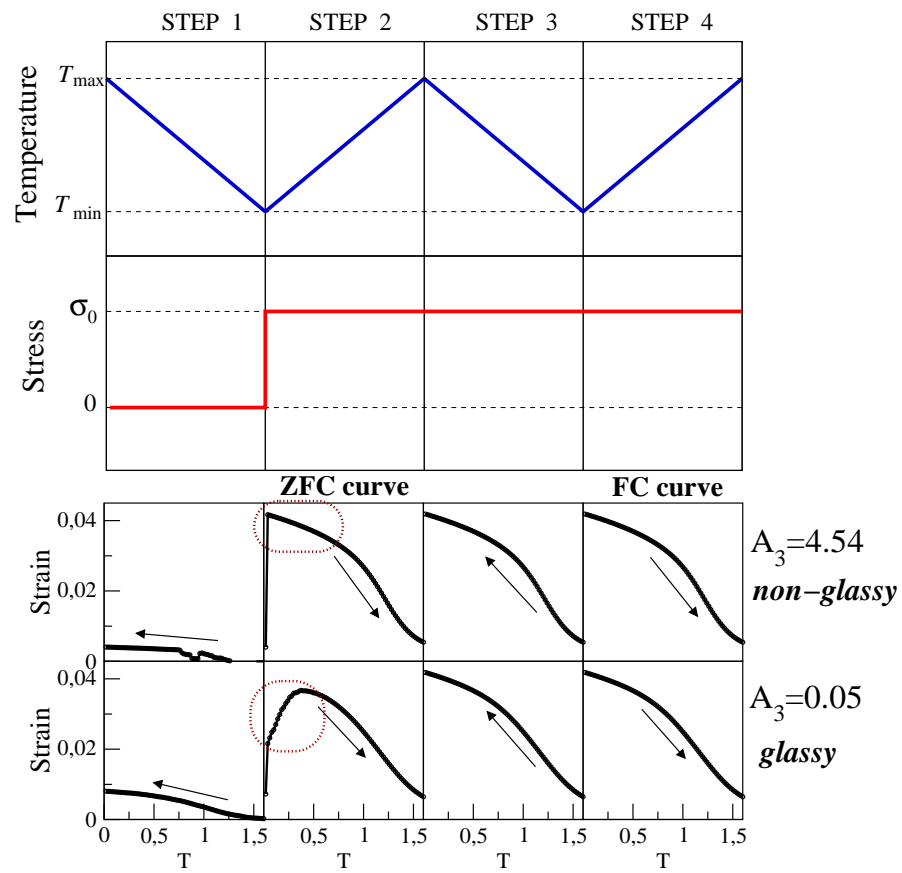
Figure 4.8: Upper panel: schematic representation of the procedure of ZFC/FC experiments. Lower panels: ZFC/FC simulation experiments for high and low values of A_3. Dotted regions indicate the relevant behavior of the system.
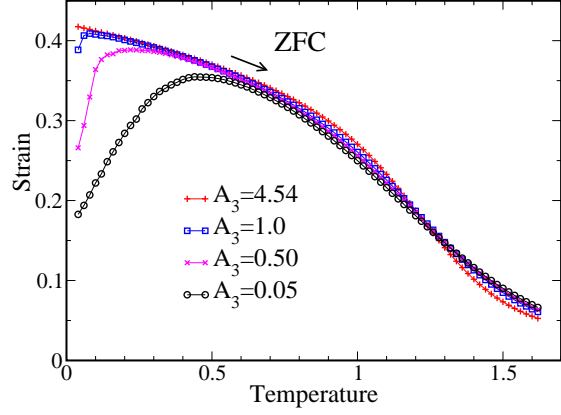
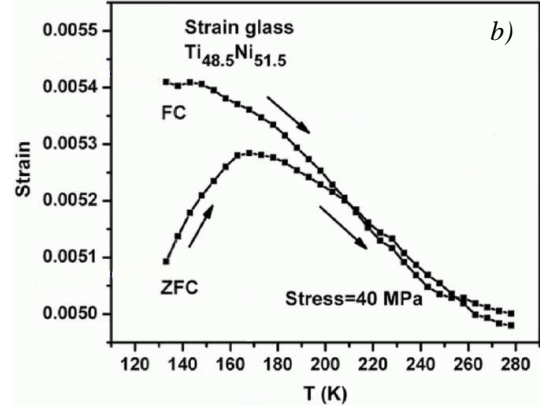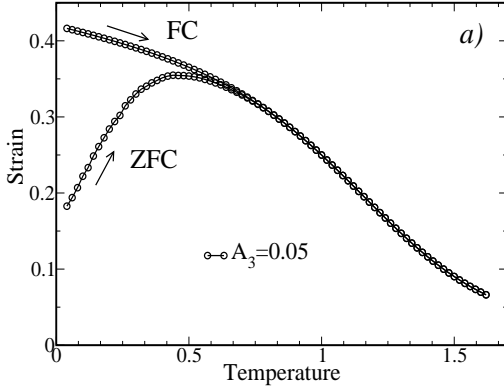**Figure 4.9:** The ZFC curves for different values of elastic anisotropy A_3, for $\zeta \simeq 0.3$.

Figure 4.10: (*a*) ZFC/FC curves obtained in simulation experiments for the value $A_3 = 0.05$ and $\zeta \simeq 0.3$. (*b*) ZFC/FC experiments in $Ti_{48.5}$-$Ni_{51.5}$, extracted from Ref. [68].

Results

Figure 4.9 shows ZFC simulations for different values of A_3 and keeping $\zeta \simeq 0.3$ constant. For $A_3 = 0.05$ the curve represents an elastic behavior that deviates from the FC curve below the peak temperature, which is indicative of glassy behavior. As expected, our simulations in Fig. 4.9 show that this behavior progressively disappears for increasing values of A_3. This trend indeed corresponds to an increase in the elastic anisotropy A and favors the development of long-range order. For comparison both ZFC and FC curves for this value of A_3 are shown in Fig. 4.10 This is in very good agreement with experimental results in $Ni_{51.5}Ti_{48.5}$ shown Fig. 4.10(*b*) mentioned above. Figure 4.11 shows the ZFC curves obtained for different values of ζ and A_3. Here the FC curves have been omitted for clarity and their behavior is in all cases very similar to those in Fig. 4.8. In the three cases (*a*)-(*c*) one observes that glassy behavior is obtained for values of ζ above a critical value that exactly coincides with that obtained previously from the behavior of
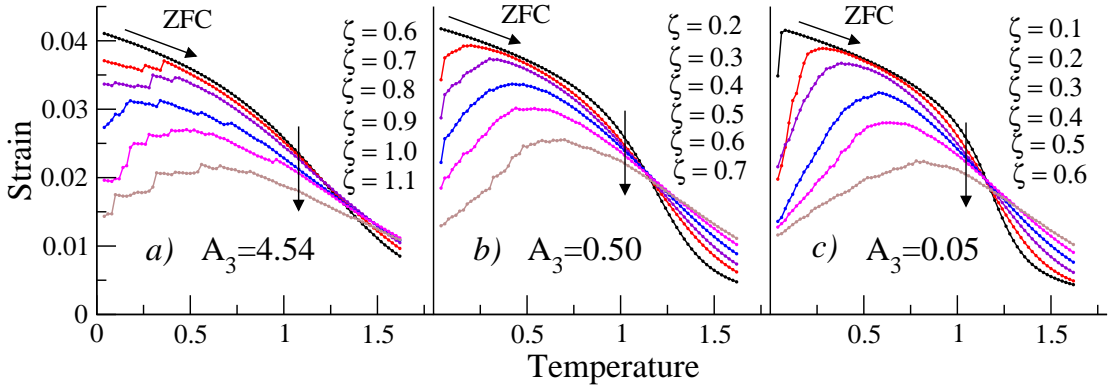
Figure 4.11: ZFC curves for different values of A_3 and ζ. Vertical arrows indicate progressively increasing values of ζ.

f in Fig 4.7. We can then conclude that metastability observed in Fig. 4.7 does indicate glassy states. A comparison with Fig. 4.9 reveals that, indeed, similar effects are obtained either by reducing anisotropy or increasing disorder. Moreover, some small but important differences can still be observed between these cases. Focusing, on the value $A_3 = 4.54$ [case (a)], the ZFC curve is more flat than for lower values of A_3 [cases (b) and (c)], indicating a more blocked dynamics that prevents the system from reaching the FC curve. The low stress field is not able to make the system evolve smoothly toward the monovariant state. Instead, some small sharp jumps are observed due to the sudden correlations of different broken domains of a particular variant selected by the stress field. After a certain number of jumps, the system does reach the monovariant state and thus the FC curve. In that sense, the same factor (i.e., the anisotropy) that for $\zeta < \zeta^*(A_3)$ enables the system to form long-range twinned structures, for $\zeta > \zeta^*(A_3)$, however, causes a higher degree of freezing than for lower values of (A_3). Actually, this can be related to the behavior of f in Fig. 4.7(a)-(c), where it can be observed that in the glassy regime $[\zeta > \zeta^*(A_3)]$, the degree of metastability i.e., the larger the deviation from the free energy in the global minimum increases with A_3 whereas in the twinned regime $[\zeta < \zeta^*(A_3)]$ all the curves approximately coincide.

In principle one could expect the appearance of domains to be deliberate due to surviving long range interactions, although weak or partially blocked by the presence of disorder. In that sense, long range anisotropic interactions would not be able to induce a strong directionality in the domain structure due to disorder, but would establish a particular short range distribution of non-directional domains by promoting the selection of a particular variant for each domain during its evolutions. This selection could depend on the surrounding configuration of domain variants due to a possible tendency toward global strain minimization. Then, by decreasing the temperature, the corresponding growth of these domains
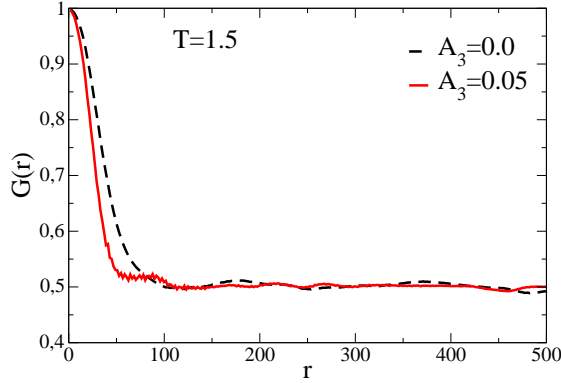
Figure 4.12: Pair correlation $G(r)$ between domains of the same variant. The decay is a measure of the characteristic domain size, which depends on the value of A_3, among others. More interestingly, note that the correlations stabilize around 0.5 indicating that the probability of nucleating a particular variant at any distance (obviously excluding short distances which still belong to the domain of origin) does not depend on the variant.

would create a low temperature configuration with a particular disordered domain distribution that would be geometrically frustrated [81], since the system would not be able to achieve the minimum of energy due to the thermodynamic reasons mentioned above.

However, simulations with strictly zero anisotropy, and thus with no long range effects also show glassy behavior. Since in the absence of long range interactions the total free energy becomes local, no energetic reasons persist to promote the selection of a particular variant in different emerging domains, but it occurs independently from each other. This supports the idea that the origin of the glassy behavior is a kinetic freezing and excludes the hypothesis of geometrical frustration. At that point we have checked that emerging domains at high T are uncorrelated in the sense that the selected variant is independent from the variants of the other domains. This is shown in Fig. 4.12 for two cases showing glassy behavior, in particular corresponding to $A_3 = 0$ and $A_3 = 0.05$ ($\zeta \simeq 0.3$ in both cases). Placing in a given domain 1, both curves show that given a second domain 2 placed at a distance r from domain 1, the probability that domain 2 belongs to the same variant of 1 is 0.5, and hence equal to the probability for domain 2 to belong to the another variant.

4.5 Crossover behavior in anisotropy and disorder

We call T_s the temperature at which ZFC and FC curves split. More precisely, in order to be consistent in the computation of T_s, it has been defined arbitrarily as
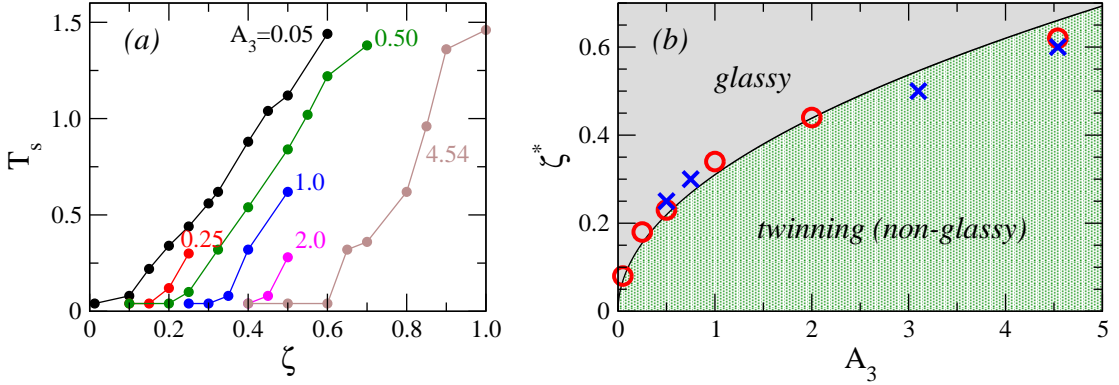
Figure 4.13: (*a*) Splitting temperature (T_s) as a function of disorder for different values of anisotropy. (*b*) Points indicate the crossover behavior in the material parameters. Glassy behavior is obtained for high values of disorder with respect to anisotropy and for low values of anisotropy with respect to disorder. Circles correspond to the vanishing T_s in (*a*) whereas crosses correspond to the arrows in Fig. 4.7. The continuous line is the function $\zeta^* \sim \sqrt{A_3}$.

the temperature at which $e_2(FC) - e_2(ZFC) \simeq 3 \cdot 10^{-4}\%$. Figure 4.13(a) shows the splitting temperatures T_s as a function of disorder and for different values of anisotropy. For martensite twinned structures T_s drops to zero whereas in the glassy regime T_s increases with ζ. Also, for a given value of disorder, the higher the anisotropy the lower the T_s. Moreover, for low values of anisotropy, T_s shows a regular behavior constant slope whereas at high values of A_3, the T_s dependence becomes more irregular, consistent with the jumping behavior mentioned above. The disorder values at which T_s vanishes indicate that the ZFC deviation glassy behavior starts to arise. Figure 4.13(b) displays the crossover behavior in terms of critical values for the model parameters A_3. Circles are taken from the vanishing T_s in Fig. 4.13(a) whereas crosses are taken from the arrows in Fig. 4.7. We have found that such a crossover behaves approximately as $\zeta^* \sim \sqrt{A_3}$ indicated by the curve. It is worth noting that the behavior of the heat capacity $\mathcal{C}$ coincides with such crossover: The existence of the peak is related with the twinning, non-glassy regime whereas the suppression of the peak corresponds to the glassy behavior.

4.6 Variations on the disorder's correlation length

In Sec. 2.4 we have seen that the specific correlation length ξ of the disorder affects the energy barriers present in the model, which can influence the behavior of the system. To analyze the magnitude of this effect, we have performed some simulations with a value of ξ ($\xi = 10$) lower than that used previously, that
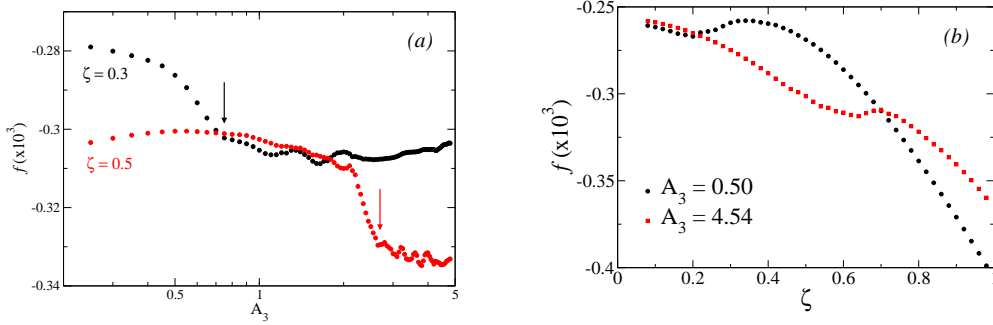
Figure 4.14: (*a*) Free energy f as a function of the parameter A_3 for two values of ζ. (*b*) f as a function of the disorder intensity ζ for two values of A_3. The value for the correlation length of the disorder is $\xi = 10$ in all cases.

increases the energy barriers. In particular, in Fig. 4.14 we have studied the metastability of the configurations at low temperatures by calculating the total free energy f as a function of both anistropy and disorder intensity, analogously to results shown in Fig. 4.7. The general behavior of f as well as the specific values of anisotropy ($A^*_{3_{\lambda=10}}$) and disorder ($\zeta^*_{\lambda=10}$) by which it is observed a drastic change in the free energy, are very similar to those observed in Fig. 4.7.

We have also performed simulations of the ZFC/FC experiments for $\xi = 10$ and we have found that the limiting values of A_3 and ζ that start to exhibit a splitting between ZFC and FC curves (and hence glassy behavior) are very similar to ZFC/FC results for the previous value of ξ ($\xi = 20$) shown in Fig. 4.11 (in particular $\{A_3, \zeta\} = \{4.54, 0.7\}, \{1.0, 0.35\}, \{0.50, 0.3\}$). They are depicted in Fig. 4.15. It is worth noting that they coincide with the previous Fig. 4.11 both in general trends and specific peculiarities.

From the results above we can state that variations on ξ do not contribute to any additional physical insights and give us confidence about the robustness of the results obtained previously.

4.7   Crossover at high temperatures

Motivated by the crossover found at low temperatures when varying A_3 from twinned martensite to ramified droplets, we ask ourselves if similar behavior exists at high temperatures between pretransitional structures, from tweed to mottled structure. Thus, we have performed simulations of the model for many different values of A_3 (from $A_3 = 0$ to $A_3 = 10$ ($\zeta \simeq 0.3$) with intervals $\Delta A_3 = 0.05$) at two different high temperatures in the precursor regime ($T = 1.25, 1.5$). Results are shown in Fig. 4.16, where the free-energy density f averaged over 7 independent
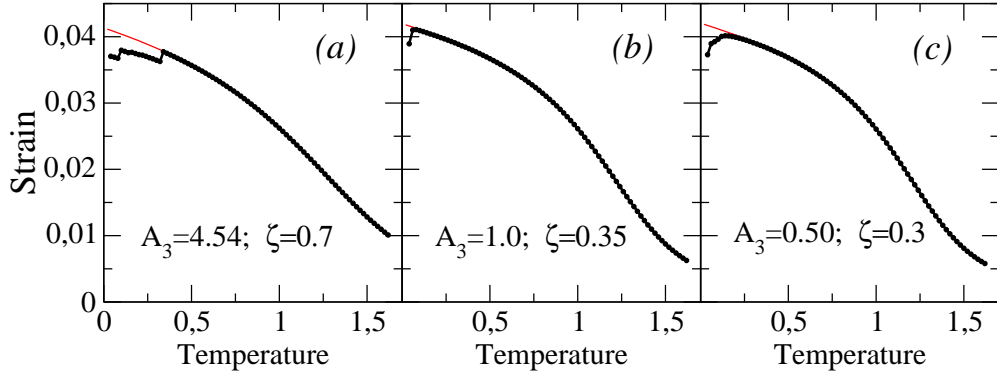
Figure 4.15: (a)-(c) ZFC (black) and FC (red) curves for three different sets of values of $\{A_3, \zeta\}$. The value for the correlation length of the disorder is $\xi = 10$ in all cases
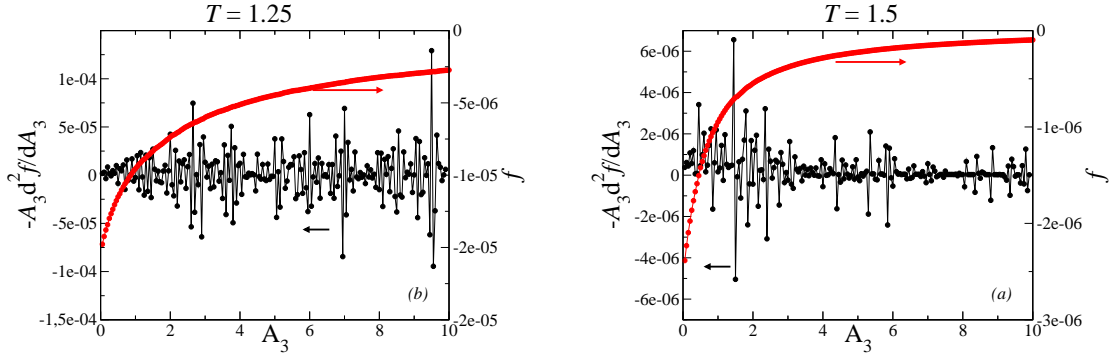
Figure 4.16: Free-energy density f and response function $-A_3 d^2 f/dA_3^2$ as a function of A_3 at two different high temperatures in the precursor regime.

realizations of the disorder is toghether with the corresponding response function[1] $-A_3 d^2 f/dA_3^2$. In all cases the behavior does not exhibit anomalies: no drastic changes are obtained in the behavior of f and no peak is obtained for the response function. Consequently, we can conclude that there is no crossover at high temperatures.

---

[1]We have calculated the response function according to this expression in analogy with the heat capacity, where the temperature plays the role of the parameter A_3

Chapter 5

Thermomechanical behavior

In this section we study the thermomechanical behavior of the system when applying and removing an external stress field. In particular, we analyze the shape memory effect (SME) and superelastic behavior.

Since the stress-free stability is crucial for the final unloaded structures, it may be useful to recall the characteristic temperatures that result from a simple stability analysis of the Landau potential. With T_c being the low stability limit of the high-temperature phase, the equilibrium transition temperature is $T_0 = T_c + \frac{3\beta^2}{16\gamma}$ and the high stability limit of the low-temperature phase $T_i = T_c + \frac{3\beta^2}{4\gamma}$. Taking into account the athermal character of the transition [46], we expect the system to show pseudoplasticity (which can give rise to SME) below T_i, when the martensite phase is stable or metastable, and superelasticity above T_i, when the martensite phase is unstable. However, in the presence of disorder and considering long-range anisotropic interactions the transition path determining the stress-strain behavior may be different. We still expect the system to exhibit superelasticity *well* above T_i, and pseudoplasticity *well* below T_0, but the stress-strain behavior may be particularly different from the clean-limit scheme in the martensite metastability regime, i.e $T_0 < T < T_i$, and close to it. Thus, we focus the study of the stress-strain behavior in this temperature range.

Usually, in stress-strain experiments the variable under control is the strain and therefore stress-strain curves show the strain as the independent variable, in the x-axis. Because we are used to this representation we find appropriate to mantain the representation with the strain in the x-axis, although we perform stress-driven transitions [178].

Before going into the results, it should be pointed out that the value of β has been decreased to $\beta = -10^3$ to broaden the temperature ranges. Consequently, here $T_0 = 1.38$ and $T_i = 1.51$, and the values of disorder and anisotropy are not in direct correspondence to those previously used. We can easily map their values

to the ones used in previous chapters by rescaling the model with β^2. In that sense, high and low values of anisotropy and disorder are always relative to each other. In any case this does not affect the qualitative results and therefore the conclusions.

5.1   Shape-memory effect

5.1.1   Preliminaries

The SME is related to the internal twinned microstructure resulting from the self-accommodation process which allows for a martensitic phase with no macroscopic change of shape (nor volume). Upon loading, the sample may undergo a permanent deformation, since it remains unchanged when the stress field is removed. However, the system can recover the initial shape upon heating up to temperatures above the transition.

Now we focus on the twinned martensite as the starting point for the SME. In practice, the martensite nucleates within an austenite matrix, with the presence of habit planes (phase boundaries) and domain boundaries that make the martensite adopt a twinned structure. At the end of the transformation of a given sample, the whole sample is in the martensitic phase. At that point, the external borders of the martensitic phase are free surfaces, which means that they do not need to be invariant since the phase boundaries do not exist any more[1]. However, once formed, the existing microstructures survive, provided that the sample is neither loaded beyond the elastic regime nor heated above the transformation temperature.

Therefore, to perform simulations of the SME, a realistic microstructure (i.e. twinning giving rise to a zero net strain) is needed. In the following considerations we limit ourselves to the case of $A_3 = 4.54$ and $\zeta = 0.1$. In the original model explained in Chap. 2, the ground state of the free-energy at low temperatures corresponds to a single variant, although typically, broad twins arise as long-lived metastable states, with a low number of domain boundaries. In any case, the typical stabilized configuration does not fulfill the property of zero global strain and hence, finite size effects are required. As considered in Sec. 3.4, to take them into account we recall that we can proceed two different ways: (A) by applying a potential with the Fourier kernel $1/|k_y|$ or (B) by directly simulating an habit plane by imposing a vanishing $T_c(\mathbf{r})$ in the region which is desired to be retained in the austenite phase. Once the desired zero net strain configuration is obtained,

---

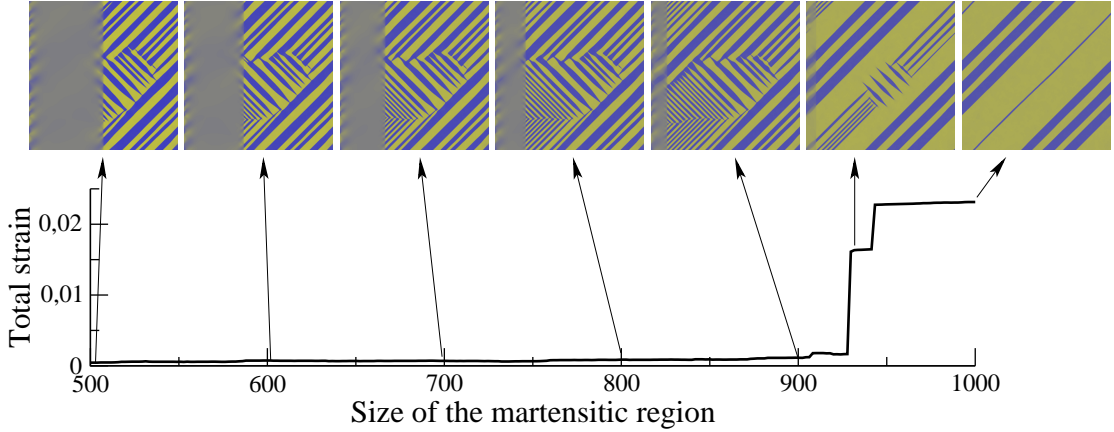[1] This does not occur in twins emerging from domain boundaries.

Figure 5.1: Evolution of the total strain of a single configuration, accompanied by snapshots of the configuration at a given step. The initial low-temperature square configuration consists of half austenite and half martensite. As the low-T_c region is gradually reduced, the martensite region increases. When almost the whole system is transformed to martensite, the twins widen, thus changing the structure significantly.

finite size effects must be removed prior to apply the stress field. Otherwise, the loading curve would be biased since a fictitious, extra driving force would act against the applied field, attempting to keep the twins unaltered in order to mantain the habit plane invariant. Consequently, the required stress for domain switching would be higher than the expected. However, in the simulations it is typically obtained that when removing finite size effects from the system, the thin twins are not able to hold but they become coarse, with the resulting configuration of non-vanishing net strain, which is not appropriate to perform simulations of the SME. We now analyze each case separately. Using the method A we just have to remove the additional potential from the fully relaxed configuration and let the system relax again before loading. Using method B we use two different ways to remove surface effects. In one hand, we may reduce progressively the region where T_c vanishes (that is the austenite region), thus allowing more zones to transform to martensite. It is shown in Fig. 5.1. When the austenite is completely removed, the twins are no longer thin but also become coarse and the system does not fulfill any more the condition of zero net strain. Actually, this occurs before completely removing the austenite region, but when it is small enough in order the twins to connect overcoming the artificial habit planes (and thus eliminating them) due to the periodic boundary conditions (PBC). On the other hand we select a martensitic square region from the initial configuration and let it relax. This is shown in Fig. 5.2. Typically, it is observed that the thin twins disappear again [case (I)]. Few clarifications should be pointed out for completeness: First, occasionally, thin twins may hold after removing the finite size effects, although it

Figure 5.2: Starting from a low-temperature configuration with an austenite region (left), a martensitic square region (denoted by the dashed boxes) is relaxed independently (right). Typically, twins broaden [case (I)], although occasionally, thin twinning may hold [(II)].
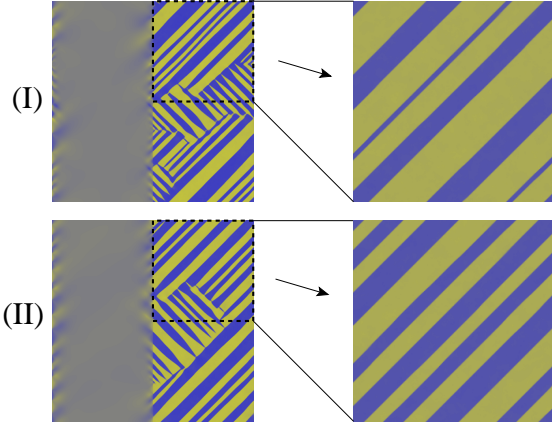
does not occur typically. This is shown in case (II) of Fig. 5.2 for the method B, although it has been also obtained in case A. Second, it is important to remark that in method B, PBC play an active role in determining the microstructure, by restricting the possible twin configurations. Notice that, in case (b), these effects can be even more important, since PBC are imposed in areas where they did not exist previously. However, this does not necessarily lead to broader twins, so that we can conclude that the changes in the microstructure in the sense of twin broadening are indeed due to the absence of finite size effects, and PBC does not affect significantly the twin width.

Therefore, unfortunately we finally have had to shelve the previous methods, came back to the original model and resort to a statistical (thermodynamic) averaging of configurations of non-vanishing net strain to obtain the desired effect. However, even in this case it was difficult to obtain a zero averaged total strain, because the dispersion of the total strains of single configurations is very large. Indeed, the typical total strains move around $1-3\%$ and, even often they may take values up to $\sim 5\%$ which corresponds to a single domain. As an example, after running 200 independent seeds, the averaged total strain was still around 1%. Additionally, since loading, unloading and heating curves had to be computed for each independent seed, another strategy was needed in order to save computation time and data storage. Then, we proceeded the following way: We took a given initial configuration and applied the transformation $e_2(\mathbf{r}) = -e_2(\mathbf{r})$ so that we change the sign of the strain everywhere in the system. Recall that the free-energy density of the system is symmetric with respect to e_2, i.e., it is invariant under this transformation, so we could do that without modifying the local and thermodynamic stability of the configuration. This way we made sure to get a zero net averaged strain in the initial loading curve. The loading, unloading and heating curves were then computed independently. The fact that the stress field was always applied in the same direction entails that both set of curves are not necessarily correlated. To further reduce the correlations, we repeated this

procedure for 50 independent seeds and averaged over the resulting 100 curves. As an inconvenient, the details of the particular curves were smoothed, but we checked that the required stress for domain switching σ_y (for yielding stress) was almost independent of the disorder seed. Therefore, it can be identified with the averaged value.

5.1.2   Results

To illustrate the SME, in Fig. 5.3 we show the $(\sigma - e_2 - T)$ curves obtained for different values of A_3 and ζ. Case (I) corresponds to $\{A_3, \zeta\} = \{0.05, 0.13\}$, case (II) to $\{4.54, 0.13\}$, case (III) to $\{0.05, 0.04\}$ and case (IV) to $\{4.54, 0.04\}$. Arrows in the external margins point towards increasing values of A_3 and ζ for clarity. The system is first loaded at $T = 0.7$ $(< T_c)$ until the single domain state is reached. Then, it is unloaded and finally heated up to a temperature above the transition. The stress increments (and decrements) are $\Delta\sigma \simeq 7 \cdot 10^{-4}$ and the temperature step is $\Delta T = 0.02$. Snapshots show representative configurations at a given value of (σ, e_2, T). They have been labeled to make clear the order of the sequence. Focusing on the $(\sigma - e_2)$ curve at $T = 0.7$ $(< T_c)$, in the four cases pseudoplastic behavior is observed. However, each curve exhibits specific peculiarities. When $\mathcal{A}$ is increased and/or ζ decreased, the critical stress needed for domain switching increases. The high value of $\mathcal{A}$ [(II) and (IV)] shows initial twinned states whereas low $\mathcal{A}$ values do not allow the system to form twins, but ramified droplets of typical domain size that decrease with ζ (This has been analyzed in Chap. 3). It has been checked that by continuing to increase the disorder, even the highest value of $\mathcal{A}$ is not enough to induce twin formation. It is important to remark that the configuration of low value of $\mathcal{A}$ and high ζ [(I)] exhibits glassy behavior in ZFC/FC simulation experiments. Of course, for all cases upon unloading the strain is not recovered but the single domain state is maintained, since in this temperature regime any ferroelastic variant is stable. However, upon heating the system undergoes the reverse transformation, ending in a zero net strain and thus recovering the initial macroscopic shape (SME). Some differences are observed between the various heating curves. In fact, they differ in a way analogous to that in the corresponding loading curves mentioned above, from the point of view of sharpness of the profiles.
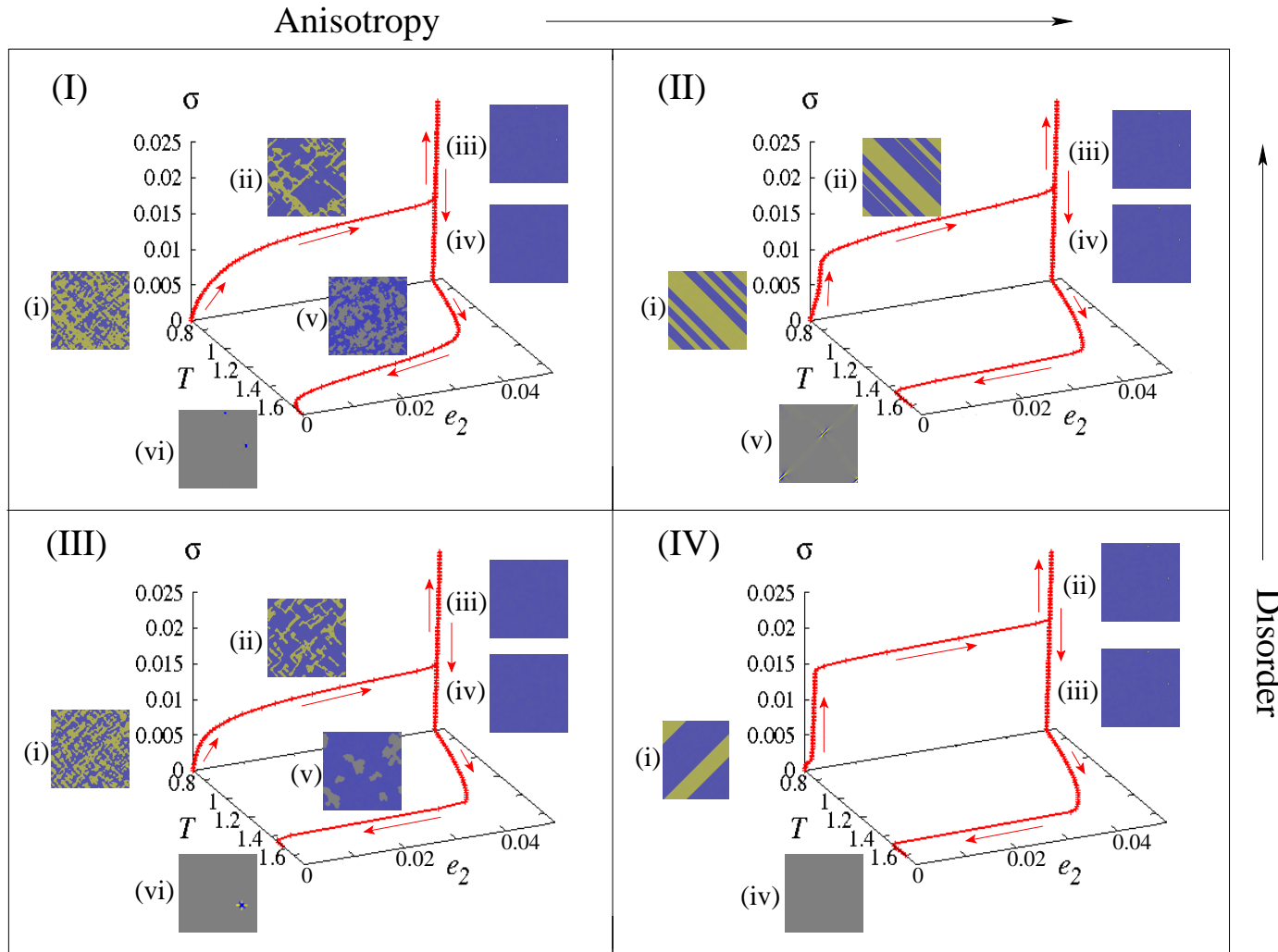
Figure 5.3: Stress-strain-temperature curves for different values of A_3 and ζ, giving rise to the SME. The particular values for cases (I)-(IV) are respectively: $\{A_3, \zeta\} = \{0.05, 0.13\}$, $\{4.54, 0.13\}$, $\{0.05, 0.04\}$ and $\{4.54, 0.04\}$. The SME can be appreciated in the fact that the initial and final net strains are equal (i.e. both vanish), although the corresponding internal microstructures are essentially different.

5.2 Superelasticity

After the analysis of the SME, and in particular the stress-strain $(\sigma - e_2)$ curves for $T < T_c$, we now proceed to study the mechanical behavior at temperatures above T_c. Figure 5.4 shows an increasing-T series [(a) to (e)] of stress-strain curves. For each value of T, the same set of values of A_3 and ζ of Fig. 5.3 are used in the corresponding cases (I)-(IV). For a reference framework, the analytical behavior corresponding to the homogeneous Landau free energy is also depicted. Dashed lines correspond to the thermodynamic equilibrium behavior whereas dotted lines denote the maximal metastability regimes. Concerning the temperature evolution of the $\sigma - e_2$ curves the expected behavior is observed for each case. Pseudoplasticity is obtained at low T and then it evolves toward the superelastic regime when T is increased.

Regardless of the differences due to temperature regimes, several common features can be extracted:
(i) Case (IV) shows a sharp, clean stress-induced transition whereas in (I) the transition takes place smoothly and gradually. (II) and (III) exhibit intermediate behavior.
(ii) In (I) and (IV) pseudoplastic behavior is observed up to temperatures higher than in (II) and (III), although the underlying behaviors are very different.
(iii) (IV) shows the highest transition stress whereas the lowest is observed in (I). (II) and (III) show similar intermediate values.
(iv) In the superelastic regime regime, the backward transition occurs at lower stresses in (IV) than in the other cases.
(v) Combining features (ii) and (iii), it results in a high hysteresis area in (IV) and lower ones for the other cases.

From all this, we can remark that the effect of decreasing anisotropy (from right to left) is similar to an increase in the disorder (from down to up), that is consistent with the results obtained in the previous chapter. Actually, all these trends are intimately related, as will be discussed below.

Discussion

Often, long-range and local effects compete and have opposite consequences. The former contributes to the cohesion of the system by correlating different remotes sites of the lattice. Instead, the latter often tries to screen the former and to split the system into uncorrelated pieces. In that sense, high anisotropy values (that increase the strength of the long-range interactions) and/or low disorder favor the stability of each of the thermodynamic phases. It results in a sudden, sharp transition, as it is revealed by the flat plateau in the $(\sigma - e_2)$ curves in Fig. 5.4.
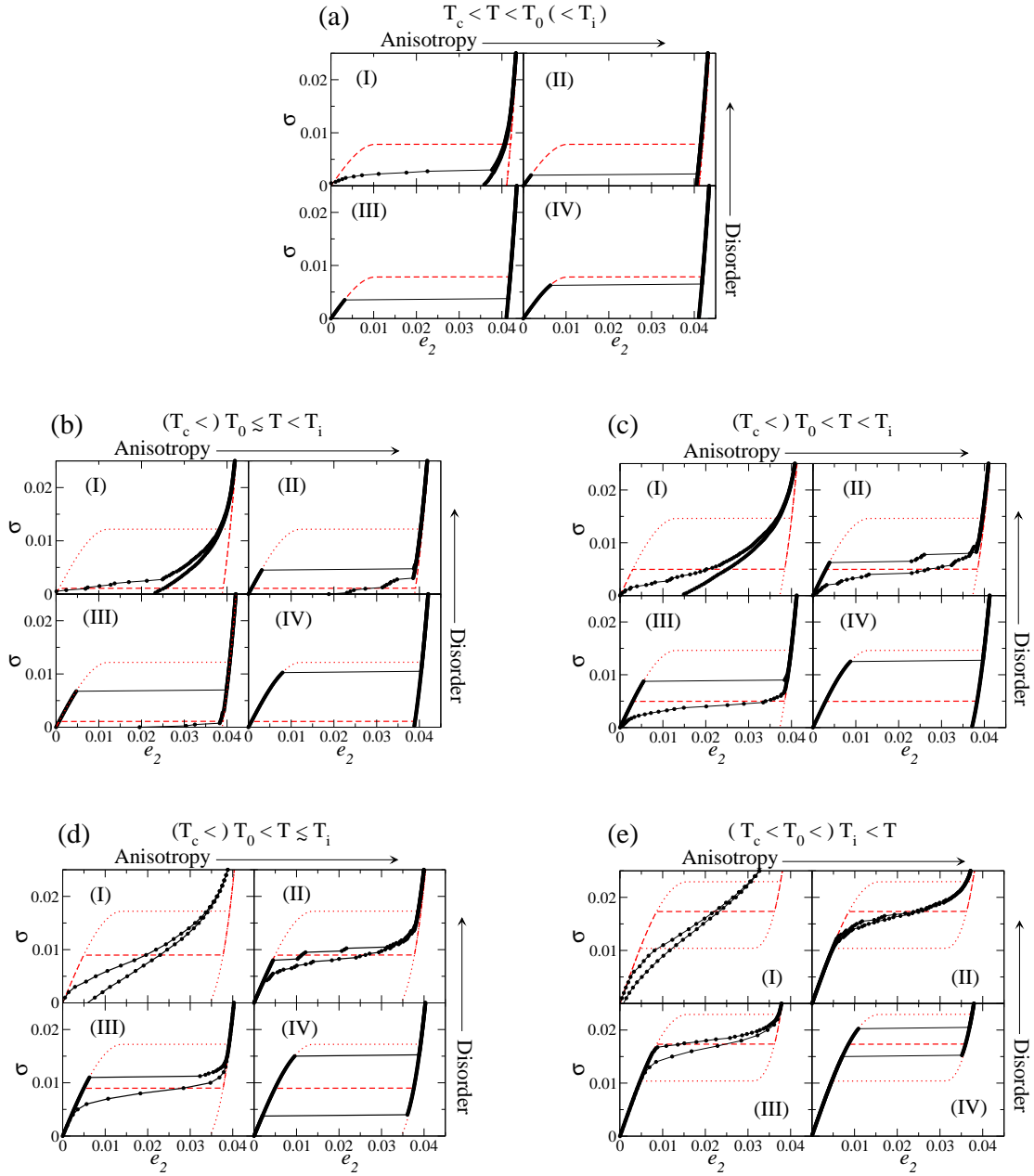
Figure 5.4: Stress-strain curves for different values of A_3 and ζ in different temperature regimes. The same set of values $\{A_3, \zeta\}$ as those in Fig. 5.3 are used in the corresponding cases (I)-(IV).

Also, in the paraelastic (i.e. austenite) phase, the larger the anisotropy and/or the lower the disorder, the larger the critical stress field needed to overcome such interactions and thus to carry out the ferroelastic transition. The opposite holds for the reverse transition: as already mentioned, the larger the anisotropy values and/or the lower the disorder, the more stable is the ferroelastic phase and hence, the lower the level of stress at which the system transforms back to the austenite. From this, it follows that there are two main consequences: first, large values of anisotropy and/or low values of disorder result in a larger hysteresis area. Second, the pseudoplastic behavior is observed at higher temperatures.

On the other hand, low values of anisotropy and/or high values of disorder result in a decoupling of the different parts of the system, that may behave uncorrelated from each other. Consequently, the stability becomes short-ranged and the notion of a phase stability for the whole system does not have a meaning any more. We then observe a set of different, independent critical stresses acting in well defined regions, i.e. a spatial distribution of critical stresses. It leads to a gradual, smooth transition of the system that starts with the lowest critical stress, corresponding to the transformation of the most unstable region. By increasing the stress field, the system keeps on transforming progressively in moderately stable regions and finishes with the highest critical stress that transforms the most stable zone. Hence, it is not unusual that, at a given temperature, some regions whose stress-free paraelastic stability is weak–or even metastable–, may remain anchored in the ferroelastic phase when the stress field is completely removed, either in a weakly stable or metastable state. This is the reason why the total strain is not fully but only partially recovered.

Stress-strain regimes in the parameter space

Figure 5.5 qualitatively displays the different stress-strain regimes in the parameter space (T, A_3, ζ), which has been derived from the results in the figures above. Nontrivial behavior is obtained. The dark gray and white regions correspond to the superelastic and pseudoplastic regimes, respectively. In the region in-between (light gray) partial strain recovery is obtained. As can be seen, for large $\mathcal{A}$ and low ζ [(IV) in $\sigma - e_2$ curves], this light gray region is very small[2]. Indeed, the system exhibits either pure pseudoplastic or pure superelastic behavior. If we now increase ζ [(II)] or decrease $\mathcal{A}$ [(III)] the system starts to exhibit (partial)

---

[2]Let us point out that the origin of the axes does not necessarily correspond to vanishing anisotropy and disorder. Actually, in the limit of no disorder, no partial pseudoelasticity can be observed, i.e. no clear gray area exists. Hence, in the zero-disorder plane the dashed lines meet, thus removing this region. It has not been done this way since the dependence of the regimes as function of $\mathcal{A}$ for low values of disorder is more clearly depicted as in Fig. 5.5.

superelasticity in a region where pseudoplasticity was obtained previously [i.e. in
(IV)]. However, if we now proceed to decrease $\mathcal{A}$ and increase ζ simultaneously,
the partial superelastic region spreads out into both the previous pseudoplastic
and pure superelastic regions.

The largest superelastic regime is achieved when disorder and anisotropy have
comparable strength, i.e. neither dominates the other but the behavior is the
result of a situation of a balance between both factors. In the simulation results
it is observed when A_3 and ζ values are either both low or both high, as can be
seen in Fig. 5.5 and, more specifically, in (II) and (III) of Fig. 5.4.

In short, disorder may shift the superelastic regime either to higher or lower
temperatures depending on the strength of the elastic anisotropy factor, and con-
versely. This results in a wide range of mechanical responses, which, interestingly,
is also observed experimentally.
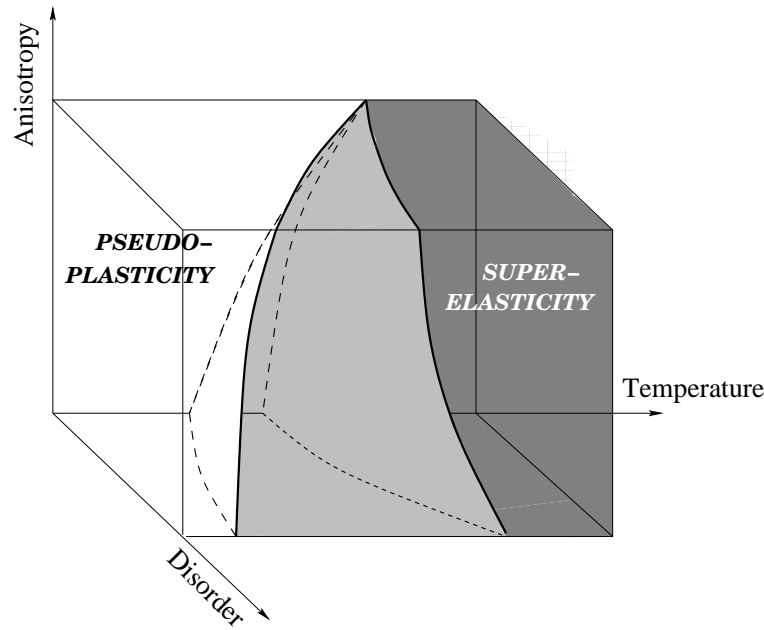
Figure 5.5: Different mechanical regimes of the system expressed schematically in the
parameter space (T, A_3, ζ)

Comparison with experiments

It is worth reminding that the specific composition has been observed to crucially
determine the stability regimes of a given SMA, as well as other characteristics
of technological importance. In this sense, the tuning of the alloys by means of
either varying the composition or doping has been performed over decades. As an

example, in $Ti_{50-x}Ni_{50+x}$ the temperature separating superelastic and pseudoplastic regimes decreases drastically when the composition is varied from $x = 0.6$ [19] to $x = 1.5$ [20]. Similarly, many other alloys like Au-Cd [21], Ti-Ni-Cu [22], Ni-Co-Mn-In [24], Ni-Mn-Ga [23], etc. have been observed to exhibit changes in the transition stress, hysteresis area, percentage of strain recovery, temperature regimes and particular shape of the stress-strain curves when varying the relative concentration of the constitutive elements. Interestingly, recent research [179–181] has been focused on exploring different compositions of some alloys [in particular, of Ti-Ni-(Cu-Pd-Pt-Au)] to find the specific composition that shows the smallest hysteresis width, which is of technological interest.

The rich landscape offered by our model may account for all this phenomenology, and therefore is in general agreement with the behavior observed in these alloys. More specificvally, for instance, our findings are qualitatively similar to experiments in Ni-Co-Mn-In [24] showing that, at a given temperature, they change from pseudoplastic to partial superelastic and finally to pure superelastic behavior when the In content is increased at the expense of Mn. Also, by looking at the experimental results in Ti-Ni-Cu [22] one can notice that our simulations agree with the decrease in the hysteresis area when the content of Cu is increased. To further illustrate this comparison, in Fig. 5.6 we show experimental results concerning the strain-induced stress-strain behavior in off-stoichiometric Ni-Mn-Ga for two different compositions [23]. It can be observed that slight variations in the composition entail changes in the onset temperature of the superelastic regime. In particular as the composition is more far from the stoichiometry, this onset is observed at higher temperatures, which is consistent with our results.

5.3 Transition and yielding stresses

Figure 5.7 displays the transition stresses, σ_t, as a function of temperature (linked symbols)[3]. At high temperatures, where superelastic behavior is observed, σ_t corresponds to the required level of stress for the ferroelastic transition to occur. The relation between σ_t and T is described, in general, by the Clausius-Clapeyron equation [182]: $d\sigma/dT = \Delta S(T)/\Delta\epsilon(T)$. Here S is the entropy and ϵ the strain. In particular, in all cases we obtain a linear dependence, which is indeed experimentally observed in martensites [13, 19–21, 23, 102, 183]. Straight lines of constant slope of 0.5 are displayed for comparison between different cases. Nevertheless, it is observed that increasing the amount of disorder or lowering anisotropy results

---

[3]For clarity, not all the $\sigma - e_2$ curves from which the critical stresses have been extracted are shown here.
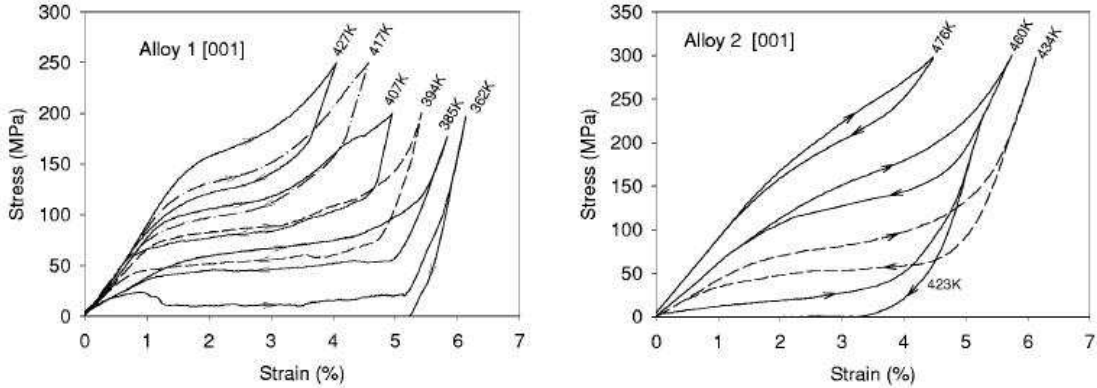
Figure 5.6: Strain-induced stress-strain behavior at different temperatures for two different compositions of Ni-Mn-Ga alloy: Alloy 1 corresponds to $Ni_{51.1}Mn_{26.6}Ga_{20.3}$ and alloy 2 to $Ni_{51.2}Mn_{31.1}Ga_{17.7}$. The latter is more far than the former from the stoichiometric composition $Ni_{50}Mn_{25}Ga_{25}$, and shows a shift of onset of the superelastic regime to higher temperatures. Our model is qualitatively consistent with such a behavior. Extracted from Ref. [23].

in lower transition stresses, as mentioned above. When the transition temperature is approached, the slope of the curve decreases. Below the transition, the yielding stress, σ_y, does not induce a transition but it is responsible for the domain wall motion and growth of the selected martensitic variant. It is observed that σ_y increases with decreasing temperature, also in qualitative agreement with experiments [13, 19–21, 102]. These different regimes occur due to the Landau contribution in the free energy. The presence of long-range interactions and disorder do not modify this general picture but introduce specific ways for the system to behave. For comparison, the σ_t corresponding to the Landau global minimum is depicted with a dashed line whereas the σ_t corresponding to the maximum metastability regime is represented by a dotted line. As can be seen, the slope of the curves in both Clausius-Clapeyron and pseudoplastic regimes approximates well to the maximal metastability regime than to the equilibrium one.

Nevertheless, the transition stress in Ti-Ni-Cu is observed to increase with Cu content whereas our model shows a decrease of the transition stress when the amount of disorder is increased. Doping has been shown to increase the transition stress also in Ti-Ni when adding off-stoichiometric Ni content [19, 20]. Our results also come into conflict with these experiments, since they show that the slope of the curve changes when changing composition.

Instead, our simulations agree with other strain-induced $\sigma - e_2$ simulations [146] where the transition stress was observed to decrease with the size of a single defect, in accordance with the known fact that defects may act as pinning sites
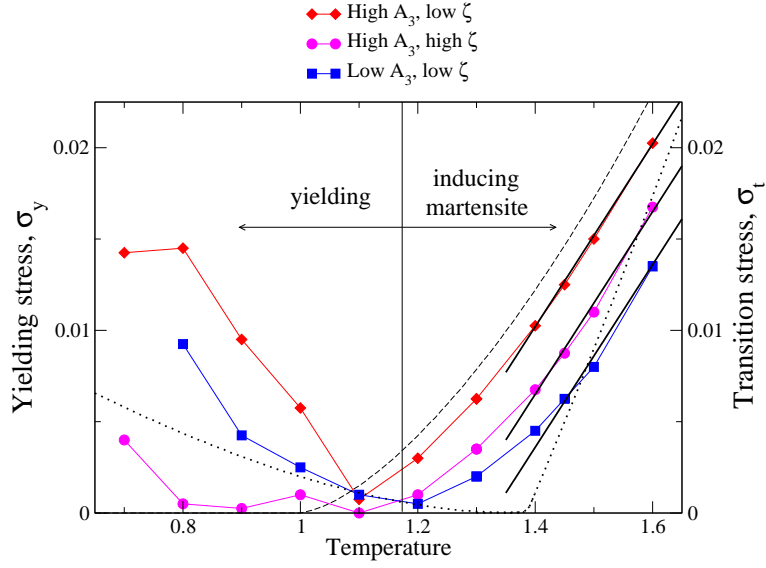
Figure 5.7: Symbols: transition (right) and yielding (left) stresses as a function of temperature for different values of anisotropy and disorder. Straight lines with same slope are guide to the eye. Dashed and dotted lines correspond to equilibrium and maximum metastability regimes of the Landau contribution to the free energy.

for nucleation and growth of martensite.

5.4 Elastocaloric effect

The elastocaloric effect is the mechanical analogue of the magnetocaloric effect [184]. It is related to the isothermal change of entropy or to the adiabatic change of temperature that takes place in the system when an external stress is applied or removed. As in the magnetocaloric case, large effects are expected in the vicinity of first-order phase transitions where large entropy changes occur [183]. Here, the study of the elastocaloric effect is interesting since it summarizes the information related to the temperature dependence of stress-strain behavior. It has been quantified by means of an isothermal stress-induced entropy change which has been computed from the $\sigma - e_2$ curves as follows: According to thermodynamics [16]:

$$dS = \left(\frac{\partial S}{\partial \sigma}\right)_T d\sigma + \left(\frac{\partial S}{\partial T}\right)_\sigma dT \tag{5.1}$$

During an isothermal process the second term on the right-hand side vanishes, and the total entropy change can be calculated as the following integral:

$$\Delta S(0 \to \sigma) = \int_0^\sigma \left(\partial S/\partial \sigma\right) d\sigma = \int_0^\sigma \left(\partial e_2/\partial T\right) d\sigma$$
$$\simeq \frac{1}{\Delta T}\left\{\int_0^\sigma e_2(T + \Delta T, \sigma)d\sigma - \int_0^\sigma e_2(T, \sigma)d\sigma\right\}. \tag{5.2}$$
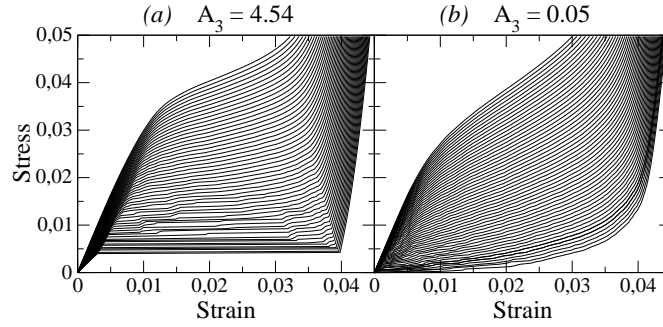
Figure 5.8: Set of stress-strain curves corresponding to a single realization of disorder for two different values of A_3. Ten independent seeds have been used to compute the elastocaloric effect for each value of A_3.

It should be noted that for an ideal first-order transition occurring in equilibrium, this entropy change should coincide with the difference of entropy between the two phases. Here, due to the existence of disorder the transition extends over a broad range. Therefore the obtained behavior will differ from this simple behavior.

Simulation results are shown in Fig. 5.9. Although the $\sigma - e_2$ curves of the two cases are significantly different (as can be appreciated in Fig. 5.8), the resulting stress-induced entropy change is similar. The peaks are placed in different positions and the tails show different behavior but the area under the curve remains essentially constant. Moreover, the Landau contribution to the free energy is represented by a dashed line. As can be seen, the presence of disorder (both continuous lines) results in a rounding and decrease of the peak with respect to the Landau contribution.

Although the magnetocaloric effect is quite different from the elastic analogue presented here, very similar Landau theory based models have been used to perform simulations in ferromagnetic systems. Such models are known to be sensitive to disorder [18] and dipolar interactions in a similar way to that presented here. For instance, in Ref. [185], it was found that the presence of disorder resulted in a decrease of the magnetocaloric peak, compared to the homogeneous case, which agrees with our results. Encouraged by this, we further emphasize the comparison with magnetocaloric experiments in [186] $Gd_5(Si_xGe_{1-x})_4$, where an increase of x results in a shift of the critical stress and the Clausius-Clapeyron slope is approximately independent of doping, which would be consistent with our results.
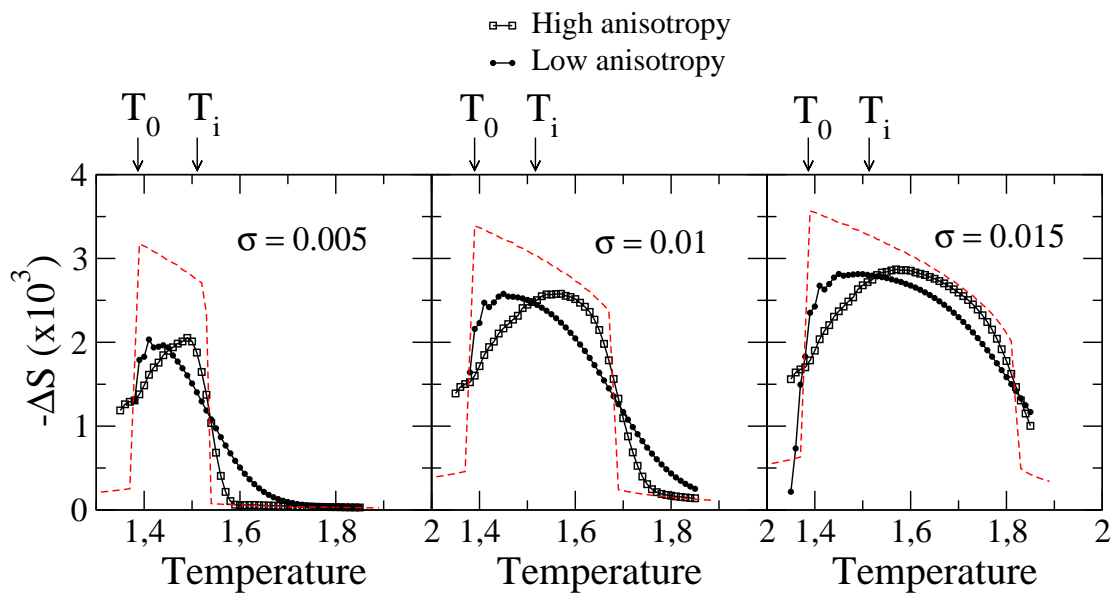
Figure 5.9: Elastocaloric effect: Entropy change as a function of temperature for different values of the applied stress and for different anisotropy values. Dashed line corresponds to the Landau contribution to the free energy.

Chapter 6

The magnetoelastic model

6.1 Introduction

Multiferroics were briefly introduced in Chapter 1 as materials that exhibit a cross-variable, ferroic response. For instance, sometimes polarization can be controlled by a stress field, and an electric field can affect the structure. Undoubtedly, they attract a lot of interest since expand the horizons in technological applications. Maybe, the magnetoelastic coupling arises as one of the most important topics in this field, leadind to interesting phenomena. The Ferromagnetic Shape Memory effect [76] (FSME) allows for shape recovery due to inducing the structural transformation by means of a magnetic field instead of stress. Recently, the Metamagnetic SME has also been reported [24] where the original shape is recovered from magnetic-field-induced backward transformation. The mangetocaloric effect [184], consisting in isothermal entropy changes or, more interestingly, in adiabatic temperature changes due to the presence of an external magnetic field, has been observed to considerably increase its magnitude in the vicinity of a structural phase transition, which is of technological importance for cooling applications. The inverse magnetocaloric effect has been also recently discovered [187]. Magnetostriction effects [51], which consists in showing magnetic-field induced volume changes are another consequence of the coupling between elastic and magnetic degrees of freedom. Other aspects have been also adressed [188].

Micromagnetism has been widely used to model the magnetization in magnetoelastic systems. Elasticity has been taken into account by means of, for instance, Khachaturyan's microelasticity [133, 189] and Landau theory [190, 191]. In this chapter we develop a magnetoelastic model based on an extension of the previous pure elastic Landau-based model, that includes magnetic degrees of freedom as well as a coupling between magnetic and strain variables. Before going into model details, it is important to point out that, as will be seen, from the elastic point

of view, the model allows the crystallographic lattice to undergo a ferroelastic Martensitic Transition (MT), that can be induced either upon cooling or by applying a stress or magnetic external field. Instead, the temperature does not play any role for the magnetic degrees of freedom, but the magnetization of the lattice is assumed to remain at all times in the ferromagnetic phase, well below the Curie temperature[1].

Modeling of the magnetic energy is presented in Sec. 6.2.1. In Sec. 6.2.2 the magnetoelastic coupling is described and the elastic part briefly reviewed. In Sec. 6.3 the dynamics concerning both the magnetic and elastic degrees of freedom is described. Finally, Sec. 6.4 presents preliminary results of the model.

6.2   Energy

The performance of the magnetic degrees of freedom is carried out by means of the theory of micromagnetism [192], according to which, the magnetization of the system is described by a three dimensional continuous vectorial (spin) field, that will be denoted by $\mathbf{M(r)}$. We can write $\mathbf{m} = \mathbf{M}/M_s$, where M_s is the saturation magnetization and $\mathbf{m} = (m_x, m_y, m_z)$ is the unit magnetization vector, that must fulfill $|\mathbf{m}| = 1$. This description is known to apply to both atomistic and mesoscopic scales. On the other hand, The elastic part is described by the extended Ginzburg-Landau model explained in Chapter 2, with the deviatoric strain e_2 as the order parameter (OP).

Note that, although the elastic part is purely 2D, the 2D magnetic model allows the spins to have the third component m_z, that is out-of-plane. This is due to the intrinsic 3D nature of the theory of micromagnetism (involving *curl* operators, etc.). However, the third component may be forced to remain in the 2D plane in several ways, such as introducing an extra anisotropic term penalizing this component. In fact, as will be seen, the magnetoelastic coupling itself does strongly force m_z to vanish at all times. Nevertheless, a direct consequence of the 3D real world is that no internal magnetic in-plane microstructure is needed for the magnetic lines to close, since they can close in the third dimension. Instead, a pure 2D magnetic system must indeed exhibit a 2D magnetic domains structure in order the lines to close. This can be easily seen in Fig. 6.1 where both cases are displayed.

---

[1]If wanted, the temperature should be introduced as thermal fluctuations by means of the fluctuation-dissipation theorem as it will be briefly mentioned later.
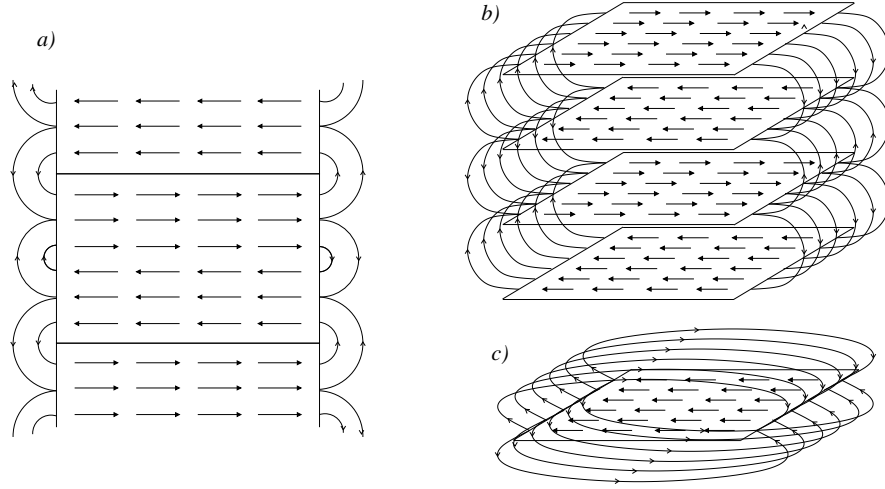
Figure 6.1: (*a*) A pure 2D magnetic system requires internal microstructure for the magnetic lines to close. (*b*)-(*c*) In a 3D world, no in-plane magnetic domains are needed since the mangetic lines can close in the third dimension, either by means of a 3D mangetic structure (*b*) or freely (*c*).

6.2.1 Magnetic energy

In a solid magnetic body the magnetic energy can be decomposed as a sum of the following contributions:

$$F_{\mathrm{m}} = F_{\mathrm{an}} + F_{\mathrm{exch}} + F_{\mathrm{ms}} + F_{\mathrm{ext}}, \tag{6.1}$$

Here, F_{an} is the anisotropic energy, that accounts for the interaction of the magnetization with the underlying anisotropic, crystallographic lattice. This leads the spins to have preferred, soft specific directions to point at. In a cubic system this term takes the following form:

$$F_{\mathrm{an}} = \int [K_1(m_x{}^2 m_y{}^2 + m_x{}^2 m_z{}^2 + m_y{}^2 m_z{}^2) + K_2 m_x{}^2 m_y{}^2 m_z{}^2]dV \tag{6.2}$$

where K_1 and K_2 are the magnetocrystalline anisotropy constants. This potential has eight minima at $\mathbf{m} = (\pm 1/\sqrt{3}, \pm 1/\sqrt{3}, \pm 1/\sqrt{3})$. A projection of it, is shown in Fig. 6.2 as a function of m_x and m_y. Hence, this term will favor the diagonal directions.

Note that, indeed, this term already performs a *magnetostructural* coupling, since it describes how the magnetization is affected by the crystallographic symmetry elements. However, up to now, no deformations of the lattice are taken into account. In that sense, by the moment K_1 and K_2 are kept constant so that we cannot talk about *magnetoelastic* coupling. Precisely, as will be seen , the
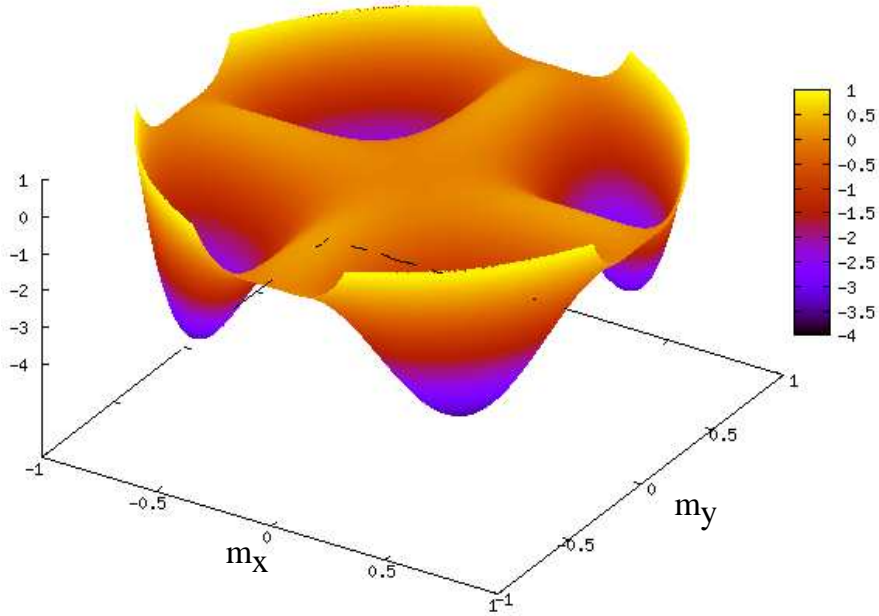
Figure 6.2: Projection of the mangetic anisotropic energy in the $\{m_x, m_y\}$ plane: Four wells at $\left(\pm 1/\sqrt{2}, \pm 1/\sqrt{2}\right)$ show that diagonal directions are favored

magnetoelastic coupling will be introduced by suposing K_1 and K_2 as function of the strain and calculating derivatives.

The term F_{exch} in eq. (6.1) corresponds to the energy of the exchange interaction. It takes into account interactions between nearest neighbors in the same thread of thought of the Heisenberg model[2]. In a continuous model, it can be expressed through derivatives as:

$$F_{\text{exch}} = A \int [(\partial_x m_x)^2 + (\partial_y m_x)^2 + (\partial_z m_x)^2 + (\partial_x m_y)^2 + (\partial_y m_y)^2 + (\partial_z m_y)^2$$
$$+ (\partial_x m_z)^2 + (\partial_y m_z)^2 + (\partial_z m_z)^2] dV$$

$$(6.3)$$

where we have used the compact notation $\partial_i m_j = \partial m_j / \partial i$, with $i = x, y, z$. Here A is the exchange stiffness constant, that is negative (positive) for a ferromagnetic (antiferromagnetic) system. In our ferromagnetic case, this interaction will try to keep the spins parallel to each other.

In addition to the previous local interaction, each spin is affected by any other spin in the system due to the long-range, dipolar interaction. Thus, the magnetization in the whole body, given by the specific, total spin configuration, creates the so-called demagnetizing or magnetostatic field, which in turn acts over each individual spin. It is important to note that this field is responsible for the fulfillment of the Maxwell equation $\nabla \cdot \mathbf{B} = 0$, that essentially forces the magnetic

---

[2] This term is often called the *Heisenberg* energy.

lines to form closed loops, i.e. to prevent the existence of magnetic monopoles. This may strongly depend on the specific shape of the specimen and it is at the origin of magnetic domains, vortices, [47] etc.

The corresponding magnetostatic energy can be expressed in several ways as:

$$F_{\text{ms}} = -\frac{1}{2}\mu_0 M_s \int_\Omega \mathbf{H}_d \cdot \mathbf{m} dV = -\frac{1}{2}\mu_0 M_s \int_\Omega \left(\nabla \cdot \mathbf{M}(\mathbf{r})\right) \phi(\mathbf{r}) dV = \frac{1}{2}\mu_0 \int_\Re H_d^2 dV, \tag{6.4}$$

where μ_0 is the permeability of the free space, $\mathbf{H}_d$ is the above mentioned demagnetizing field (which is also a vectorial field) and Ω and $\Re$ refer to the sample and to all the space respectively. The knowledge of H_d requires an integral involving the magnetization over the whole system that, when introduced in eq. (6.4), is at the origin of the long-range character of the magnetostatic term. The resulting double integral entails difficulties and large computation time ($\sim N^2$), leading to many efforts devoted to optimize its calculation [193, 194]. Here the calculation is carried out in Fourier space, that improves considerably the required time ($\sim N \log N$), similarly to the long-range elastic interactions explained in Chap. 2. In order not to interrupt the line of argument regarding this model, a detailed explanation of the computation concerning this term can be found in App. B.2. Here we only point out that the contribution corresponding to the wave vector $\mathbf{k} = 0$ is a singularity in the Fourier expression and hence is not taken into account (and set to zero). Therefore, the single domain configuration is not specifically penalized by this term. This can be easily seen from the fact that the computation in Fourier space requires periodic boundary conditions, which lead to an infinite system size and, consequently, to the absence of finite size and shape effects which are at the origin of magnetic domains. We recall that a similar problem arose in the elastic case. Also, here some methos will be explored to effectively account for finite size and shape.

Finally F_{ext} is the interaction energy between the magnetization and the external field:

$$F_{\text{ext}} = -\mu_0 M_s \int \mathbf{H}_{\text{ex}} \cdot \mathbf{m} dV \tag{6.5}$$

6.2.2   Magnetoelastic coupling and elastic energy

As mentioned in Sec. 6.2.1, the anisotropic magnetic term denoted by F_{an} [eq. (6.2)] accounts for the specific spatial distribution of the spins, that obviously is in direct correspondence with the underlying crystallographic lattice, with which shares the same symmetries. In particular, the lattice has square symmetry. However, since the mangetocrystalline anisotropy parameters K_1 and K_2 are constant,
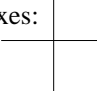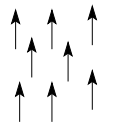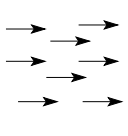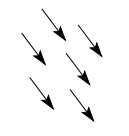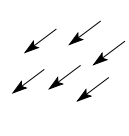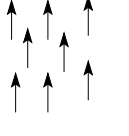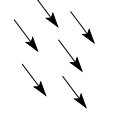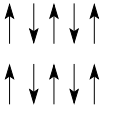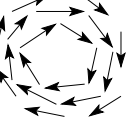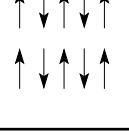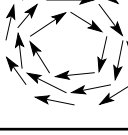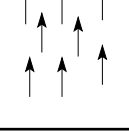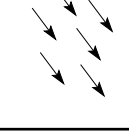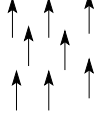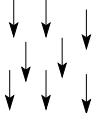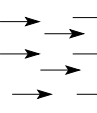
Energy	Favorable configurations		Unfavorable configurations	
Anisotropy Easy axes:				
Exchange				
Magnetostatic				
External field				

Figure 6.3: Favorable and unfavorable spin configurations with respect to each energetic contribution.

F_{an} always refers to the square symmetry and does not take into account new simmetries arising from any deformation of the lattice. Precisely, we are interested in studying the effects of elastic deformations in the magnetic lattice, and the other way round, i.e. how mangnetism may affect the crystallographic lattice. Therefore, a new contribution in the free energy, termed magnetoelastic energy, is required to accounts for these effects.

Then, from now on we assume that the lattice where the spins are located undergoes a square-to-rectangular MT. It entails a symmetry loss of the elastic lattice and, correspondingly, of the spin lattice, that results in a change in the soft magnetic directions, given by the anisotropic magnetic term. Following Kittel [195], we assume that this change is small (as it occurs in real materials) and therefore we may calculate the new magnetic anisotropic term as a Taylor expansion around the equilibrium value given by the undistorted lattice, thus obtaining $F'_{an} = F_{an} + F_{me}$. Here F_{me} refers to the free energy of the magnetoelastic coupling emerging from the derivatives of F_{an} in the Taylor expansion. Taking also into account symmetry-allowed requirements, it gives rise to the following expression for F_{me}:

$$F_{me} = \int \left(\frac{B_1}{\sqrt{2}} \left(m_x^2 + m_y^2 \right) e_1 + \frac{B_1}{\sqrt{2}} \left(m_x^2 - m_y^2 \right) e_2 + B_2 m_x m_y e_3 \right) d\mathbf{r} \qquad (6.6)$$

We recall that the elastic free-energy density can be written as follows:

$$f_{\mathrm{el}} = \frac{A_1}{2}e_1^2 + \frac{A_3}{2}e_3^2 + \frac{A_2}{2}e_2^2 - \frac{\beta}{4}e_2^4 + \frac{\gamma}{6}e_2^6 + \frac{\kappa}{2}\left(\nabla e_2\right) \qquad (6.7)$$

Note that F_{el} and F_{me} terms depend on the three symmetry-allowed strains e_1, e_2 and e_3. As seen in Chap. 2 they are not independent but they are related by the Saint-Vénant compatibility equation, so that we can express the free energy in terms of only two of them, say, for instance, e_1 and the OP e_2. We then minimize the total free energy with respect to e_1 and obtain an expression for the free energy only in terms of e_2. Note that now, in addition to the term F_{el} we have to include the magnetoelastic contribution F_{me} in the energy minimization, since it also contains the variables e_1, e_2 and e_3. The mathematical details can be found in App. B. The final expression for F_{me} becomes:

$$\begin{aligned} F_{\mathrm{me}} = {} & \tfrac{B_1}{\sqrt{2}} \int \left[m_x^2(\mathbf{r}) - \mathbf{m_y^2}(\mathbf{r})\right] e_2(\mathbf{r})d\mathbf{r} \\ & + \tfrac{1}{(2\pi)^2}\tfrac{B_1}{\sqrt{2}} \int A_{c_1}(\mathbf{k})e_2(\mathbf{k})d\mathbf{k}\mathsf{F}\left(m_x^2(\mathbf{r}) - m_y^2(\mathbf{r})\right) \\ & - \tfrac{1}{(2\pi)^2}\tfrac{B_2}{2\sqrt{2}} \int A_{c_3}(\mathbf{k})e_2(\mathbf{k})d\mathbf{k}\mathsf{F}\left(m_x(\mathbf{r})m_y(\mathbf{r})\right) \end{aligned} \qquad (6.8)$$

where $A_{c_1}(\mathbf{k})$ and $A_{c_3}(\mathbf{k})$ are functions that only depend on $\mathbf{k}$ and are defined in eq. (B.52), and $\mathsf{F}(f(\mathbf{r}))$ stands for the Fourier Transformation of a given function $f(\mathbf{r})$. On the other hand, the final expression for the elastic part only coincides with that one found in eq. (2.9) in Chap. 2.

6.3   Dynamics

The aim of the model is the study of stabilized states, which in this case consist of magnetization and strain configurations that minimize the magnetic and elastic energies respectively. On one hand, the micromagnetic dynamical equation makes the magnetization evolve according to the Landau-Lifshitz-Gilbert (LLG) equation:

$$(1 + \alpha^2)\frac{\partial \mathbf{M}}{\partial t} = -\gamma_0 \mathbf{M} \times \mathbf{H}_{\mathrm{eff}} - \frac{\gamma_0 \alpha}{M_s}\mathbf{M} \times (\mathbf{M} \times \mathbf{H}_{\mathrm{eff}}) \qquad (6.9)$$

As can be seen, the right side of the equation consists of two contributions. First term comes from the conservation of the angular momentum, forcing the spins to make a precessional motion [196] around an effective magnetic field $\mathbf{H}_{\mathrm{eff}}$. Therefore, γ is the gyromagnetic ratio. The second term is a purely phenomenological damping term [197], that has been observed experimentally but not deduced from atomistic basis, which makes reduce the precession of the spins up to reach a static state of minimum energy. Here α is a dimensionless damping constant. From micromagnetic arguments, the effective field can be calculated as $\mathbf{H}_{\mathrm{eff}} = -\frac{M_s}{\mu_0}\frac{\partial F}{\partial \mathbf{M}}$.

In App. B.5.2 it is shown that this equation conserves the modulus of each spin. Figure 6.3 shows the spin configurations that minimize and maximize each energetic contribution. The balance between the terms, which of course depends on the corresponding weights, will determine the final spin configuration. On the other hand, the stabilized configuration of the strain is reached by means of a pure relaxational dynamics as shown in Chap. 2: $\frac{\partial e_2}{\partial t} = -\frac{\delta F}{\delta e_2}$. It is worth noting that the magnetoelastic coupling contributes to both dynamics, which gives rise to the desired correlations between the strain and magnetization configurations, that is magnetoelastic behavior. The detailed mathematical calculation of both the elastic and magnetic energy derivatives can be found in B.4. The parameter values and model units can be found in App. C.

It must be pointed out that, although the LLG equation allows to analyze the magnetic dynamic behavior, the magnetoelastic coupling links both the micromagnetic and elastic dynamics and, since the latter is not realistic, it prevents us the study of the dynamic evolution and we focus only on static configurations.

In order to integrate the eq. (B.54) we have tested Euler and Runge-Kutta fourth order (RK4). If interested only in reaching the minimum of energy, Euler is good enough and faster than RK4. When studying the dynamics of the system, RK4 should be better. A detailed study about that has not been carried out.

6.4   Preliminary results

Micromagnetics in spherical coordinates

As seen, in the micromagnetic theory the spins are classical vectors $\mathbf{m}$ with constant modulus $|\mathbf{m}|$ =const. As discussed previously, this is considered by the LLG equation, since it is easy to see that this vectorial equation keeps $|\mathbf{m}|$ constant. According to the formulation in cartesian coordinates presented there, we deal with a vector of three components (m_x, m_y, m_z), and therefore LLG equation becomes a set of three equations, one for each component. Moreover, the conservation of the modulus $|\mathbf{m}|$ is automatically imposed by LLG equation but when it is implemented numerically, this condition is violated very slightly, and the error acumulates due to the recursive iterations of the LLG equation and may become too large. Hence, the initial small error must be corrected every certain *small* number of iterations by normalizing the spin vectors. Therefore it seems natural to deal with spherical coordinates (m_r, m_θ, m_ϕ), which makes easier the numerical integration since it imposes automatically the condition of modulus constant through the identity $m_r = 1$. Moreover, it leads to deal only with two components, (m_θ, m_ϕ) and the LLG equation becomes a set of only two equations.

Motivated by this argument, we have converted the model to spherical variables, first in cartesian coordinates, and second in spherical coordinates, whose mathematical details are presented in the following. Sadly, the final expressions involve trigonometric expressions like sinus, cosinus, etc. in such a way that, although the mathematical form is simpler, the spherical version is more costly from the computation point of view than the cartesian one. Consequently, we have finally used the latter coordinates.

It is worth mentioning that a two-dimensional version of the LLG equation has been developed elsewhere [198, 199] for systems within which the spins are confined to precess in a plane, due to anisotropy forces or whatever. In this case, the spins are expressed in spherical coordinates and the LLG is expressed in a very simple form, which makes sure a faster computation time and an appropriate pure two-dimensional magnetoelastic system.

Pure magnetic evolution

As a first check of the model we analyze the pure magnetic contribution. A dynamical evolution of the magnetization in a 32×32 square lattice with periodic boundary conditions is shown in Figures[3] 6.4 and 6.5. The configurations show the projection of the spin vectors in the xy-plane. Starting from a random configuration [shown in (a)], the spins rapidly look for aligning with the nearest neighbors [(b)]. The local directionality of the alignment differs from one region to another, which induces the formation of (embrionic) vortices (favored by the magnetostatic energy) in the regions inbetween [(c)-(d)] and other smooth interfaces [200]. The consolidation of such vortices may give rise to asymmetric Bloch walls [(e)-(h)] [201–203]. Simultaneously, vortices can merge or disappear, mediated by the spin flip in the z (out-of-plane)-direction, [(f)-(i)]. Other vortices may appear although the system evolves to a globally more ordered configuration. After a while all the vortices have disappeared, all the spins being almost parallel [(j)]. Then, the spin precession becomes more visible as can be seen in the fact that in (j) the dominant component is the vertical whereas in (k) it is the horizontal. This highlights the precession around the diagonal direction, as finally it does occur [(l)]. It can be seen that the stabilized state consists of a single domain configuration with the spins pointing to a diagonal direction. As seen above, this configuration is favored by the magnetocrystalline anisotropy and the exchange energy.

The absence of magnetic domains can be explained mathematically by the low simulation cell size together with the periodic boundary conditions leading to an

---

[3]The time intervals between the spin configurations in the series is not homogeneous, but they are chosen to highlight specific magnetic states.
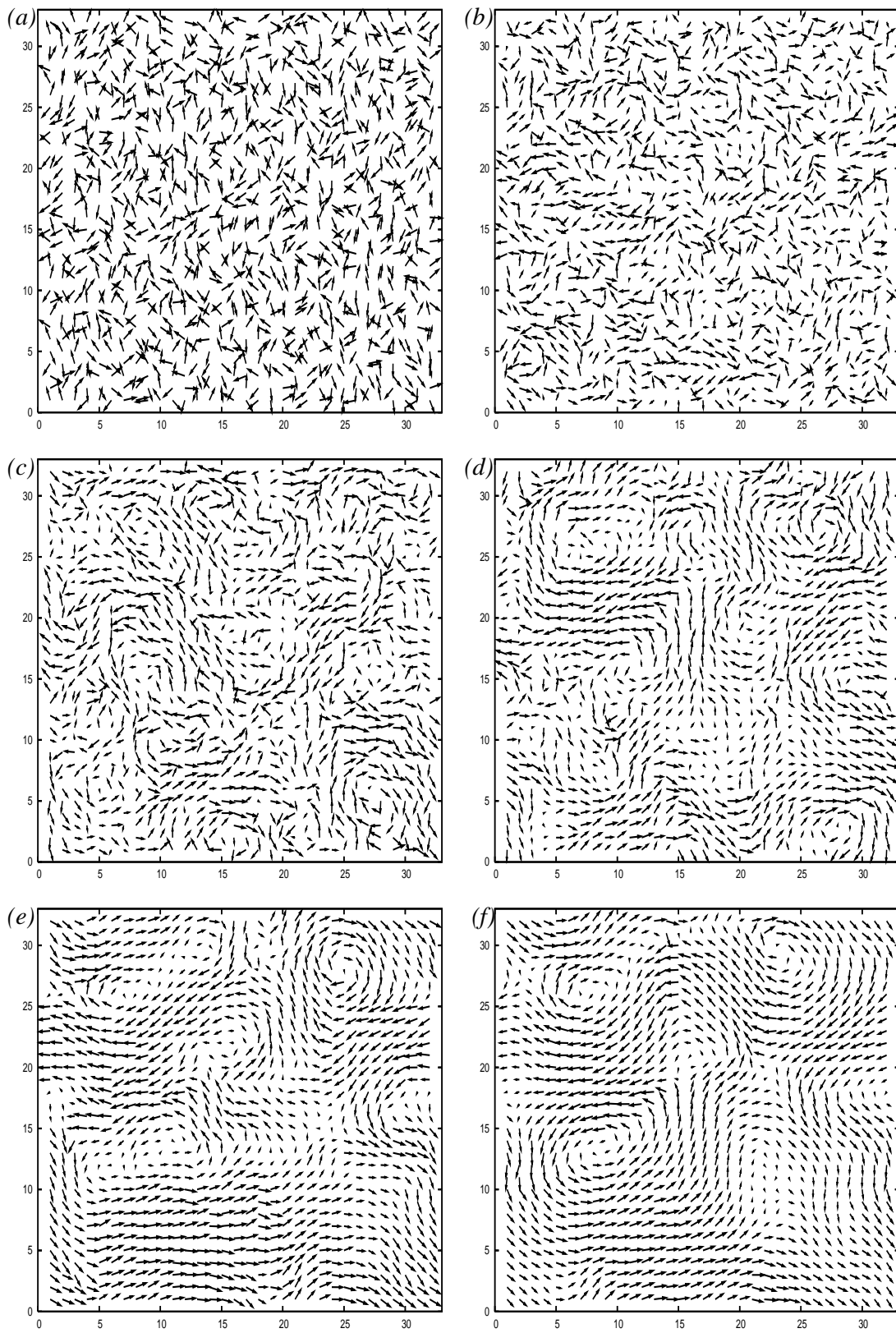
Figure 6.4: Spin field evolution I.
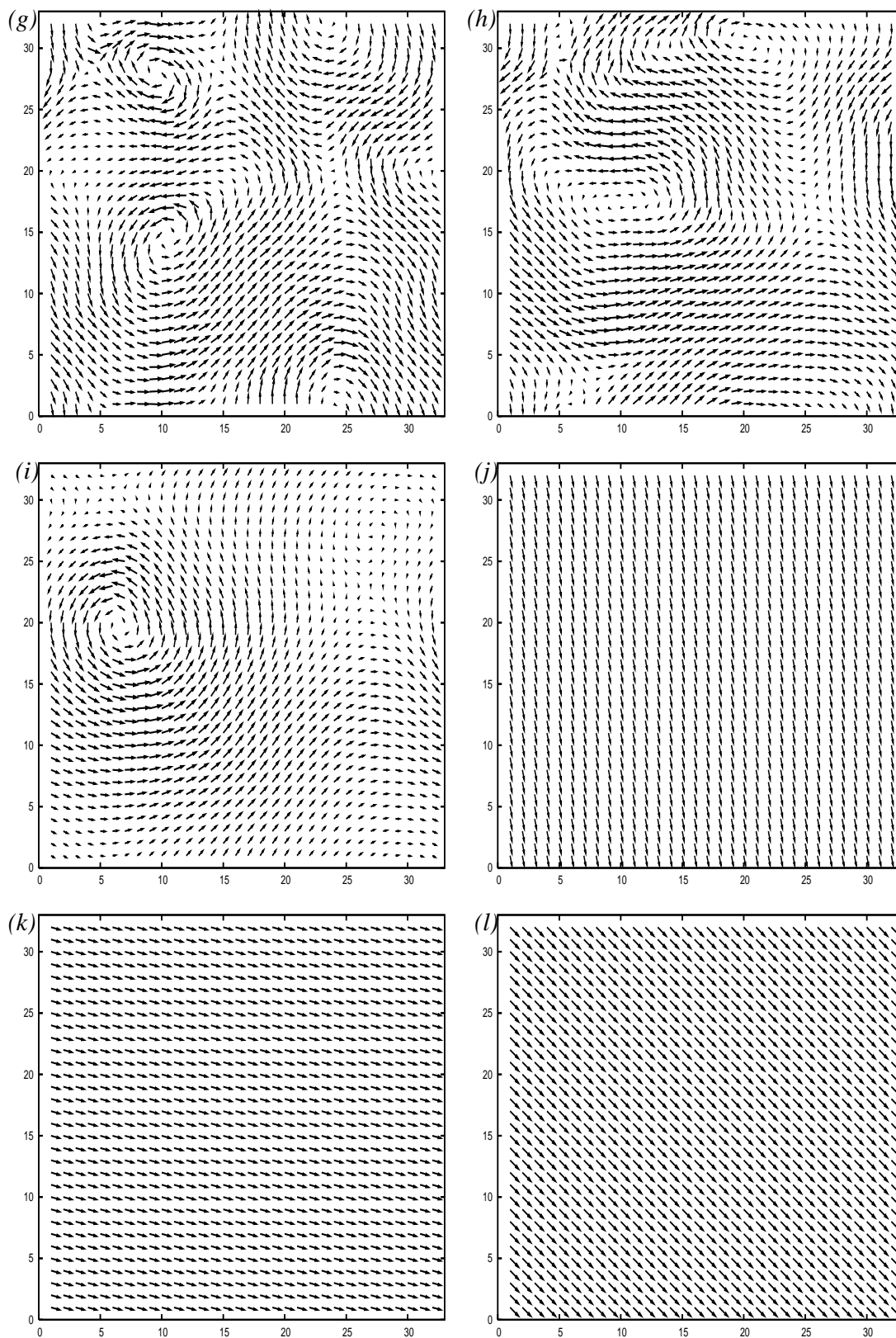
Figure 6.5: Spin field evolution II.
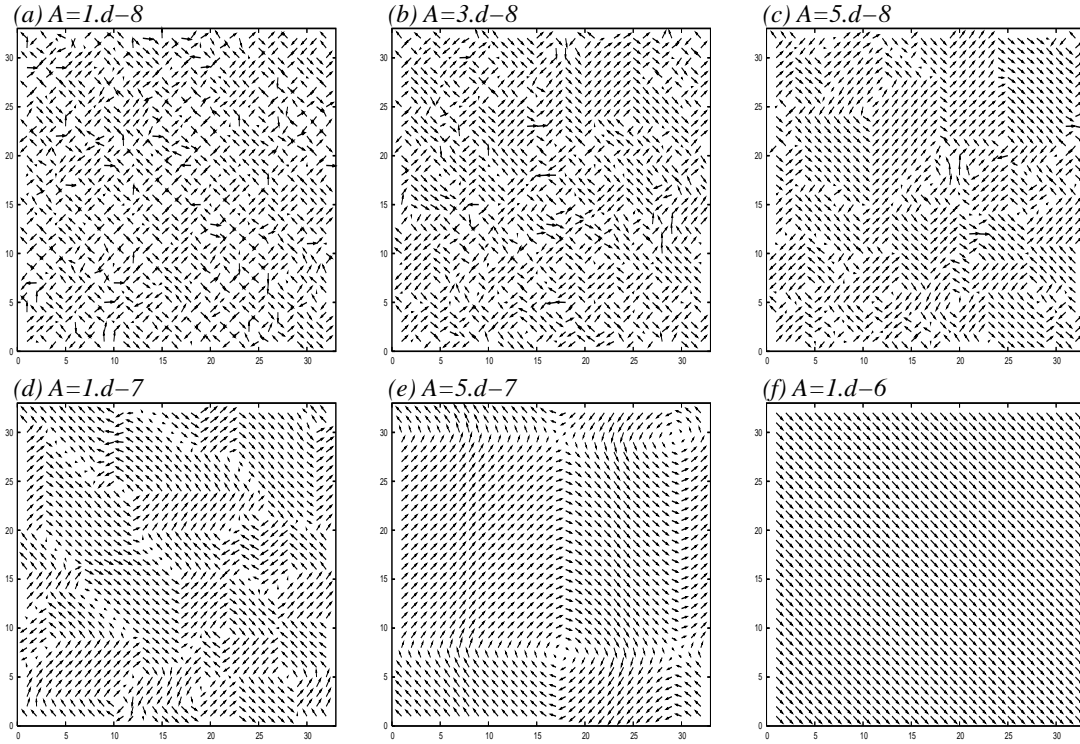
Figure 6.6: Stabilized configurations for different values of the stiffness constant A.

effective infinite system size which, therefore, does not take into account finite size and shape effects. We recall that the existence of magnetic domains is the result of an energetic balance between the long-range magnetostatic interactions and the exchange contribution when finite size and shape effects are taken into account. This balance is the magnetic analogous to the elastic case, where domains arise as a compromise between long-range elastic interactions and the Ginzburg energy. Moreover, the magnetostatic effects are more important as the system size increases, whereas the exchange effects become important in small-size systems. Hence, the fact that the simulation cell is much lower than the system size (which is mathematically infinite) cannot be given as a physical argument for the absence of magnetic domains.

To obtain a magnetic multidomain structure we have explored two simple methods: On one hand, we have carried out some simulations with a low value of the exchange, stiffness constant A to show that in this case, magnetic multidomain configuration stabilize. This is shown in Fig. 6.6. We can see that the lower value of A the smaller the domain size (and hence the larger the number of domains). We can also appreciate that neighbor domains never consist of spins of one domain pointing to the spins of the another($\rightarrow\leftarrow$). Instead, they consist of perpendicular spins ($\uparrow\rightarrow$) or spins perpendicular to the modulation of the magnetization ($\uparrow\downarrow$).

If we now modify the simulation cell size, it is observed that the higher the domain size the higher the value A below which multidomain structure appears. This is observed in Fig. 6.7(a) where, for a value of the stiffness constant $A = 10^{-6}$, a 128×128 spin lattice shows two magnetic domains. Note that for this value of A, a 32×32 spin lattice does not show magnetic domains but a single domain, as it is shown in Fig. 6.6(f). For clarity, each spin in the 128×128 snapshot is the average over 16 nearest neighbor spins. However, it must be noted that the value of the stiffness constant is in any case much lower that the nominal value for Fe-Pd, so that the system size that should be used to obtain a multidomain configuration with this real value is expected to be too large for computational purposes.

On the other hand, the second method to obtain a multidomain configuration consists of introducing an additional condition for the spins in the lattice that plays the role of an effective shape for the system. For instance, we can impose extra energetic penalties for the averages of both the x- and y-spin components over all the cells of the system denoted as $\langle m_x \rangle$ and $\langle m_y \rangle$ respectively. Thus, if these penalties are high enough, the configurations whose $\langle m_x \rangle$ and $\langle m_x \rangle$ vanish become favorable. Such configurations must contain at least two magnetic domains with spins pointing to opposite directions. Figure 6.7(b) show a 64×64 multidomain magnetic configuration stabilized by means of introducing such penalties. Here, each spin in the snapshot is the average over 4 nearest neighbor spins.

In fact, this additional term can be interpreted as accounting for the modulations corresponding to the wave vector $\mathbf{k} = 0$, which, as pointed out in Sec. 6.2.1, is not taken into account by the Fourier expression used to compute the long-range magnetostatic field. As explained in App. B.2.3 it can be introduced through the demagnetizing factor which depends on the specific shape of the system.

Magnetoelastic results

Once we have checked that the magnetic part works as expected, we perform simulations of the full magnetoelastic model. Simulation results show that the magnetoelastic coupling is strong for Fe-Pd. In the martensitic phase the stabilized states show typical strain configurations and the magnetization stabilizes according to the strain. Consequently, the magnetic domains are subjected to the elastic domains. The pure magnetic terms turn out to be less relevant than the magnetoelastic coupling, although they determine fine details like the width of the walls. In the austenite phase, the coupling vanishes because the strain is zero (in the absence of precursors) and magnetization may evolve as in pure magnetic systems analyzed above.
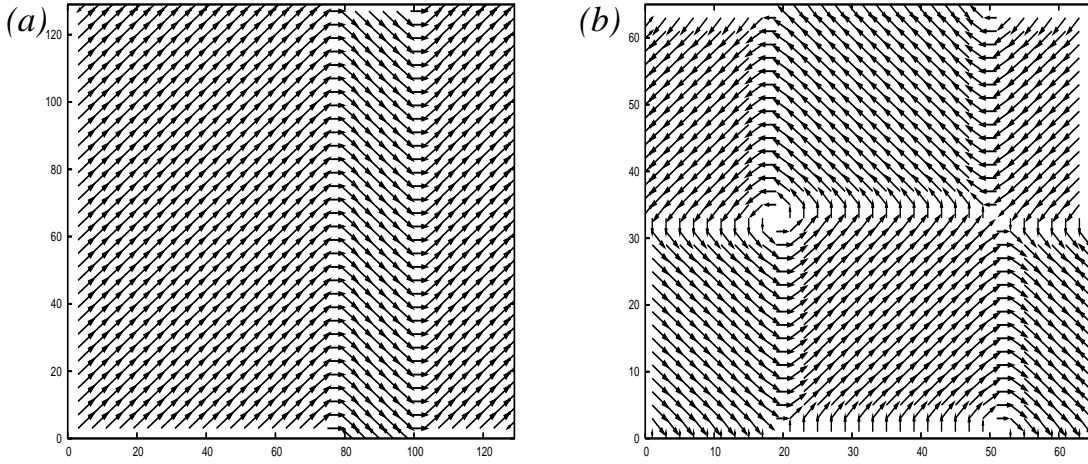
Figure 6.7: Stabilized multidomain structures either by using a large 128×128 spin lattice (a) or through penalizing the nonvanishing averages of the x- and y-spin components in a 64×64 spin lattice (b).

All this can be observed in Fig. 6.8, where we have used the method of simulating austenite described in Sec. 3.4.2 to obtain fine twinning in the transformable region for a 512×512 cells system, with linear size $L = 10^3$. In particular, (a) shows the strain configuration, which indeed is similar to those obtained in Sec. 3.4.2. Since the system size is very large, the representation of the spin field has been detailed in two snapshots for clarity. In (b) the absolute magnitude of the x-component of the magnetization $|m_x(\mathbf{r})|$ is shown (the darker the region the higher the x-component) whereas in (c) we can observe a projection of the spins in the xy-plane, where each spin is the average over 36 nearest neighbor spins. Both snapshots show clearly that in the martensitic phase, the magnetization form twins according to elastic twins. Also, in the austenite phase, mangetization evolves freely towards a configuration consisting of a region where the magnetization points to a diagonal direction according to the magnetocrystalline anisotropy, and a vortex formed elsewhere. Note that the center of the vortex in (b) is not in the circle but in the white (blue) strip just below it. This is logical since the spins in the center of a vortex lying in the xy-plane point to the z-direction (out-of-plane) and hence they have no x-component. It can be also observed that the decaying fields in the austenite also affect the magnetization.
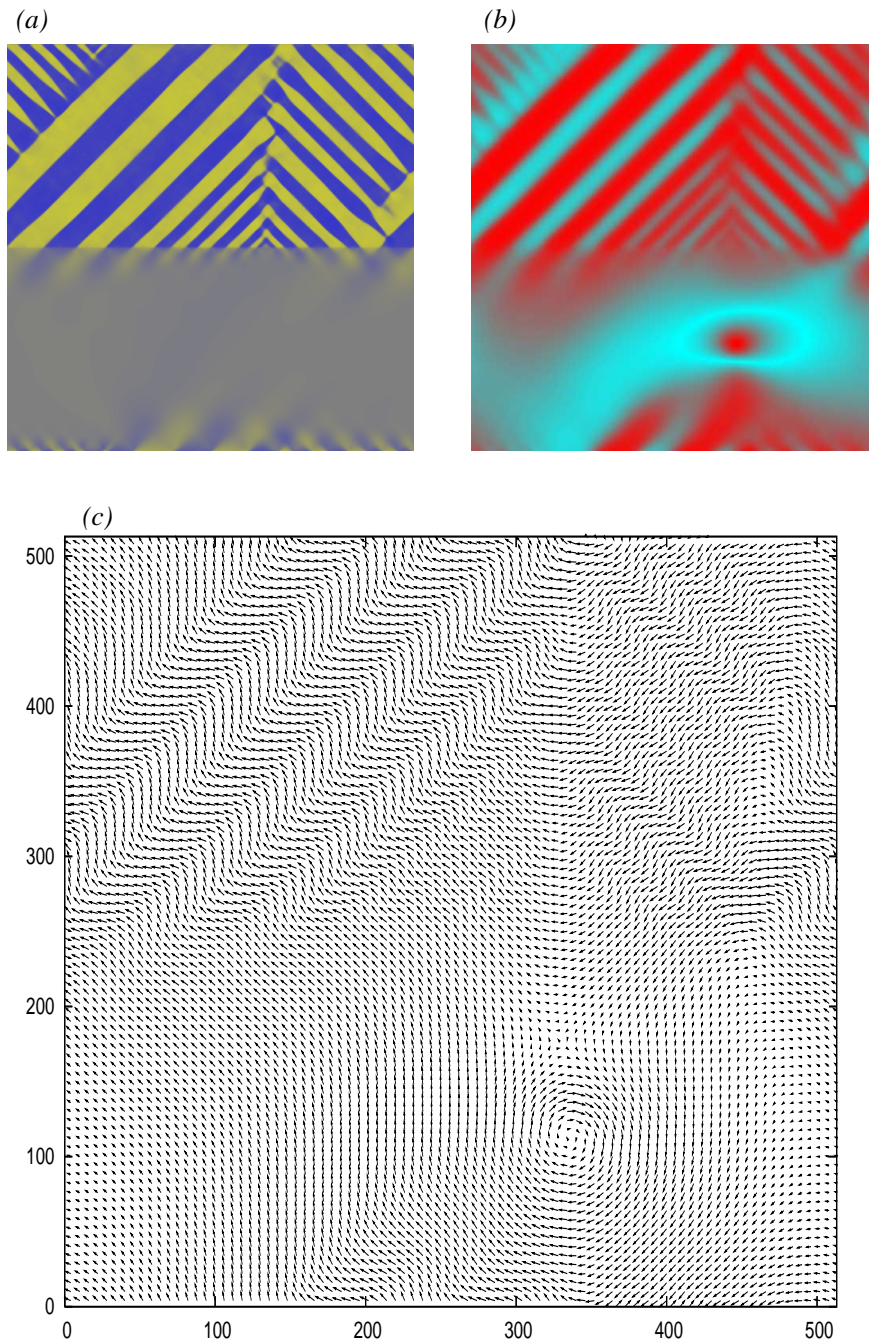
Figure 6.8:

Chapter 7

Summary and conclusions

In this thesis we have approached the problem of competing interactions between anisotropy and disorder in ferroelastic martensites. Motivated by experimental evidence which points to these two parameters to play a decisive role in the resulting ferroelastic behavior, we have perfomed simulations by means of a Ginzburg-Landau model extended to include long-range interactions and disorder. The model has been shown to be powerful enough to account for a wide variety of phenomena like characteristics of the microstructure, thermodynamic behavior and thermomechanical properties. Beyond the interest as basic, theoretical research, this work concerns an issue of many technological relevance as doping in SMAs. Besides the great amount of historical literature about this subject, due to the recent publication of relevant papers in important physical magazines, it has emerged as a current experimental cutting research. Our results are, in general, in good qualitative agreement with many experiments in different alloy families and thus provides a simple, unified framework which allows to go depth into the understanding of ferroelastics. In the following, we highlight the main results/accomplishments/achievements of this thesis and propose some improvements for the model. Finally, we also summarize the theoretical conclusions and propose some future experimental work.

Main Results

– Quenched-in disorder is a necessary ingredient for pretransitional textures to exist. In systems with high anisotropy, disorder cooperates with long-range anisotropic interactions giving rise to a *middle*-range cross-hatched pattern, the so-called tweed, which has been widely observed in experiments. By *middle*-range modulation we mean that the length scale associated to tweed considerably overcomes the typical length scale of disorder but is notably smaller than the characteristic twin size. In contrast with that, systems with low anisotropy exhibit short-range

pretransitional textures of almost spherical shape (mottled structure), which have been experimentally observed in Ti-Ni-based systems. Indeed, such alloys are particularly characterized by a very low anisotropy value.

– For relative small amounts of disorder, upon cooling the system transforms to the martensitic phase, being the arising twinned structures completely uncorrelated with the high temperature pretransitional patterns. Correct twin width is obtained by introducing an extra energetic contribution derived from surface effects, i.e. of imposing the existence of an habit plane. Phenomenological methods have also succeed in yielding the correct length scale. Other important features of the twinned microstructure, like needles, have been also reproduced.

– For a given value of the anisotropy, as the amount of disorder is increased, the ferroelastic transition is rounded, shifted to low temperatures and finally suppressed, which is revealed by the corresponding smoothing, shift and suppression of the peak in the heat capacity C, and by a notable flatening in the elastic response C'. This is in very good agreement with experiments that analyze the behavior of C as a function of the relative concentration of the elements in a given alloy family. The higher the value of the anisotropy the higher the amount of disorder needed to inhibit the transition.

– When the transition is suppressed, both tweed and mottled structures are retained at low temperatures. This is experimentally observed when increasing doping in SMAs. These low temperature patterns differ from those at high temperature in the sense that show a degree of freeezing that is revealed by ZFC/FC simulation experiments, where ZFC and FC curves split. This deviation, which is indicative of glassy behavior, is particularly important in the low anisotropy case, whereas it is rather small in the high anisotropy case. ZFC/FC results are also in very good agreement with experiments in low anisotropy alloys. No experimental results in high anisotropy systems are available. By looking at the energy of these frozen structures, we have detected that they are metastable states, in contrast with the similar structures in the precursor regime, where they seem to be thermodynamically stable. Simulations with zero anisotropy show uncorrelated emerging domains, which suggest that frustration is not at the origin of the glassy behavior but this occurs due to kinetic freezing because of the competition among growing domains. Thus, the thermodynamic stable state exist but it is unaccessible.

– Thermomechanical properties have been analyzed. Stress-strain curves show a very rich, nontrivial phenomenology as a consequence of anisotropy and disorder. Variations in their values result in changes in the transition stress, hysteresis area, transition dynamics and temperature ranges where pseudoplasticity and superelasticity regimes are observed. However, the response of the system may be in opposite directions depending on the value of the two parameters. In some

cases the disorder favors superelasticity whereas in some others cases prevents it. This two-fold effect of the disorder has been observed experimentally. The following general trends may be also recognized: As expected, superelasticity has been observed at high temperatures. The Clausius-Clapeyron relationship is linear, which is in agreement with experimental observations in many different martensitic systems when varying doping. It is worth mentioning that the SME has been obtained not only in twinned martensite but also in the glassy system, which is in agreement with experiments. To summarize stress-strain properties, the elastocaloric effect has been studied.

Model Improvements

– The model may be improved in several ways: A more realistic, inertial dynamics may be included, which would introduce the time as an external parameter to be taken into account, and would allow for important simulations like frequency-dependence of the elastic response, from which we can extract Volger-Fülcher relations related to glassy behavior, cooling rate-dependent simulations, cycling, aging, etc. Moreover, due to the phenomenological nature of disorder, any tuning of it would be welcome to get closer to experiments.

– Regarding the magnetoelastic model, it would be interesting to explore the wide range of phenomena like magnetic domains, stress(magnetic)-induced magnetic (strain) domain switching, ferromagnetic SME, magnetic textures in the premartensitic regime, etc. Beyond this, freezing of the spins induced by frozen strains could also be studied in the case of large disorder.

Theoretical Conclusions and Proposed Experiments

Up to date, the suppression of the transition due to changes in composition has been experimentally associated with an intrinsic thermodynamic instability of the martensite. However, mechanical-induced transitions in the nonmartensitic, glassy Ti-Ni-based alloys point to the nontwinned martensitic state to be actually thermodynamically (meta)stable, since upon unloading the martensitic phase is retained. This is further revealed by diffraction experiments. Our simulation results support this finding. It would be interesting to explore the possibility of the two-way SME through thermomechanical treatment, whose existence would reinforce this argument. Moreover, the fact that these alloys exhibit SME implies that the nontwinned martensite, after being stabilized through loading-unloading processes, undergoes a temperature-induced backward transition upon heating which allows the sample to recover the initial shape. With respect to this, it would also be of interest to check the existence of the corresponding peak in the

heat capacity and other thermodynamic signatures of the transition in magnitudes like resistivity and elastic response.

On the other hand, since the strain glass state has been only observed in very low anisotropy systems, a couple of additional questions proposals still come to our mind, complementary those above: First, does glassy features also occur in high anisotropy systems at high amounts of doping? In other words, are the tweed textures observed in high anisotropy materials a glassy state when obtained at low temperatures in the nontransforming composition regime? Analogous to the low anisotropy case, this could be tested through ZFC/FC experiments and others. To further compare tweed with the mottled glassy state, at least one important question remains unanswered: Why is the martensitic phase unaccessible under certain conditions? is it due to a thermodynamical instability, or is it due to a kinetic freezing, which gives rise to the glassy state? Directly related to that, we can also ask ourselves wether such a system also exhibits SME or not.

Answers to all these questions would help to go deeper into the understanding of the intringuing mechanisms governing these systems, and perhaps we would be able address a fundamental question concerning this thesis: Does the anisotropy play any role in determining the observed behavior?

Chapter 8

Resum

Des de fa temps s'ha anat observant que els materials que exhibeixen estats espaialment inhomogenis a l'escala mesoscòpica poden presentar propietats noves i interessants des del punt de vista tecnològic i fonamental. Dins de l'ampli ventall dels materials funcionals, podem citar superconductors d'alta temperatura, manganites exhibint magnetoresistència colossal, conductors iònics i ferroics en general com a exemples de sistemes en els que les inhomogeneitats juguen un paper crucial a l'hora de determinar-ne les seves propietats.

En particular, els materials ferroics són sistemes que es caracteritzen per una transició de fase induïda per temperatura, en la que una magnitud física s'ordena espontàniament donant lloc a una mesoestructura interna típicament multidomini. Aquesta autoorganització sorgeix de la combinació entre tres factors: un perfil energètic consistent en varis pous degenerats (variants o *twins* en anglès), l'existència d'unes forces de llarg abast de tipus dipolar i efectes de forma i tamany finit. La transició també pot ser induïda per l'aplicació d'un camp extern. Així mateix, la fase ordenada es caracteritza pel fet que les diferents variants poden ser convertides d'una a una altra fàcilment per mitjà d'un camp extern, donant lloc a una sèrie de particularitats com el cicle d'histèresi, amb l'existència d'un camp coercitiu, etc.

Els exemples paradigmàtics de materials ferroics són els sistemes ferromagnètics, ferroelèctrics i ferroelàstics, on la magnetització, la polarització i la deformació són les magnituds físiques de rellevància respectivament. Cal posar de manifest l'existència de materials multiferroics, com per exemple magnetoelàstics o magnetoelèctrics, on l'acoblament entre les diferents magnituds és important. Això dóna lloc a una resposta creuada significativa entre una variable i el camp conjugat d'una altra, que permet una fenomenologia variada amb importants aplicacions tecnològiques.

Aquest estudi es focalitza en els materials ferroelàstics, en els que durant la

transició apareix una deformació de la xarxa cristal·lina, que canvia d'estructura de tal manera que els processos dominants són displacius i no hi ha difusió d'àtoms per la xarxa. Típicament les cel.les unitat de les dues fases mantenen una relació de grup-subgrup, cosa que dóna lloc a l'existència de més d'una variant orientacional. Usualment, la fase ferroelàstica nuclea dins d'una matriu paraelàstica. La multiplicitat de les variants orientacionals permet que l'encaix de la inclusió emergent i posterior creixement de la fase ferroelàstica no sigui dramàtica per la matriu mare des del punt de vista de la deformaci'ó sinó que té lloc mantenint el pla que forma la frontera entre fases (pla d'hàbit) macroscòpicament invariant, mitjançant l'alternança de les mencionades variants. L'efecte dominó, que és l'essència del llarg abast de les interaccions elàstiques, fa que aquesta alternança es propagui dins el volum de la fase martensita, donant lloc d'aquesta manera a una estructura interna de dominis orientacionals. De fet la modulació ι de la deformació segueix una llei del tipus $l \propto \sqrt{L}$.

Léxistència d'aquesta microestructura permet dos fenòmens importants: en primer lloc, la superelasticitat, que consisteix en el fet que el sistema pot deformar-se més enllà del llindar elàstic mitjançant l'aplicació d'un esforç que indueixi la transició ferroelàstica, amb la conseqüent aparició d'una única variant, seleccionada per les especifitats del camp. Quan s'elimina l'esforç, el material pateix la transformació inversa i recupera així la seva forma original. En segon lloc, trobem l'efecte de memòria de forma (SME), que es basa en el fet que el material manté la seva forma original macroscòpica quan pateix la transició al disminuir la temperatura gràcies a l'estructura multidomini. L'aplicació d'un esforç a aquesta fase ordenada provoca el creixement de la variant afavorida pel camp en detriment de les altres i la conseqüent deformació del sistema. El potserior escalfament de la mostra provoca la transició inversa i, per tant, la recuperació de la forma original. Entre els materials ferroelàstics cal destacar les martensites termoelàstiques, que poden recuperar deformacions de gairebé fins al 10%, i que tenen importants aplicacions tecnològiques com a actuadors, sensors, vàlvules de control, etc. en camps molt diversos que van des de l'aeronàutica a la medicina. Com a exemples de martensites termoelàstiques trobem multitud d'aliatges intermetàl·lics, entre els que destacarem el Ti-Ni per la seva rellevància tecnològica, i aliatges basats en Ti i Ti-Ni. Cal destacar també l'efecte de memòria de forma magnetica (FSME) en materials magnetoelàstics citats abans, on un camp magnètic juga el paper del camp d'esforços. Aquí podem mencionar el Fe-Pd.

Com s'ha dit, en aquests sistemes la transició està dominada per forces elàstiques de llarg abast, que a la vegada depenen fortament de les simetries específiques de la xarxa així com de les constants elàstiques, que determinen les direccions toves del cristall. Per tant, aquestes forces poden ser altament anisotròpiques, i poden afectar de manera crucial la morfologia de les mesoestructures internes.

Tanmateix, aquesta descripció es veu alterada per la presència d'inhomogeneïtats, com les fluctuacions composicionals intrínsiques a qualsevol aliatge. Aquest desordre intrínsec pot erigir barreres d'energia i entropia de tal manera que poden apantallar les correlacions de llarg abast. És àmpliament sabut, per exemple, que desviacions de l'estequiometria en aliatges així com el *doping* (que típicament porten a un augment de les fluctuacions composicionals respecte els aliatges originals), introdueix variacions molt significatives en els rangs de temperatura i esforç en els que s'observen el SME i la superelasticitat així com la histèresi, cosa que és molt important per al disseny d'aliatges amb memòria de forma, que necessiten règims operatius determinats. Per això hi ha una quantitat de literatura experimental molt important que concerneix les propietats termoelàstiques en funció de la composició. De manera més fonamental, també s'observen anomalies en respostes termodinàmiques com la capacitat calorífica, la resistivitat, canvis en les constants elàstiques, etc. Cal mencionar les estructures pretransicionals com el *tweed* que resulten de la cooperació entre la presència d'inhomogeneïtats i les forces anisotròpiques de llarg abast. El present estudi es focalitza precisament en l'anàlisi numèric de l'efecte de l'anisotropia i el desordre en les estructures i respostes termodinàmiques en sistemes ferroelàstics. S'utilitza una extensió d'un model de Ginzburg-Landau que inclou desordre i interaccions de llarg abast anisotròpiques.

Model

D'acord amb la teoria de l'elasticitat, qualsevol deformació d'un sistema amb simetria quadrada es pot expressar com a combinació de tres deformacions fonamentals (més una rotació), que són les deformacions de volum (e_1), deviatòrica (e_2) i de cisalla (e_3). En particular, el nostre objectiu és modelar un sistema que pateix una transició de simetria quadrada a rectangular. que és el cas bidimensional corresponent a la transició real de cúbica a tetragonal. Per tant, la deformació de transformació és la deviatòrica, que esdevindrà el paràmetre d'ordre (OP) de l'energia lliure de Ginzburg-Landau. Les consideracions d'una transició de primer ordre i de simetria de paritat duu a la següent expressió: $F_{\mathrm{GL}}(e_2) = \int (\alpha_T(T - T_c)e_2^2(\mathbf{r}) - \frac{\beta}{4}e_2^4(\mathbf{r}) + \frac{\gamma}{6}e_2^6(\mathbf{r}) + |\nabla e_2(\mathbf{r})|^2)d\mathbf{r}$.

A la introducció s'ha comentat que els aliatges mostren una sensibilitat molt gran de la temperatura de transformació a la composició específica del material. Aquest fet, juntament amb les fluctuacions composicionals inherents als aliatges, recolza la introducció del desordre com un camp aleatori fluctuant acoblant-se a l'OP a través del terme harmònic, ja que el coeficient d'aquest terme determina parcialment les temperatures característiques de la transició. En particular el camp ve descrit per una variable aleatòria $\eta(\mathbf{r})$, distribuïda gaussianament i correlacionada espaialment segons una funció de correlació a parelles exponencial.

Els paràmetres que determinen la variable $\eta(\mathbf{r})$ són, per tant, la mitjana μ i la desviació estàndard ζ de la distribució i la longitud de correlació ξ. En un altre model molt similar a l'actual, s'ha observat que les estructures de dominis són molt robustes respecte la funcionalitat específica de la distribució i correlació del desordre. Així mateix, és evident que el valor de μ només desplaça la fenomenologia al voltant del valor escollit, però no aporta resultats qualitativament diferents.

La discretització del desordre, necessària per a la implementació numèrica en la malla de simulació, introdueix diferències finites en les temperatures característiques de les cel.les veïnes, que determinen de manera crucial les barreres locals d'energia lliure. Ja que els valors de ζ i ξ varien sensiblement aquestes diferéncies, són susceptibles d'afectar de manera rellevant els resultats obtinguts. De totes maneres, s'observa que el comportament del sistema és bastant robust respecte variacions en ξ i en cap cas dóna lloc a resultats qualitatius diferents que els obtinguts al variar el valor de ζ. Per tant, ξ es deixarà constant i l'estudi en funció del desordre es durà a terme només en funció de ζ.

Addicionalment, s'afegeix una contribució energètica d'ordre harmònic de les deformacions que no corresponen a l'OP, és a dir, de volum i cisalla ($F_{\text{non-OP}}(e_1, e_3) = \int \left(\frac{A_1}{2} e_1^2(\mathbf{r}) + \frac{A_3}{2} e_3^2(\mathbf{r}) \right) d\mathbf{r}$), on A_1 i A_3 estan relacionats amb els mòduls de volum i cisalla respectivament. Donat que en 2 dimensions els graus de llibertat reals són únicament dos, descrits pel camp de desplaçaments, les tres deformacions e_1, e_2 i e_3 estan lligades per mitjà de la condició de compatibilitat de Saint Vénant, que és una equació que garanteix la integritat de la xarxa. Això possibilita escriure l'energia lliure total en termes només de l'OP i d'una de les deformacions e_1 o e_3 (per exemple, $F_{\text{T}}(e_1, e_2) = F_{\text{GL}}(e_2) + F_{\text{non-OP}}(e_1, e_2)$). Si, a més a més, minimitzem l'energia lliure total F_T respecte e_1, obtenim una condició addicional que ens permet obtenir una expressió per F_{T} només en termes de l'OP. L'expressió resultant per $F_{\text{non-OP}}(e_2)$ és no local a l'espai real: $F_{\text{non-OP}}(e_2) = \int d\mathbf{r} \int e_2(\mathbf{r}) U(\mathbf{r} - \mathbf{r}') e_2(\mathbf{r}') d\mathbf{r}'$, però esdevé local a l'espai de Fourier: $F_{\text{non-OP}}(e_2) = \frac{A_3}{2} \int V(\mathbf{k}) \tilde{e}_2(\mathbf{k}) d\mathbf{k}$, amb un kernel $V(\mathbf{k})$ que posa de manifest l'anisotropia d'aquestes interaccions: $V(\mathbf{k}) = \frac{(k_x^2 - k_y^2)^2}{\frac{A_3}{A_1} k^4 + 8 k_x^2 k_y^2}$. Efectivament, aquest terme es minimitza quan la deformació deviatòrica es modula segons les direccions diagonals respecte els eixos cristal·logràfics de la fase quadrada, i explica per tant les modulacions creuades observades experimentalment en les textures pretransicionals tipus tweed així com la morfologia lineal de les fronteres entre dominis dels twins i les juncions perpendiculars en monocristalls.

D'altra banda, es pot demostrar que en realitat $V(\mathbf{k}) = V(\mathbf{k}/k)$, és a dir, no afavoreix cap longitud d'ona sinó que només selecciona la direcció de les modulacions. De fet, aquesta característica no s'ajusta a la realitat, ja que resulta de no tenir en compte condicions de mida finita de la martensita, cosa que, com

s'ha comentat anteriorment, és essencial per l'aparició de dominis amb una modulació determinada. Tanmateix, la consideració de mida infinita és necessària per poder obtenir una expressió tan senzilla per $F_{\text{non-OP}}(e_2)$. Això permet, mitjançant condicions periòdiques de contorn, un càlcul computacional molt més ràpid i amb una mida de cel·la de simulació superior (ordre $N \log N$, on N és el nombre de cel·les unitat) que no pas el temps que comportaria el càlcul no local a l'espai real (d'ordre N^2). En qualsevol cas, això tampoc resulta fonamental per les estructures obtingudes des del punt de vista del nostre interès, ja que la dinàmica utilitzada al model és purament relaxacional i això dóna lloc a l'estabilització d'estats metaestables, amb interfases entre dominis orientades diagonalment. Cal dir, no obstant, que s'han dedicat part dels esforços d'aquest treball a l'estudi de possibles mètodes per introduir efectes de mida finita.

S'ha estudiat la dependència de les forces de llarg abast així com el comportament del sistema en funció d'A_3 i del quocient A_3/A_1, ja que són coeficients que apareixen en la interacció de llarg abast. La fenomenologia que s'obté al variar A_3/A_1 és qualitativament equivalent a la obtinguda al variar A_3. Per tant, deixarem A_3/A_1 constant. És important remarcar el fet que A_3 i el factor d'anisotropia elàstica són proporcionals a temperatura constant. Aquesta relació posa en evidència el fet que l'anisotropia està directament relacionada amb el pes del terme de llarg abast. Així, podem analitzar l'efecte de l'anisotropia introduïnt variacions en el paràmetre A_3.

Resultats

En primer lloc es fa una anàlisi de la morfologia de les estructures que s'obtenen en diverses situacions. Per valors alts de l'anisotropia i valors intermitjos de desordre, s'observa tweed pretransitional, que evoluciona cap a dominis twin quan la temperatura disminueix per sota la transició. A mesura que el valor de l'anisotropia disminueix, les estructures pretransicionals perden direccionalitat i els twins es trenquen. Per sota d'un llindar deixa d'observar-se modulació en la deformació i les estructures són bàsicament en forma de gotes gairebé esfèriques. Al disminuir la temperatura, van apareixent noves gotes i les ja existents evolucionen poc, només augmentant una mica la seva mida. Experimentalment també s'ha observat una dependència similar de les estructures pretransicionals a l'anisotropia. Així, materials amb alta anisotropia com el Fe-Pd i el Ni-Al exhibeixen tweed mentre que aliatges amb baixa anisotropia com el Ti-Ni i el Ti-Ni dopat amb Fe presenten una estructura pretransicional de gotes.

Una fenomenologia similar es pot obtenir mantenint una anisotropia constant i variant el desordre. Un augment de la intensitat del desordre és equivalent a

disminuir l'anisotropia i a l'inrevés. Per valors intermitjos d'anisotropia i de desordre, ja no s'obté tweed en el règim pretransicional però es poden seguir obtenint twins (semitrencats) a baixa temperatura. Quan s'augmenta el desordre, els twins deixen de formar-se i l'estructura pretransicional es manté fins a baixa temperatura. Si l'anisotropia és gran la intensitat de desordre necessària per inhibir la formació és conseqüentment més gran. La inhibició dels twins i la supervivència de les estructures premartensítiques a baixa temperatura s'ha observat en molts aliatges al canviar la composició relativa dels elements constituents o a . D'aquesta manera, el $Ti_{1-x}Ni_{1+x}$ no mostra twins per $x > 1.5$, sinó que l'estructura de gotes es manté fins a 0 K. El superconductor Y-Ba-Cu-0 mostra tweed pretransicional, però quan es dopa amb Co o Fe en detriment de Cu per sobre d'un cert llindar, el tweed també sobreviu fins a 0 K.

Les estructures s'han caracteritzat per diferents mètodes: s'ha calculat la distribució de la deformació local, la intensitat de la transformada de Fourier, que està relacionada amb el patró de difracció i finalment s'ha mesurat la mida dels dominis. Per poder dur a terme aquest últim càlcul, s'han hagut d'introduir efectes de mida finita que, com s'ha comentat a la introducció, és la responsable de la longitud característica de l'estructura de dominis. Per a aquest propòsit s'han utilitzat tres mètodes diferents: en primer lloc, mitjançant un càlcul analític rigorós s'ha derivat el potencial real que afecta la martensita com a conseqüència de minimitzar l'energia corresponent a un sistema consistent en una martensita envoltada d'una matriu d'austenita. Aquest nou potencial inclou el kernel anterior $V(k)$ i un de nou que es pot aproximar a $1/|k|$, essent k el vector d'ones de la modulació de la deformació. Això afavoreix longituds de modulació petites. Un balanç entre el terme de Ginzburg i aquest nou kernel permet l'obtenció de la llei d'escala $l \propto \sqrt{L}$ mencionada anteriorment. També s'ha estudiat els efectes de mida petita, i s'ha obtingut que per sota d'un certa mida de la zona susceptible de nuclear la martensita, el twinning s'inhibeix i en el seu lloc apareix un patró en forma de quadrícula, que alterna dominis de variants martensítiques amb dominis de fase austenita.

Aquesta mateixa fenomenologia s'ha obtingut introduïnt els efects de superfície d'una manera menys física però molt més simple: a través d'una distribució de desordre (és a dir, de temperatures característiques) que obligui una zona del sistema a romandre a la fase mare. Aquest mètode té l'avantatge que no és més costós des del punt de vista computacional i en permet l'ús sistemàtic pel càlcul de les mides dels dominis i la seva evolució en temperatura per varis valors de l'anisotropia i el desordre. Consistentment amb les simulacions inicials del model en aquests termes, i també amb resultats que es descriuen més endavant, s'observa que per valors baixos d'anisotropia respecte del desordre, la mida de les gotes gairebé no evoluciona en temperatura sinó que es congelen, de tal manera

que les estructures del sistema a baixa temperatura vénen determinades en gran mesura pels patrons pretransicionals. Això evidentment no passa quan la fase de baixa temperatura presenta twins, ja que típicament aquests tenen una longitud característica més gran que les textures premartensítiques, ja siguin tipus tweed o en forma de gotes. Bàsicament, la mida dels twins és independent de les característiques del desordre mentre que en el tweed i sobretot en les gotes, el desordre hi juga un paper fonamental.

L'últim mètode utilitzat per obtenir una estructura de dominis amb longitud característica ha consistit en la introducció d'un potencial fenomenològic amb un kernel tipus $1/|k|$, que és en essència el mateix que prèviament s'ha derivat analíticament. S'han comprovat alguns aspectes dels comentats anteriorment.

Cal mencionar que els dos últims mètodes han permès l'aparició de twins trencats a alta anisotropia. Això dóna lloc a juncions perpendiculars, on s'observa que els dominis es deformen en forma d'agulles. A mesura que ens allunyem de les juncions, les agulles o bé desapareixen o bé s'eixamplen per donar llocs a twins de llarg abast. Aquests detalls de les estructures també s'han observat àmpliament en experiments.

Per corroborar els efectes de l'anisotropia i el desordre en el sistema, s'han analitzat diverses funcions resposta. En primer lloc, hem determinat la capacitat calorífica C en funció de l'anisotropia. Per valors alts d'$\mathcal{A}$, C presenta un pic abrupte corresponent a la transició, i una anomalia en forma de gep corresponent a les estructures premartensítiques. Quan l'anisotropia disminueix, el pic es suavitza i es desplaça cap a baixes temperatures. Finalment, per valors molt baixos d'$\mathcal{A}$ el pic se suprimeix. Aquest desplaçament cap a baixes temperatures és degut al fet que les simulacions s'han fet refredant per tal de seguir el procediment experimental habitual. Simulacions addicionals dutes a terme escalfant mostren un un desplaçament del pic cap a altes temperatures, indicant que el pic correspon a límits d'estabilitat. Paral·lelament, el càlcul de la primera derivada de la fracció transformada mostra un pic amb una dependència en l'anisotropia molt similar al pic en C, cosa que és una mostra de la robustesa del pic. Aquest comportament del pic en C s'ha vist experimentalment en molts aliatges com el Ti-Ni, Ti-Ni-Fe, Ti-Pd-Cr, i d'altres, al augmentar el grau de desordre. La supressió del pic indica la supressió de la transició martensítica, fet que ja havia estat anunciat estructuralment per la absència de twins indicada anteriorment, tant en les nostres simulacions com en els experiments.

També s'ha calculat la resposta elàstica del sistema per dos valors de l'anisotropia, i, d'acord amb experiments en Ti-Ni, la supressió de la transició martensítica resulta en un aplanament de la corba respecte la forma que presenta transició.

Els resultats anteriors ens porten a fer una anàlisi de l'energia de les estructures

obtingudes, per tal de saber si corresponen a l'equilibri termodinàmic o són estats
metaestables. L'equilibri termondinàmic ens el dóna l'energia lliure de Landau
amb presència de desordre. Així, es troba que l'energia del sistema és molt propera
a l'equilibri per valors d'anisotropia i desordre que permeten la fromació de twins,
mentre que quan s'inhibeix la seva aparició l'energia és notablement més gran que
la d'equilibri, indicant que les estructures són metaestables.

Motivats pels recents experiments en Ti-Ni que analitzen la supressió de la
transició martensítica des del punt de vista del comportament dinàmic tipus
vidriós, s'han dut a terme simulacions de l'experiment *zero-field-cooling/field-
cooling* (ZFC/FC). En aquest experiment el material se sotmet a 4 processos
consecutius: (*a*) refredament sense camp, (*b*) escalfament amb camp, (*c*) refreda-
ment amb camp i (*d*) escalfament amb camp. L'evolució de la deformació en
temperatura durant el procés (*b*) dóna lloc a la corba anomenada ZFC i l'evolució
durant el procés (*d*) s'anomena corba FC. Desviacions entre ambdues corbes (que
ocorren sempre a baix temperatura) són indicatives de dinámica congelada, i per
tant, de sistema vidriós. En el Ti-Ni, la desviació s'observa per la mateixa com-
posició que inhibeix la transició. Basat en aquest i altres experiments, els autors
etiqueten aquest tipus de sistemes com a *strain glass* (vidre de deformació).

Bàsicamet s'ha observat que en els sistemes que presenten transició estructural
abrupta amb twins correlacionant tot el sistema les corbes ZFC i FC coincideixen
en tot el seu recorregut. A mesura que la transició es va suavitztant i els twins es
comencen a trencar, la corba ZFC es comença a desviar de la FC. La desviació es-
devé significativa per valors relativament alts del desordre respecte de l'anisotropia
que porten a la supressió de la transició. Una vegada més, aquests resultats es-
tan qualitativament d'acord amb els experiments en Ti-Ni. També, és important
remarcar que la desviació entre les corbes ZFC/FC s'obté tant a l'augmentar el
desordre per sobre d'un cert llindar ζ^* com per disminuir l'anisotropia per sota
d'un cert valor crític A_3^*. Per saber si aquest comportament prové de certa frus-
tració geomètrica en el sistema hem realitzat dos càlculs. Per una banda, hem vist
que no hi ha correlacions entre les variants específiques que adopten els dominis
en els seus estats inicials. És a dir, que les variants se seleccionen de manera
aleatòria. D'altra banda, hem comprovat que en absència total de forces de llarg
abast també hi ha desviació entre les corbes ZFC i FC. D'acord amb això podem
concluir que el comportament vidriós no resulta de frustració geomètrica sinó que
és un problema més aviat cinètic.

Els valors crítics del desordre (o de l'anisotropia) que porten a la supressió de
la transició i a un congelament de les estructures són consistents entre les diferents
magnituds i simulacions que hem dut a terme: la capacitat calorífica, l'anàlisi de
la metaestabilitat de l'energia, les corbes ZFC/FC, etc. Donat que el valor de ζ^*
depèn d'A_3 i a l'inrevés, podem esbossar en l'espai de paràmetres (Anisotropia,

Desordre) la regió on s'obté comportament vidriós i la regió on s'observa transició, amb dominis tipus twin.

Finalment, s'han analitzat el comportament esforç-deformació induït per esforç. En particular, s'ha estudiat el SME i la superelasticitat per dos valors d'anisotropia i dos de desordre. Els valors específics d'aquests paràmetres són importants per determinar l'estructura fina d'aquestes corbes. S'ha trobat un ventall molt ampli de comportaments, amb canvis en els rangs de temperatura en els que s'observen l'SME i la superelasticitat, canvis en l'esforç necessari per induir o bé la transformació, o bé el creixement dels dominis de la variant seleccionada, canvis en l'àrea d'histèresi, el percentatge de recuperació de la deformació, la suavitat de les corbes, etc. Aquesta fenomenologia tan rica s'ha observat també experimentalment quan es varia la composició específica d'un aliatge en concret o es dopa amb un element addicional. Exemples en són el Ti-Ni, Au-Cd, Ti-Ni-Cu, Ni-Mn-Ga, Ni-Co-Mn-In, etc. En particular s'ha obtingut que els rangs de temperatura en els que s'observa el SME i la superelasticitat depenen no trivialment dels paràmetres.

El rang superelasitic esdevé màxim quan els valors d'anisotropia i de desordre tenen una força comparable i ni un ni l'altre dominen la dinàmica del sistema, sinó que és resultat d'un balanç entre els dos. La histèresi de la transicı'o és màxima per valors grans d'anisotropia i petits de desordre, cosa que també afavoreix una transició abrupta.

Tanmateix, s'ha obtingut que la dependència de l'esforç de transformació en funció de la temperatura, que ve descrita per l'equació de Clausius-Clapeyron, és lineal i que el pendent de la recta no depèn dels valors particulars d'anisotropia i desordre. En efecte, experiments en diversos aliatges com per exemple el Ti-Ni, Au-Cd, Ni-Mn-Ga, Cu-Zn-Al, Ni-Ga-Fe, etc. mostren que aquesta relació és lineal creixent en les martensites. S'ha de dir, no obstant, que en el cas del Ti-Ni el pendent depèn de la composició específica, fet que contradiu els nostres resultats. A la fase de baixa temperatura, l'esforç necessari per fer creixer els dominis creix a mesura que la temperatura decreix, fet que també s'observa experimentalment.

Per completar l'estudi termomecànic s'ha calculat l'efecte elastocalòric que és l'anàleg mecànic del ben conegut efecte magnetocalòric. Està relacionat amb el canvi isoterm d'entropia o amb el canvi adiabàtic de temperatura que el sistema pateix quan se li aplica o se li retira un esforç. Aquest efecte es veu augmentat en la proximitat d'una transició de fase de primer ordre, que dóna lloc a grans canvis d'entropia. En el nostre model s'observa que la forma de la corba del canvi d'entropia en funció de la temperatura canvia lleugerament al modificar la anisotropia però la magnitud del canvi d'entropia es manté pràcticament constant.

Cal mencionar que s'ha dedicat un temps a l'elaboració d'un model magnetoelàstic, que inclou graus de llibertat magnètics i elàstics que estan acoblats

entre sí, permetent fenòmens com l'efecte de memòria de forma ferromagnètic. S'utilitza la teoria micromagnètica segons la qual la magnetització evoluciona d'acord amb l'equació de Landau-Lifshitz-Gilbert, que inclou un terme de precessió i un d'amortiguació. L'energia del sistema inclou un terme d'anisotropia cristal.lina, un terme d'intercanvi, un terme magnetostàtic i un possible terme d'interacció amb un camp magnètic extern. Addicionalment s'hi afegeix un terme energètic corresponent a l'acoblament magnetoelàstic.

El terme que comporta més problemes és el magnetostàtic, ja que és no local i depèn fortament de la mida i forma del sistema. El fet que nosaltres utilitzem condicions periòdiques de contorn afavoreix un càlcul ràpid d'aquest terme a l'espai de Fourier i dóna lloc a una dinàmica realista del camp d'spins. No obstant, aquest mètode no 'aconsegueix estabilitzar una estructura de dominis, sinó que el sistema acaba evolucionant cap al monodomini, afavorit pel coeficient d'intercanvi. Com a alternativa per obtenir una estructura multidomini es disminueix notablement el coeficient d'intercanvi (que afavoreix el monodomini) i/o s'introdueix un terme que penalitzi el monodomini a mode d'efectes de forma i mida finita.

Es presenten resultats preliminars de l'evolució purament magnètica, mostrant l'aparició de vortexs, parets de Bloch, de Néel, de Bloch asimètriques, el moviment de precessió al voltant de la direcció seleccionada per l'anisotropia cristal.lina, etc.

La introducció dels graus de llibertat elàstics es duu a terme mitjançant el model purament elàstic utilitzat anteriorment. Amb aquest model ens hem quedat gairebé a les portes de poder començar a treure resultats.

Appendix A

Notes about the elastic model

A.1 Introduction to the theory of elasticity

Here some basics concepts about the theory of elasticity [154] are briefly submitted. In particular, linear elasticity deals with solid bodies regarded as continuous media that undergo small changes in shape and volume.

A.1.1 Strain and stress tensors

In general, a deformation of a body entails the displacement of any point in it. Such motion can be mathematically described by the so-called *displacement vector*, $\mathbf{u} = \mathbf{r}' - \mathbf{r}$, where $\mathbf{r}$ and $\mathbf{r}'$ refer to the position of a particular point before and after the deformation respectively. Suppose now that the distance between two very close points in the non-deformed body $dl^2 = d\mathbf{r}^2$. After the deformation, the corresponding distance will be $dl'^2 = d\mathbf{r}'^2 = (d\mathbf{r} + d\mathbf{u})^2$. Being $\mathbf{u} = \{u_i\}$ and $\mathbf{r} = \{x_i\}$ then $d\mathbf{u} = (\partial u_i/\partial x_k)\, dx_k$. Thus, dl' can be written as:

$$dl'^2 = dl^2 + 2\sum_{ik} \frac{\partial u_i}{\partial x_k} dx_i dx_k + \sum_{ikl} \frac{\partial u_i}{\partial x_k} \frac{\partial u_i}{\partial x_l} dx_k dx_l \qquad (A.1)$$

that, after some rearrangements can be rewritten as $dl'^2 = dl^2 + 2\sum_{ik} \epsilon_{ik} dx_i dx_k$ where ϵ_{ik} is the *strain tensor*, defined as:

$$\epsilon_{ik} = \frac{1}{2}\left(\frac{\partial u_i}{\partial x_k} + \frac{\partial u_k}{\partial x_i} + \sum_l \frac{\partial u_l}{\partial x_i} \frac{\partial u_l}{\partial x_k} \right) \qquad (A.2)$$

It can be easily seen that ϵ_{ik} is symmetrical and hence has only six different components. Since linear elasticity considers only small deformations, the last

term in eq. (A.2) can be neglected, so we obtain:

$$\epsilon_{ik} \simeq \frac{1}{2}\left(\frac{\partial u_i}{\partial x_k} + \frac{\partial u_k}{\partial x_i}\right) \tag{A.3}$$

Considering a general deformation e_{ij} such that $e_{ij} = \partial u_i/\partial u_j$ (and hence $\epsilon_{ij} = 1/2(e_{ij} + e_{ji})$) it is easy to see that it can be expressed as the combination of a pure strain ϵ_{ij} and a rotation ω_{ij} [16], since we can write $e_{ij} = \epsilon_{ij} + \omega_{ij}$, where $\omega_{ij} = 1/2(e_{ij} - e_{ji})$. This can be graphically seen in figure A.1. Let us consider
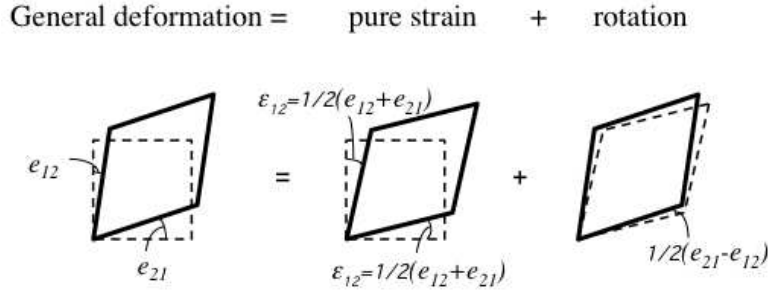
Figure A.1: A general deformation can be decomposed as the sum between a pure strain plus a rotation.

now an volume element dV of a body undergoing a deformation in absence of external body-forces[1]. Since the internal volume forces cancel by the Newton's third law, the total force $\mathbf{F} = \int \mathbf{f}dV$ acting on it can be understood as the sum of the forces acting on the surface of dV, let us say $d\mathbf{S}$. Due to the divergence theorem, $\mathbf{F}$ can be expressed as the integral of the divergence of a tensor of rank two over the surface dS delimiting dV. Thus, if f_i is the i-component of the force per unit volume,

$$f_i = \sum_k \frac{\partial \sigma_{ik}}{\partial x_k} \tag{A.4}$$

so that

$$\mathbf{F} = \int \mathbf{f}dV = \int \sum_k \frac{\partial \sigma_{ik}}{\partial x_k} d\mathbf{S} \tag{A.5}$$

where σ_{ik} is called *stress tensor*.

A.1.2 The elastic modulus tensor and the Hooke's law

The free energy of a deformed body can be written as

$$F = \frac{1}{2}\sum_{ijkl} C_{ijkl}\epsilon_{ij}\epsilon_{kl} \tag{A.6}$$

---

[1]Here *body-forces* refer to forces such as gravity, wich are volume forces that act to the whole body.

where C_{ijkl} is a tensor of rank four called *elastic modulus tensor* (or *elastic constants tensor*) that, since ϵ_{ij} is symmetrical, fulfills $C_{ijkl} = C_{jikl} = C_{ijlk} = C_{klij}$. From this it can be deduced that at the most there are only 21 different components for C_{ijkl}. This leads to an alternative notation, called *Voigt notation*, according to which only two subindices are needed: $xx \to 1$, $yy \to 2$, $zz \to 3$, $yz \to 4$, $xz \to 5$ and $xy \to 6$. This is the notation used in this thesis. In fact, for a crystal with additional symmetries, the number of components of C_{ijkl} is still reduced. For instance, cubic symmetry has only three different elastic constants, with the following corresponding energy:

$$
\begin{aligned}
F = \tfrac{1}{2}C_{xxxx}\left(\epsilon_{xx}^2 + \epsilon_{yy}^2 + \epsilon_{zz}^2\right) + C_{xxyy}(\epsilon_{xx}\epsilon_{yy} + \epsilon_{xx}\epsilon_{zz} + \epsilon_{yy}\epsilon_{zz}) \\
+ 2C_{xyxy}\left(\epsilon_{xy}^2 + \epsilon_{xz} + \epsilon_{yz}\right)
\end{aligned}
\tag{A.7}
$$

Since $\sigma_{ij} = \partial F / \partial \epsilon_{ij}$, the stress tensor is related to the strain tensor by means of the elastic contants tensor:

$$
\sigma_{ij} = \sum_{kl} \frac{\partial F}{\partial \epsilon_{ij}} C_{ijkl}\epsilon_{kl}
\tag{A.8}
$$

that is called Hooke's law[2]. Recall that this is valid only for small deformations, i.e. for linear elasticity.

A.2 Non-order parameter energy: Long-range elastic interactions

In this section we first examine in detail the compatibility constraints that link the three symmetry adapted strains and derive the specific mathematical expression for a square system in 2 dimensions. Then, we present the mathematical details that allow to convert the expression for the long-range anisotropic interactions from a nonorder parameter (nonOP), nonlocal expression in real space to a local expression in Fourier space as a function of the order parameter (OP) only. The method consists basically of taking advantage of two additional mathematical expressions linking e_1, e_2 and e_3: One is precisely the Saint Vénant compatibility equation and the another comes from energy minimization principles. This will be shown in Sec. A.2.2.

---

[2]Eq. (A.8) is the corresponding general law for a extended solid body to the well known Hooke's law for a spring, $\mathbf{F} = -k\mathbf{x}$ where k is the elastic constant of the spring. Also, the energy of a spring is $E = -\tfrac{1}{2}kx^2$, in correspondence with eq. (A.6).

A.2.1   St. Vénant compatibility conditions

The six different components of the 3-dimensional strain tensor ϵ_{ij} are not independent, since they have been defined from the underlying displacement field $\mathbf{u}$ that has only three different components, i.e. the "true" degrees of freedom. Hence, there must exist some constraints that link the different components of ϵ_{ij}. These are called St. Vénant compatibility conditions [140], that in 3 dimensions can be expressed in the following compact notation:

$$\text{Inc}\epsilon(\mathbf{r}) \equiv \nabla \times [\nabla \times \epsilon(\mathbf{r})]^\top = 0 \tag{A.9}$$

In what follows the corresponding 2D equations are deduced. Let's consider

$$d\mathbf{u} = du_x(x, y)\hat{\imath} + du_y(x, y)\hat{\jmath} \Rightarrow \mathbf{u}(\mathbf{r}) = \int_{\mathbf{r}_0}^{\mathbf{r}} d\mathbf{u} \tag{A.10}$$

Since this integral cannot depend on the contour joining $\mathbf{r}_0$ and $\mathbf{r}$:

$$du_x = \frac{\partial u_x}{\partial x}dx + \frac{\partial u_x}{\partial y}dy; \qquad \frac{\partial^2 u_x}{\partial y \partial x} = \frac{\partial^2 u_x}{\partial x \partial y} \tag{A.11}$$

and similar for u_y. Using the strain tensor notation:

$$\epsilon_{xx} = \frac{\partial u_x}{\partial x}\epsilon_{yy} = \frac{\partial u_y}{\partial y}2\epsilon_{xy} = \frac{\partial u_x}{\partial y} + \frac{\partial u_y}{\partial x} \tag{A.12}$$

$$\frac{\partial}{\partial y}\left(\frac{\partial u_x}{\partial x}\right) = \frac{\partial \epsilon_{xx}}{\partial y} = \frac{\partial}{\partial x}\left(\frac{\partial u_x}{\partial y}\right) = 2\frac{\partial \epsilon_{xy}}{\partial x} - \frac{\partial^2 u_y}{\partial x^2}$$
$$\frac{\partial}{\partial x}\left(\frac{\partial u_y}{\partial y}\right) = \frac{\partial \epsilon_{yy}}{\partial x} = \frac{\partial}{\partial y}\left(\frac{\partial u_y}{\partial x}\right) = 2\frac{\partial \epsilon_{xy}}{\partial y} - \frac{\partial^2 u_x}{\partial y^2} \tag{A.13}$$

$$\frac{\partial^2 \epsilon_{xx}}{\partial y^2} = 2\frac{\partial^2 \epsilon_{xy}}{\partial x \partial y} - \frac{\partial^2}{\partial x \partial y}\left(\frac{\partial u_y}{\partial x}\right); \qquad \frac{\partial^2 \epsilon_{yy}}{\partial x^2} = 2\frac{\partial^2 \epsilon_{xy}}{\partial x \partial y} - \frac{\partial^2}{\partial x \partial y}\left(\frac{\partial u_x}{\partial y}\right) \tag{A.14}$$

Adding the two last equations:

$$\frac{\partial^2 \epsilon_{xx}}{\partial y^2} + \frac{\partial^2 \epsilon_{yy}}{\partial x^2} = 4\frac{\partial^2 \epsilon_{xy}}{\partial x \partial y} - \frac{\partial^2}{\partial x \partial y}\underbrace{\left(\frac{\partial u_x}{\partial u_y} + \frac{\partial u_y}{\partial x}\right)}_{2\epsilon_{xy}} \tag{A.15}$$

So finally

$$\frac{\partial^2 \epsilon_{xx}}{\partial y^2} + \frac{\partial^2 \epsilon_{yy}}{\partial x^2} = 2\frac{\partial^2 \epsilon_{xy}}{\partial x \partial y} \tag{A.16}$$

This relation stablish a unique relation between ϵ and $\mathbf{u}(\mathbf{r})$. In terms of the symmetry adapted strains:

$$\frac{\sqrt{2}}{2}\left(\frac{\partial^2}{\partial x^2} + \frac{\partial^2}{\partial y^2}\right)e_1 - \frac{\sqrt{2}}{2}\left(\frac{\partial^2}{\partial x^2} - \frac{\partial^2}{\partial y^2}\right)e_2 = 2\frac{\partial^2 e_3}{\partial x \partial y} \tag{A.17}$$

A.2.2   Energy minimization

The total free energy of the pure elastic model is expressed in terms of the symmetry adapted strains e_1, e_2 and e_3:

$$F_T = F_{\text{nonOP}}(e_1(\mathbf{r}), e_3(\mathbf{r})) + F(e_2(\mathbf{r})) \tag{A.18}$$

where

$$F_{\text{nonOP}} = \int \left(\frac{A_1}{2} e_1^2(\mathbf{r}) + \frac{A_3}{2} e_3^2(\mathbf{r}) \right) d\mathbf{r} \tag{A.19}$$

Due to the elastic compatibility relation explained above, one of the strains can be expressed in terms of the other two. Since the elastic compatibility equation is a partial differential equation, the Fourier transform of eq. A.17 allows to express easily e_3 in terms of e_1 and e_2:

$$e_3(\mathbf{k}) = \frac{(k_x^2 + k_y^2)}{2\sqrt{2}k_x k_y} e_1(\mathbf{k}) - \frac{(k_x^2 - k_y^2)}{2\sqrt{2}k_x k_y} e_2(\mathbf{k}) \tag{A.20}$$

First we need to express eq. (A.19) in Fourier space and then we will be able to introduce eq. (A.20). Therefore we focus on the term $\int e_1^2(\mathbf{r}) d\mathbf{r}$: Making the inverse Fourier transform of $e_1(\mathbf{r})$ we can express it as a function of $e_1(\mathbf{k})$: $e_1(\mathbf{r}) = 1/(2\pi)^2 \int e^{i\mathbf{k}\cdot\mathbf{r}} e_1(\mathbf{k}) d\mathbf{k}$. Thus, the integral can be expressed as:

$$\int e_1^2(\mathbf{r}) d\mathbf{r} = \frac{1}{(2\pi)^4} \int d\mathbf{r} \int e^{i\mathbf{k}\cdot\mathbf{r}} e_1(\mathbf{k}) d\mathbf{k} \int e^{i\mathbf{k}'\cdot\mathbf{r}} e_1(\mathbf{k}') d\mathbf{k}'$$

$$= \frac{1}{(2\pi)^4} \int e_1(\mathbf{k}) d\mathbf{k} \int e_1(\mathbf{k}') d\mathbf{k}' \int e^{i(\mathbf{k}+\mathbf{k}')\cdot\mathbf{r}} d\mathbf{r} \tag{A.21}$$

$$= \frac{1}{(2\pi)^4} \int e_1(\mathbf{k}) d\mathbf{k} \int e_1(\mathbf{k}') d\mathbf{k}' (2\pi)^2 \delta(\mathbf{k}+\mathbf{k}') = \frac{1}{(2\pi)^2} \int e_1(\mathbf{k}) e_1(-\mathbf{k}) d\mathbf{k},$$

and similarly for the integral $\int e_3(\mathbf{r}) d\mathbf{r}$. Then, eq. (A.19) can be expressed as:

$$F_{\text{nonOP}} = \frac{A_1}{2} \frac{1}{(2\pi)^2} \int e_1(\mathbf{k}) e_1(-\mathbf{k}) d\mathbf{k} + \frac{A_3}{2} \frac{1}{(2\pi)^2} \int e_3(\mathbf{k}) e_3(-\mathbf{k}) d\mathbf{k} \tag{A.22}$$

Now we introduce eq. (A.20):

$$F_{\text{nonOP}} = \frac{1}{(2\pi)^2} \int \left[\frac{A_1}{2} e_1(\mathbf{k}) e_1(-\mathbf{k}) + \frac{A_3}{2} \left(\frac{(k_x^2+k_y^2)}{2\sqrt{2}k_x k_y} e_1(\mathbf{k}) - \frac{(k_x^2-k_y^2)}{2\sqrt{2}k_x k_y} e_2(\mathbf{k}) \right) \cdot \right.$$

$$\left. \cdot \left(\frac{(k_x^2+k_y^2)}{2\sqrt{2}k_x k_y} e_1(-\mathbf{k}') - \frac{(k_x^2-k_y^2)}{2\sqrt{2}k_x k_y} e_2(-\mathbf{k}) \right) \right] d\mathbf{k} \tag{A.23}$$

Since $e_1(\mathbf{k})$ is a complex variable we can do $e_1(\mathbf{k}) = x(\mathbf{k}) + iy(\mathbf{k})$. Then, $e_1(-\mathbf{k}) = e^*(\mathbf{k}) = x(\mathbf{k}) - iy(\mathbf{k})$ and $e_1(\mathbf{k}) e_1(-\mathbf{k}) = x^2(\mathbf{k}) + y^2(\mathbf{k})$. Rearranging terms, we can rewrite the energy this way:

$$F_{\text{nonOP}} = \int \left[\frac{1}{(2\pi)^2} \left(\frac{A_1}{2} + \frac{A_3}{16} \frac{(k_x^2+k_y^2)^2}{k_x^2 k_y^2} \right) (x^2(\mathbf{k}) + y^2(\mathbf{k})) \right.$$

$$\left. - \frac{1}{(2\pi)^2} \frac{A_3}{16} \frac{(k_x^2+k_y^2)(k_x^2-k_y^2)}{k_x^2 k_y^2} ((x(\mathbf{k}) + iy(\mathbf{k})) e_2(-\mathbf{k}) + (x(\mathbf{k}) - iy(\mathbf{k})) e_2(\mathbf{k})) \right] d\mathbf{k} + g(e_2)$$

$$\tag{A.24}$$

where $g(e_2) = \frac{1}{(2\pi)^2}\frac{A_3}{16}\int \frac{(k_x^2 - k_y^2)^2}{(k_x k_y)^2}e_2(\mathbf{k})e_2(-\mathbf{k})d\mathbf{k}$ is a function which depends only on e_2. To simplify this expression we define the following functions:

$$Q_2(\mathbf{k}) \equiv \frac{1}{(2\pi)^2}\frac{A_1}{2} + \frac{A_3}{16}\frac{(k_x^2 + k_y^2)^2}{k_x^2 k_y^2}; \qquad Q_3(\mathbf{k}) \equiv -\frac{1}{(2\pi)^2}\frac{A_3}{16}\frac{(k_x^2 + k_y^2)(k_x^2 - k_y^2)}{k_x^2 k_y^2}$$

$$(A.25)$$

Using these definitions we can write the energy as follows:

$$F_{\text{nonOP}} = \int [Q_2(\mathbf{k})\left(x^2(\mathbf{k}) + y^2(\mathbf{k})\right) + Q_3(\mathbf{k})\left((x(\mathbf{k}) + iy(\mathbf{k}))e_2(-\mathbf{k})\right.$$
$$\left. +(x(\mathbf{k}) - iy(\mathbf{k}))e_2(\mathbf{k}))\right]d\mathbf{k} + g(e_2)$$

$$(A.26)$$

Now we have the energy in terms only of e_1 and e_2. Considering that e_1 evolves in such a way that minimizes the free energy, we proceed to minimize the previous expression with respect to e_1. Consequently, we will be able to express e_1 in terms of e_2. In order to do that we have to minimize the energy with respect to the real (x) and imaginary part (y) of e_1:

$$\delta F_{\text{nonOP}} = \int \frac{\partial F_{\text{nonOP}}}{\partial e_1(\mathbf{k}")}\delta e_1(\mathbf{k}")d\mathbf{k}" = \int \left[\frac{\partial F_{\text{nonOP}}}{\partial x(\mathbf{k}")}\delta x(\mathbf{k}") + \frac{\partial F_{\text{nonOP}}}{\partial y(\mathbf{k}")}\delta y(\mathbf{k}")\right]d\mathbf{k}" = 0$$

$$(A.27)$$

Doing so, and taking into account that $\partial g(e_2)/\partial e_1 = 0$ we get

$$\delta F_{\text{nonOP}} = \int d\mathbf{k}" \int d\mathbf{k}\{[2Q_2(\mathbf{k})x(\mathbf{k}) + Q_3(\mathbf{k})\left(e_2(-\mathbf{k}) + e_2(\mathbf{k})\right)]\delta(\mathbf{k} - \mathbf{k}")\delta x(\mathbf{k}")$$
$$+ [2Q_2(\mathbf{k})y(\mathbf{k}) + iQ_3(\mathbf{k})\left(e_2(-\mathbf{k}) - e_2(\mathbf{k})\right)]\delta(\mathbf{k} - \mathbf{k}")\delta y(\mathbf{k}")\}$$

$$(A.28)$$

First, $e_2(-\mathbf{k}) + e_2(\mathbf{k}) = 2\Re(e_2(\mathbf{k}))$ and $i\left(e_2(-\mathbf{k}) + e_2(\mathbf{k})\right) = 2\Im(e_2(\mathbf{k}))$. Second, the $\delta(\mathbf{k} - \mathbf{k}")$ will anihilate the integral over $\mathbf{k}$. As $\delta x(\mathbf{k}")$ and $\delta y(\mathbf{k}")$ are any variation of the respective variables and $\delta F_{\text{nonOP}} = 0$, the coeficients of these variations must vanish separately, i.e.:

$$2Q_2(\mathbf{k})x(\mathbf{k}) + 2Q_3(\mathbf{k})\Re(e_2(\mathbf{k})) = 0$$
$$2Q_2(\mathbf{k})y(\mathbf{k}) + 2Q_3(\mathbf{k})\Im(e_2(\mathbf{k})) = 0$$

$$(A.29)$$

where we have renamed the remaining variable ($\mathbf{k}"$) as $\mathbf{k}$. Now, we can isolate $x(\mathbf{k})$ and $y(\mathbf{k})$:

$$x(\mathbf{k}) = \frac{-Q_3(\mathbf{k})\Re(e_2(\mathbf{k}))}{Q_2(\mathbf{k})}; \qquad y(\mathbf{k}) = \frac{-Q_3(\mathbf{k})\Im(e_2(\mathbf{k}))}{Q_2(\mathbf{k})}$$

$$(A.30)$$

Since $e_1(\mathbf{k}) = x(\mathbf{k}) + iy(\mathbf{k})$ we can write:

$$e_1(\mathbf{k}) = \frac{-Q_3(\mathbf{k})\Re(e_2(\mathbf{k}))}{Q_2(\mathbf{k})} + i\frac{-Q_3(\mathbf{k})\Im(e_2(\mathbf{k}))}{Q_2(\mathbf{k})}$$
$$= -\frac{Q_3(\mathbf{k})}{Q_2(\mathbf{k})}\left(\Re(e_2(\mathbf{k})) + i\Im(e_2(\mathbf{k}))\right) = -\frac{Q_3(\mathbf{k})}{Q_2(\mathbf{k})}e_2(\mathbf{k})$$

$$(A.31)$$

Finally, we can write the contribution of the non-order parameter to the total energy in terms of the desired variable e_2 as:

$$F_{\text{nonOP}} = \int [Q_2 e_1(\mathbf{k}) e_1(-\mathbf{k}) + Q_3 \left(e_1(\mathbf{k}) e_2(-\mathbf{k}) + e_1(-\mathbf{k}) e_2(\mathbf{k})\right)] d\mathbf{k}$$
$$+ \frac{1}{(2\pi)^2} \frac{A_3}{16} \int \frac{(k_x^2 - k_y^2)^2}{(k_x k_y)^2} e_2(\mathbf{k}) e_2(-\mathbf{k}) d\mathbf{k} \tag{A.32}$$

$$= \int \left[\frac{Q_3^2(\mathbf{k})}{Q_2(\mathbf{k})} e_2(\mathbf{k}) e_2(-\mathbf{k}) - 2 \frac{Q_3^2(\mathbf{k})}{Q_2(\mathbf{k})} e_2(\mathbf{k}) e_2(-\mathbf{k}) + \frac{1}{(2\pi)^2} \frac{A_3}{16} \frac{(k_x^2 - k_y^2)^2}{(k_x k_y)^2} e_2(\mathbf{k}) e_2(-\mathbf{k}) \right] d\mathbf{k} \tag{A.33}$$

$$= \int \left(-\frac{Q_3^2(\mathbf{k})}{Q_2(\mathbf{k})} + \frac{1}{(2\pi)^2} \frac{A_3}{16} \frac{(k_x^2 - k_y^2)^2}{(k_x k_y)^2} \right) e_2(\mathbf{k}) e_2(-\mathbf{k}) d\mathbf{k} \tag{A.34}$$

Taking into account the defintions of $Q_j(\mathbf{k})$, $j = 2, 3$, and simplifying terms, we get the final expression for the non-order parameter contribution to the energy:

$$F_{\text{nonOP}} = \frac{1}{(2\pi)^2} \frac{A_3}{2} \int \frac{\left(k_x^2 - k_y^2\right)^2}{\left(8 k_x^2 k_y^2 + \frac{A_3}{A_1}(k_x^2 + k_y^2)^2\right)} e_2(\mathbf{k}) e_2(-\mathbf{k}) d\mathbf{k} \tag{A.35}$$

A.3 Numerical details

For completeness, in Sec. A.3.1 we present the discretized expressions for the free energy that we have used for numerical computation. Moreover, from these expressions we have been able to calculate the functional derivatives of the free energy that are required for the pure relaxational dynamics used in the model. According to this dynamics, $\frac{\partial e_2}{\partial t} = -\frac{\delta F_T}{\delta e_2}$, where $F_T = F_L + F_G + F_{\text{nonOP}} + F_\eta$. This is done in Sec. A.3.2. Finally, in Sec. A.3.3 we present the mathematical method used to build the disorder function, which is Gaussian distributed and it is spatially correlated by means of a exponential pair correlation function.

A.3.1 Discretization of the free energy

We recall that F_L, F_G and F_{nonOP} stand for the Landau, Ginzburg and non-order parameter energetic contributions respectively. In the following expressions we will use i, j, k, l, m, n for real space variables and p, q for Fourier variables.

$$F_L = \sum_{i=1}^{N_x} a \sum_{j=1}^{N_y} a \left(\frac{A_2}{2} e_2^2(i, j) - \frac{\beta}{4} e_2^4(i, j) + \frac{\gamma}{6} e_2^6(i, j) \right) \tag{A.36}$$

$$F_G = \frac{\kappa}{2} \sum_{i=1}^{N_x} a \sum_{j=1}^{N_y} a \left(\left(\frac{e_2(i+1, j) - e_2(i, j)}{a} \right)^2 + \left(\frac{e_2(i, j+1) - e_2(i, j)}{a} \right)^2 \right) \tag{A.37}$$

$$F_{\text{nonOP}} = \frac{1}{(2\pi)^2} \frac{1}{2} \sum_{p=0}^{N_x-1} \frac{2\pi}{aN_x} \sum_{q=0}^{N_y-1} \frac{2\pi}{aN_y} A_3 \frac{\left(\left(\frac{2\pi}{aN_x}p\right)^2 - \left(\frac{2\pi}{aN_y}q\right)^2\right)^2 e_2(p,q)e_2(-p,-q)}{\frac{A_3}{A_1}\left(\left(\frac{2\pi}{aN_x}p\right)^2 + \left(\frac{2\pi}{aN_y}q\right)^2\right)^2 + 8\left(\frac{2\pi}{aN_x}p\frac{2\pi}{aN_y}q\right)^2}$$

$$(A.38)$$

Moreover, the discretization of the phenomenologic surface potential F_S used in Sec. ?? leads to:

$$F_S = C_s \sum_{i=1}^{N_x} a \sum_{q=0}^{N_y-1} \frac{2\pi}{aN_y} \frac{1}{\frac{2\pi}{aN_y}|q|} e_2(i,q)e_2(i,-q) \qquad (A.39)$$

A.3.2 Relaxational dynamics: Energy derivatives

Landau term:

$$\frac{\delta F_L}{\delta e_2(k,l)} = a^2 \sum_{i=1}^{N_x} \sum_{j=1}^{N_y} \left(A_2 e_2(i,j)\delta_{i,k}\delta_{j,l} - \beta e_2(i,j)^3\delta_{i,k}\delta_{j,l} + \gamma e_2(i,j)^5\delta_{i,k}\delta_{j,l}\right)$$
$$= a^2 \left(A_2 e_2(k,l) - \beta e_2(k,l)^3 + \gamma e_2(k,l)^5\right)$$

$$(A.40)$$

Ginzburg energy:

$$\frac{\delta F_G}{\delta e_2(k,l)} = a^2 \frac{\kappa}{2} \sum_{i=1}^{N_x} \sum_{j=1}^{N_y} \left(\frac{2}{a^2}\left(e_2(i+1,j) - e_2(i,j)\right)\left(\delta_{i+1,k}\delta_{j,l} - \delta_{i,k}\delta_{j,l}\right)\right.$$
$$\left. +\frac{2}{a^2}\left(e_2(i,j+1) - e_2(i,j)\right)\left(\delta_{i,k}\delta_{j+1,l} - \delta_{i,k}\delta_{j,l}\right)\right)$$
$$= \kappa\left(4e_2(k,l) - e_2(k+1,l) - e_2(k-1,l) - e_2(k,l+1) - e_2(k,l-1)\right)$$

$$(A.41)$$

Long-range anisotropic energy:

$$\frac{\delta F_{\text{nonOP}}}{\delta e_2(\mathbf{r})} = \frac{1}{(2\pi)^2} \sum_{p=0}^{N_x-1} \sum_{q=0}^{N_y-1} \frac{1}{2}\left(\frac{2\pi}{aN_x}\right)\left(\frac{2\pi}{aN_y}\right) U(\mathbf{k})\left(\frac{\partial e_2(\mathbf{k})}{\partial e_2(\mathbf{r})}e_2^*(\mathbf{k}) + e_2(\mathbf{k})\frac{\partial e_2^*(\mathbf{k})}{\partial e_2(\mathbf{r})}\right)$$
$$= \frac{1}{(2\pi)^2} \sum_{p=0}^{N_x-1} \sum_{q=0}^{N_y-1} \frac{1}{2}\left(\frac{2\pi}{aN_x}\right)\left(\frac{2\pi}{aN_y}\right) U(\mathbf{k})\cdot$$
$$\cdot\left[\frac{\partial}{\partial e_2(\mathbf{r})}\left(\sum_{\mathbf{r}'} a^2 e^{i\mathbf{k}\cdot\mathbf{r}'}e_2(\mathbf{r}')\right)e_2^*(\mathbf{k}) + e_2(\mathbf{k})\frac{\partial}{\partial e_2(\mathbf{r})}\left(\sum_{\mathbf{r}''} a^2 e^{-i\mathbf{k}\cdot\mathbf{r}''}e_2(\mathbf{r}'')\right)\right]$$
$$= \frac{1}{(2\pi)^2} \sum_{p=0}^{N_x-1} \sum_{q=0}^{N_y-1} \frac{1}{2}\left(\frac{2\pi}{aN_x}\right)\left(\frac{2\pi}{aN_y}\right) U(\mathbf{k})\cdot$$
$$\cdot\left[\left(\sum_{\mathbf{r}'} a^2 e^{i\mathbf{k}\cdot\mathbf{r}'}\delta_{\mathbf{r},\mathbf{r}'}\right)e_2^*(\mathbf{k}) + e_2(\mathbf{k})\left(\sum_{\mathbf{r}''} a^2 e^{i\mathbf{k}\cdot\mathbf{r}''}\delta_{\mathbf{r},\mathbf{r}''}\right)\right]$$
$$= \frac{1}{(2\pi)^2} \sum_{p=0}^{N_x-1} \sum_{q=0}^{N_y-1} \frac{1}{2}\left(\frac{2\pi}{aN_x}\right)\left(\frac{2\pi}{aN_y}\right) U(\mathbf{k})\cdot\left(a^2 e^{i\mathbf{k}\cdot\mathbf{r}}e_2^*(\mathbf{k}) + e_2(\mathbf{k})a^2 e^{-i\mathbf{k}\cdot\mathbf{r}}\right)$$
$$= \frac{a^2}{(2\pi)^2} \sum_{p=0}^{N_x-1} \sum_{q=0}^{N_y-1} \frac{1}{2}\left(\frac{2\pi}{aN_x}\right)\left(\frac{2\pi}{aN_y}\right) e^{i\mathbf{k}\cdot\mathbf{r}}U(\mathbf{k})e_2^*(\mathbf{k})$$
$$+ \frac{a^2}{(2\pi)^2} \sum_{p=0}^{N_x-1} \sum_{q=0}^{N_y-1} \frac{1}{2}\left(\frac{2\pi}{aN_x}\right)\left(\frac{2\pi}{aN_y}\right) e^{-i\mathbf{k}\cdot\mathbf{r}}U(\mathbf{k})e_2(\mathbf{k}),$$

$$(A.42)$$

where we have used the notation $\delta_{\mathbf{r},\mathbf{r}'} = \delta_{i,k}\delta_{j,l}$, with $\mathbf{r} = (i,j)$ and $\mathbf{r}' = (k,l)$ and $\delta_{i,k}$ is the usual Kronecker delta. We have also used $\mathbf{k} = (p,q)$ and

$$U(\mathbf{k}) = U(p,q) = A_3 \frac{\left(\left(\frac{2\pi}{aN_x}p\right)^2 - \left(\frac{2\pi}{aN_y}q\right)^2\right)^2}{\frac{A_3}{A_1}\left(\left(\frac{2\pi}{aN_x}p\right)^2 + \left(\frac{2\pi}{aN_y}q\right)^2\right)^2 + 8\left(\frac{2\pi}{aN_x}p\frac{2\pi}{aN_y}q\right)^2} \tag{A.43}$$

Since $U(\mathbf{k}) = U(-\mathbf{k})$ and $e_2^*(\mathbf{k}) = e_2(-\mathbf{k})$ we make the change of variables $\mathbf{k} \to -\mathbf{k}$ in the first summation so that the two summations become identical:

$$\frac{\delta F_{\text{nonOP}}}{\delta e_2(i,j)} = \frac{a^2}{(2\pi)^2}\sum_{p=0}^{N_x-1}\sum_{q=0}^{N_y-1}\left(\frac{2\pi}{aN_x}\right)\left(\frac{2\pi}{aN_y}\right)e^{-i(p,q)\cdot(i,j)}U(p,q)e_2(p,q)$$
$$= a^2\mathsf{F}^{-1}\left[U(\mathbf{k})\phi(\mathbf{k});\mathbf{k}\right], \tag{A.44}$$

where F^{-1} stands for the inverse Fourier transform with respect the variable $\mathbf{k}$. We recall that $e_2(i,j)$ and $e_2(p,q)$ belong to real and Fourier space respectively.

Finally, we calculate in a very similar way the derivatives of the phenomenologic potential F_{S}. We denote $g(k_y) = g(q) = \frac{1}{\frac{2\pi}{aN_y}|q|}$

$$\frac{\delta F_{\text{S}}}{\delta e_2(x,y)} = C_s \sum_{i=1}^{N_x} a \sum_{q=0}^{N_y-1}\frac{2\pi}{aN_y}g(k_y)\left(\frac{\partial e_2(x',k_y)}{\partial e_2(x,y)}e_2(x',-k_y) + e_2(x',k_y)\frac{\partial e_2(x',-k_y)}{\partial e_2(x,y)}\right)$$
$$= C_s \sum_{i=1}^{N_x} a \sum_{q=0}^{N_y-1}\frac{2\pi}{aN_y}g(k_y)\left[\frac{\partial}{\partial e_2(x,y)}\left(\sum_{y'}ae^{ik_yy'}e_2(x',y')\right)e_2(x',-k_y)\right.$$
$$\left.+e_2(x',k_y)\frac{\partial}{\partial e_2(x,y)}\left(\sum_{y''}ae^{-ik_yy''}e_2(x',y'')\right)\right]$$
$$= C_s \sum_{i=1}^{N_x} a \sum_{q=0}^{N_y-1}\frac{2\pi}{aN_y}g(k_y)\left[\left(\sum_{y'}ae^{ik_yy'}\delta_{x,x'}\delta_{y,y'}\right)e_2(x',-k_y)\right.$$
$$\left.+e_2(x',k_y)\left(\sum_{y''}ae^{-ik_yy''}\delta_{x,x'}\delta_{y,y''}\right)\right]$$
$$= C_s a \sum_{q=0}^{N_y-1}\frac{2\pi}{aN_y}g(k_y)\left[ae^{ik_yy}e_2(x,-k_y) + e_2(x,k_y)ae^{-ik_yy}\right]$$
$$= C_s a \sum_{q=0}^{N_y-1}\frac{2\pi}{aN_y}g(k_y)ae^{ik_yy}e_2(x,-k_y) + C_s a \sum_{q=0}^{N_y-1}\frac{2\pi}{aN_y}g(k_y)e_2(x,k_y)ae^{-ik_yy}$$
$$\tag{A.45}$$

We now make the change of variables $k_y \to k_y$ in the first summation. Taking into account that $g(k_y) = g(-k_y)$ we get the final expression:

$$\frac{\delta F_{\text{S}}}{\delta e_2(m,n)} = C_s a \sum_{q=0}^{N_y-1}\frac{2\pi}{aN_y}g(q)ae^{-iqn}e_2(m,q) = C_s a 2\pi\mathsf{F}^{-1}[g(q)e_2(m,q);q] \tag{A.46}$$

Since the coefficient C_s is arbitrary, it can absorb the other remaining factors.

A.3.3   Spatially correlated quenched-in disorder

A random variable $\eta\left(\mathbf{r}\right)$ Gaussian distributed and spatially correlated by means of an exponential pair correlation function is desired. That is to say, mathematically:

$$\langle\eta(\mathbf{r})\eta(\mathbf{r}')\rangle = G(|\mathbf{r}-\mathbf{r}'|) = \frac{A}{2\pi\lambda^2}e^{-|\mathbf{r}-\mathbf{r}'|/\lambda}$$

and $g(\eta) = \frac{1}{\sqrt{2\pi}\zeta}e^{-\frac{\eta^2}{2\zeta^2}}$ where ζ stands for the standard deviation of the Gaussian distribution. Then, $\eta(\mathbf{r})$ may be built as follows:

$$\eta(\mathbf{k}) = \alpha\sqrt{G(\mathbf{k})} \tag{A.47}$$

where α is a random variable Gaussian distributed with zero mean and unit variance, i.e. $g(\alpha) = N(0,1)$ and $G(\mathbf{k})$ is the Fourier transform of $G(|\mathbf{r}-\mathbf{r}'|)$. The inverse Fourier transform provides $\eta(\mathbf{r})$ with the required characteristics[3].
This can be easily seen since the autocorrelation is $G(0) = \langle\eta(\mathbf{r})^2\rangle = \frac{A}{2\pi\lambda^2}$. Then, since $\langle\eta(\mathbf{r})\rangle = 0$, $\zeta = \sqrt{\langle\eta(\mathbf{r})^2\rangle - \langle\eta(\mathbf{r})\rangle^2} = \sqrt{\frac{A}{2\pi\lambda^2}}$.

---

[3]The way of generating a random variable of such characteristics (eq. A.47) can be generalized to any distribution and pair correlation function [204].

Appendix B

Notes about the magnetoelastic model

B.1 Discrete Fourier transform

We have seen that the magnetoelastic model involves three long-range energetic contributions, coming from the pure elastic, pure magnetic and magnetoelastic energies. The nonlocal character of these terms is given through the fact that the particular value of the deviatoric strain/magnetization at each point of the body depends on the configuration of the strain/magnetization in the whole body. This entails the computation of a double integral, that is of the order of N^2, where N is the number of the unit cells of the simulation cell. It is unacceptable from the point of view of the computation time. Luckily, the order of N^2 can be reduced to $N \log N$ by reformulating the nonlocal expressions in real space as local expressions in Fourier space. However, the numerical implementation of the Fourier expressions may be nontrivial due to the discretization process. In the case of the pure elastic long-range interactions, the particular expression fulfills some symmetry properties that make avoid any problem and therefore, this has not been commented previously. Instead, in the case of long-range interactions coming from the magnetoelastic coupling term as well as the magnetostatic field, Fourier transforms caused these unexpected problems that made us reformulate the method of computing such terms. In the first two sections of this appendix we analyze these numerical problems. In this section we define the discrete Fourier transform and show that there are some properties of the continuous Fourier transform that may be extrapolated to discrete space only under certain conditions. In the second section we approach the discrete computation of the magnetostatic field.

First of all, we define the continuous Fourier transform in one dimension for

simplicity, although it can be easily rewritten in more dimensions.

$$\mathsf{F}\left[f(x);k\right] \equiv f(k) \equiv \int_{-\infty}^{\infty} e^{-ikx} f(x)dx \tag{B.1}$$

and its inverse

$$\mathsf{F}^{-1}\left[f(k);x\right] \equiv f(x) \equiv \frac{1}{2\pi} \int_{-\infty}^{\infty} e^{ikx} f(k)dk \tag{B.2}$$

However, for numerical purposes we work in a discrete real space, consisting of N cells, whose positions may be defined as: $x = aj$; $\quad j = 0\ldots, N-1$ where a is the discretization parameter. Here, since N is finite, the Fourier transform automatically imposes periodic boundary conditions. Then, in real space, the *total system* consists of an infinite number of copies of the *simulation cell*, that in turn contains N *unit cells*. The corresponding reciprocal space is infinite, with a discrete set of k values, taking the values $k = \frac{2\pi}{L}l$; $\quad l = 0, \ldots,$ where $L = aN$ is the size of the simulation cell. However, the relevant information can be restricted to the First Brillouin Zone, from which the whole Fourier space can be reproduced. Then, the relevant values for k are $k = \frac{2\pi}{L}l$; $\quad l = 0, \ldots, N-1$.

In this framework, we will associate j variable with real space and l variable with the reciprocal space. Now let us define the discretized Fourier transform as:

$$\mathsf{F}\left[f(j);l\right] \equiv f(l) \equiv \sum_{j=0}^{N-1} e^{-i\frac{2\pi}{N}lj} f(j)a \tag{B.3}$$

and its inverse

$$\mathsf{F}^{-1}\left[f(l);j\right] \equiv f(j) \equiv \frac{1}{L} \sum_{l=0}^{N-1} e^{i\frac{2\pi}{N}lj} f(l) \tag{B.4}$$

Once defined these transformations, we are prepared to check rigorously a couple of properties of the continuous Fourier transform in discretized form.

B.1.1   Fourier transform of a shifted function

If we make a simple change of variables $x = x' + b$ and we introduce it in the definition of the Fourier transform we get:

$$\mathsf{F}\left[f(x);k\right] \equiv f(k) = \int_{-\infty}^{\infty} e^{-ik(x'+b)} f(x'+b)dx' = e^{-ikb} \int_{-\infty}^{\infty} e^{-ikx'} f(x'+b)dx' \tag{B.5}$$

where we can rename x' as x. On the other hand, according to the definition eq. (B.1) we have:

$$\mathsf{F}\left[f(x+b);k\right] \equiv \int_{-\infty}^{\infty} e^{-ikx} f(x+b)dx \tag{B.6}$$

Comparing last two equations we have that

$$\mathsf{F}\left[f(x+b);k\right] = e^{ikb}\mathsf{F}\left[f(x);k\right] \tag{B.7}$$

We now verify whether this relation is also fulfilled in discretized form: Proceeding the same way, first we make the change of variables $j = j' + n$: We can do that as n successives changes of variables $j = j' + 1$, so let us do it with this last change of variables:

$$
\begin{aligned}
f(l) = e^{-i\frac{2\pi}{N}l}(\sum_{j'=-1}^{N-2} e^{-i\frac{2\pi}{N}lj'}f(j'+1))a = e^{-i\frac{2\pi}{N}l}\sum_{j'=0}^{N-2} e^{-i\frac{2\pi}{N}lj'}f(j'+1) \\
+ e^{i\frac{2\pi}{N}l}f(0) + e^{-i\frac{2\pi}{N}l(N-1)}f(N) - e^{-i\frac{2\pi}{N}l(N-1)}f(N))a
\end{aligned}
\tag{B.8}
$$

Taking into account periodic boundary conditions, we have that $f(0) = f(N)$, and we get

$$f(l) = e^{-i\frac{2\pi}{N}l}a\sum_{j'=0}^{N-1} e^{-i\frac{2\pi}{N}lj'}f(j'+1) + af(N)(1 - e^{-i2\pi l}) \tag{B.9}$$

As $e^{-i2\pi l} = 1 \ \forall l \in \mathbb{Z}$, last term vanishes and we get:

$$f(l) = e^{-i\frac{2\pi}{N}l}a\sum_{j'=0}^{N-1} e^{-i\frac{2\pi}{N}lj'}f(j'+1) \tag{B.10}$$

Being

$$\mathsf{F}\left[f(j+1);l\right] = a\sum_{j'=0}^{N-1} e^{-i\frac{2\pi}{N}lj'}f(j'+1) \tag{B.11}$$

we get the relation we were looking for:

$$\mathsf{F}\left[f(j+1);l\right] = e^{i\frac{2\pi}{N}l}f(l) \tag{B.12}$$

that is the discretized form of eq. (B.7), for $b = 1$. Note that it is valid when shifting the function to another positions belonging to the discrete space, but it is not valid when the function is shifted to a position out of the discrete space, for instance $j = j' + n/2$. It occurs, for example, when computing first derivatives of a discrete function with forward or backward differences. In these cases, derivatives are computed in the middle points between two nearest neighbours, i.e. out of the discrete lattice, and, if dealing in Fourier space, they cannot be shifted to the original lattice by means of this relation. We find this kind of problem when computing the divergence of the magnetization in order to get the magnetostatic field.

B.1.2 Fourier transform of a derivative

Again we will show a problem arising when computing derivatives with finite differences methods. These are only approximations of first (forward and backward differences), second (centered differences) or higher order in a taylor expansion to the continuous derivatives. Hence, this feature makes that the well known property of the continuous fourier transform of a derivative,

$$\mathsf{F}[\partial_x f(x); k] = ikf(k) \tag{B.13}$$

is strictly not valid in discretized form, but only an approximation. Let us see it for the case when computing a first derivative with forward differences. We define:

$$\frac{\partial f(j)}{\partial j} \equiv \frac{f(j+1) - f(j)}{a} \tag{B.14}$$

Hence,

$$\mathsf{F}\left[\frac{\partial f(j)}{\partial j}; l\right] = \frac{1}{a}\left(\mathsf{F}\left[f(j+1); l\right] - \mathsf{F}\left[f(j); l\right]\right) \tag{B.15}$$

As we have seen above, we can express the first Fourier transform as:

$$\mathsf{F}\left[f(j+1); l\right] = e^{i\frac{2\pi}{N}l}f(l) \tag{B.16}$$

so we get:

$$\mathsf{F}\left[\frac{\partial f(j)}{\partial j}; l\right] = \frac{1}{a}f(l)\left(e^{i\frac{2\pi}{N}l} - 1\right) \tag{B.17}$$

Comparing with eq. (B.13), where $k = \frac{2\pi}{L}l$ we have:

$$\frac{1}{a}\left(e^{i\frac{2\pi}{N}l} - 1\right) = i\frac{2\pi}{L}l \Rightarrow e^{i\frac{2\pi}{N}l} = 1 + i\frac{2\pi}{N}l \tag{B.18}$$

One can see that this is just a Taylor expansion up to the first order of the exponential function, valid for $\frac{2\pi}{L}l \ll 1 \rightarrow l \ll 1$, that means long wave lengths, that is an approximation to the continuum. Indeed, the continuum does not allow sharp changes in f (in our case the magnetization, for instance an antiferromagnetic configuration) but they have to be smooth (the interfaces must have a certain width).

B.2 Magnetostatic energy

B.2.1 Mathematical expressions for the magnetostatic energy

The computation of the magnetostatic term has been object of intense research due to its intrinsic difficulty. It may be expressed in multiple ways, each one

giving rise to its own range of ways to solve it. We have explored some of them in order to get a general overview and thus criterium to decide which one is the most convenient in each case. Here we review some analytical and numerical aspects concerning this term. From $\mathbf{B} = \mu_0(\mathbf{H}+\mathbf{M})$ and from Maxwell equation $\nabla \cdot \mathbf{B} = 0$, we get $\nabla \cdot \mathbf{H} = -\nabla \cdot \mathbf{M}$. From Maxwell equation $\nabla \times \mathbf{H} = 0$, we get $\mathbf{H} = -\nabla \phi$ Then, we obtain the so-called the Poisson equation:

$$\Delta \phi = \nabla \cdot \mathbf{M} \tag{B.19}$$

This is the equation we have to solve. Once we have ϕ, by means of eq. (B.33) we get H_d and hence we get the magnetostatic energy. To solve eq. (B.19) we will go into Fourier space. Making use of the property $\mathsf{F}\left[\partial_x f(x)\right] = ikf(k)$ this equation transforms into:

$$\phi(\mathbf{k}) = -iM_s \frac{k_x m_x(\mathbf{k}) + k_y m_y(\mathbf{k}) + k_z m_z(\mathbf{k})}{k_x^2 + k_y^2 + k_z^2} \tag{B.20}$$

Using $\mathbf{H} = -\nabla\phi$ and eq. (B.20) we can rewrite the magnetostatic energy this way:

$$F_{\mathrm{ms}} = -\tfrac{1}{2}\mu_0 \int \mathbf{H}_d(\mathbf{r})\mathbf{M}(\mathbf{r})d\mathbf{r}$$

$$= \tfrac{1}{2}\mu_0 \int \left(\tfrac{\partial\phi(\mathbf{r})}{\partial x}M_x(\mathbf{r}) + \tfrac{\partial\phi(\mathbf{r})}{\partial y}M_y(\mathbf{r}) + \tfrac{\partial\phi(\mathbf{r})}{\partial z}M_z(\mathbf{r}) \right) d\mathbf{r}$$

$$= \tfrac{1}{2}\mu_0 \int d\mathbf{r}(M_x(\mathbf{r})\tfrac{\partial}{\partial x}\int e^{i\mathbf{kr}}\phi(\mathbf{k})d\mathbf{k} + M_y(\mathbf{r})\tfrac{\partial}{\partial y}\int e^{i\mathbf{kr}}\phi(\mathbf{k})d\mathbf{k}$$

$$+M_z(\mathbf{r})\tfrac{\partial}{\partial z}\int e^{i\mathbf{kr}}\phi(\mathbf{k})d\mathbf{k})$$

$$= \tfrac{i}{2}\mu_0 \int d\mathbf{r}(M_x(\mathbf{r})\int k_x e^{i\mathbf{kr}}\phi(\mathbf{k})d\mathbf{k} + M_y(\mathbf{r})\int k_y e^{i\mathbf{kr}}\phi(\mathbf{k})d\mathbf{k}$$

$$+M_z(\mathbf{r})\int k_z e^{i\mathbf{kr}}\phi(\mathbf{k})d\mathbf{k})$$

$$= \tfrac{i}{2}\mu_0 \int d\mathbf{k}\phi(\mathbf{k})(k_x \int M_x(\mathbf{r})e^{i\mathbf{kr}}d\mathbf{r} + k_y \int M_y(\mathbf{r})e^{i\mathbf{kr}}d\mathbf{r} + k_z \int M_z(\mathbf{r})e^{i\mathbf{kr}}d\mathbf{r})$$

$$= \tfrac{i}{2}\mu_0 \int d\mathbf{k}\phi(\mathbf{k}) \left(k_x M_x(-\mathbf{k}) + k_y M_y(-\mathbf{k}) + k_z M_z(-\mathbf{k}) \right)$$

$$= \tfrac{\mu_0}{2} \int d\mathbf{k}\phi(\mathbf{k})\phi(-\mathbf{k}) \left(k_x^2 + k_y^2 + k_z^2 \right) = \tfrac{\mu_0}{2} \int d\mathbf{k}|\phi(\mathbf{k})|^2 (\mathbf{k}^2)$$

$$\tag{B.21}$$

or

$$F_{\mathrm{ms}} = \frac{\mu_0}{2} \int d\mathbf{k}\frac{|k_x M_x(\mathbf{k}) + k_y M_y(\mathbf{k}) + k_z M_z(\mathbf{k})|^2}{\left(k_x^2 + k_y^2 + k_z^2\right)} = \frac{\mu_0}{2} \int d\mathbf{k}|\mathbf{M}(\mathbf{k})\frac{\mathbf{k}}{k}|^2 \quad \text{(B.22)}$$

This expression for the magnetostatic energy shows two important features: $F_{\mathrm{ms}} \geq 0$ always and F_{ms} only depends on the direction of $\mathbf{k}$, not on its modulus. F_{ms} will vanish if the magnetization is perpendicular to the modulations, no matter wich wave length have. Then, the ground state will be a single domain because the exchange term prefers no interfaces. This scheme changes when dealing with non periodic boundary conditions.

B.2.2   Computation of the magnetostatic field

There are several ways to solve it, as for example by means of finite differences method. Doing things this way we can find two main problems, one of storage and another of computation speed. Let's discuss it. In discrete form, using finite differences the eq. (B.19) takes the following form:

$$
\begin{aligned}
\phi(i+1,j) &+ \phi(i-1,j) + \phi(i,j+1) \\
&+ \phi(i,j-1) - 4\phi(i,j) \\
= \tfrac{1}{a}(M_x(i+1,j) &- M_x(i,j) + M_y(i,j+1) - M_y(i,j))
\end{aligned}
\tag{B.23}
$$

We will have such an equation for every (i,j), so we will have $N_x \times N_y$ equations. We can express this array of equations as a matrix equation: $Ax = b$ where A is a matrix and b and x are vectors. In our case, $b \equiv \nabla \cdot \mathbf{M}$ and $x \equiv \phi$ so they are vectors of size $N_x \times N_y$. A represents the Δ operator and has a size of $(N_x \times N_y) \times (N_x \times N_y)$. Here we find the first problem: the size of the matrix A becomes too large for sizes of the system of our interest (for instance, $N_x = N_y = 512$). There is a way of avoiding this problem. The point is that A has only a small amount of non-zero matrix elements (sparse matrix), so we only have to store them. Once we have $Ax = b$, a way of solving this equation is doing $x = A^{-1}b$ but we cannot compute the inverse A^{-1} because this is not a sparse matrix but has many non-zero matrix elements and hence we cannot store them. The way of solving this problem is to find the solution of the matrix equation not by computing A^{-1} but with iterative methods, like the *biconjugate gradient method* or the *successive overrelaxation with Chevishev acceleration* [162]. These iterative methods involve too large computation times for our interests, so we will not use them.

As we have already said, we will solve the eq. (B.19) in Fourier space. Following [133] we can do that as explained in eq. (B.20) but this way we find the following problem with the k in the first Brillouin zone border: since $\phi(\mathbf{r})$ is real, due to the properties of the fourier transform, $\Re[\phi(\mathbf{k})]$ must be even and $\Im[\phi(\mathbf{k})]$ must be odd. Obviously, we also know that $\mathbf{M}(\mathbf{r})$ is real, so $\Re[\mathbf{M}(\mathbf{k})]$ is even and $\Im[\mathbf{M}(\mathbf{k})]$ is odd. Then, we construct ϕ with $\mathbf{M}(\mathbf{k})$ and $\mathbf{k}$ from eq. (B.20). $f(\mathbf{k}) = \mathbf{k}$ is of course an odd function, so $\mathbf{M}(\mathbf{k}) \cdot \mathbf{k}$ will have the real part odd and the imaginary part even. Then, multiplying it by i we will have what we wanted, that is the real part even and the imaginary odd. Let's write this matematically:

$$
\mathbf{M}(\mathbf{r}) \in \mathbb{R} \;\; \Rightarrow \;\;
\begin{cases}
\Re[\mathbf{M}(-\mathbf{k})] = \Re[\mathbf{M}(\mathbf{k})] \\
\Im[\mathbf{M}(-\mathbf{k})] = -\Im[\mathbf{M}(\mathbf{k})]
\end{cases}
\Rightarrow
\begin{cases}
\Re[\mathbf{M}(-\mathbf{k})(-\mathbf{k})] = -\Re[\mathbf{M}(\mathbf{k})\mathbf{k}] \\
\Im[\mathbf{M}(-\mathbf{k})(-\mathbf{k})] = \Im[\mathbf{M}(\mathbf{k})\mathbf{k}]
\end{cases}
\tag{B.24}
$$

$$\Rightarrow \quad \begin{cases} \Re[i\mathbf{M}(-\mathbf{k})(-\mathbf{k})] = \Re[i\mathbf{M}(\mathbf{k})\mathbf{k}] \\ \Im[i\mathbf{M}(-\mathbf{k})(-\mathbf{k})] = -\Im[i\mathbf{M}(\mathbf{k})\mathbf{k}] \end{cases} \tag{B.25}$$

Then,

$$\phi = -i\frac{\mathbf{M}(\mathbf{k})\mathbf{k}}{\mathbf{k}^2} \Rightarrow \begin{cases} \Re[\phi(-\mathbf{k})] = \Re[\phi(\mathbf{k})] \\ \Im[\phi(-\mathbf{k})] = -\Im[\phi(\mathbf{k})] \end{cases} \Rightarrow \quad \phi(\mathbf{r}) \in \mathbb{R} \tag{B.26}$$

that is what we want. It only shows us that everything is consistent. Problems arise when we discretize these expressions and impose periodic boundary conditions. At the border of the first Brillouin zone. At $k_x = \pi/a$, for instance, we know from the eq. (B.20) that

$$\phi(\mathbf{k}) = -iM_s\frac{\frac{\pi}{a}m_x(\mathbf{k}) + k_y m_y(\mathbf{k})}{\left(\frac{\pi}{a}\right)^2 + k_y^2} \tag{B.27}$$

and at $k_x = -\pi/a$

$$\phi(\mathbf{k}) = -iM_s\frac{-\frac{\pi}{a}m_x(\mathbf{k}) + k_y m_y(\mathbf{k})}{\left(\frac{\pi}{a}\right)^2 + k_y^2} \tag{B.28}$$

$\Rightarrow \quad \phi(-\pi/a, k_y) \neq \phi(\pi/a, k_y)$, but periodic boundary conditions imply that $\phi(-\pi/a, k_y) = \phi(\pi/a, k_y)$, so we have a problem. The way to solve it, is making the term $M_x k_x$ vanish at $k_x = \pm\pi/a$. Similarly, the term $M_y k_y$ must vanish at $k_y = \pm\pi/a$. It is like averaging the $\mathbf{k}_{max}$ contribution and it makes that the magnetostatic field due to this modulation is not well computed. This kind of problem always arises when dealing with odd functions of $\mathbf{k}$ and periodic boundary conditions. We will find it again when computing the magnetoelastic term.

A way of avoiding this problem is to compute first the $\nabla \cdot \mathbf{M}(\mathbf{r})$ in real space and then to compute the fourier transform of it. Then, the scalar potential can be written as:

$$\phi(\mathbf{k}) = -\frac{\mathsf{F}\left[\nabla \cdot \mathbf{M}(\mathbf{r})\right]}{k_x^2 + k_y^2} \tag{B.29}$$

This way we do not have to compute any odd function of $\mathbf{k}$ but we find the same kind of problem but in real space. Using forward differences,

$$\nabla \cdot \mathbf{M}(\mathbf{r}) = \frac{1}{a}(m_x(i+1, j) - m_x(i, j) + m_y(i, j+1) - m_y(i, j)) \tag{B.30}$$

The problem is that $\partial_x m_x(\mathbf{r})$ and $\partial_y m_y(\mathbf{r})$ are computed in different middle points of the lattice ($(i + 1/2, j)$ and $(i, j + 1/2)$ respectively). Of course with backward differences we would find the same problem. Then, we are multiplying and adding things at differents points like they were at the same. Because of that, the two different (but obviously equivalent) ways to compute F_{ms}, shown in eq. (6.4), do not give the same result. As explained in the appendix, we cannot use phase factors in fourier space to shift these points ($(i + 1/2, j)$ and $(i, j + 1/2)$) to the

original lattice (i, j) precisely because these points do not belong to the lattice, i.e. the shifted length is not a whole number but a half $((i + b, j)$ can be shifted to (i, j) if and only if $b \in \mathbb{Z}$).

The simplest way of solving it, is computing $\nabla \cdot \mathbf{M}(\mathbf{r})$ with centered differences, so this way we will compute both derivatives at the same point, but we will not be able to distinguish modulations corresponding to the shortest wave length possible in the system, i.e. the maximum $\mathbf{k}$. We then find the same problem we had when computing ϕ with eq. (B.20). Due to that we will use another way to compute $\nabla \cdot \mathbf{M}(\mathbf{r})$ in real space, that avoids each problem of forward and centered differences. This is the way used by Berkov *et al.* [205] and consists in what follows: if we consider, for instance, that our spins are located at the nodes of our lattice, i.e. at the corners of our cells, $\nabla \cdot \mathbf{M}(\mathbf{r})$ is computed in the center of the cells as an average of the derivatives of the magnetization at the corresponding four corners of that cell, like being a source or a sink of magnetization in its corners. Matematically, it can be expressed like this:

$$
\begin{aligned}
(\nabla \cdot \mathbf{M}(i, j)) \left(i - \tfrac{1}{2}, j - \tfrac{1}{2}\right) = -\tfrac{1}{2a}(m_x(i, j) \\
-m_x(i - 1, j) + m_x(i, j - 1) - m_x(i - 1, j - 1) \\
+m_y(i, j) - m_y(i, j - 1) + m_y(i - 1, j) - m_y(i - 1, j - 1))
\end{aligned}
\tag{B.31}
$$

This way we will calculate the scalar potential also at the center of the cells (points $(i - \tfrac{1}{2}, j - \tfrac{1}{2})$). Using the same definition in eq. (B.33) in order to compute the magnetostatic field at the corners of the cells (points (i, j)), where the magnetization is located, we get:

$$
\begin{aligned}
H_{d_x}(i, j) = -\tfrac{1}{2a}(\phi(i + \tfrac{1}{2}, j + \tfrac{1}{2}) - \phi(i - \tfrac{1}{2}, j + \tfrac{1}{2}) \\
+ \phi(i + \tfrac{1}{2}, j - \tfrac{1}{2}) + \phi(i - \tfrac{1}{2}, j - \tfrac{1}{2})) \\
H_{d_y}(i, j) = -\tfrac{1}{2a}(\phi(i + \tfrac{1}{2}, j + \tfrac{1}{2}) - \phi(i + \tfrac{1}{2}, j - \tfrac{1}{2}) \\
+ \phi(i - \tfrac{1}{2}, j + \tfrac{1}{2}) + \phi(i - \tfrac{1}{2}, j - \tfrac{1}{2}))
\end{aligned}
\tag{B.32}
$$

Then, whatever definition we use to compute F_{ms} in eq. (6.4) we get the same result because we are always multiplying factors at the same points of the lattice and, hence, doing things in the right way.

B.2.3 The demagnetizing factor

A general solution for eq. B.19 is [47]:

$$
\phi(\mathbf{r}) = \frac{M_s}{4\pi} \left[\int_V \frac{-\nabla \cdot \mathbf{m}(\mathbf{r}')}{|\mathbf{r} - \mathbf{r}'|} dV' + \int_S \frac{\mathbf{m}(\mathbf{r}') \cdot \mathbf{n}(\mathbf{r}')}{|\mathbf{r} - \mathbf{r}'|} dS' \right]
\tag{B.33}
$$

where $\mathbf{n}$ is a vector perpendicular to the surface. The first and the second terms correspond to the contribution due to the volume and surface charge densities respectively ($\nabla \cdot \mathbf{m}$ and $\mathbf{m} \cdot \mathbf{n}$ may be considered 'magnetic charges'). An alternative method to solve eq. (B.19) is in Fourier space, as done in eq. (B.20). However, this equation is useful only to solve the volume part, since the surface part corresponds to the contribution of $\mathbf{k} = 0$ and it is a singularity in eq. (B.20). In other words, we may separate the magnetizing in two different contributions: $\mathbf{M}(\mathbf{r}) = \overline{\mathbf{M}} + \delta \mathbf{M}(\mathbf{r})$, where $\overline{\mathbf{M}}$ stands for the average magnetization of the system and $\delta \mathbf{M}(\mathbf{r})$ corresponds to the local variations with respect to $\overline{\mathbf{M}}$. In Fourier space we are only able to compute the demagnetizing field due to the heterogeneous part $\delta \mathbf{M}(\mathbf{r})$.

When the magnetization is uniform in the whole body, $\nabla \cdot \mathbf{m}(\mathbf{r}) = 0$ and the first term in eq. (B.33) vanishes. Then, by using $\mathbf{H} = -\nabla \phi$, the demagnetizing field due to the remaining term can be expressed as $\mathbf{H}_\mathrm{d}(\mathbf{r}) = \mathbf{N}(\mathbf{r} - \mathbf{r}')M(\mathbf{r}')$, where $\mathbf{N}(\mathbf{r} - \mathbf{r}')$ is a tensor called 'demagnetizing factor', that consists of an integral over the surface of the body that only depends on its shape. For certain regular shapes, like ellipses, it has an analytical expression.

This reasoning may be also applied independently to each cell of the system [206, 207]. Indeed, a coarse-grained lattice often consists of an array of cells whithin which the magnetization is assumed to be uniform. Hence, we may compute the demagnetizing factor $\mathbf{N}$ for each cell. If the cells are of equal shape, as it is often the case[1] we have to compute $\mathbf{N}$ only once, and then deduce $\mathbf{H}_\mathrm{d}$ from $\mathbf{H}_\mathrm{d}(\mathbf{r}) = \sum_{\mathbf{r}'} \mathbf{N}(\mathbf{r} - \mathbf{r}')\mathbf{M}(\mathbf{r}')$, where the sum is over all the cells of the system. This is a convolution (order N^2 in computation time) that, if using periodic boundary conditions, can be transformed to a scalar product in Fourier space (order $N \log N$).

B.3 Non-order parameter energy: Long-range elastic and magnetoelastic interactions

In the pure elastic model, long-range interactions arose from applying the Saint Vénant compatibility equation and energy minimization to the non-order parameter symmetry adapted strains e_1 and e_3. In the magnetoelastic model, in addition to the pure elastic contribution, the magnetoelastic coupling contains an additional contribution of e_1 and e_3. This entails that the energy minimization with respect to e_1 wich is carried out after applying the compatibility constraint must be recalculated in order to incorporate the magnetoelastic term. Here we give the

---

[1]This is not the case of finite elements method.

mathematical details of the calculation. Actually, we shall see that the dependence of e_1 and e_3 with respect to the OP e_2 is the same as in the pure elastic model. We will derive also the mathematical expression for the magnetoelastic coupling in Fourier space.

Since we will be interested in deriving $F_{\mathrm{me}} + F\mathrm{el}$ with respect to e_1 in order to minimize the free energy, we focus only on the non-OP contribution, i.e. terms containing only e_1 and e_3. From now on, we will make explicit wether the strain variables belong to the real ($\mathbf{r}$) or Fourier ($\mathbf{k}$) space, since we will deal with both spaces. Instead, the magnetization $\mathbf{m}$ will remain in the real space all the time. However, for the sake of clarity, we also will make explicit its dependence. Thus, we recover the mathematical expression for the non-order parameter free energy:

$$F_{\mathrm{nonOP}} = \int \left[\frac{B_1}{\sqrt{2}} (m_x^2(\mathbf{r}) + m_y^2(\mathbf{r})) e_1(\mathbf{r}) + B_2 m_x(\mathbf{r}) m_y(\mathbf{r}) e_3(\mathbf{r}) \right.$$
$$\left. + \frac{A_1}{2} e_1^2(\mathbf{r}) + \frac{A_3}{2} e_3^2(\mathbf{r}) \right] d\mathbf{r} \tag{B.34}$$

We now rewrite the Saint-Vénant compatibility equation in Fourier space and express e_3 in terms of e_1 and e_2:

$$e_3(\mathbf{k}) = \frac{(k_x^2 + k_y^2)}{2\sqrt{2}k_x k_y} e_1(\mathbf{k}) - \frac{(k_x^2 - k_y^2)}{2\sqrt{2}k_x k_y} e_2(\mathbf{k}) \tag{B.35}$$

Then, we introduce this expression for e_3 in the non-OP contribution F_{nonOP} [eq. (B.34)] that, consequently, will become a function only of e_1 and the OP e_2.

$$F_{\mathrm{nonOP}} = \int \left[\frac{B_1}{\sqrt{2}} (m_x^2(\mathbf{r}) + m_y^2(\mathbf{r})) e_1(\mathbf{r}) + \frac{A_1}{2} e_1^2(\mathbf{r}) \right.$$
$$+ B_2 m_x(\mathbf{r}) m_y(\mathbf{r}) \frac{1}{(2\pi)^2} \int e^{i\mathbf{k}\mathbf{r}} e_3(\mathbf{k}) d\mathbf{k}$$
$$\left. + \frac{A_3}{2} \frac{1}{(2\pi)^4} \int e^{i\mathbf{k}\mathbf{r}} e_3(\mathbf{k}) d\mathbf{k} \int e^{i\mathbf{k'}\mathbf{r}} e_3(\mathbf{k'}) d\mathbf{k'} \right] d\mathbf{r} \tag{B.36}$$

$$= \int \left[\frac{B_1}{\sqrt{2}} \left(m_x^2(\mathbf{r}) + m_y^2(\mathbf{r}) \right) e_1(\mathbf{r}) + \frac{A_1}{2} e_1^2(\mathbf{r}) \right.$$
$$+ m_x(\mathbf{r}) m_y(\mathbf{r}) \frac{B_2}{(2\pi)^2} \int e^{i\mathbf{k}\mathbf{r}} \left(\frac{(k_x^2+k_y^2)}{2\sqrt{2}k_x k_y} e_1(\mathbf{k}) - \frac{(k_x^2-k_y^2)}{2\sqrt{2}k_x k_y} e_2(\mathbf{k}) \right) d\mathbf{k}$$
$$+ \frac{A_3}{2(2\pi)^4} \int e^{i\mathbf{k}\mathbf{r}} \left(\frac{(k_x^2+k_y^2)}{2\sqrt{2}k_x k_y} e_1(\mathbf{k}) - \frac{(k_x^2-k_y^2)}{2\sqrt{2}k_x k_y} e_2(\mathbf{k}) \right) d\mathbf{k} \cdot$$
$$\left. \cdot \int e^{i\mathbf{k'}\mathbf{r}} \left(\frac{(k_x'^2+k_y'^2)}{2\sqrt{2}k_x' k_y'} e_1(\mathbf{k'}) - \frac{(k_x'^2-k_y'^2)}{2\sqrt{2}k_x' k_y'} e_2(\mathbf{k'}) \right) d\mathbf{k'} \right] d\mathbf{r} \tag{B.37}$$

Now we make fourier transforms of $e_1(\mathbf{r})$, i.e. $e_1(\mathbf{r}) = 1/(2\pi)^2 \int e^{ikr} e_1(\mathbf{k}) d\mathbf{k}$ and change the order of the integrals. As in Sec. A.2.2 we also use the fact that

$\int e^{i\mathbf{r}(\mathbf{k}+\mathbf{k}')}d\mathbf{r} = (2\pi)^2\delta(\mathbf{k}+\mathbf{k}')$. As $e_1(\mathbf{k})$ is a complex variable we can do $e_1(\mathbf{k}) = x(\mathbf{k}) + iy(\mathbf{k})$, and, rearranging terms, we can rewrite the energy this way:

$$F_{\text{nonOP}} = \int \left[\frac{1}{(2\pi)^2} \left(\frac{B_1}{\sqrt{2}} \int e^{i\mathbf{k}\mathbf{r}}(m_x^2(\mathbf{r}) + m_y^2(\mathbf{r}))d\mathbf{r} \right. \right.$$
$$\left. + B_2 \int e^{i\mathbf{k}\mathbf{r}}m_x(\mathbf{r})m_y(\mathbf{r})d\mathbf{r}\frac{(k_x^2+k_y^2)}{2\sqrt{2}k_xk_y} \right) (x(\mathbf{k})+iy(\mathbf{k}))$$
$$+ \frac{1}{(2\pi)^2}\left(\frac{A_1}{2} + \frac{A_3}{16}\frac{(k_x^2+k_y^2)^2}{k_x^2k_y^2} \right)(x^2(\mathbf{k})+y^2(\mathbf{k})) \qquad \text{(B.38)}$$
$$- \frac{1}{(2\pi)^2}\frac{A_3}{16}\frac{(k_x^2+k_y^2)(k_x^2-k_y^2)}{k_x^2k_y^2}\left((x(\mathbf{k})+iy(\mathbf{k}))e_2(-\mathbf{k}) \right.$$
$$\left. \vphantom{\frac{1}{1}} + (x(\mathbf{k})-iy(\mathbf{k}))e_2(\mathbf{k})) \right] d\mathbf{k} + F_{\text{nonOP}}(e_2)$$

where $F_{\text{nonOP}}(e_2)$ is a function depending only on e_2. To simplify this expression we define the following functions:

$$Q_1(\mathbf{k}) \equiv \frac{1}{(2\pi)^2}\int e^{i\mathbf{k}\mathbf{r}}\left(\frac{B_1}{\sqrt{2}}(m_x^2(\mathbf{r})+m_y^2(\mathbf{r})) + \frac{B_2}{2\sqrt{2}}\frac{(k_x^2+k_y^2)}{k_xk_y}m_x(\mathbf{r})m_y(\mathbf{r}) \right)d\mathbf{r}$$
$$Q_2(\mathbf{k}) \equiv \frac{1}{(2\pi)^2}\left(\frac{A_1}{2} + \frac{A_3}{16}\frac{(k_x^2+k_y^2)^2}{k_x^2k_y^2} \right) \qquad \text{(B.39)}$$
$$Q_3(\mathbf{k}) \equiv -\frac{1}{(2\pi)^2}\frac{A_3}{16}\frac{(k_x^2+k_y^2)(k_x^2-k_y^2)}{k_x^2k_y^2}$$

Using these definitions we can rewrite the energy as follows:

$$F_{\text{nonOP}} = \int [Q_1(\mathbf{k})(x(\mathbf{k})+iy(\mathbf{k})) + Q_2(\mathbf{k})(x^2(\mathbf{k})+y^2(\mathbf{k}))$$
$$+ Q_3(\mathbf{k})((x(\mathbf{k})+iy(\mathbf{k}))e_2(-\mathbf{k}) + (x(\mathbf{k})-iy(\mathbf{k}))e_2(\mathbf{k}))] d\mathbf{k} + F_{\text{nonOP}}(e_2) \qquad \text{(B.40)}$$

So now we have the energy in terms only of e_1 and e_2. As we only want to perform simulations of e_2 we will minimize the energy with respect to e_1, so we will be able to express e_1 in terms of e_2. In order to do that we have to minimize the energy with respect to the real (x) and imaginary part (y) of e_1:

$$\delta F_{\text{nonOP}} = \int \frac{\partial F_{\text{nonOP}}}{\partial e_1(\mathbf{k}")}\delta e_1(\mathbf{k}")d\mathbf{k}"$$
$$= \int \left[\frac{\partial F_{\text{nonOP}}}{\partial x(\mathbf{k}")}\delta x(\mathbf{k}") + \frac{\partial F_{\text{nonOP}}}{\partial y(\mathbf{k}")}\delta y(\mathbf{k}") \right] d\mathbf{k}" = 0 \qquad \text{(B.41)}$$

Now we carry out these derivatives. Note that $\partial F_{\text{nonOP}}(e_2)/\partial e_1 = 0$. We get

$$\delta F_{\text{nonOP}} = \int d\mathbf{k}"\int d\mathbf{k}\{[Q_1(\mathbf{k}) + 2Q_2(\mathbf{k})x(\mathbf{k})$$
$$+ Q_3(\mathbf{k})(e_2(-\mathbf{k}) + e_2(\mathbf{k}))] \delta(\mathbf{k}-\mathbf{k}")\delta x(\mathbf{k}") \qquad \text{(B.42)}$$
$$+ [iQ_1(\mathbf{k}) + 2Q_2(\mathbf{k})y(\mathbf{k}) + iQ_3(\mathbf{k})(e_2(-\mathbf{k}) - e_2(\mathbf{k}))] \delta(\mathbf{k}-\mathbf{k}")\delta y(\mathbf{k}")\}$$

First, $e_2(-\mathbf{k}) + e_2(\mathbf{k}) = 2\Re(e_2(\mathbf{k}))$ and $i(e_2(-\mathbf{k}) + e_2(\mathbf{k}) = 2\Im(e_2(\mathbf{k}))$. Second, the $\delta(\mathbf{k}-\mathbf{k}")$ will anihilate the integral over $\mathbf{k}$. As $\delta x(\mathbf{k}")$ and $\delta y(\mathbf{k}")$ are any variation

of the respective variables and $\delta F_{nop} = 0$, the coeficients of these variations must vanish independently, i.e.:

$$Q_1(\mathbf{k}) + 2Q_2(\mathbf{k})x(\mathbf{k}) + 2Q_3(\mathbf{k})\Re(e_2(\mathbf{k})) = 0 \qquad (B.43)$$

$$iQ_1(\mathbf{k}) + 2Q_2(\mathbf{k})y(\mathbf{k}) + 2Q_3(\mathbf{k})\Im(e_2(\mathbf{k})) = 0 \qquad (B.44)$$

where we have renamed the remaining variable ($\mathbf{k}$") as $\mathbf{k}$. Now, we can isolate $x(\mathbf{k})$ and $y(\mathbf{k})$:

$$x(\mathbf{k}) = \frac{-Q_1(\mathbf{k}) - 2Q_3(\mathbf{k})\Re(e_2(\mathbf{k}))}{2Q_2(\mathbf{k})} \qquad (B.45)$$

$$y(\mathbf{k}) = \frac{-iQ_1(\mathbf{k}) - 2Q_3(\mathbf{k})\Im(e_2(\mathbf{k}))}{2Q_2(\mathbf{k})} \qquad (B.46)$$

As $e_1(\mathbf{k}) = x(\mathbf{k}) + iy(\mathbf{k})$ we can write:

$$e_1(\mathbf{k}) = \frac{-Q_1(\mathbf{k}) - 2Q_3(\mathbf{k})\Re(e_2(\mathbf{k}))}{2Q_2(\mathbf{k})} + i\frac{-iQ_1(\mathbf{k}) - 2Q_3(\mathbf{k})\Im(e_2(\mathbf{k}))}{2Q_2(\mathbf{k})}$$

$$= \frac{1}{2Q_2(\mathbf{k})}\left[-Q_1(\mathbf{k}) - 2Q_3(\mathbf{k})\Re(e_2(\mathbf{k})) + Q_1(\mathbf{k}) - 2iQ_3(\mathbf{k})\Im(e_2(\mathbf{k}))\right] \qquad (B.47)$$

$$= -\frac{Q_3(\mathbf{k})}{Q_2(\mathbf{k})}\left(\Re(e_2(\mathbf{k})) + i\Im(e_2(\mathbf{k}))\right) = -\frac{Q_3(\mathbf{k})}{Q_2(\mathbf{k})}e_2(\mathbf{k})$$

that is the same result that we obtained for the pure elastic case, i.e. without taking into account the magnetoelastic coupling. Finally, we can write the contribution of the non-order parameter to the total energy in terms of the desired variables $\mathbf{m}$ and e_2 as:

$$F_{\text{nonOP}} = \int[Q_1 e_1(\mathbf{k}) + Q_2 e_1(\mathbf{k})e_1(-\mathbf{k}) + Q_3\left(e_1(\mathbf{k})e_2(-\mathbf{k}) + e_1(-\mathbf{k})e_2(\mathbf{k})\right)]d\mathbf{k}$$

$$-\frac{1}{(2\pi)^2}\frac{B_2}{2\sqrt{2}}\int\frac{(k_x^2 - k_y^2)}{k_x k_y}e_2(\mathbf{k})d\mathbf{k}\int e^{i\mathbf{k}\mathbf{r}}m_x(\mathbf{r})m_y(\mathbf{r})d\mathbf{r} + \frac{1}{(2\pi)^2}\frac{A_3}{16}\int\frac{(k_x^2 - k_y^2)^2}{(k_x k_y)^2}e_2(\mathbf{k})e_2(-\mathbf{k})d\mathbf{k}$$

$$\qquad (B.48)$$

$$= \int\left[-\frac{Q_3(\mathbf{k})Q_1(\mathbf{k})}{Q_2(\mathbf{k})}e_2(\mathbf{k}) + \frac{Q_3^2(\mathbf{k})}{Q_2(\mathbf{k})}e_2(\mathbf{k})e_2(-\mathbf{k}) - 2\frac{Q_3^2(\mathbf{k})}{Q_2(\mathbf{k})}e_2(\mathbf{k})e_2(-\mathbf{k})\right.$$

$$\left. +\frac{1}{(2\pi)^2}\frac{A_3}{16}\frac{(k_x^2 - k_y^2)^2}{(k_x k_y)^2}e_2(\mathbf{k})e_2(-\mathbf{k}) - \frac{1}{(2\pi)^2}\frac{B_2}{2\sqrt{2}}\frac{(k_x^2 - k_y^2)}{k_x k_y}e_2(\mathbf{k})\int e^{i\mathbf{k}\mathbf{r}}m_x(\mathbf{r})m_y(\mathbf{r})d\mathbf{r}\right]d\mathbf{k}$$

$$\qquad (B.49)$$

$$= \int\left[\left(-\frac{Q_3^2(\mathbf{k})}{Q_2(\mathbf{k})} + \frac{1}{(2\pi)^2}\frac{A_3}{16}\frac{(k_x^2 - k_y^2)^2}{(k_x k_y)^2}\right)e_2(\mathbf{k})e_2(-\mathbf{k})\right.$$

$$\left. -\left(\frac{Q_3(\mathbf{k})Q_1(\mathbf{k})}{Q_2(\mathbf{k})} + \frac{1}{(2\pi)^2}\frac{B_2}{2\sqrt{2}}\frac{(k_x^2 - k_y^2)}{k_x k_y}\int e^{i\mathbf{k}\mathbf{r}}m_x(\mathbf{r})m_y(\mathbf{r})d\mathbf{r}\right)e_2(\mathbf{k})\right]d\mathbf{k}$$

$$\qquad (B.50)$$

Taking into account the defintions of $Q_j(\mathbf{k})$, $j = 1, 2, 3$, and simplifying terms, we get the final expression for the non-order parameter contribution to the energy:

$$F_{\text{nonOP}} = \frac{1}{(2\pi)^2}\int\frac{\left(k_x^2 - k_y^2\right)}{\left(8k_x^2 k_y^2 + \frac{A_3}{A_1}(k_x^2 + k_y^2)^2\right)}\left\{\frac{A_3\left(k_x^2 - k_y^2\right)}{2}e_2(\mathbf{k})e_2(-\mathbf{k})\right.$$

$$+\left[\frac{A_3\left(k_x^2 + k_y^2\right)}{A_1}\frac{B_1}{\sqrt{2}}\int e^{i\mathbf{k}\mathbf{r}}\left(m_x^2(\mathbf{r}) + m_y^2(\mathbf{r})\right)d\mathbf{r}\right. \qquad (B.51)$$

$$\left.\left. -8k_x k_y\frac{B_2}{2\sqrt{2}}\int e^{i\mathbf{k}\mathbf{r}}\left(m_x(\mathbf{r})m_y(\mathbf{r})\right)d\mathbf{r}\right]e_2(\mathbf{k})\right\}d\mathbf{k}$$

The first term coincides with the long-range interaction obtained in the pure elastic case and the second one is an extra contribution due to the magnetoelastic coupling. To simplify expressions we will use the following definitions:

$$A_{c_1}(\mathbf{k}) \equiv \frac{A_3\left(k_x^2 - k_y^2\right)\left(k_x^2 + k_y^2\right)}{A_1\left(8k_x^2 k_y^2 + \frac{A_3}{A_1}(k_x^2 + k_y^2)^2\right)}$$

$$A_{c_2}(\mathbf{k}) \equiv \frac{A_3\left(k_x^2 - k_y^2\right)^2}{2\left(8k_x^2 k_y^2 + \frac{A_3}{A_1}(k_x^2 + k_y^2)^2\right)} \tag{B.52}$$

$$A_{c_3}(\mathbf{k}) \equiv -\frac{8\left(k_x^2 - k_y^2\right)k_x k_y}{\left(8k_x^2 k_y^2 + \frac{A_3}{A_1}(k_x^2 + k_y^2)^2\right)}$$

Therefore, the non-OP free energy can be written as follows:

$$F_{\mathrm{nonOP}} = \frac{1}{(2\pi)^2} \int \Bigg\{ A_{c_2}(\mathbf{k}) e_2(\mathbf{k}) e_2(-\mathbf{k}) + \Bigg[A_{c_1}(\mathbf{k}) \frac{B_1}{\sqrt{2}} \int e^{i\mathbf{k}\mathbf{r}} \left(m_x^2(\mathbf{r}) + m_y^2(\mathbf{r}) \right) d\mathbf{r}$$
$$+ A_{c_3}(\mathbf{k}) \frac{B_2}{2\sqrt{2}} \int e^{i\mathbf{k}\mathbf{r}} \left(m_x(\mathbf{r}) m_y(\mathbf{r}) \right) d\mathbf{r} \Bigg] e_2(\mathbf{k}) \Bigg\} d\mathbf{k}$$

$$\tag{B.53}$$

B.4 Magnetoelastic dynamics

The dynamics of the magnetoelastic model concerns the evolution of both the magnetization $\mathbf{m}$ and the deviatoric strain e_2. As mentioned in Chap. 6, the former evolves according to the LLG equation and the latter according to a pure relaxational dynamics. Since the dynamic equations lead to the configuration of $\mathbf{m}(\mathbf{r})$ and $e_2(\mathbf{r})$ that minimize of the total energy, both equations involve functional derivatives of the energy with respect to the corresponding variable. Here we give the mathematical details of the calculation of such derivatives.

B.4.1 Magnetic dynamics

We can rewrite eq. 6.9 in a dimensionless form [133]:

$$\frac{\partial \mathbf{m}}{\partial \tau} = -\mathbf{m} \times \mathbf{h}_{\mathrm{eff}} - \alpha \mathbf{m} \times (\mathbf{m} \times \mathbf{h}_{\mathrm{eff}}) \tag{B.54}$$

where

$$\mathbf{h}_{\mathrm{eff}} = \frac{\mathbf{H}_{\mathrm{eff}}}{M_s}; \qquad \tau = \frac{\gamma_0 M_s}{1 + \alpha^2} t \tag{B.55}$$

From energy minimization arguments, it can be deduced that $\mathbf{h}_{\mathrm{eff}}$ can be expressed as [208]

$$\mathbf{h}_{\mathrm{eff}} = -\frac{1}{\mu_0} \frac{\partial F}{\partial \mathbf{M}} = -\frac{1}{\mu_0 M_s} \frac{\partial F}{\partial \mathbf{m}} \tag{B.56}$$

where $\frac{\partial F}{\partial \mathbf{m}} = \left(\frac{\partial F}{\partial m_x}, \frac{\partial F}{\partial m_y}, \frac{\partial F}{\partial m_z}\right)$. Introducing eq. 6.1 we get

$$
\begin{aligned}
\mathbf{h}_{\text{eff}} &= -\frac{1}{\mu_0 M_s}\left(\frac{\partial F_{\text{an}}}{\partial \mathbf{m}} + \frac{\partial F_{\text{exch}}}{\partial \mathbf{m}} + \frac{\partial F_{\text{ms}}}{\partial \mathbf{m}} + \frac{\partial F_{\text{ext}}}{\partial \mathbf{m}} + \frac{\partial F_{\text{me}}}{\partial \mathbf{m}}\right) \\
&= \mathbf{h}_{\text{an}} + \mathbf{h}_{\text{exch}} + \mathbf{h}_{\text{ms}} + \mathbf{h}_{\text{ext}} + \mathbf{h}_{\text{me}}
\end{aligned}
\tag{B.57}
$$

where $\mathbf{h}_{\text{an}}$, $\mathbf{h}_{\text{exch}}$, $\mathbf{h}_{\text{ms}}$, $\mathbf{h}_{\text{ext}}$ and $\mathbf{h}_{\text{ext}}$ correspond to the effective fields due to the anisotropic, exchange, magnetostatic, external and magnetoelastic terms respectively. They can be expressed as:

$$
\begin{aligned}
\mathbf{h}_{\text{an}} = -\frac{2}{\mu_0 M_s^2}\Big[&m_x K_1\left(m_y^2 + m_z^2\right) + K_2 m_y^2 m_z^2, m_y K_1\left(m_x^2 + m_z^2\right) + K_2 m_x^2 m_z^2, \\
&m_z K_1\left(m_x^2 + m_y^2\right) + K_2 m_x^2 m_y^2\Big]
\end{aligned}
\tag{B.58}
$$

$$
\mathbf{h}_{\text{exch}} = \frac{2A}{\mu_0 M_s^2}(\partial_{xx}\mathbf{m} + \partial_{yy}\mathbf{m} + \partial_{zz}\mathbf{m})
\tag{B.59}
$$

$$
\mathbf{h}_{\text{ms}} = \frac{1}{M_s}\mathbf{H}_{\text{d}}
\tag{B.60}
$$

$$
\mathbf{h}_{\text{ext}} = \frac{1}{M_s}\mathbf{H}_{\text{ext}}
\tag{B.61}
$$

The calculation of $\mathbf{h}_{\text{an}}$, $\mathbf{h}_{\text{exch}}$ and $\mathbf{h}_{\text{ext}}$ is straightforward. The calculation $\mathbf{h}_{\text{ms}}$ is more laborious and can be found in Sec. B.2.

The contribution of the magnetoelastic term to the effective field is:

$$
\mathbf{h}_{\text{eff}} = -\frac{1}{\mu_0 M_s^2}\frac{\partial f_{\text{me}}}{\partial \mathbf{m}}
\tag{B.62}
$$

In components:

$$
\begin{aligned}
h_{\text{eff}_x}(\mathbf{r}) = -\frac{1}{\mu_0 M_s^2}\frac{\partial f_{\text{me}}}{\partial m_x(\mathbf{r})} = -\frac{1}{\mu_0 M_s^2}\Big[&\frac{B_1}{\sqrt{2}}2m_x(\mathbf{r})e_2(\mathbf{r}) + \frac{1}{(2\pi)^2}\frac{B_1}{\sqrt{2}}2m_x(\mathbf{r})\int e^{i\mathbf{kr}}A_{c_1}e_2(\mathbf{k})d\mathbf{k} \\
&+ \frac{1}{(2\pi)^2}\frac{B_2}{2\sqrt{2}}m_y(\mathbf{r})\int e^{i\mathbf{kr}}A_{c_3}e_2(\mathbf{k})d\mathbf{k}\Big]
\end{aligned}
\tag{B.63}
$$

$$
\begin{aligned}
h_{\text{eff}_y}(\mathbf{r}) = -\frac{1}{\mu_0 M_s^2}\frac{\partial f_{\text{me}}}{\partial m_y(\mathbf{r})} = -\frac{1}{\mu_0 M_s^2}\Big[&-\frac{B_1}{\sqrt{2}}2m_y(\mathbf{r})e_2(\mathbf{r}) + \frac{1}{(2\pi)^2}\frac{B_1}{\sqrt{2}}2m_y(\mathbf{r})\int e^{i\mathbf{kr}}A_{c_1}e_2(\mathbf{k})d\mathbf{k} \\
&+ \frac{1}{(2\pi)^2}\frac{B_2}{2\sqrt{2}}m_x(\mathbf{r})\int e^{i\mathbf{kr}}A_{c_3}e_2(\mathbf{k})d\mathbf{k}\Big]
\end{aligned}
\tag{B.64}
$$

Although our model deals with spins of three components, the magnetoelastic coupling includes only m_x and m_y because m_z should couple with ϵ_{zj}, being $j = x, y, z$ and the elastic part, in two dimensions, does not include these strain tensor components. Hence, $h_{\text{eff}_z}(\mathbf{r}) = 0$.

B.4.2   Elastic dynamics

The dynamics used for the elastic evolution is the same as in Chapter **??**, i.e. purely relaxational: $\frac{\partial e_2}{\partial \tau} = -\frac{\delta F}{\delta e_2}$. The functional derivatives concerning de pure elastic part $\left(\frac{\delta F_e}{\delta e_2}\right)$ have been already computed in Sec. A.3.2. In addition, here we have the contribution coming from the magnetoelastic coupling $\left(\frac{\delta F_{me}}{\delta e_2}\right)$, whose calculation is shown below. Let us start rewriting eq. (6.8) more explicitly:

$$
F_{me} = \frac{B_1}{\sqrt{2}} \int \left(m_x^2(\mathbf{r}) - m_y^2(\mathbf{r})\right) e_2(\mathbf{r})d\mathbf{r}
$$
$$
+ \frac{1}{(2\pi)^2} \int A_{c_1}(\mathbf{k})e_2(\mathbf{k})d\mathbf{k}\frac{B_1}{\sqrt{2}} \int e^{i\mathbf{kr}} \left(m_x^2(\mathbf{r}) + m_y^2(\mathbf{r})\right) d\mathbf{r} \qquad \text{(B.65)}
$$
$$
+ \frac{1}{(2\pi)^2} \int A_{c_3}(\mathbf{k})e_2(\mathbf{k})d\mathbf{k}\frac{B_2}{2\sqrt{2}} \int e^{i\mathbf{kr}} \left(m_x(\mathbf{r})m_y(\mathbf{r})\right) d\mathbf{r}
$$

In order to take derivatives of $e_2(\mathbf{r})$) we have to express $e_2(\mathbf{k})$) as a Fourier transform of $e_2(\mathbf{r})$):

$$
F_{me} = \frac{B_1}{\sqrt{2}} \int \left(m_x^2(\mathbf{r}) - m_y^2(\mathbf{r})\right) e_2(\mathbf{r})d\mathbf{r}
$$
$$
+ \frac{1}{(2\pi)^2} \int A_{c_1}(\mathbf{k})d\mathbf{k} \int e^{-i\mathbf{kr”}}e_2(\mathbf{r”})d\mathbf{r”}\frac{B_1}{\sqrt{2}} \int e^{i\mathbf{kr}} \left(m_x^2(\mathbf{r}) + m_y^2(\mathbf{r})\right) d\mathbf{r} \qquad \text{(B.66)}
$$
$$
+ \frac{1}{(2\pi)^2} \int A_{c_3}(\mathbf{k})d\mathbf{k} \int e^{-i\mathbf{kr”}}e_2(\mathbf{r”})d\mathbf{r”}\frac{B_2}{2\sqrt{2}} \int e^{i\mathbf{kr}} \left(m_x(\mathbf{r})m_y(\mathbf{r})\right) d\mathbf{r}
$$

Now we can take derivatives:

$$
\frac{\delta F_{me}}{\delta e_2(\mathbf{r'})} = \frac{B_1}{\sqrt{2}} \int \left(m_x^2(\mathbf{r}) - m_y^2(\mathbf{r})\right) \delta(\mathbf{r} - \mathbf{r'})d\mathbf{r}
$$
$$
+ \frac{1}{(2\pi)^2} \int A_{c_1}(\mathbf{k})d\mathbf{k} \int e^{-i\mathbf{kr”}}\delta(\mathbf{r”} - \mathbf{r'})d\mathbf{r”} \cdot \frac{B_1}{\sqrt{2}} \int e^{i\mathbf{kr}} \left(m_x^2(\mathbf{r}) + m_y^2(\mathbf{r})\right) d\mathbf{r} \qquad \text{(B.67)}
$$
$$
+ \frac{1}{(2\pi)^2} \int A_{c_3}(\mathbf{k})d\mathbf{k} \int e^{-i\mathbf{kr”}}\delta(\mathbf{r”} - \mathbf{r'})d\mathbf{r”} \cdot \frac{B_2}{2\sqrt{2}} \int e^{i\mathbf{kr}}m_x(\mathbf{r})m_y(\mathbf{r})d\mathbf{r} =
$$

$$
\frac{B_1}{\sqrt{2}} \left(m_x^2(\mathbf{r}) - m_y^2(\mathbf{r})\right) + \frac{1}{(2\pi)^2} \int e^{-i\mathbf{kr'}} A_{c_1}(\mathbf{k})d\mathbf{k}\frac{B_1}{\sqrt{2}} \int e^{i\mathbf{kr}} \left(m_x^2(\mathbf{r}) + m_y^2(\mathbf{r})\right) d\mathbf{r}
$$
$$
+ \frac{1}{(2\pi)^2} \int e^{-i\mathbf{kr'}} A_{c_3}(\mathbf{k})d\mathbf{k}\frac{B_2}{2\sqrt{2}} \int e^{i\mathbf{kr}}m_x(\mathbf{r})m_y(\mathbf{r})d\mathbf{r}
$$
$$
\text{(B.68)}
$$

Finally, making the change $\mathbf{k} \to -\mathbf{k}$, we get:

$$
\frac{\delta F_{me}}{\delta e_2(\mathbf{r'})} = \frac{B_1}{\sqrt{2}} \left(m_x^2(\mathbf{r}) - m_y^2(\mathbf{r})\right)
$$
$$
+ \frac{B_1}{\sqrt{2}}\mathsf{F}^{-1} \left[A_{c_1}\mathsf{F} \left(m_x^2(\mathbf{r}) + m_y^2(\mathbf{r})\right)\right] + \frac{B_2}{2\sqrt{2}}\mathsf{F}^{-1} \left[A_{c_3}\mathsf{F} \left(m_x(\mathbf{r})m_y(\mathbf{r})\right)\right] \qquad \text{(B.69)}
$$

where F^{-1} denotes the inverse Fourier transformation.

B.5   Micromagnetics in spherical variables

As mentioned in chapter 6, the spherical coordinates seem to be the natural framework within which develop the micromagnetic model. Here the mathematical details concerning the LLG dynamics in these coordinates can be found. We
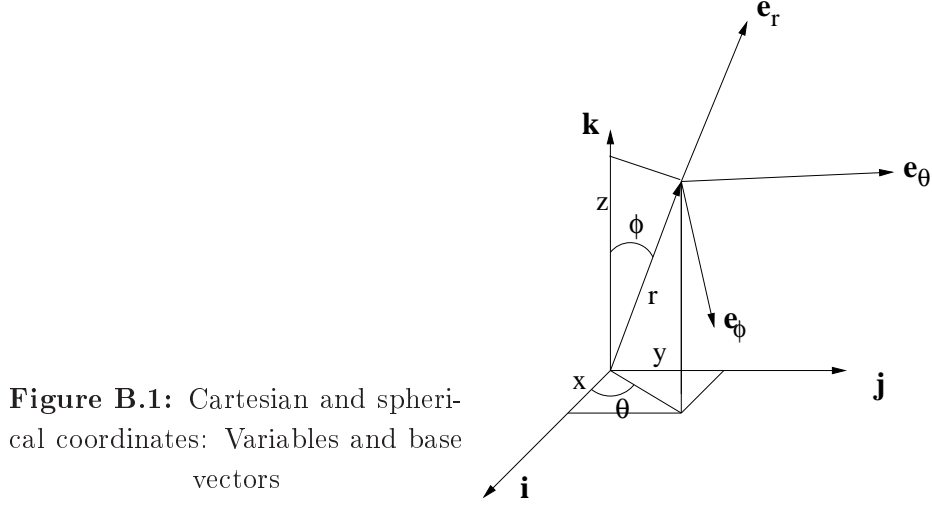
Figure B.1: Cartesian and spherical coordinates: Variables and base vectors

have a spin vector (m_x, m_y, m_z). We recall the spherical to cartesian change of variables:

$$m_x = r \cos\theta \sin\phi; \qquad m_y = r \sin\theta \sin\phi; \qquad m_z = r \cos\phi \qquad \text{(B.70)}$$

where instead of (m_r, m_θ, m_ϕ) we have denoted (r, θ, ϕ) for simplicity. Cartesian to spherical coordinates:

$$r = \sqrt{m_x^2 + m_y^2 + m_z^2}; \qquad \theta = \begin{cases} \arctan\left(\frac{m_y}{m_x}\right) & m_x > 0 \\ \frac{\pi}{2}\text{sgn}(m_y) & x = 0 \\ \pi + \arctan\left(\frac{m_y}{m_x}\right) & m_x < 0 \end{cases};$$

$$\phi = \begin{cases} \arctan\left(\frac{\sqrt{m_x^2 + m_y^2}}{m_z}\right) & m_z > 0 \\ \frac{\pi}{2} & m_z = 0 \\ \pi + \arctan\left(\frac{\sqrt{m_x^2 + m_y^2}}{m_z}\right) & m_z < 0 \end{cases}$$

$$\text{(B.71)}$$

Base vectors:
$$\hat{\imath} = \cos\theta \sin\phi \hat{e}_r + \cos\theta \cos\phi \hat{e}_\phi - \sin\theta \hat{e}_\theta$$
$$\hat{\jmath} = \sin\theta \sin\phi \hat{e}_r + \sin\theta \cos\phi \hat{e}_\phi + \cos\theta \hat{e}_\theta \qquad \text{(B.72)}$$
$$\hat{k} = \cos\phi \hat{e}_r - \sin\phi \hat{e}_\phi$$

The relations between the variables and between the base vectors of cartesian and spherical coordinates can be easily derived from Fig. B.1.

B.5.1   Cartesian coordinates

Our first attempt consists of finding the full mathematical expression of the LLG equation in spherical variables with respect to cartesian coordinates. As starting

point we recall the LLG dynamic equation:

$$\frac{\partial \mathbf{m}}{\partial \tau} = -\mathbf{m} \times \mathbf{h}_{\text{eff}} - \alpha \mathbf{m} \times (\mathbf{m} \times \mathbf{h}_{\text{eff}}) \tag{B.73}$$

Let us write explicitly the second and third terms:

$$\mathbf{m} \times \mathbf{h}_{\text{eff}} = \begin{vmatrix} \hat{\imath} & \hat{\jmath} & \hat{k} \\ m_x & m_y & m_z \\ h_{\text{eff}x} & h_{\text{eff}y} & h_{\text{eff}z} \end{vmatrix} = (m_y h_{\text{eff}z} - m_z h_{\text{eff}y})\hat{\imath} + (m_z h_{\text{eff}x} - m_x h_{\text{eff}z})\hat{\jmath}$$

$$+ (m_x h_{\text{eff}y} - m_y h_{\text{eff}x})\hat{k} \tag{B.74}$$

Third term:

$$\mathbf{m} \times (\mathbf{m} \times \mathbf{h}_{\text{eff}}) = \left[m_y(m_x h_{\text{eff}y} - m_y h_{\text{eff}x}) - m_z(m_z h_{\text{eff}x} - m_x h_{\text{eff}z}) \right] \hat{\imath}$$

$$+ \left[m_z(m_y h_{\text{eff}z} - m_z h_{\text{eff}y}) - m_x(m_x h_{\text{eff}y} - m_y h_{\text{eff}x}) \right] \hat{\jmath} \tag{B.75}$$

$$+ \left[m_x(m_z h_{\text{eff}x} - m_x h_{\text{eff}z}) - m_y(m_y h_{\text{eff}z} - m_z h_{\text{eff}y}) \right] \hat{k}$$

Now we can write LLG equation in components:

$$\frac{\partial m_x}{\partial \tau} = -(m_y h_{\text{eff}z} - m_z h_{\text{eff}y}) - \alpha \left[m_y(m_x h_{\text{eff}y} - m_y h_{\text{eff}x}) - m_z(m_z h_{\text{eff}x} - m_x h_{\text{eff}z}) \right]$$

$$\frac{\partial m_y}{\partial \tau} = -(m_z h_{\text{eff}x} - m_x h_{\text{eff}z}) - \alpha \left[m_z(m_y h_{\text{eff}z} - m_z h_{\text{eff}y}) - m_x(m_x h_{\text{eff}y} - m_y h_{\text{eff}x}) \right]$$

$$\frac{\partial m_z}{\partial \tau} = -(m_x h_{\text{eff}y} - m_y h_{\text{eff}x}) - \alpha \left[m_x(m_z h_{\text{eff}x} - m_x h_{\text{eff}z}) - m_y(m_y h_{\text{eff}z} - m_z h_{\text{eff}y}) \right]$$

$$\tag{B.76}$$

We make the following change of variables:

$$\mathbf{m} = (m_x, m_y, m_z) = (\cos\theta \sin\phi, \sin\theta \sin\phi, \cos\phi) \tag{B.77}$$

We compute now the left side of the LLG equation:

$$\frac{\partial m_x}{\partial \tau} = \frac{\partial(\cos\theta \sin\phi)}{\partial \tau} = -\sin\theta \sin\phi \frac{\partial\theta}{\partial\tau} + \cos\theta \cos\phi \frac{\partial\phi}{\partial\tau}$$

$$\frac{\partial m_y}{\partial \tau} = \frac{\partial(\sin\theta \sin\phi)}{\partial \tau} = \cos\theta \sin\phi \frac{\partial\theta}{\partial\tau} + \sin\theta \cos\phi \frac{\partial\phi}{\partial\tau} \tag{B.78}$$

$$\frac{\partial m_z}{\partial \tau} = \frac{\partial(\cos\phi)}{\partial \tau} = -\sin\phi \frac{\partial\phi}{\partial\tau}$$

Thus, the LLG equation in new variables becomes: Component x:

$$-\sin\theta \sin\phi \frac{\partial\theta}{\partial\tau} + \cos\theta \cos\phi \frac{\partial\phi}{\partial\tau} = -(\sin\theta \sin\phi h_z - \cos\phi h_y)$$

$$-\alpha[\sin\theta \sin\phi(\cos\theta \sin\phi h_y - \sin\theta \sin\phi h_x) - \cos\phi(\cos\phi h_x - \cos\theta \sin\phi h_z)] \tag{B.79}$$

Component y:

$$\cos\theta \sin\phi \frac{\partial\theta}{\partial\tau} + \sin\theta \cos\phi \frac{\partial\phi}{\partial\tau} = -(\cos\phi h_x - \cos\theta \sin\phi h_z)$$

$$-\alpha[\cos\phi(\sin\theta \sin\phi h_z - \cos\phi h_y) - \cos\theta \sin\phi(\cos\theta \sin\phi h_y - \sin\theta \sin\phi h_x)] \tag{B.80}$$

Component z:

$$-\sin\phi\frac{\partial\phi}{\partial\tau} = -(\cos\theta\sin\phi h_y - \sin\theta\sin\phi h_x)$$
$$-\alpha[\cos\theta\sin\phi(cos\phi h_x - \cos\theta\sin\phi h_z) - \sin\theta\sin\phi(\sin\theta\sin\phi h_z - \cos\phi h_y)]$$
$$(B.81)$$

Now we divide eq. B.81 over $(-\sin\phi)$:

$$\frac{\partial\phi}{\partial\tau} = \cos\theta h_y - \sin\theta h_x + \alpha[\cos\theta(\cos\phi h_x - \cos\theta\sin\phi h_z)$$
$$- \sin\theta(\sin\theta\sin\phi h_z - \cos\phi h_y)]$$
$$(B.82)$$

Rearranging terms we get the dynamic equation for ϕ:

$$\frac{\partial\phi}{\partial\tau} = \cos\theta h_y - \sin\theta h_x + \alpha[\cos\phi(\cos\theta h_x + \sin\theta h_y) - \sin\phi h_z] \qquad (B.83)$$

We can also obtain the expression above by multiplying eq. B.79 by $\cos\theta$ and eq. B.80 by $\sin\theta$ and adding up the resulting equations.
Now we multiply eq. B.79 by $(-\sin\theta)$ and eq. B.80 by $\cos\theta$. Then, we add the two resulting equations. At the left hand side of the equation we get:

$$\sin^2\theta\sin\phi\frac{\partial\theta}{\partial\tau} - \sin\theta\cos\theta\cos\phi\frac{\partial\phi}{\partial\tau} + \cos^2\theta\sin\phi\frac{\partial\theta}{\partial\tau} + \cos\theta\sin\theta\cos\phi\frac{\partial\phi}{\partial\tau} = \sin\phi\frac{\partial\theta}{\partial\tau}$$
$$(B.84)$$

At the right hand side of the equation we obtain:

$$(\sin^2\theta\sin\phi h_z - \sin\theta\cos\phi h_y) + \alpha[\sin^2\theta\sin\phi(cos\theta\sin\phi h_y - \sin\theta\sin\phi h_x)$$
$$- \sin\theta\cos\phi(\cos\phi h_x - \cos\theta\sin\phi h_z)] - (\cos\theta\cos\phi h_x - \cos^2\theta\sin\phi h_z)$$
$$-\alpha[\cos\theta\cos\phi(sin\theta\sin\phi h_z - \cos\phi h_y) - \cos^2\theta\sin\phi(\cos\theta\sin\phi h_y - \sin\theta\sin\phi h_x)]$$
$$= \sin\phi h_z - \cos\phi(\sin\theta h_y + \cos\theta h_x)$$
$$+\alpha[\sin^2\phi(\cos\theta h_y - \sin\theta h_x) + \cos^2\phi(\cos\theta h_y - \sin\theta h_x)]$$
$$= \sin\phi h_z - \cos\phi(\sin\theta h_y + \cos\theta h_x) + \alpha(\cos\theta h_y - \sin\theta h_x)$$
$$(B.85)$$

Hence, the dynamic equation for θ is:

$$\frac{\partial\theta}{\partial\tau} = h_z - \cot\phi(\sin\theta h_y + \cos\theta h_x) + \alpha\csc\phi(\cos\theta h_y - \sin\theta h_x) \qquad (B.86)$$

B.5.2   Spherical coordinates

First we calculate $\mathbf{m}$ in the spherical base:

$$\mathbf{m} = m_x \hat{\imath} + m_y \hat{\jmath} + m_z \hat{k} = \cos\theta \sin\phi (\cos\theta \sin\phi \hat{e}_r + \cos\theta \cos\phi \hat{e}_\phi - \sin\theta \hat{e}_\theta)$$
$$+ \sin\theta \sin\phi (\sin\theta \sin\phi \hat{e}_r + \sin\theta \cos\phi \hat{e}_\phi + \cos\theta \hat{e}_\theta) + \cos\theta (\cos\phi \hat{e}_r - \sin\phi \hat{e}_\phi)$$
$$= (\cos^2\theta \sin^2\phi + \sin^2\theta \sin^2\phi + \cos^2\phi)\hat{e}_r +$$
$$(\cos^2\theta \sin\phi \cos\phi + \sin^2\theta \sin\phi \cos\phi - \cos\phi \sin\phi)\hat{e}_\phi +$$
$$(-\cos\theta \sin\phi \sin\theta + \sin\theta \sin\phi \cos\theta)\hat{e}_\theta = \hat{e}_r$$

$$(\text{B.87})$$

Thus, as expected, $\mathbf{m} = (1, 0, 0)$ in spherical coordinates. Now, we write any vector $\mathbf{h} = (h_x, h_y, h_z) = (r_h \cos\theta_h \sin\phi_h, r_h \sin\theta_h \sin\phi_h, r_h \cos\phi_h)$ with respect to the base vectors $\{\hat{e}_r, \hat{e}_\theta, \hat{e}_\phi\}$:

$$\mathbf{h} = h_x \hat{\imath} + h_y \hat{\jmath} + h_z \hat{k} == r_h \cos\theta_h \sin\phi_h (\cos\theta \sin\phi \hat{e}_r + \cos\theta \cos\phi \hat{e}_\phi - \sin\theta \hat{e}_\theta)$$
$$+ r_h \sin\theta_h \sin\phi_h (\sin\theta \sin\phi \hat{e}_r + \sin\theta \cos\phi \hat{e}_\phi + \cos\theta \hat{e}_\theta)$$
$$+ r_h \cos\phi_h (\cos\phi \hat{e}_r - \sin\phi \hat{e}_\phi)$$
$$= r_h \left[\sin\phi_h \sin\phi \cos(\theta_h - \theta) + \cos\phi_h \cos\phi \right] \hat{e}_r + r_h \sin\phi_h \sin(\theta_h - \theta)\hat{e}_\theta +$$
$$+ r_h \left[\sin\phi_h \cos\phi \cos(\theta_h - \theta) - \cos\phi_h \sin\phi \right] \hat{e}_\phi = (h_r, h_\theta, h_\phi)$$

$$(\text{B.88})$$

In spherical coordinates the second and third terms of LLG equation are expressed as:

$$\mathbf{m} \times \mathbf{h}_{\text{eff}} = -h_\phi \hat{e}_\theta + h_\theta \hat{e}_\phi; \qquad \mathbf{m} \times (\mathbf{m} \times \mathbf{h}_{\text{eff}}) = -h_\theta \hat{e}_\theta - h_\phi \hat{e}_\phi \qquad (\text{B.89})$$

The first term of LLG equation can be numerically calculated to the first order as:

$$\frac{\partial \mathbf{m}}{\partial \tau} \simeq \frac{\mathbf{m}_{t+\Delta t} - \mathbf{m}_t}{\Delta\tau} = \frac{(m_r, m_\theta, m_\phi) - (1, 0, 0)}{\Delta\tau} \qquad (\text{B.90})$$

Then, LLG equation expressed in the spherical coordinate system takes the following form:

$$(m_r, m_\theta, m_\phi) = (1, 0, 0) - [(0, -h_\phi, h_\theta) + \alpha(0, -h_\theta, -h_\phi)]\Delta\tau \qquad (\text{B.91})$$

In components:

$$m_r = 1 \qquad\qquad m_\theta = (h_\phi + \alpha h_\theta)\Delta\tau \qquad\qquad m_\phi = (h_\theta + \alpha h_\theta)\Delta\tau, \qquad (\text{B.92})$$

where it can be seen from the radial component that LLG equation automatically keeps the modulus of the spin constant. Now we proceed to calculate the specific expression for the effective field. For this we need to rewrite in spherical coordinates every energetic contribution, which is done in the following.

Exchange field (I):

Let us recall the continuous and discrete expression in cartesian coordinates:

$$\mathbf{h}_{\text{exch}} = \frac{2A}{\mu_0 M_s^2} \left[\left(\frac{\partial^2 m_x}{\partial x^2} + \frac{\partial^2 m_x}{\partial y^2} \right) \hat{\imath} + + \left(\frac{\partial^2 m_y}{\partial x^2} + \frac{\partial^2 m_y}{\partial y^2} \right) \hat{\jmath} + \left(\frac{\partial^2 m_z}{\partial x^2} + \frac{\partial^2 m_z}{\partial y^2} \right) \hat{k} \right]$$

$$= \frac{2A}{\mu_0 M_s^2} \left[(m_x(i+1,j) + m_x(i-1,j) + m_x(i,j+1) + \right.$$

$$+ m_x(i,j-1) - 4m_x(i,j))\hat{\imath} +$$

$$+ (m_y(i+1,j) + m_y(i-1,j) + m_y(i,j+1) + m_y(i,j-1) - 4m_y(i,j))\hat{\jmath} +$$

$$+ (m_z(i+1,j) + m_z(i-1,j) + m_z(i,j+1) + m_z(i,j-1) - 4m_z(i,j))\hat{k} \bigg]$$

$$\text{(B.93)}$$

At this point, it can be helpful to recall that m_x, m_y, m_z are the components of a given spin, and therefore the value of the components are given with respect to the origin of the given spin. These components are being calculated in spherical coordinates. Moreover, in our system we have a vectorial field, that is a field of spins each one located in a cell of a square lattice. Since the coordinates of the cells and the components of the spins are independent, it is more convenient the coordinates of the cells to be kept in cartesian coordinates (x, y, z). According to this, we will make explicit the cartesian spatial dependence of the spin components, either in cartesian coordinates $(m_x(x, y,), m_y(x, y), m_z(x, y))$ or in spherical ones $(r(x, y), \theta(x, y), \phi(x, y))$. In a discretized mesh $(x, y) \rightarrow (i, j)$ where $i, j \in N$. Note that, although the spins are 3-dimensional vectors, the lattice is only 2-dimensional, so that the z-component is not taken into account and all the derivatives $\partial/\partial z$, $\partial^2/\partial z^2$ will vanish.

Now we may come back to the mathematical calculus. Using eq. B.70 and B.72:

$$\mathbf{h}_{\text{exch}} = \frac{2A}{\mu_0 M_s^2} \left[(A_1 \cos \theta(i,j) \sin \phi(i,j) \right.$$

$$+ A_2 \sin \theta(i,j) \sin \phi(i,j) + A_3 \cos \phi(i,j)) \hat{e}_r + (-A_1 \sin \theta(i,j) + A_2 \cos \theta(i,j)) \hat{e}_\theta$$

$$+ (A_1 \cos \theta(i,j) \cos \phi(i,j) + A_2 \sin \theta(i,j) \cos \phi(i,j) - - A_3 \sin \phi(i,j)) \hat{e}_\phi \bigg]$$

$$\text{(B.94)}$$

where

$$A_1 = \cos \theta(i+1,j) \sin \phi(i+1,j) + \cos \theta(i-1,j) \sin \phi(i-1,j)$$

$$+ \cos \theta(i,j+1) \sin \phi(i,j+1) + \cos \theta(i,j-1) \sin \phi(i,j-1) - 4 \cos \theta(i,j) \sin \phi(i,j)$$

$$A_2 = \sin \theta(i+1,j) \sin \phi(i+1,j) + \sin \theta(i-1,j) \sin \phi(i-1,j)$$

$$+ \sin \theta(i,j+1) \sin \phi(i,j+1) + \sin \theta(i,j-1) \sin \phi(i,j-1) - 4 \sin \theta(i,j) \sin \phi(i,j)$$

$$A_3 = \cos \phi(i+1,j) + \cos \phi(i-1,j) + \cos \phi(i,j+1) + \cos \phi(i,j-1) - 4 \cos \phi(i,j)$$

$$\text{(B.95)}$$

Introducing eq. B.95 in eq. B.94, we get in components:
Component $\hat{e}_r$:

$$
\begin{aligned}
A_1 &\cos \theta(i,j) \sin \phi(i,j) + A_2 \sin \theta(i,j) \sin \phi(i,j) + A_3 \cos \phi(i,j) \\
&= \sin \phi(i,j) \left[\sin \phi(i+1,j) \cos \left(\theta(i+1,j) - \theta(i,j) \right) \right. \\
&+ \sin \phi(i-1,j) \cos \left(\theta(i-1,j) - \theta(i,j) \right) + \sin \phi(i,j+1) \cos \left(\theta(i,j+1) - \theta(i,j) \right) \\
&\left. + \sin \phi(i,j-1) \cos \left(\theta(i,j-1) - \theta(i,j) \right) \right] \\
&+ \cos \phi(i,j)(\cos \phi(i+1,j) + \cos \phi(i-1,j) + \cos \phi(i,j+1) + \cos \phi(i,j-1)) - 4
\end{aligned}
$$

$$(\text{B.96})$$

Component $\hat{e}_\theta$:

$$
\begin{aligned}
-A_1 &\sin \theta(i,j) + A_2 \cos \theta(i,j) = \\
&\sin \phi(i+1,j)[\cos \theta(i,j) \sin \theta(i+1,j) - \cos \theta(i+1,j) \sin \theta(i,j)] \\
&+ \sin \phi(i-1,j)[\cos \theta(i,j) \sin \theta(i-1,j) - \cos \theta(i-1,j) \sin \theta(i,j)] \\
&+ \sin \phi(i,j+1)[\cos \theta(i,j) \sin \theta(i,j+1) - \cos \theta(i,j+1) \sin \theta(i,j)] \\
&+ \sin \phi(i,j-1)[\cos \theta(i,j) \sin \theta(i,j-1) - \cos \theta(i,j-1) \sin \theta(i,j)] \\
&+ 4 \cos \theta(i,j) \sin \theta(i,j) \sin \phi(i,j) - 4 \cos \theta(i,j) \sin \theta(i,j) \sin \phi(i,j) = \\
&= \sin \phi(i+1,j) \sin \left(\theta(i+1,j) - \theta(i,j) \right) + \sin \phi(i-1,j) \sin \left(\theta(i-1,j) - \theta(i,j) \right) \\
&+ \sin \phi(i,j+1) \sin \left(\theta(i,j+1) - \theta(i,j) \right) + \sin \phi(i,j-1) \sin \left(\theta(i,j-1) - \theta(i,j) \right)
\end{aligned}
$$

$$(\text{B.97})$$

Component $\hat{e}_\phi$:

$$
\begin{aligned}
A_1 &\cos \theta(i,j) \cos \phi(i,j) + A_2 \sin \theta(i,j) \cos \phi(i,j) - A_3 \sin \phi(i,j) \\
&= \cos \phi(i,j) \left[\sin \phi(i+1,j) \cos \left(\theta(i+1,j) - \theta(i,j) \right) \right. \\
&+ \sin \phi(i-1,j) \cos \left(\theta(i-1,j) - \theta(i,j) \right) + \sin \phi(i,j+1) \cos \left(\theta(i,j+1) - \theta(i,j) \right) \\
&\left. + \sin \phi(i,j-1) \cos \left(\theta(i,j-1) - \theta(i,j) \right) \right] \\
&- \sin \phi(i,j)(\cos \phi(i+1,j) + \cos \phi(i-1,j) + \cos \phi(i,j+1) + \cos \phi(i,j-1))
\end{aligned}
$$

$$(\text{B.98})$$

Exchange field (II):

Now we compute the exchange field another way. Starting from B.93:

$$\frac{\partial^2 m_{x_i}}{\partial x_j^2} = \frac{\partial}{\partial x_j}\left(\frac{\partial m_{x_i}}{\partial x_j}\right) = \frac{\partial}{\partial x_j}\left(\frac{\partial m_{x_i}}{\partial \theta}\frac{\partial \theta}{\partial x_j} + \frac{\partial m_{x_i}}{\partial \phi}\frac{\partial \phi}{\partial x_j}\right)$$

$$= \frac{\partial^2 m_{x_i}}{\partial x_j \partial \theta}\frac{\partial \theta}{\partial x_j} + \frac{\partial m_{x_i}}{\partial \theta}\frac{\partial^2 \theta}{\partial x_j^2} + \frac{\partial^2 m_{x_i}}{\partial x_j \partial \phi}\frac{\partial \phi}{\partial x_j} + \frac{\partial m_{x_i}}{\partial \phi}\frac{\partial^2 \phi}{\partial x_j^2}$$

$$= \frac{\partial^2 m_{x_i}}{\partial \theta^2}\left(\frac{\partial \theta}{\partial x_j}\right)^2 + \frac{\partial^2 m_{x_i}}{\partial \phi \partial \theta}\frac{\partial \phi}{\partial x_j}\frac{\partial \theta}{\partial x_j} + \frac{\partial m_{x_i}}{\partial \theta}\frac{\partial^2 \theta}{\partial x_j^2} + \frac{\partial^2 m_{x_i}}{\partial \phi^2}\left(\frac{\partial \phi}{\partial x_j}\right)^2 + \frac{\partial^2 m_{x_i}}{\partial \theta \partial \phi}\frac{\partial \theta}{\partial x_j}\frac{\partial \phi}{\partial x_j} + \frac{\partial m_{x_i}}{\partial \phi}\frac{\partial^2 \phi}{\partial x_j^2}$$

$$\text{(B.99)}$$

where $i, j = 1, 2, 3$ and $x_{1,2,3} = x, y, z$ respectively. As mentioned previously, we have $\partial m_{x_i}/\partial z = 0$. Now let's compute the derivatives: For $m_x = \cos\theta\sin\phi$:

$$\frac{\partial m_x}{\partial \theta} = -\sin\theta\sin\phi; \qquad \frac{\partial m_x}{\partial \phi} = \cos\theta\cos\phi$$

$$\frac{\partial^2 m_x}{\partial \theta^2} = \frac{\partial^2 m_x}{\partial \phi^2} = -\cos\theta\sin\phi; \qquad \frac{\partial^2 m_x}{\partial \theta \partial \phi} = \frac{\partial^2 m_x}{\partial \phi \partial \theta} = -\sin\theta\cos\phi$$

$$\text{(B.100)}$$

For $m_y = \sin\theta\sin\phi$:

$$\frac{\partial m_y}{\partial \theta} = \cos\theta\sin\phi; \qquad \frac{\partial m_y}{\partial \phi} = \sin\theta\cos\phi$$

$$\frac{\partial^2 m_y}{\partial \theta^2} = \frac{\partial^2 m_x}{\partial \phi^2} = -\sin\theta\sin\phi; \qquad \frac{\partial^2 m_y}{\partial \theta \partial \phi} = \frac{\partial^2 m_y}{\partial \phi \partial \theta} = \cos\theta\cos\phi$$

$$\text{(B.101)}$$

For $m_z = \cos\phi$:

$$\frac{\partial m_z}{\partial \theta} = \frac{\partial^2 m_z}{\partial \theta^2} = \frac{\partial^2 m_z}{\partial \theta \partial \phi} = \frac{\partial^2 m_z}{\partial \phi \partial \theta} = 0$$

$$\frac{\partial m_z}{\partial \phi} = -\sin\phi; \qquad \frac{\partial^2 m_z}{\partial \phi^2} = -\cos\phi$$

$$\text{(B.102)}$$

Let's name

$$h_{x_i} = \left(\frac{\partial^2 m_{x_i}}{\partial x^2} + \frac{\partial^2 m_{x_i}}{\partial y^2}\right) \tag{B.103}$$

Then, using eq. B.72 we can rewrite eq. B.93 as follows:

$$\mathbf{h}_{\text{exch}} = \frac{2A}{\mu_0 M_s^2}\left[h_x\hat{\imath} + h_y\hat{\jmath} + h_z\hat{k}\right] = \frac{2A}{\mu_0 M_s^2}\left[(h_x\cos\theta\sin\phi + h_y\sin\theta\sin\phi + h_z\cos\phi)\,\hat{e}_r\right.$$

$$\left. + (h_x(-\sin\theta) + h_y\cos\theta)\,\hat{e}_\theta + (h_x\cos\theta\cos\phi + h_y\sin\theta\cos\phi - h_z\sin\phi)\,\hat{e}_\phi\right]$$

$$\text{(B.104)}$$

Component $\hat{e}_r$:

$$h_x \cos\theta \sin\phi + h_y \sin\theta \sin\phi + h_z \cos\phi = \left[\left(\frac{\partial\theta}{\partial x}\right)^2 + \left(\frac{\partial\theta}{\partial y}\right)^2 + \left(\frac{\partial\phi}{\partial x}\right)^2 + \left(\frac{\partial\phi}{\partial y}\right)^2\right] \cdot$$

$$\cdot \left(\cos\theta \sin\phi \frac{\partial^2 m_x}{\partial\theta^2} + \sin\theta \sin\phi \frac{\partial^2 m_y}{\partial\theta^2} + \cos\phi \frac{\partial^2 m_z}{\partial\theta^2}\right)$$

$$+ \left[\frac{\partial^2\theta}{\partial x^2} + \frac{\partial^2\theta}{\partial y^2}\right] \cdot \left(\cos\theta \sin\phi \frac{\partial m_x}{\partial\theta} + \sin\theta \sin\phi \frac{\partial m_y}{\partial\theta} + \cos\phi \frac{\partial m_z}{\partial\theta}\right)$$

$$+ \left[\frac{\partial^2\phi}{\partial x^2} + \frac{\partial^2\phi}{\partial y^2}\right] \cdot \left(\cos\theta \sin\phi \frac{\partial m_x}{\partial\phi} + \sin\theta \sin\phi \frac{\partial m_y}{\partial\phi} + \cos\phi \frac{\partial m_z}{\partial\phi}\right)$$

$$+2 \left[\frac{\partial\theta}{\partial x}\frac{\partial\phi}{\partial x} + \frac{\partial\theta}{\partial y}\frac{\partial\phi}{\partial y}\right] \cdot \left(\cos\theta \sin\phi \frac{\partial^2 m_x}{\partial\theta\partial\phi} + \sin\theta \sin\phi \frac{\partial^2 m_y}{\partial\theta\partial\phi} + \cos\phi \frac{\partial^2 m_z}{\partial\theta\partial\phi}\right)$$

$$= -\left(\left(\frac{\partial\theta}{\partial x}\right)^2 + \left(\frac{\partial\theta}{\partial y}\right)^2 + \left(\frac{\partial\phi}{\partial x}\right)^2 + \left(\frac{\partial\phi}{\partial y}\right)^2\right)$$

(B.105)

Component $\hat{e}_\theta$:

$$-\sin\theta h_x + \cos\theta h_y = \left[\left(\frac{\partial\theta}{\partial x}\right)^2 + \left(\frac{\partial\theta}{\partial y}\right)^2 + \left(\frac{\partial\phi}{\partial x}\right)^2 + \left(\frac{\partial\phi}{\partial y}\right)^2\right] \cdot \left(-\sin\theta \frac{\partial^2 m_x}{\partial\theta^2} + \cos\theta \frac{\partial^2 m_y}{\partial\theta^2}\right)$$

$$+ \left[\frac{\partial^2\theta}{\partial x^2} + \frac{\partial^2\theta}{\partial y^2}\right] \cdot \left(-\sin\theta \frac{\partial m_x}{\partial\theta} + \cos\theta \frac{\partial m_y}{\partial\theta}\right) + \left[\frac{\partial^2\phi}{\partial x^2} + \frac{\partial^2\phi}{\partial y^2}\right] \cdot \left(-\sin\theta \frac{\partial m_x}{\partial\phi} + \cos\theta \frac{\partial m_y}{\partial\phi}\right)$$

$$+2 \left[\frac{\partial\theta}{\partial x}\frac{\partial\phi}{\partial x} + \frac{\partial\theta}{\partial y}\frac{\partial\phi}{\partial y}\right] \cdot \left(-\sin\theta \frac{\partial^2 m_x}{\partial\theta\partial\phi} + \cos\theta \frac{\partial^2 m_y}{\partial\theta\partial\phi}\right)$$

$$= \sin\phi \left(\frac{\partial^2\theta}{\partial x^2} + \frac{\partial^2\theta}{\partial y^2}\right) + 2\cos\phi \left(\frac{\partial\theta}{\partial x}\frac{\partial\phi}{\partial x} + \frac{\partial\theta}{\partial y}\frac{\partial\phi}{\partial y}\right)$$

(B.106)

Component $\hat{e}_\phi$:

$$h_x \cos\theta \cos\phi + h_y \sin\theta \cos\phi - h_z \sin\phi = \left[\left(\frac{\partial\theta}{\partial x}\right)^2 + \left(\frac{\partial\theta}{\partial y}\right)^2 + \left(\frac{\partial\phi}{\partial x}\right)^2 + \left(\frac{\partial\phi}{\partial y}\right)^2\right] \cdot$$

$$\cdot \left(\cos\theta \cos\phi \frac{\partial^2 m_x}{\partial\theta^2} + \sin\theta \cos\phi \frac{\partial^2 m_y}{\partial\theta^2} - \sin\phi \frac{\partial^2 m_z}{\partial\theta^2}\right) +$$

$$+ \left[\frac{\partial^2\theta}{\partial x^2} + \frac{\partial^2\theta}{\partial y^2}\right] \cdot \left(\cos\theta \cos\phi \frac{\partial m_x}{\partial\theta} + \sin\theta \cos\phi \frac{\partial m_y}{\partial\theta} - \sin\phi \frac{\partial m_z}{\partial\theta}\right)$$

$$+ \left[\frac{\partial^2\phi}{\partial x^2} + \frac{\partial^2\phi}{\partial y^2}\right] \cdot \left(\cos\theta \cos\phi \frac{\partial m_x}{\partial\phi} + \sin\theta \cos\phi \frac{\partial m_y}{\partial\phi} - \sin\phi \frac{\partial m_z}{\partial\phi}\right)$$

$$+2 \left[\frac{\partial\theta}{\partial x}\frac{\partial\phi}{\partial x} + \frac{\partial\theta}{\partial y}\frac{\partial\phi}{\partial y}\right] \cdot \left(\cos\theta \cos\phi \frac{\partial^2 m_x}{\partial\theta\partial\phi} + \sin\theta \cos\phi \frac{\partial^2 m_y}{\partial\theta\partial\phi} - \sin\phi \frac{\partial^2 m_z}{\partial\theta\partial\phi}\right) = \left(\frac{\partial^2\phi}{\partial x^2} + \frac{\partial^2\phi}{\partial y^2}\right)$$

(B.107)

Anisotropic field:

In cartesian coordinates:

$$\mathbf{h}_{\text{an}} = -\frac{2}{\mu_0 M_s^2}(m_x \left(K_1 \left(m_y^2 + m_z^2\right) + K_2 m_y^2 m_z^2\right),$$

$$m_y \left(K_1 \left(m_x^2 + m_z^2\right) + K_2 m_x^2 m_z^2\right), m_z \left(K_1 \left(m_x^2 + m_y^2\right) + K_2 m_x^2 m_y^2\right))$$

(B.108)

In spherical variables, using eq. B.70 and B.72:

Component $\hat{e}_r$:

$$h_{\mathrm{an}r} = -\frac{2}{\mu_0 M_s^2} \left[K_1 2(\cos^2\phi \sin^2\phi + \sin^4\phi \sin^2\theta \cos^2\theta) \right.$$
$$\left. + K_2 3 \sin^2\theta \cos^2\theta \sin^4\phi \cos^2\phi \right] \tag{B.109}$$
$$= -\frac{2}{\mu_0 M_s^2} \left[\frac{K_1}{2}(\sin^2 2\phi + \sin^4\phi \sin^2 2\theta) + K_2 \frac{3}{4}\sin^2 2\theta \sin^2 2\phi \sin^2\phi \right]$$

Component $\hat{e}_\theta$:

$$h_{\mathrm{an}\theta} = -\frac{2}{\mu_0 M_s^2} \left[K_1 \sin^3\phi(\sin\theta\cos^3\theta - \sin^3\theta\cos\theta) \right.$$
$$\left. + K_2 \sin^3\phi \cos^2\phi(\sin\theta\cos^3\theta - \sin^3\theta\cos\theta) \right] \tag{B.110}$$
$$= -\frac{2\sin^3\phi}{\mu_0 M_s^2} \left[\frac{K_1}{4}\sin 4\theta + \frac{K_2\cos^2\phi}{4}\sin 4\theta \right] = -\frac{\sin^3\phi \sin 4\theta}{2\mu_0 M_s^2}\left[K_1 + K_2\cos^2\phi \right]$$

Component $\hat{e}_\phi$

$$h_{\mathrm{an}\phi} = -\frac{2}{\mu_0 M_s^2} \left[K_1(\sin\theta\cos^3\theta - \sin^3\theta\cos\theta + 2\cos\phi\sin^3\phi\sin^2\theta\cos^2\theta) \right.$$
$$\left. + K_2 \sin^2\theta\cos^2\theta\sin^3\phi\cos\phi(3\cos^2\phi - 1) \right]$$
$$= -\frac{2}{\mu_0 M_s^2} \left[K_1\frac{1}{4}\sin 4\theta + \frac{1}{4}\sin^2 2\theta\left(\frac{1}{4}(\sin 2\phi - \frac{1}{2}\sin 4\phi)(2K_1 - K_2) + \frac{3K_2}{8}\sin^3 2\phi \right) \right]$$
$$\tag{B.111}$$

Magnetostatic field:

The magnetostatic field in cartesian coordinates is computed this way:

$$\left. \begin{array}{l} \mathbf{h}_d = -\nabla\psi \\ \nabla \cdot \mathbf{h}_d = -\nabla \cdot \mathbf{m} \end{array} \right\} \Rightarrow \Delta\psi = \nabla \cdot \mathbf{m} \Rightarrow \psi(\mathbf{k}) = -\frac{\mathsf{F}[\nabla \cdot \mathbf{m}(\mathbf{r})]}{k_x^2 + k_y^2} \tag{B.112}$$

where ψ denotes the scalar potential and F a Fourier Transform. In 2D $\nabla \cdot \mathbf{m}$ is:

$$\nabla \cdot \mathbf{m} = \frac{\partial m_x}{\partial x} + \frac{\partial m_y}{\partial y} \tag{B.113}$$

In discretized form:

$$(\nabla \cdot \mathbf{m})(i - \tfrac{1}{2}, j - \tfrac{1}{2}) = m_x(i,j) - m_x(i-1,j) + m_x(i,j-1) - m_x(i-1,j-1)$$
$$+ m_y(i,j) - m_y(i,j-1) + m_y(i-1,j) - m_y(i-1,j-1) \tag{B.114}$$

Finally, using B.112 we get the demagnetizing field:

$$h_{d_x}(i,j) = -\frac{1}{2a}(\psi(i+\tfrac{1}{2},j+\tfrac{1}{2}) - \psi(i-\tfrac{1}{2},j+\tfrac{1}{2})$$
$$+ \psi(i+\tfrac{1}{2},j-\tfrac{1}{2}) + \psi(i-\tfrac{1}{2},j-\tfrac{1}{2}))$$
$$h_{d_y}(i,j) = -\frac{1}{2a}(\psi(i+\tfrac{1}{2},j+\tfrac{1}{2}) - \psi(i+\tfrac{1}{2},j-\tfrac{1}{2}) \tag{B.115}$$
$$+ \psi(i-\tfrac{1}{2},j+\tfrac{1}{2}) + \psi(i-\tfrac{1}{2},j-\tfrac{1}{2}))$$

Eq. B.113 in spherical variables:

$$\nabla \cdot \mathbf{m} = \frac{\partial(\cos\theta\sin\phi)}{\partial x} + \frac{\partial(\sin\theta\sin\phi)}{\partial y}$$

$$= \sin\theta\sin\phi\frac{\partial\theta}{\partial x} + \cos\theta\cos\phi\frac{\partial\phi}{\partial x} + \cos\theta\sin\phi\frac{\partial\theta}{\partial y} + \sin\theta\cos\phi\frac{\partial\phi}{\partial y} \tag{B.116}$$

In discretized form, we also want $(\nabla \cdot \mathbf{m})\left(i - \frac{1}{2}, j - \frac{1}{2}\right)$. Then,

$$\frac{\partial\theta}{\partial x} = \theta(i,j) - \theta(i-1,j) + \theta(i,j-1) - \theta(i-1,j-1) \tag{B.117}$$

and similarly for $\partial\theta/\partial y$, $\partial\phi/\partial y$ and $\partial\phi/\partial y$. For the same purpose, $\sin\theta$, $\cos\theta$, $\sin\phi$ and $\cos\phi$ must be computed at the center of each cell, i.e. as an average of the magnetization at the four corners of each cell. For instance:

$$\sin\theta(i - \tfrac{1}{2}, j - \tfrac{1}{2}) = \tfrac{1}{4}(\sin\theta(i,j) + \sin\theta(i-1,j)$$

$$+ \sin\theta(i,j-1) + \sin\theta(i-1,j-1)) \tag{B.118}$$

Once done that, then we get the scalar potential ψ via fourier transform. Finally, we can get the demagnetizing field:

$$\mathbf{h}_d = -\frac{\partial\psi}{\partial x}\hat{i} - \frac{\partial\psi}{\partial y}\hat{j} = -\left[\sin\phi\left(\cos\theta\frac{\partial\psi}{\partial x} + \sin\theta\frac{\partial\psi}{\partial y}\right)\hat{e}_r\right.$$

$$\left. + \left(-\sin\theta\frac{\partial\psi}{\partial x} + \cos\theta\frac{\partial\psi}{\partial y}\right)\hat{e}_\theta + \cos\phi\left(\cos\theta\frac{\partial\psi}{\partial x} + \sin\theta\frac{\partial\psi}{\partial y}\right)\hat{e}_\phi\right] \tag{B.119}$$

Magnetoelastic part (I): Magnetic dynamics

In cartesian coordinates:

$$\mathbf{h}_{\text{me}} = -\frac{1}{\mu_0 M_s^2 a^2}\left[((A+B)m_x + Cm_y)\,\hat{i} + ((-A+B)m_y + Cm_x)\,\hat{j}\right] \tag{B.120}$$

where

$$A = \frac{2B_1}{\sqrt{2}}; \qquad B = \frac{2B_1}{\sqrt{2}}\mathsf{F}^{-1}\left[A_{c_1}(\mathbf{k})e_2(\mathbf{k})\right]; \qquad C = \frac{B_2}{2\sqrt{2}}\mathsf{F}^{-1}\left[A_{c_3}(\mathbf{k})e_2(\mathbf{k})\right] \tag{B.121}$$

Then, in spherical coordinates:

$$\mathbf{h}_{\text{me}} = -\frac{1}{\mu_0 M_s^2 a^2}\left[\sin^2\phi\left(A\cos 2\theta + B + C\sin 2\theta\right)\hat{e}_r\right.$$

$$\left. + \sin\phi\left(C\cos 2\theta - A\sin 2\theta\right)\hat{e}_\theta + \tfrac{1}{2}\sin 2\phi\left(A\cos 2\theta + B + C\sin 2\theta\right)\hat{e}_\phi\right] \tag{B.122}$$

Magnetoelastic part (II): Elastic dynamics

The elastic part contains the follow expressions:

$$m_x^2 - m_y^2 = \sin^2\phi\cos 2\theta; \qquad m_x^2 + m_y^2 = \sin^2\phi; \qquad m_x m_y = \frac{1}{2}\sin^2\phi\sin 2\theta \tag{B.123}$$

B.6   Thermal fluctuations

We can also add a noisy term in the dynamics in order to take into account the thermal fluctuations by means of the fluctuation-dissipation theorem. As this term will be added to the effective field ($\mathbf{h}_{\mathrm{eff}_{\mathrm{total}}} = \mathbf{h}_{\mathrm{eff}} + \mathbf{h}_{\mathrm{th}}$), like a random field, it will multiply the magnetization, so it will be treated like multiplicative noise.

Following Scholz [209], we can write this random field as:

$$\mathbf{h}_{\mathrm{th}}(\mathbf{r}) = \frac{\upsilon(\mathbf{r})}{M_s}\sqrt{\frac{2\alpha k_B T}{(1+\alpha^2)\,\mu_0 a^3 d\tau}} \tag{B.124}$$

Here $\upsilon\eta(\mathbf{r})$ is a random vairable, gaussian distributed, with zero mean and unit variance. T is the temperature, k_B is the Boltzmann constant and $d\tau$ is the time step. The other parameters have been already defined.

Appendix C

Parameters values and model units

In this appendix we expose in detail the parameter values and the reduced units used in the models explained before. Since, actually, the magnetoelastic model is an extension of the elastic Landau-based model, the former includes all the parameters of the latter and, therefore, we present all of them together. The material parameters that we chose for the simulations are taken from experimental data for $Fe_{70}Pd_{30}$ [33, 122].

Elastic parameters

First we focus on the pure elastic part. We have four independent magnitudes that are *force* (N), *length* (m) and *temperature* (K). We will use the the strain gradient coeficient κ to define the units of force ($u.f.$): $\kappa = 3.5306 \cdot 10^{-9} N = 1u.f.$ We use T_c to define the temperature units ($u.T.$): $T_c = 257K = 1u.T.$ We use α_T to define the units of length ($u.l.$):

$$\alpha_T = 2.4 \cdot 10^8 N/(m^2 K) = 1(u.f.)/((u.l.)^2(u.T.))$$

$$\Rightarrow 1u.l. \equiv l_0 = \sqrt{\frac{1u.f.m^2K}{1u.T.2.4\cdot10^8N}} = \sqrt{\frac{3.5306\cdot10^{-9}Nm^2K}{257K2.4\cdot10^8N}} = 2.3925 \cdot 10^{-10}m \qquad \text{(C.1)}$$

The value for the standard deviation of the disorder variable η, that is the disorder amplitude ζ has been chosen in such a way that the system approximately exhibits tweed up to 100 K above the transition point, as it is stated in Ref. [33]. Moreover, the correlation length ξ is chosen according to the characteristic length of the tweed modulation. This quantitative agreement between experimental tweed in Fe-Pd and our simulations, which has been shown in Chap. 3. The values of the other parameters in the model units can be easily derived from the relations above. They can be found in table C.1.

Magnetic and magnetoelastic parameters

We use M_s to define the units of current intensity ($u.i.$):

$$M_s = 1.08 \cdot 10^6 \text{A}/m = 1u.i./1u.l. \Rightarrow 1u.i. = 1.08 \cdot 10^6 (\text{A}/m) \cdot u.l.$$
$$= 1.08 \cdot 10^6 \text{A}/m \cdot 2.3925 \cdot 10^{-10} m = 2.5839 \cdot 10^{-4} \text{A} \tag{C.2}$$

The exchange parameter A has been estimated in the following way: what we have done is to compare the form of the Heisenber hamiltonian and the form of the exchange term of the micromagnetic model, in order to get a relation between the interaction constant J of the Heisenberg model and our exchange parameter A. We can obtain J through the Curie temperature T_{Curie}[1] by means of the exact solution of Ising model in 2D. Let's show it matematically: The hamiltonian of the Heisenberg model is the following:

$$H = -J \sum_{<i,j>} \mathbf{m}_i \cdot \mathbf{m}_j \tag{C.3}$$

where i, j are the positions of the spins in a lattice. Rewriting $\mathbf{m}_i \cdot \mathbf{m}_j = \frac{1}{2} \left(\mathbf{m}_i^2 + \mathbf{m}_j^2 - (\mathbf{m}_i - \mathbf{m}_j)^2 \right)$ in the hamiltonian, and taking into account that $\mathbf{m}_i^2 = 1$ we get:

$$H = J \sum_{<i,j>} \left(-1 + \frac{1}{2} (\mathbf{m}_i - \mathbf{m}_j)^2 \right) \tag{C.4}$$

Now we shift the origin of energy to absorb the constant in the hamiltonian. We then obtain:

$$H = \frac{J}{2} \sum_{<i,j>} (\mathbf{m}_i - \mathbf{m}_j)^2 \tag{C.5}$$

Multiplying and dividing by a'^2 and a'^3 (where a is the distance between spins) we get:

$$H = \frac{Ja'^2}{2a'^3} \sum_{<i,j>} \left(\frac{\mathbf{m}_i - \mathbf{m}_j}{a'} \right)^2 a'^3 \tag{C.6}$$

Comparing with the discretized expression of the exchange term, we get $A = J/2a'$. We also know the exact solution of the Ising model in 2D, $J = k_B T_{Curie}/4$ so we can obtain A from $A = k_B T_{Curie}/8a'$, where for $Fe_{70}Pd_{30}$ $T_{Curie} \sim 750K$. In our model the lattice constant of the material and the unit cell size are of the same order of magnitude. Therefore, we can choose a to take one of both values. The resulting A is of the same order of magnitude of the experimental values of another similar materials [210–215]: $A \sim 10^{-12} - 10^{-13} J/m$.

---

[1]We denote the Curie temperature as T_{Curie} in order to avoid confusion with the low stability limit of the high temperature phase of the martensitic transition T_c.

Experimental parameters λ_{111} and λ_{100} are related to the magnetoelastic coupling parameters B_1 and B_2 through the following relations:

$$\lambda_{100} = -\frac{2}{3}\frac{B_1}{A_2} \qquad \lambda_{111} = -\frac{1}{3}\frac{B_2}{A_3} \tag{C.7}$$

Let also remember a couple of constants used in this model:

$$\mu_0 = 4\pi \cdot 10^{-7}\text{N/A}^2; \qquad k_B = 1.3806503 \cdot 10^{-23}\text{N/(m} \cdot \text{K)} \tag{C.8}$$

In table C.1 we summarize the values of all the parameters in S.I. units and in reduced units, together with the corresponding mathematical symbols.

Magnitude	Symbol	Numerical value (S.I. units)	Numerical value (Model units)
Deviatoric elastic constant	α_T	$2.4 \cdot 10^8 \mathrm{N}/(\mathrm{m}^2\mathrm{K})$	$1(\text{u.f.})/((\text{u.l.})^2(\text{u.T.}))$
Shear elastic constant	A_3	$28 \cdot 10^{10} \mathrm{~N}/\mathrm{m}^2$	$4.5396(\text{u.f.})/(\text{u.l.})^2$
Bulk Modulus	A_1	$14 \cdot 10^{10}\mathrm{N}/\mathrm{m}^2$	$2.2698(\text{u.f.})/(\text{u.l.})^2$
Low stability limit of the high-T phase	T_c	257	$1(\text{u.T.})$
4th order Landau coefficient	β	$1,7 \cdot 10^{13}\mathrm{N}/\mathrm{m}^2$	$275.62(\text{u.f.})/(\text{u.l.})^2$
6th order Landau coefficient	γ	$3 \cdot 10^{16}\mathrm{N}/\mathrm{m}^2$	$4.864 \cdot 10^5(\text{u.f.})/(\text{u.l.})^2$
Ginzburg coefficient	κ	$3.5306 \cdot 10^{-9}\mathrm{N}$	$1(\text{u.f.})$
Disorder's correlation length	ξ	$4.785 \cdot 10^{-10}\mathrm{m}$	$20(\text{u.l.})$
Disorder's standard deviation	ζ	$83.3\mathrm{K}$	$0.324(\text{u.T.})$
Unit cell length	Λ	$4.55 \cdot 10^{-10}\mathrm{m}$	$1.9(\text{u.l.})$
Saturation magnetization	M_s	$1.08 \cdot 10^6\mathrm{A}/\mathrm{m}$	$1(\text{u.i.})/(\text{u.l.})$
Magnetocrystalline anisotropy constant	K_1	$-5.2 \cdot 10^2 \mathrm{~N}/\mathrm{m}^2$	$-8.106 \cdot 10^{-9}\text{u.f.}/(\text{u.l.})^2$
Magnetocrystalline anisotropy constant	K_2	$-6.6 \cdot 10^4 \mathrm{~N}/\mathrm{m}^2$	$-1.07 \cdot 10^{-6}\text{u.f.}/(\text{u.l.})^2$
Magnetoelastic coupling parameter	λ_{100}	$2 \cdot 10^{-4}$	$2 \cdot 10^{-4}$
Magnetoelastic coupling parameter	λ_{111}	$8 \cdot 10^{-5}$	$8 \cdot 10^{-5}$
Exchange parameter	A	$10^{-12} - 10^{-13} \mathrm{~N}/\mathrm{m}^2$	$3 \cdot (10^{-4} - 10^{-5}) \text{ u.f.}/(\text{u.l.})^2$
Vacuum permeability	μ_0	$4\pi \cdot 10^{-7}\mathrm{N}/\mathrm{A}^2$	$4\pi \cdot 1.891 \cdot 10^{-6}\text{u.f.}/(\text{u.i.})^2$
Bolzmann constant	k_B	$1.3806503 \cdot 10^{-23}\mathrm{N}/(\mathrm{m}\cdot\mathrm{K})$	$42.006486 \cdot 10^{-4}(\text{u.f.})(\text{u.l.})/(\text{u.T.})$

Table C.1: Symbols and values in S.I. and reduced units of the parameters of the model.

References

[1] S. Miyazaki and K. Otsuka, "Development of shape memory alloys", ISIJ Int. **29**(5), 353–377 (1989).

[2] A. Planes, L. Mañosa and A. Saxena, *Magnetism and Structure in Functional Materials* (Springer, Berlin, 2005).

[3] A. Saxena and G. Barsch, "Lattice dynamics representation theory versus isotropy subgroup method with application to M_5^- mode instability in CsCl structure", Phase Transitions **46**, 89–142 (1994).

[4] V. K. Wadhawan, *Introduction to ferroic materials* (Gordon and Breach Science Publishers, Amsterdam, 2000).

[5] E. K. Salje, *Phase transitions in ferroelastic and co-elastic crystals* (Cambridge University Press, Cambridge, 1990).

[6] A. Khachaturyan, "Domain structure in martensitic transformation", Trans. Mat. Res. Soc. Jpn. **18B**, 799–808 (1994).

[7] A. Bratkovsky, V. H. S.C. Marais and E. Salje, "The theory of fluctuations and texture embryos in structural phase transitions mediated by strain", J. Phys.: Condens. Matter **6**, 3678–3696 (1994).

[8] Y. Ma, C. Jiang, G. Feng and H. Xu, "Thermal stability of the $Ni_{54}Mn_{25}Ga_{21}$ Heusler alloy with high temperature transformation", Scr. Mater. **48**, 365–369 (2003).

[9] C. Manolikas and S. Amelinckx, "Phase transitions in ferroelastic lead orto-vanadate as observed by means of electron microscopy and electron diffraction (I). Static observations", Phys. Stat. Sol. A **60**, 607–617 (1980).

[10] G. Arlt, D. Hennings and G. de With, "Dielectric properties of fine-grained barium titanate ceramics", J. Appl. Phys. **58**(4), 1619–1625 (1985).

[11] L. S. Chumbley, J. D. Verhoeven, M. R. Kim, A. L. Cornelius and M. J. Kramer, "Measurement and correlation of optical and TEM twins in $Y_1Ba_2Cu_3O_{7-\delta}$", IEEE Trans. Magn. **25**(2), 2337–2340 (1989).

[12] T. Roy and T. E. Mitchell, "Twin boundary energies in $Y_1Ba_2Cu_3O_{7-\delta}$ and La_2Cu0_4", Phil. Mag. A **63**(2), 225–232 (1991).

[13] K. Battacharya, *Microstructure of martensite* (Oxforfd University Press, New York, USA, 2003).

[14] M. Ahlers, "The martensitic transformation: Mechanisms and stabilities", unpublished.

[15] *Shape Memory Materials*, edited by K. Otsuka and C. M. Wayman (Cambridge University Press, Cambridge, UK, 1998).

[16] J. Nye, *Physical properties of crystals* (Oxford University Press, London, UK, 1957).

[17] A. Millis, "Towards a classification of the effects of disorder on material properties", Solid State Commun. **126**, 3–8 (2003).

[18] Y. Imry and M. Wortis, "Influence of quenched impurities on first-order phase transitions", Phys. Rev. B **19**(7), 3580–3585 (1979).

[19] S. Miyazaki, K. Otsuka and Y. Suzuki, "Transformation pseudoelasticity and deformation behavior in a Ti-50.6at%Ni alloy", Scr. Metall. **15**(3), 287–292 (1981).

[20] Y. Wang, X. Ren, K. Otsuka and A. Saxena, "Temperature-stress phase diagram of strain glass $Ti_{48.5}Ni_{51.5}$", Acta Mater. **56**(12), 2885–2896 (2008).

[21] N. Nakanishi, T. Mori, S. Miura, Y. Murakami and S. Kachi, "Pseudoelasticity in Au-Cd thermoelastic martensite", Phil. Mag. **28**(2), 277–292 (1973).

[22] T.-H. Nam, J.-H. Kim, T.-Y. Kim, Y.-K. Lee and Y.-W. Kim, "Superelasticity of Ti-Ni-Cu alloy ribbons fabricated by melt spinning", J. Mat. Sci. Lett. **21**, 1851–1853 (2002).

[23] V. A. Chernenko, V. L'vov, J. Pons and E. Cesari, "Superelasticity in high temperature Ni-Mn-Ga alloys", J. Appl. Phys. **93**, 2394–2399 (2003).

[24] R. Kainuma, Y. Imano, W. Ito, Y. Sutou, H. Morito, S. Okamoto, O. Kitakami, A. F. K. Oikawa, T. Kanomata and K. Ishida, "Magnetic-field-induced shape recovery by reverse phase transformation", Nature Lett. **439**(23), 957–960 (2006).

[25] S. M. Shapiro, B. X. Yang, Y. Noda, L. E. Tanner and D. Schryvers, "Neutron-scattering and electron-microscopy studies of the premartensitic phenomena in Ni_xAl_{100-x} alloys", Phys. Rev. B **44**, 9301 (1991).

[26] S. M. Shapiro, J. Z. Larese, Y. Noda, S. C. Moss and L. E. Tanner, "Neutron scattering study of premartensitic behavior in Ni-Al alloys", Phys. Rev. Lett. **57**(25), 3199–3202 (1986).

[27] S. Muto, R. Oshima and F. Fujita, "Elastic softening and elastic strain energy consideration in the f.c.c.–f.c.t. transformation of Fe-Pd alloys", Acta Metall. Mater. **38**(4), 685–694 (1990).

[28] D. Schryvers, D. E. Lahjouji, B. Slootmaekers and P. L. Potapov, "HREM investigation of martensite precursor effects and stacking sequences in Ni-Mn-Ti alloys", Scr. Mater. **35**(10), 1235–1241 (1996).

[29] J. A. Krumhansl and Y. Yamada, "Some new aspects of first-order displacive phase transformations: martensites", Mater. Sci. Eng. A **127**, 167 (1990).

[30] Y. Murakami, H. Shibuya and D. Shindo, "Precursor effects of martensitic transformations in Ti-based alloys studied by electron microscopy with energy filtering", J. Microsc. **203**, 22–33 (2001).

[31] L. Tanner, A. Pelton and R. Gronsky, "The characterization of pretransformation morphologies: Periodic strain modulations", J. Phys. (Paris) Colloq. **43**(C4), 169–172 (1982).

[32] G. V. Tendeloo, M. Chandrasekaran and F. C. Lovey, "Modulated microstructures in β Cu-Zn-Al", Metall. Trans. A **17A**, 2153–2161 (1986).

[33] S. Kartha, J. A. Krumhansl, J. P. Sethna and L. K. Wickham, "Disorder-driven pretransitional tweed pattern in martensitic transformations", Phys. Rev. B **52**(2), 803–822 (1995).

[34] S. Sarkar, X. Ren and K. Otsuka, "Evidence for Strain Glass in the Ferroelastic-Martensitic System $Ti_{50-x}Ni_{50+x}$", Phys. Rev. Lett. **95**(20), 205702-1–205702-4 (2005).

[35] I. M. Robertson and C. M. Wayman, "Tweed microstructures III. Origin of the tweed contrast in β and γ Ni-Al alloys", Phil. Mag. A **48**(4), 629–647 (1983).

[36] A. Planes, L. M. nosa and E. Vives, "Vibrational behavior of bcc Cu-based shape-memory alloys close to the martensitic transition", Phys. Rev. B **53**(6), 3039–3046 (1996).

[37] X. Ren, N. Miura, J. Zhang, K. Otsuka, K. Tanaka, M. Koiwa, T. Suzuki, Y. Chumlyakov and M. Asai, "A comparative study of elastic constants of Ti-Ni-based alloys prior to martensitic transformation", Mat. Sci. Eng. A **312**, 196–206 (2001).

[38] J. Worgull, E. Petti and J. Trivisonno, "Behavior of the elastic properties near an intermediate phase transition in Ni_2MnGa", Phys. Rev. B **54**(22), 15695–15699 (1996).

[39] E. Cesari, V. A. Chernenko, V. V. Kokorin, J. Pons and C. Seguí, "Internal friction associated with the structural phase transformations in Ni-Mn-Ga alloys", Acta Mater. **45**(3), 999–1004 (1997).

[40] S. M. Shapiro, G. Xu, B. L. Winn, D. L. Schlagel, T. Lograsso and R. Erwin, "Anomalous phonon behavior in the high-temperature shape-memory alloy $Ti_{50}Pd_{50-x}Cr_x$", Phys. Rev. B **76**(5), 054305-1–054305-8 (2007).

[41] S. M. Shapiro, B. L. Winn, D. L. Schlagel, T. Lograsso and R. Erwin, "Phonon precursors to the high temperature martensitic transformation in $Ti_{50}Pd_{42}Cr_8$", J. Phys. IV France **112**, 1047–1050 (2003).

[42] A. J. Schwartz and L. E. Tanner, "Phase transformations and phase relations in the TiPd-Cr pseudobinary system I. Experimental observations", Scr. Metall. Mater. **32**(5), 675–680 (1995).

[43] Z. Nishiyama, *Martensitic Transformation* (Academic press, London, UK, 1978).

[44] M. Ahlers, "The martensitic transformation: Mechanisms and crystallography", Phil. Mag. A **82**(6), 1093–1114 (2002).

[45] A. Planes and L. Mañosa, "Vibrational Properties of Shape-Memory Alloys", Solid State Phys. **55**, 159–267 (2001).

[46] F. Pérez-Reche, E. Vives, L. Mañosa and A. Planes, "Athermal Character of Structural Phase Transitions", Phys. Rev. Lett. **87**(19), 195701-1–195701-4 (2001).

[47] A. Hubert and R. Schafer, *Magnetic domains. The analysis of magnetic microstructures* (Springer, Berlin, 1998).

[48] D. Jiles, "Recent advances and future directions in magnetic materials", Acta Mater. **51**(19), 5907–5939 (2003).

[49] F. Saurenbach and B. D. Terris, "Imaging of ferroelectric domain walls by force microscopy", Appl. Phys. Lett. **56**(17), 1703–1705 (1990).

[50] J. F. Scott, "Nanoferroelectrics: statics and dynamics", J. Phys.: Condens. Matter **18**(17), R361–R386 (2006).

[51] R. James and M. Wuttig, "Magnetostriction of martensite", Phil. Mag. A **77**, 1273–1299 (1998).

[52] T. Fukuda, T. Sakamoto, T. Kakeshita, T. Takeuchi and K. Kishio, "Re-arrangement of Martensite Variants in Iron-Based Ferromagnetic Shape Memory Alloys under Magnetic Field", Mater. Trans. **45**(2), 188–192 (2004).

[53] M. Uehara, S. Mori, C. Chen and S.-W. Cheong, "Percolative phase separation underlies colossal magnetoresistance in mixed-valent manganites", Nature **399**, 560–563 (1999).

[54] N. A. Spaldin and M. Fiebig, "The renaissance of magnetoelectric multiferroics", Science **309**, 391–392 (2005).

[55] E. Dagotto, "Open questions in CMR manganites, relevance of clustered states and analogies with other compounds including cuprates", New J. Phys. **7**, 1–28 (2005).

[56] K. Ahn, T. Lookman and A. Bishop, "Strain-induced metal-insulator phase coexistence in perovskite manganites", Nature **428**, 401–404 (2004).

[57] A. Moreo, M. Mayr, A. Feiguin, S. Yunoki and E. Dagotto, "Giant cluster co-existence in doped manganites and other compounds", Phys. Rev. Lett. **84**(24), 5568–5571 (2000).

[58] G. Xu, J. Wen, C. Stock and P. Gehring, "Phase instability induced by polar nanoregions in a relaxor ferroelectric system", Nature Mat. **7**, 562–566 (2008).

[59] E. Dagotto, "Complexity in Strongly Correlated Electronic Systems", Science **309**(5732), 257–262 (2005).

[60] A. Bishop, T. Lookman, A. Saxena and S. Shenoy, "Elasticity-driven nanoscale texturing in complex electronic materials", Europhys. Lett. **63**(2), 289–295 (2003).

[61] Y. Murakami, D. Shindo, K. Oikawa, R. Kainuma and K. Ishida, "Magnetic domain structures in Co-Ni-Al shape memory alloys studied by Lorentz microscopy and electron holography", Acta Mater. **50**(8), 2173–2184 (2002).

[62] M. Porta, T. Castán, A. Planes and A. Saxena, "Precursor nanoscale modulations in ferromagnets: Modeling and thermodynamic characterization", Phys. Rev. B **72**(5), 054111 (2005).

[63] N. Mathur and P. Littlewood, "Nanotechnology: The third way", Nature Materials **3**(4), 207–209 (2004).

[64] R. B. Griffiths, "Nonanalytic behavior above the critical point in a random Ising ferromagnet", Phys. Rev. Lett. **23**, 17–19 (1969).

[65] J. Deisenhofer, D. Braak, H.-A. K. von Nidda, J. Hemberger, R. Eremina, V. Ivanshin, A. Balbashov, G.Jug, A. Loidl, T. Kimura and Y. Tokura, "Observation of a Griffiths phase in paramagnetic $La_{1-x}Sr_xMnO_3$", Phys. Rev. Lett. **95**(25), 257202-1–257202-4 (2005).

[66] A. Saxena, T. Castán, A. Planes, M. Porta, Y. Kishi, T. A. Lograsso, D. Viehland, M. Wuttig and M. De Graef, "Origin of Magnetic and Magnetoelastic Tweedlike Precursor Modulations in Ferroic Materials", Phys. Rev. Lett. **92**(19), 197203-1–197203-4 (2004).

[67] Y. Wang, X. Ren and K. Otsuka, "Shape Memory Effect and Superelasticity in a Strain Glass Alloy", Phys. Rev. Lett **97**(22), 225703-1–225703-4 (2006).

[68] Y. Wang, X. Ren, K. Otsuka and A. Saxena, "Evidence for broken ergodicity in strain glass", Phys. Rev. B **76**(13), 132201-1–132201-4 (2007).

[69] Y. Wang, X. Ren and K. Otsuka, "Strain Glasss: Glassy Martensite", Mater. Sci. Forum **583**(22), 67–84 (2008).

[70] Y. Zhou, D. Xue, X. Ding, K. Otsuka, J. Sun and X. Ren, "High temperature strain glass in $Ti_50(Pd_{50-x}Cr_x)$ alloy and the associated shape memory effect and superelasticity", Appl. Phys. Lett. **95**, 151906-1–151906-3 (2009).

[71] X. Ren, Y. Wang, Y. Zhou, Z. Zhang, D. Wang, G. Fan, K. Otsuka, T. Suzuki, Y. Ji, J. Zhang, Y. Tian, S. Hou and X. Ding, "Strain glass in ferroelastic systems–premartensitic tweed vs. strain glass", unpublished.

[72] Z. Zhang, Y. Wang, D. Wang, Y. Zhou, K. Otsuka and X. Ren, "Strain glass phase diagram of $Ti_{50-x}Ni_{50+x}$", unpublished.

[73] Y. Zhou, D. Xue, X. Ding, Y. Wang, J. Zhang, Z. Zhang, K. Otsuka, J. Sun and X. Ren, "Strain glass in doped $Ti_50(Ni_{50-x}D_x)$(D=Co, Cr, Mn) alloys. Implication for the generality of strain glass in defect-containing ferroelastic systems", unpublished.

[74] C. Angell, "Formation of Glasses from Liquids and Biopolymers", Science **267**, 1924–1935 (1995).

[75] C. Kittel, *Introduction to solid state physics*, 8 ed. (Wiley, New York, USA, 2005).

[76] J. M. D. Coey and P. W. Readman, "New spin structure in an amorphous ferric gel", Nature **246**, 476–478 (1973).

[77] R. Brand, P. Lunkenheimer and A. Loidl, "Relaxation dynamics in plastic crystals", J. Chem. Phys. **116**, 10386–10401 (2002).

[78] D. Viehland, J. F. Li, S. J. Jang, L. E. Cross and M. Wuttig, "Glassy polarization behavior of relaxor ferroelectrics", Phys. Rev. B **46**, 8013–8017 (1992).

[79] C. Dekker, W. Eidelloth and R. H. Koch, "Measurement of the Exponent μ in the Low-Temperature Phase of $YBa_2Cu_3O_{7-\delta}$ Films in a Magnetic Field: Direct Evidence for a Vortex-Glass Phase", Phys. Rev. Lett. **68**(22), 3347–3350 (1992).

[80] C. Angell, "Entropy, Fragility, "landscapes" and the glass transition", in *Complex behaviour of glassy systems* (Springer Berlin, Heidelberg, 1997), vol. 492, Chap. 1, pp. 1–21.

[81] R. Moessner and P. Ramirez, "Geometrical Frustration", Physics today **59**, 24–29 (2006).

[82] Y. Han, Y. Shokef, A. Alsayed, P. Yunker, T. Lubesnky and A. Yodh, "Geometric frustration in buckled colloidal monolayers", Nature **456**, 898–903 (2008).

[83] R. Wang, C. Nisoli, R. Freitas, J. Li, W. McConville, B. Cooley, M. Lund, N. Samarth, C. Leighton, V. Crespi and P. Schiffer, "Artificial 'spin ice' in a geometrically frustrated lattice of nanoscale ferromagnetic islands", Nature **439**, 303–306 (2006).

[84] E. Duman, M. Acet, Y. Elerman, A. Elmali and E. Wasserman, "Magnetic interactions in $Pr_{1-x}Tb_xMn_2Ge_2$", J. Magn. Magn. Mater. **238**(1), 11–21 (2002).

[85] S. Shenoy and T. Lookman, "Strain pseudospins with power-law interactions: Glassy textures of a cooled coupled-map lattice", Phys. Rev. B **78**(14), 144103-1–144103-17 (2008).

[86] A. Olander, "The crystal structure of AuCd", Zeitschrift Für Kristallographie **83**(1/2), 145–148 (1932).

[87] S. Muto, R. Oshima and F. Fujita, "Electron microscope study on martensitic transformations in Fe-Pt alloys: General features of internal structure", Metall. Mater. Trans. **19**(11), 2723–2731 (1988).

[88] K. Jee, P. Potapov, S. Song and M. Shin, "Shape memory effect in NiAl and NiMn-based alloys", Scr. Mater. **36**(2), 207–212 (1997).

[89] H. Tas, L. Delaey and A. Deruyttere, "Stress induced phase transformations and the shape memory effect in β_1' copper-aluminum martensite", Scr. Metall. **5**(12), 1117–1124 (1971).

[90] M. Nishida, T. Hara, Y. Morizono, A. Ikeya, H. Kijima and A. Chiba, "Transmission electron microscopy of twins in martensite in Ti-Pd shape memory alloy", Acta Mater. **45**(11), 4847–4853 (1997).

[91] Z. Basinki and J. Christian, "Crystallography of deformation by twin boundary movements in indium-thallium alloys", Acta Metall. **2**, 101–116 (1954).

[92] T. Schroeder and C. Wayman, "Pseudoelastic effects in Cu-Zn single crystals", Acta Metall. **27**, 405–417 (1979).

[93] R. Fonda, H. Jones and R. Vandemeer, "The shape memory effect in equiatomic TaRu and NbRu alloys", Scr. Metall. **39**(8), 1031–1037 (1998).

[94] G. Barcelo, R. Rapacioli and M. Ahlers, "The rubber effect in Cu-Zn-Al martensite", Scr. Metall. **12**, 1069–1074 (1978).

[95] S. Miura, S. Maeda and N. Nakanishi, "Pseudoelasticity in Au-Cu-Zn thermoelastic martensite", Phil. Mag. **30**, 565–581 (1974).

[96] H. Sakamoto, Y. Kijima, K. Shimizu and K. Otsuka, "Twinning pseudoelasticity caused by cyclic stress in a single crystal Cu-Al-Ni alloy", Scr. Metall. **15**, 281–285 (1981).

[97] S. Belkahla, H. Flores-Zuñiga and G. Guenin, "Elaboration and characterization of new low temperature shape memory Cu-Al-Be alloys", Mater. Sci. Eng. **169**(1-2), 119–124 (1993).

[98] H. Ishikawa, Y. Sutou, T. Omori, K. Oikawa, K. Ishida, A. Yoshikawa, R. Umetsu and R. Kainuma, "Pd-In-Fe shape memory alloy", App. Phys. Lett. **90**, 261906-1–261906-3 (2007).

[99] J. Dadda, H. J. Maier, I. Karaman and Y. I. Chumlyakov, "Cyclic deformation and austenite stabilization in $Co_{35}Ni_{35}Al_{30}$ single crystalline high-temperature shape memory alloys", Acta Mater. **57**(20), 6123–6134 (2009).

[100] T. Krenke, M. Acet, E. F. Wassermann, X. Moya, L. Mañosa and A. Planes, "Martensitic transitions and the nature of ferromagnetism in the austenitic and martensitic states of Ni-Mn-Sn alloys", Phys. Rev. B **72**(1), 014412-1–014412-9 (2005).

[101] T. Krenke, M. Acet, E. F. Wassermann, X. Moya, L. Mañosa and A. Planes, "Ferromagnetism in the austenitic and martensitic states of Ni-Mn-In alloys", Phys. Rev. B **73**(17), 174413-1–174413-10 (2006).

[102] Y. Sutou, N. Kamiya, T. Omori, R. Kainuma, K. Ishida and K. Oikawa, "Stress-strain characteristics in Ni-Ga-Fe ferromagnetic shape memory alloys", Appl. Phys. Lett. **84**(8), 1275–1277 (2004).

[103] Z. H. Liu, M. Zhang, W. Q. Wang, W. H. Wang, J. L. Chen and G. H. Wu, "Magnetic properties and martensitic transformation in quaternary Heusler alloy of NiMnFeGa", J. Appl. Phys. **92**(9), 5006–5010 (2002).

[104] M. Ohtsuka, M. Matsumoto and K. Itagaki, "Effect of iron and cobalt addition on magnetic and shape memory properties of Ni_2MnGa sputtered films", Mater. Sci. Eng. **438–440**, 935–939 (2006).

[105] M. Khan, I. Dubenko, S. Stadler and N. Ali, "Magnetic and structural phase transitions in Heusler type alloys $Ni_2MnGa_{1-x}In_x$", J. Phys.: Condens. Matter **16**, 5259–5266 (2004).

[106] J. Juárez-Islas, R. Pérez and S. Savage, "HREM studies of rapidly solidified Ni-Fe-Al-B shape memory alloys", Mater. lett. **14**(1), 1–6 (1992).

[107] P. Sittner, V. Novák and N. Zárubová, "Martensitic transformations in [001] CuAlZnMn single crystals", Acta. Mater. **46**(4), 1265–1281 (1998).

[108] F. Dalle, A. Pasko, P. Vermaut, V. Kolomytsev, P. Ochin and R. Portier, "Melt-spun ribbons of Ti-Hf-Ni-Re shape memory alloys: first investigations", Scr. Mater. **43**(4), 331–335 (2000).

[109] T. Sohmura, R. Oshima and F. Fujita, "Thermoelastic FFC-FCT martensitic transformation in Fe-Pd alloy", Scr. Metall. **14**(8), 855–856 (1980).

[110] R. Oshima, "Successive martensitic transformations in Fe-Pd alloys", Scr. Metall. **15**(8), 829–833 (1981).

[111] M. Sugiyama, S. Harada and R. Oshima, "Change in young's modulus of thermoelastic martensite Fe-Pd alloys", Scr. Metall. **19**(3), 315–317 (1985).

[112] R. Oshima, M. Sugiyama and F. Fujita, "Tweed structures associated with Fcc-Fct transformations in Fe-Pd alloys", Metall. Mater. Trans. A **19**(4), 803–810 (1988).

[113] S. Muto, S. Takeda and R. Oshima, "Analysis of lattice modulations in the tweed structure of an Fe-Pd alloy by image processing of a high-resolution electron micrograph", Jpn. J. Appl. Phys. **29**(10), 2066–2071 (1990).

[114] K. Otsuka and X. Ren, "Physical metallurgy of Ti-Ni-based shape memory alloys", Prog. Mater. Sci. **50**(5), 511–678 (2005).

[115] H. Seto, Y. Noda and Y. Yamada, "Precursor Phenomena at Martensitic Phase Transition in Fe-Pd Alloy. I. Two-Tetragonal-Mixed Phase and Crest-Riding-Periodon", J. Phys. Soc. Jpn. **59**, 965–977 (1990).

[116] H. Seto, Y. Noda and Y. Yamada, "Precursor Phenomena at Martensitic Phase Transition in Fe-Pd Alloy. II. Diffuse Scattering and Embryonic Fluctuations", J. Phys. Soc. Jpn. **59**, 978–986 (1990).

[117] V. Sánchez-Alarcos, V. Recarte, J. I. Pérez-Landazábal, C. Gómez-Polo, V. A. Chernenko and M. A. González, "Reversible and irreversible martensitic transformations in Fe-Pd and Fe-Pd-Co alloys", Eur. Phys. J. **158**(1), 107–112 (2008).

[118] S. Shabalovskaya, "Surface, corrosion and biocompatibility aspects of nitinol as an implant material", Bio-Med. Mater. Engin. **12**, 69–109 (2002).

[119] H. Kato, Y. Liang and M. Taya, "Stress-induced FCC/FCT phase transformation in Fe-Pd alloy", Scr. Mater. **46**, 471–475 (2002).

[120] T. Wada, Y. Liang, H. Kato, T. Tagawa, M. Taya and T.Mori, "Structural change and straining in Fe-Pd polycrystals by magnetic field", Mat. Sci. Eng. A **361**, 75–82 (2003).

[121] T. Kakeshita and K. Ullakko, "Giant Magnetostriction in Ferromagnetic Shape-Memory Alloys", MRS Bull. **27**(2), 105–109 (2002).

[122] J. Cui, T. W. Shield and R. D. James, "Phase transformation and magnetic anisotropy of an iron-palladium ferromagnetic shape-memory alloy", Acta Mater. **52**(1), 35–47 (2004).

[123] T. Kakeshita and T.Fukuda, "Magnetic field-induced martensitic transformations in some ferrous alloys", Trans. Mat. Res. Soc. Jpn. **25**(2), 475–480 (2000).

[124] S. Gururaja, M. Taya and Y. S. Kang, "Design of ferromagnetic shape memory alloy composite made of Fe and TiNi particles", J. Appl. Phys. **102**(6), 064910-1–6 (2007).

[125] Y. M. T. Tagawa, T. Wada and M. Taya, "Design of ferromagnetic shape memory alloy composites based on TiNi for robust and fast actuators", in *Smart Structures and Materials 2002: Active Materials: Behavior and Mechanics*, edited by C. S. Lynch (Proc. SPIE, San Diego, CA, USA, 2002), vol. 4699, pp. 172–181.

[126] G. Barsch, B. Horovitz and J. Krumhansl, "Dynamics of twin boundaries in martensites", Phys. Rev. Lett. **59**, 1251–1254 (1987).

[127] J. Eshelby, "The Determination of the Elastic Field of an Ellipsoidal Inclusion, and Related Problems", Proc. R. Soc. Lond. A **241**, 376–396 (1957).

[128] A. G. Khachaturyan, *The Theory of Structural Transformations in Solids* (Wiley, New York, 1983).

[129] A. Roitburd, "The domain structure of crystals formed in the solid state", Sov. Phys. Solid State **10**(12), 2870–2876 (1969).

[130] A. G. Khachaturyan and G. A. Shatalov, "Theory of macroscopic periodicity for a phase transition in the solid state", Sov. Phys. JETP **29**, 557–661 (1969).

[131] A. Artemev, Y. jin and A. G. Khachaturyan, "Three-dimensional phase field model of proper martensitic transformation", Acta mater. **49**, 1165–1177 (2001).

[132] Y. Jin, A. Artemev and A. G. Khachaturyan, "Three-dimensional phase field model of low-symmetry martensitic transformation in polycrystal: Simuation of ζ_2' martensite in AuCd alloys", Acta mater. **49**, 2309–2320 (2001).

[133] J. Zhang and L. Chen, "Phase-field microelasticity theory and micromagnetic simulations of domain structures in giant magnetostrictive materials", Acta Mater. **53**(9), 2845–2855 (2005).

[134] M. Wechsler, D. Lieberman and T. Read, "On the theory of the formation of martensite", Trans. Metall. Soc. AIME **197**, 1503–1515 (1953).

[135] J. Ball and R. James, "Fine phase mixtures as minimizers of energy", Arch. ration. Mech. Analysis **100**, 13–52 (1987).

[136] F. Falk, "Model free energy, mechanics, and themordynamics of shape memory alloys", Acta Metall. **28**, 1773–1780 (1980).

[137] F. Falk, "Ginzburg-Landau Theory of Static Domain Walls in Shape-Memory Alloys", Z. Phys. B **51**, 177–185 (1983).

[138] A. Jacobs, "Solitons of the square-rectangular martensitic transition", Phys. Rev. B **31**, 5984–5989 (1985).

[139] G. Barsch and J. Krumhansl, "Nonlinear and nonlocal continuum model of transformation precursors in martensites", Metall. Trans. A **19**(4), 761–775 (1988).

[140] A. Saxena and T. Lookman, in *Handbook of materials modeling*, edited by S. Yip (Springer, Berlin, 2005), pp. 2143–2155.

[141] P. Podio-Guidugli, "The compatibility constraint in linear elasticity", J. Elas. **59**, 393-398 (2000).

[142] W. Kerr, M. Killough, A. Saxena, P. Swart and A. Bishop, "Role of elastic compatibility in martensitic texture evolution", Phase Trans. **69**, 247–270 (1999).

[143] K. Rasmussen, T. Lookman, A. Saxena, A. Bishop, R. Albers and S. Shenoy, "Three-dimensional elastic compatibility and varieties of twins in martensites", Phys. Rev. Lett. **87**, 055704-1–055704-4 (2001).

[144] T. Lookman, S. Shenoy, K. Rasmussen, A. Saxena and A. Bishop, "Ferroelastic dynamics and strain compatibility", Phys. Rev. B **67**, 024114-1–024114-27 (2003).

[145] A. Saxena, T. Lookman, A. Bishop and S. Shenoy, in *Proc. Intrinsic multiscale structure and dynamics in complex electronic oxides* (World Scientific Publishing Co. Pte. Ltd., Singapore, 2003), pp. 84–97.

[146] R. Ahluwalia, T. Lookman and A. Saxena, "Dynamic strain loading of Cubic to Tetragonal Martensites", Acta Mater. **54**(8), 2109–2120 (2006).

[147] V. I. Levitas and D. L. Preston, "Three-dimensional Landau theory for multivariant stress-induced martensitic phase transformations. I. Austenite↔martensite", Phys. Rev. B **66**, 134206-1–134206-9 (2002).

[148] V. I. Levitas and D. L. Preston, "Three-dimensional Landau theory for multivariant stress-induced martensitic phase transformations. II. Multivariant phase transformations and stress space analysis", Phys. Rev. B **66**, 134207-1–134207-15 (2002).

[149] D. Sherrington, "A simple spin glass perspective on martensitic shape-memory alloys", J. Phys.: Condens. Matter **20**(30), 304213-1–5 (2008).

[150] K. Tanaka, F. Nishimura, T. Hayashi, H. Tobushi and C. Lexcellent, "Phenomenological analysis on subloops and cyclic behavior in shape memory alloys under mechanical and/or thermal loads", Mech. Mater. **19**, 281–292 (1995).

[151] W. Yan, C. H. Wang, X. P. Zhang and Y. W. Mai, "Theoretical modelling of the effect of plasticity on reverse transformation in superelastic shape memory alloys", Mat. Sci. Eng. A **354**, 146–157 (2003).

[152] C. Maletta, A. Falvo, F. Furgiuele and J. N. Reddy, "A phenomenological model for superelasticity in NiTi alloys", Smart Mat. Str. **18**, 025005-1–9 (2009).

[153] A. Bruce and R. Cowley, *Structural Phase Transitions* (Taylor and Francis, London, 1981).

[154] L. D. Landau and E. M. Lifshitz, *Theory of Elasticity* (Pergamon Press, Oxford, 1986).

[155] A. Bray, "Theory of phase ordering kinetics", Adv. Phys. **43**, 357–459 (1994).

[156] V. I. Levitas and D. W. Lee, "Athermal resistance to interface motion in the phase-field theory of microstructure evolution", Phys. Rev. Lett. **99**, 245701-1– 245701-4 (2007).

[157] V. I. Levitas, D. W. Lee and D. L. Preston, "Interface propagation and microstructure evolution in phase field models of stress-induced martensitic phase transformations", Int. J. Plast. **26**, 395–422 (2010).

[158] T. Ichitsubo, K. Tanaka, M. Koiwa and Y. Yamazaki, "Kinetics of cubic to tetragonal transformation under external field by the time-dependent Ginzburg-Landau approach", Phys. Rev. B **62**(9), 5435-5441 (2000).

[159] C. Becquart, P. Clapp and J. Rifkin, "Molecular-dynamics simulation of tweed structure and the ω phase in Ni-Al", Phys. Rev. B **48**(1), 6–13 (1993).

[160] S. Semenovskaya and A. G. Khachaturyan, "Coherent structural transformations in random crystalline systems", Acta Mater. **45**, 4367–4384 (1997).

[161] URL: http://www.fftw.org/.

[162] W. Press, S. Teukolsky, W. Vettering and B. Flannery, *Numerical recipes in Fortran* (Cambridge University Press, New York, USA, 1992).

[163] M.-S. Choi, T. Fukuda and T. Kakeshita, "Anomalies in resistivity, magnetic susceptibility and specific heat in iron-doped Ti-Ni shape memory alloys", Scr. Mater. **53**(7), 869–873 (2005).

[164] S. Semenovskaya, Y. Zhu, M. Suenaga and A. G. Khachaturyan, "Twin and tweed microstructures in $YBa_2Cu_3O_{7-\delta}$ doped by trivalent cations", Phys. Rev. B **47**(18), 12182–12189 (1993).

[165] Y. Xu, M. Suenaga, J. Tafto, R. Sabatini, A. Moodenbaugh and P. Zolliker, "Microstructure, lattice parameters, and superconductivity of $YBa_2(Cu_{1-x}Fe_x)_3O_{7-\delta}$ for $0 \leq x \leq 0.33$", Phys. Rev. B **39**(10), 6667–6680 (1989).

[166] W. Schmahl, A. Putnis, E. Salje, P. Freeman, A. Graeme-Barber, R. Jones, K. Singh, J. Blunt, P. Edwards, J. Loram and K. Mirza, "Twin formation and structural modulations in orthorombic and tetragonal $YBa_2(Cu_{1-x}Co_x)_3O_{7-\delta}$", Phil. Mag. Lett. **60**(6), 241–248 (1989).

[167] B. Horovitz, G. Barsch and J.A.Krumhansl, "Twin bands in martensites: Statics and dynamics", Phys. Rev. B **43**, 1021–1033 (1991).

[168] S. Shenoy, T. Lookman, A. Saxena and A. Bishop, "Martensitic textures: Multiscale consequences of elastic compatibility", Phys. Rev. B **60**, R12537–R12541 (1999).

[169] C. Leroux, A. Loiseau, G. Broddin and G. V. Tendeloo, "Electron microscopy study of the coherent two-phase mixtures $L1_0 + L1_2$ in Co-Pt alloys", Phil. Mag. B **64**, 57–82 (1991).

[170] K. I. U. and, "Structural aspects of AuCu I or AuCu II and a cuboidal block configuration of fcc disordered phase in AuCu-Pt and AuCu-Ag pseudobinary alloys", Mater. Sci. Eng. A **203**, 154–164 (1995).

[171] S. Yeo, Y. Horibe, S. Mori, C. M. Tseng, C. H. Chen, A. G. Khachaturyan, C. L. Zhang and S. W. Cheong, "Solid state sel-assembly of nanocheckerboards", Appl. Phys. Lett. **89**, 233120 (2006).

[172] B. S. Guilton and P. K. Davies, "Nano-chessboard superlattices formed by spontaneous phase separation in oxides", Nature Mater. **6**, 586–591 (2007).

[173] E. Salje and Y. Ishibashi, "Mesoscopic structures in ferroelastic crystals: needle twins and right-angled domains", J. Phys.: Condens. Matter **8**(44), 8477 (1996).

[174] A. Saxena, S. R. Shenoy, A. R. Bishop, Y. Wu and T. Lookman, "Hierarchical microstructure in structural phase transitions", Phase transitions **67**, 481–498 (1998).

[175] S. Nagata, P. Keesom and H.R.Harrison, "Low-dc-field susceptibility of CuMn spin glass", Phys. Rev. B **19**(3), 1633–1638 (1979).

[176] B. Martínez, X. Obradors, L. Balcells, A. Rouret and C. Monty, "Low temperature surface spin-glass transition in γ-Fe_2O3 nanoparticles", Phys. Rev. Lett. **80**(1), 181–184 (1998).

[177] V. Canella and J. Mydosh, "Magnetic ordering in Gold-Iron Alloys", Phys. Rev. B **6**, 4220–4237 (1976).

[178] E. Bonnot, R. Romero, X. Illa, L. Mañosa, A. Planes and E. Vives, "Hysteresis in a system driven by either generalized force or displacement variables: Martensitic phase transition in single-crystalline Cu-Al-Zn", Phys. Rev. B **76**, 064105-1–064105-5 (2007).

[179] J. Cui, Y. Chu, O. Famodu, Y.Furuya, J. Hattrick-Simpers, R. James, A. Ludwig, S. Thienhaus, M. Wuttig, Z. Zhang and I. Takeuchi, "Combinatorial search of thermoelastic shape-memory alloys with extremely small hysteresis width", Nature Mat. **5**, 286–290 (2006).

[180] Z. Zhang, R. James and S. Müller, "Energy barriers and hysteresis in martensitic phase transformations", Acta Mater. **57**, 4332–4352 (2009).

[181] R. Delville, S. Kasinathan, Z. Zhang, J. V. Humbeeck, R. D. James and D. Schryvers, "Transimission electron microscopy study of phase compatibility in low hysteresis shape memory alloys", Phil. Mag. **90**(1-4), 177-195 (2010).

[182] M. W. Zemansky and R. H. Dittman, *Calor y termodinámica* (McGraw-Hill, Madrid, 1984).

[183] E. Bonnot, R. Romero, L. Mañosa, E. Vives and A. Planes, "Elastocaloric Effect Associated with the Martensitic Transition in Shape-Memory Alloys", Phys. Rev. Lett. **100**(12), 125901-1–125901-4 (2008).

[184] A. Tishin, "Magnetocaloric effect in the vicinity of magnetic phase transitions", in *Handbook of Magnetic Materials*, edited by K. Buschow (Elsevier Science, Amsterdam, 1998), vol. 12.

[185] A. Romanov and V. Silin, Phys. Met. Metallogr. **83**, 111 (1997).

[186] F. Casanova, A. Labarta, X. Batlle, J. Marcos, L. Mañosa, A. Planes and S. de Brion, "Effect of a magnetic field on the magnetostructural phase transition in $Gd_5(Si_xGe_{1-x})_4$", Phys. Rev. B **69**(10), 104416-1–104416-7 (2004).

[187] T. Krenke, E. Duman, M. Acet, E. Wassermann, X. Moya, L. Mañosa and A. Planes, "Inverse magnetocaloric effect in ferromagnetic Ni-Mn-Sn alloys", Nat. Mat. Lett. **4**, 450–454 (2005).

[188] T. Kakeshita, T. Fukuda and T. Takeuchi, "Magneto-mechanical evaluation for twinning plane movement driven by magnetic field in erromagnetic shape memory alloys", Mater. Sci. Eng. A **438–440**, 12–17 (206).

[189] Y. Zhu and G. Dui, "Micromechanical modeling of the stress-induced superelastic strain in magnetic shape memory alloy", Mech. Mater. **39**, 1025–1034 (2007).

[190] P. P. Wu, X. Q. Ma, J. X. Zhang and L. Q. Chen, "Phase-field simulations of stress-strain behavior in ferromagnetic shape memory alloy Ni$_2$MnGa", J. Appl. Phys. **104**(7), 073906-1–073906-5 (2008).

[191] N. I. Glavatska, A. A. Rudenko, I. N. Glavatskiy and V. A. L'vov, "Statistical model of magnetostrain effect in martensite", J. Magn. Magn. Mater. **265**, 142–151 (2003).

[192] A. Morrish, *The physical principles of magnetism* (Wiley, New York, USA, 1995).

[193] J. Fidler and T. Schrefl, "Micromagnetic modelling–the current state of the art", J. Phys. D: Appl Phys **33**, R135–156 (2000).

[194] R. McMichael, M. Donahue, D. Porter and J. Eicke, "Comparison of magnetostatic field calculation methods on two-dimensional square grids as applied to a micromagnetic standard problem", J. Appl. Phys. **85**(8), 5816–5818 (1999).

[195] C. Kittel, "Physical Theory of Ferromagnetic Domains", Rev. Mod. Phys. **21**(4), 541–583 (1949).

[196] J. Deutsch and A. Berger, "Spin precession and avalanches", Phys. Rev. Lett. **99**, 027207-1–027207-4 (2007).

[197] S. Iwata, S. Isomura, S. Shiomi and S. Uchiyama, "Dependence of wall dynamics on damping constant in bubble films", IEEE Trans. Magn. **18**(6), 1343–1345 (1982).

[198] T. O'Dell, *Ferromagnetodynamics: The dynamics of mangetic bubbles, domains and domain walls* (John Wiley and Sons, New York, USA, 1981).

[199] C. M. A. Capella and F. Otto, "Wave-type dynamics in ferromagnetic thin films and the motion of Néel walls", Nonlinearity **20**, 2519–2537 (2007).

[200] K. Fabian, A. Kirchner, W. Williams, F. Heider and T. Leibl, "Three-dimensional micromagnetic calculations for magnetite using FFT", Geophys. J. Int. **124**, 89–104 (1996).

[201] A. E. Labonte, "Two-dimensional Bloch-type domain walls in ferromagnetic films", J. Appl. Phys. **40**(6), 2450 (1969).

[202] S. W. Yuan and H. N. Bertram, "Domain-wall dynamic transitions in thin films", Phys. Rev. B **44**(22), 12395–12405 (1991).

[203] L. G. Korzunin, B. N. Filippov, F. A. Kassan-Ogly and I. Chaikovsky, "A novel type of domain walls with two-dimensional magnetization distribution in magnetic triaxial films", J. Magn. Magn. Mater. **298**, 1–6 (2006).

[204] J. García-Ojalvo and J. Sancho, *Noise in spatially extended systems* (Springer, New York, 1999).

[205] D. Berkov, K. Ramstöcck and A. Hubert, "Solving Micromagnetic Problems. Towards an Optimal Numerical Method", Phys. Stat. Sol. A **137**(1), 207–225 (1993).

[206] S. Yuan and H. Bertram, "Fast adaptive algorithms for micromagnetics", IEEE Trans. Magn. **28**(5), 2031–2036 (1992).

[207] N. Hayashi, K. Saito and Y. Nakatani, "Calculation of demagnetizing field distribution based on Fast Fourier Transform of convolution", Jpn. J. Appl. Phys. **35**(12A), 6065–6073 (1996).

[208] A. Aharoni, *Introduction to the theory of ferromagnetism* (Clarendon Press, Oxford, 1996).

[209] W. Scholz, "Micromagnetic simulation of thermally activated switching in fine particles", Ph.D. Thesis, Wien, 1999.

[210] S. Chikazumi and N. Imamura, "Computer calculation of fanning spin structure in magnetic thin films and determination of exchange stiffness constant", Czech. J. Phys. B **21**(4–5), 537–540 (1971).

[211] M. Ondris and Z. Frait, "Ferromagnetic resonance in thin permalloy films", Czech. J. Phys. B **11**(12), 883–885 (1961).

[212] J. Atulasimha, "Characterization and modeling of the magnetomechanical behavior of iron-gallium alloys", Ph.D. Thesis, Univ. Maryland, Maryland, 2006.

[213] J. Weston, A. Butera, T. Lograsso, M. Shamsuzzoha, I. Zana, G. Zangari and J. Barnard, "Fabrication and characterization of $Fe_{81}Ga_{19}$ thin films", IEEE Trans. Magn. **38**(5), 2832–2834 (2002).

[214] P. Hong and G. Olson, "Magnetic origin of the lattice instability of FePd alloys", J. Magn. Magn. Mat. **129**(2–3), 191–199 (1994).

[215] M. Hansen, *Constitution of binary alloys*, 2nd ed. (McGraw-Hill, New York, USA, 1958).

Publications

- M. Porta, T. Castán, P. Lloveras, A. Planes and A. Saxena, *Spatially correlated disorder in self-organized precursor magnetic nanostructures* Phys. Rev. B **76**, 054432 (2007).

- P.Lloveras, T. Castán, M. Porta, A. Planes and A. Saxena, *Influence of Elastic Anisotropy on Structural Nanoscale Textures*, Phys. Rev. Lett **100**, 165707 (2008).

- M. Porta, T. Castán, P. Lloveras, T. Lookman, A. Saxena and S.R. Shenoy, *Interfaces in ferroelastics: Fringing fields, microstructure, and size and shape effects*, Phys. Rev. B **79**, 214117 (2009).

- P.Lloveras, T. Castán, M. Porta, A. Planes and A. Saxena, *Glassy behavior in martensites: Interplay between elastic anisotropy and disorder in zero-field-cooling/field-cooling simulation experiments*, Phys. Rev. B **80**, 054107 (2009).

- X. Ren, Y. Wang, K. Otsuka, P. Lloveras, T. Castán, M. Porta, A. Planes and A. Saxena, *Ferroelastic nanostructures and nanoscale transitions: Ferroics with point defects*, MRS Bull. **34**, 838 (2009).

- P.Lloveras, T. Castán, M. Porta, A. Planes and A. Saxena, *Thermodynamics of stress-induced ferroelastic transitions: Influence of anisotropy and disorder*, Phys. Rev. B, to be published.